Workflow for Sand Control Testing of Injection Wells in Steam Assisted Gravity Drainage (SAGD)

by

Abdulla Jamal Abou-Kassem

A thesis submitted in partial fulfillment of the requirements for the degree of

Master of Science

in

Petroleum Engineering

Department of Civil and Environmental Engineering
University of Alberta

ABSTRACT

This research aims at tackling a specific production engineering problem in sand retention testing (SRT). One common practice of operational oil companies is to prevent sanding by deploying standalone screens (SAS). SAS consists of slotted liners (SL), wire wrap screens (WWS), and punched screens (PS), among others.

A systematic methodology was developed for SL design using the SRT for steam-assisted gravity drainage (SAGD) injectors. Although the solution is particular for the SAGD injector, the same or similar methodology can also be applied for any other injection or even production well. SRT investigation for SAGD injector flowback was considered as a demonstration for the capability of the proposed methodology in comparison to previous techniques. The previous techniques sometimes rely on hypothetical or invalid assumptions due to the lack of necessary field data to perform such a study. Often, field data are confidential and nearly impossible to obtain for a hazardous scenario like a thermal injector flowback.

The proposed methodology consists of three fronts. The first front is to estimate the laboratory testing variables or operational parameters based on case-specific data and reservoir simulations to assess the flowback. The simulation accounts for the unique reservoir characteristics that change from one field to another. The STARS module of the Computer Modelling Group (CMG) simulator was used to predict the consequences of SAGD injector flowback, which is the only possible way of sanding from a reservoir engineering viewpoint. Moreover, one of the natural gas flow correlations was coupled to the CMG model to ease the modification of production system variability by an interactive, in-house developed, excel program. The coupling reduces the computational-time from about 20 hours to less than 1 hour. The computational-time reduction

was due to using a 2D-model, based on symmetry, instead of the 3D-model. Accounting for thermodynamic equilibrium changes the understanding of the problem drastically by avoiding inaccurate assumptions used in the past.

The second front is to develop a new SRT set-up specialized for SAGD injector flowback laboratory testing and maintain a cost-effective research budget. Intensive testing was performed to troubleshoot the associated problems with high-velocity gas flow.

The final front was to verify the performance and efficiency of the developed testing set-up by conducting six tests. Furthermore, more representative reproducibility criteria were proposed to ensure testing repeatability.

SRT results show that the current industry practices for SL selection, which rely upon field experience or rules of thumb, are not conservative as previous researches claim. Eventually, this research should be considered as a single-step only in SRT for SAGD injector flowback, and necessary methodology enhancements and facility upgrades should be investigated in future work.

DEDICATION

To my father (Jamal Abou-Kassem), mother (Rafida Abdulghani), sisters (Hiba Eyesha and Tesneem), brother (Jameal), brother-in-law (Nimer Odtallah), and my beautiful niece (Mariam).

ACKNOWLEDGMENTS

I would like to express my sincere appreciation to all who contributed to this work.

I am grateful to my supervisor Prof. Alireza Nouri for his patience and endless support, Prof. Hassan Dehghanpour, and Prof. Andy Li for their fruitful discussions.

Further thanks to all members of the examination committee for their valuable suggestions to improve this study.

I would like to acknowledge RGL Reservoir Management Inc. for the financial support, and the Natural Sciences and Engineering Research Council of Canada (NSERC) for funding this research through their Collaborative Research and Development (CRD) Grants Program. A special thank you to Anas Sidahmed for his involvement and contribution in CMG modelling work, Omar Ktob and Dr. Mohammed Haftani for their contribution in conducting laboratory experiments, Dr. Mahmood Salimi for his help in developing testing facilities, and Menatalla Ahmed for her contribution in improving the technical writing and thesis formatting.

I sincerely thank Prof. Jamal Abou-Kassem and the Computer Modeling Group (CMG) technical support team for their reservoir simulation feedback. Many thanks to CMG for the provided, free of charge version, at the University of Alberta for educational proposes.

I owe this work to my undergraduate supervisor Prof. Hazim Al-Attar and all professors at Chemical and Petroleum Engineering Department at the United Arab Emirates University (UAEU) for motivating my research passion.

TABLE OF CONTENTS

LIST OF TABLES

LIST OF FIGURES

LIST OF SYMBOLS AND ABBREVIATIONS

Symbols

A	Cross-sectional area
A^{SHS}	Superheated steam area
$BHP_{available}^{flowback}$	Available (specified) BHP during flowback
$BHP_{required}^{flowback}$	Required BHP during flowback
d	Grain diameter
d90, d50 or *d10*	Cumulative percentage of passing grain sizes
D90, D50 or *D10*	Cumulative percentage of retained grain sizes
E	Efficiency
f	Friction factor
f	Weight percentage
ID	Inner diameter
k_g	Effective gas permeability
k_{rg}	Relative gas permeability
K	Permeability
$K_{retained}$	Retained permeability
K_{ϕ}	PSD mathematical kurtosis
K_G	PSD graphical kurtosis
md	Millidarcy
$M_{wt.}$	Gas molecular weight
M_z	PSD graphical Mean
N_{Re} or R_e	Reynolds dimensionless number
OD	Outer diameter
P	Pressure
Q_g^{sc} or Q_g	Gas volumetric flow rate at standard conditions
Q_g^{*}	Gas volumetric flow rate at specific pressure
r_{SHS}	Superheated steam radius
S_g	Gas saturation

$S_g^{FB\ t=-10}$	Gas saturation before the flowback
S_o	Oil saturation
S_w	Water saturation
SK_i	PSD graphical inclusive skewness
SK_ϕ	PSD mathematical skewness
T	Temperature
thou	Thousandths of an inch
μ	fluid viscosity
v	velocity
v^{sonic}	Sonic velocity
V	Volume
V^{SHS}	Superheated steam volume
wt.%	Weight percentage or fraction
$\bar{x}_\phi$	PSD mathematical mean size
z or z-factor	Gas compressibility factor or gas correction factor
α_c	Unit conversion factor
$\boldsymbol{\beta}$	Biot's coefficient
β*	dimensionless compressibility
$\mathcal{F}$	Friction term in Bernoulli's equation
ω	Work term in Bernoulli's equation
σ_i	PSD graphical inclusive standard deviation
σ_ϕ	PSD mathematical standard deviation
$\boldsymbol{\sigma'_{i,v}}$	Initial vertical effective stress
ρ	Fluid density
$\Delta P_{required}^{Tubing\ model}$	Tubing required pressure drop
Φ	Terminal potential
ϕ	logarithmic Phi used to describe PSD
ϕ_{50}	Median size

Abbreviations

2D	Two dimensions
3D	Three dimensions
AER	Alberta Energy Regulator
API	American petroleum institute
BHFP	Bottom hole flowing pressure
BHP	Bottom hole pressure
BHSP	Bottom hole static pressure
CDF	Cumulative distribution function
CMG	Computer modelling group
CTP	Constant terminal pressure
CTR	Constant terminal rate
CSS	Cyclic steam stimulation
CWE	Cold water equivalent
DC-1 and DC-3	Sand types representative for McMurry formation
DI-water	De-ionized liquid water
EGM	Existing gas mass
EOR	Enhanced oil recovery
FB	Flowback
HIS	Inclined Heterolithic Strata (geological structure)
HP	High-pressure
HT	High-temperature
IOIP	Initial Oil in Place
IPR or WPR	Inflow pressure performance
LGR	Local grid refinement
MFM	Mass flowmeter
NGMR	Net gas mass remaining
NSA	Nodal system analysis
OHCP	Open hole gravel pack
PDF	Probability density function
PS	Punched screens

PSD	Particle size distribution
PV	Pore volume
Rcf	Reservoir cubic foot
RGL	Service company name (RGL Reservoir Management Inc)
RHS	Right hand side
RMS or R^2	Root mean square
SAGD	Steam-assisted gravity drainage
SAS	Standalone screens
Scf	Standard cubic foot
SOP	Standard operational procedure
SHS	Superheated steam
SI	International units' system
SL	Slotted liners
SQ	Steam quality
SRT	Sand retention testing
SRT-I	Initial sand retention testing set-up
SRT-II	Modified sand retention testing set-up
SRT-III	Final sand retention testing set-up
SSSV	Subsurface safety valve
STARS	A CMG module that accounts for temperature changes
SW	Aperture size, slot width or slot aperture
TLS	Traffic light system
TPR or CPR	Outflow pressure performance
TVD	True vertical depth
USBM	U.S. Bureau of Mines
USCU	United States customary units
Well-block	Block that contains the well
WHP	Wellhead pressure
WWS	Wire wrap screens

Citation remark

if a citation appears at the end of the paragraph after the period, it indicates the citation is for the entire paragraph.

Chapter 1: INTRODUCTION

1.1 Background

Oil sand represents a unique reservoir, where the pores of unconsolidated reservoir sediments are filled with very viscous hydrocarbons like bitumen and kerogen, which requires thermal techniques to commercialize its production. (Boggs, 2009)

Alberta oil sands represent 95% of Canada's oil reserve, 10% of the world's oil reserve, and covers a total area of 142 thousand km^2. The oil sands contain over 1.7 trillion barrels of Initial Oil in Place (IOIP). Only 3% of the IOIP can be extracted by surface mining and the remaining 97% to be produced by in-situ extraction. It is economically unfeasible to yield more than 10% of IOIP, equivalent to 166 billion barrels, by the current thermal technology. The largest, in terms of areal extension, by far is Athabasca, followed by Cold Lake, and Peace River. These three regions make up the majority of Alberta oil. ("Oil Sand Geology & the Properties of Bitumen," Sep. 23, 2019)

Furthermore, McMurray formation thickness varies from few millimetres up to more than 110 meters in the eastern part of Alberta. However, the overburden thickness varies from a few centimetres present in outcrops along the Athabasca River and increases towards the southwest to reach a maximum value of 450 meters. (Hassanpour, 2009)

However, thermal recovery is one of the most efficient Enhanced Oil Recovery (EOR) techniques, which comprises steam injection and in-situ combustion. The steam injection includes cyclic steam stimulation (CSS) and steam-assisted gravity drainage (SAGD) operations that mainly involve different steam injection strategies. The aim is to reduce the viscosity of bitumen (ultra-heavy oil), which results in a production rate exceeding the economic limit. Investigation shows that steam injection temperatures ranging from 200°C to 350°C are needed to reduce bitumen viscosity dramatically. The steam drive has been considered to be a primary technique before the invention of CSS, which shows significant improvement of sweep efficiency compared to steam drive. (Green, 1998)

Moreover, the selection of the CSS or SAGD process is dictated by the geology of the reservoir. Cold Lake deposit lends itself better to CSS, whereas the Athabasca deposit responds better to SAGD. The statistics by the Alberta Energy Regulator show a dramatic increase in the in-situ bitumen production rate in the last 15 years due to the contribution of Athabasca oil sand ("In-situ

Bitumen Extraction," Sep. 23, 2018). Alberta's unconventional basin production has a decline rate of only 4 % per year compared to conventional oil basins with a typical decline rate of 20% per year. The average decline rate for shale depositions is 40% per year, which implies a continuous rig demand and associated exploration risk. ("Oil Sand Geology & the Properties of Bitumen," Sep. 23, 2019)

In general, SAGD operation involves a sand control screen in both steam injection and oil production wells. The screens are deployed to prevent the loose sand particles from entering the wellbore. In production wells, sand control aims at maintaining well productivity and preventing sand production. It results in minimizing the negative environmental impacts of processing contaminated sand with oil that requires chemical treatment before dumping. A stand-alone screen (SAS) has been proven to be a useful sand control tool in unconsolidated sand. Slotted liner (SL), wire-wrapped (WWS), punched (PS), and expandable mesh are the common SAS types. SAS performance is very dependent on the characteristic design parameters to specify slot aperture size (slot width) while plugging, mechanical integrity, and cost management are based on slot density and corresponding open area to flow. (Fattahpour et al., 2018b)

It is widely believed that in the current design procedure for SLs, the aperture size is a specific ratio to a single point of the particle size distribution (PSD), e.g. $3 \times D_{50}$ or $1.4 \times D_{10}$. The aperture size design in the SL is based on the PSD description that maintains a stable bridge of sand grains above the screen slots. However, the impact of the selected slot aperture should not cause significant permeability reduction in the near-wellbore region. A good measure of such impact can be quantified by the ratio of final permeability (K_{final}) to the initial intact permeability ($K_{initial}$). Retained permeability ($K_{retained} = K_{final}/K_{initial}$) represents the reduction in permeability because of fines migration and pore plugging due to liner's presence. The current acceptable lower limit is an aperture size that results in a retained permeability ratio of more than 50% and satisfies the upper limit to restrict sand production volume to less than 1% of the liner volume. (Fattahpour et al., 2018b; Montero, 2019; Roostaei et al., 2018)

Often, the SAS performance is evaluated by laboratory testing using sand retention testing (SRT) facilities. Most of the research works focused on sand control in SAGD producers to come up with sand control design criteria for SLs (Mahmoudi, 2017) and wire wrap screens (Montero, 2019), slots profile influence, and open hole gravel pack design (Roostaei et al., 2018).

The SL has the advantages of other SAS because of its reasonable mechanical integrity and acceptable produced sand volumes, in addition to its cost efficiency, which makes it the most favourable candidate for SAGD injectors completion (Fattahpour et al., 2018b). In steam injection wells, sand control aims to prevent sand accumulation in the wellbore while a steam injector undergoes either a normal shut-in, wellhead closure, or an unexpected flowback based on the differential potential between the reservoir and the wellbore. (Fattahpour et al., 2018a; Mahmoudi et al., 2018a)

1.2 Problem Statement

Aperture size selection is well-explored for SLs in SAGD producers, but there are no design criteria for SAGD injectors, for any SAS, other than the belief that the current design criteria for SAGD producers may work for the SAGD injectors, which may not be necessarily true under real circumstances and operational conditions. SAGD injectors in McMurry are equipped with SLs with maximum available slot density and smallest possible slot aperture to ensure sand prevention, which is considered as a conservative selection (Fattahpour et al., 2018a; Mahmoudi et al., 2018a). Often, industry practice prefers being conservative rather than risky, especially in vague sanding mechanisms and scenarios.

However, current understanding of SAGD injectors shut-in consequences, possible flowback scenarios, sanding mechanism, associated thermodynamics, and their impact on optimal SAS selection are still untouched. There were few preliminary pieces of research conducted before this investigation. Those research works were intended to explore SAS performance in SAGD injectors based on hypothetical assumptions, which may be inconsistent with SRT operational parameters, testing procedure, and SRT configurations. The experimental findings from past research did not match sand production expectations. The authors proposed a relatively large aperture size of $(1.4 \times D_{10})$ in well-sorted sand to maintain acceptable SLs performance, yet the industry prefers the smallest possible aperture size. Furthermore, the investigation was conducted for a single PSD with low clay content, which does not ensure that the proposed aperture size applies to another PSD. Finally, the flowback fluid used was liquid water to mimic low Steam Quality (SQ) flowback, which is unlikely the case for steam injection wells. (Mahmoudi et al., 2018a)

However, applying the $(1.4 \times D_{10})$ size criterion in the high SQ flowback case proposed by Fattahpour et al. (2018a) results in negligible produced sand. It means that the proposed criterion by Mahmoudi et al. (2018a) is very conservative compared to that of Fattahpour et al. (2018a). Accordingly, any criteria for slot design for SLs should maintain sand production below acceptable limits. The criteria proposed for low-SQ flowback SRT is already decided to be relatively wider than the favourable industry size. Besides, several flowback stages were conducted in each SRT test, and only the cumulative produced sand was compared with the aperture size to evaluate SAS performance. Eventually, the decision of whether the industry standards are conservative or not depends on SRT performance evaluation rather than the selected SL aperture size.

1.3 Research Hypothesis

Logic indicates that sand control design criteria are equally crucial for SAGD injector and producer. While the literature covers most aspects of design for SAGD producers, there is a considerable gap in the literature when it comes to sand control design criteria for SAGD injectors. It seems the industry overcomes this situation by being conservative, according to previous research in this field (Fattahpour et al., 2018a; Mahmoudi et al., 2018a). There is a need for a systematic SRT procedure to quantify and evaluate the sanding performance of SLs in SAGD injectors. Indeed, developing sand control design criteria for SAGD injectors may not be as easy as it is for SAGD producer, but technically it should be possible to assess SAS performance by SRT in the laboratory.

The industry tends to use small aperture size slots for SL completion. However, some researches argue that this strategy may result in considerable formation damage and injectivity loss due to fines migration in case of an injector flowback. The conclusions made by previous researches are questionable because the research neglected reservoir, production and thermodynamics principles in the assessment of testing variables. Moreover, the SRT set-up flowlines appear to consume most of the applied pressure. Accordingly, the working hypothesis of this research is the small aperture size will not cause formation damage in the SRT experiments.

1.4 Research Objectives

The primary objective of this research is to eliminate as many hypothetical assumptions as possible by exploring SAGD injector flowback possibility and incorporating reservoir engineering, reservoir simulation, and thermodynamics to evaluate representative operational parameters. The testing incorporates initial sample saturation, flowback parameters such as number of stages, flowback fluids, applied stress during testing, flowback differential pressure, and other related SRT parameters. The research examines the flowback in SAGD injector based on reservoir and production engineering concepts.

To allow emulating SAGD injection wells during flowback, the existing SRT testing facilities were modified to mimic SAGD injector flowback and yield representative results. Furthermore, another objective is to examine the industry practice for aperture size selection for SLs in SAGD injectors.

In summary, the objectives include:

- Obtain reasonable SRT operational parameters to mimic SAGD flowback.
- Operational parameters guide the modifications to the existing SRT facility.
- Propose a systematic testing scheme that best represents the SAGD injector flowback scenario.
- Examine the current industry practice by using the modified SRT facility & testing scheme.

1.5 Research Methodology

The research is performed in the following steps:

1. Acquire an in-depth understanding of SRT for SAGD injector flowback.
2. Develop a representative SAGD model using Computer Modelling Group (CMG) STARS.
3. Couple CMG model with a suitable correlation to predict flowing bottom hole pressure (BHP) during injector flowback according to nodal system analysis (NSA) concepts.
4. Obtain the operational parameters for a representative SRT testing based on the worst-case scenario.
5. Modify the existing SRT facility to adapt to SAGD injector testing.
6. Explore several testing procedures and nominate the most suitable technique.
7. Examine the current industry aperture size selection for SAGD injector through SRT experimentation.

1.6 Significance of Work

The purpose of this work is to initiate a systematic procedure for conducting SRT. The research involves using the CMG STARS model, understanding compressible fluid flow in a conduit, constructing and modifying SRT facility and scheme to help future investigations related to SAGD injector near wellbore region, and justifying the current industry selection practice in selecting the aperture size of SLs.

The CMG STARS model was used to overcome the lack of data related to possible SAGD injector failures that may follow a severe flowback. Coupling a natural gas flow correlation with the simulator expedites the simulations. The current SRT testing facility was modified to adapt a testing procedure suitable for injection flowback scenarios. Using the modified SRT proves that incomplete and misleading conclusions leading to claim that the industry practice is conservative in aperture size does not have any detectable impact on the well performance.

1.7 Thesis Layout

This thesis includes the following seven chapters.

Chapter 1: contains an introduction to Alberta oil sands, thermal EOR, and SAS importance in SAGD operation, followed by problem statement, research hypothesis, objectives, methodology, and contributions.

Chapter 2: provides a brief literature review of the concepts utilized in this study.

Chapter 3: describes the CMG STARS model, a natural gas flow correlation and emphasizes similarities in the properties between natural gas and superheated steam.

Chapter 4: combines the STARS results with gas flow correlation in an iterative technique to assess flowing BHP during injector flowback and assign the SRT operational parameters.

Chapter 5: demonstrates stages of modifications and developments for SRT facility and testing procedure.

Chapter 6: elaborates on SRT results to examine the performance of SLs based on industry selection practices, the most suitable testing program, and analysis of testing results.

Chapter 7: summarizes research findings and discusses the possible future direction of this work.

Chapter 2: **LITERATURE REVIEW**

This chapter includes essential topics related to sand control testing for SAGD wells, particularly, injection wells. It involves sand characterization, general review for oil sands and bitumen, rock and fluid properties for gas flow in porous media, thermodynamics role in SAGD production, sand control testing for SAGD, and Bernoulli's equation application.

2.1 Sand Characterization

Reservoir geology is often a valuable key for understanding some reservoir phenomena that alter petrophysical properties and may lead to reduced injectivity. Geologists believe that the chemical and physical properties of geomaterials are closely related to depositional environments and the saturating fluids.

Sedimentary rocks are classified into three fundamental types: terrigenous siliciclastic, chemical/biochemical, and carbonaceous. Each of these major groups of sedimentary rocks can be further subdivided based on grain size and mineral composition. Authigenic constituents represent minerals precipitated from pore water within prepacked sediments that form the so-called cement material. (Boggs, 2009)

The following section includes topics like the geological description of McMurray oil sand, the description of unconsolidated particles, and the classification of the McMurray formation based on the particle size distribution (PSD).

2.1.1 McMurray Oil Sand from Geology Prospective

Oil sand is oil-rich sediments that contain, on average, a weight fraction of 10% bitumen, 5% water, and 85% solids. Bitumen content can be as high as 20 wt.% in some sections. The solids are mainly formed of primarily quartz silica sand, usually over 80 wt.%, with a small fraction of fine clay and potassium feldspar. Clay material consists of chlorite, illite, kaolinite and smectite. Furthermore, there is an inversely proportional trend between fines content and bitumen weight fraction that affects reservoir quality. Moreover, water content varies from almost zero to as high as 9 wt.%. The water content has been found to be directly proportional to fines content and inversely proportional to both bitumen content and section quality. ("Oil Sand Geology & the Properties of Bitumen," Sep. 23, 2019)

The McMurray formation belongs to the lower part of the Mannville Group, which exists within the fluvial-estuarine channel point of lower Cretaceous. The upper Mannville Group in lower Cretaceous contains the Wabiskaw member, which often is considered a cap rock. The Clearwater formation and Grand Rapids formation belong to overburden layers. **Figure 2.1** presents the typical geological stratigraphy in Northern Alberta. McMurray formation thickness varies from a few millimetres up to more than 110 meters in the eastern part of Alberta. The overburden thickness varies from a few centimetres present in outcrops along the Athabasca River and increases towards the southwest to reach a maximum depth of 450 meters. A thick oil sand formation, along with considerable overburden thickness, makes the site a right candidate for SAGD operations. However, the variety of depositional environments in the McMurray formation results in a complex heterogeneity in the reservoir. (Hassanpour, 2009)

The McMurray formation is divided into the lower, middle, and upper units based on the associated depositional environment and the corresponding reservoir quality. The lower unit was deposited within the fluvial environment and had extremely poor sorted PSD ranging from highly angular fines to coarse sand. The upper unit is horizontal strata, which is often in sharp contrast to Inclined Heterolithic Strata (IHS). **Figure 2.2** presents a schematic diagram that describes the IHS. It has an upward coarsening tendency in two cycles separated by a thin layer, and within each cycle, several lithofacies are present, which indicate a significant degree of heterogeneity. (Hassanpour, 2009)

The Middle McMurry formation is the thickest part and has the best reservoir quality. It can be subdivided into two units, Large-scale Cross-stratified Sand and IHS. The first unit has a large scale cross stratified coarse sand, which is characterized by excellent permeability, porosity, and bitumen saturation. The thin segregated shale laminations that are embedded into a thick homogenous bed set, with a minimum thickness of half a meter, is believed to be due to the marine tidal depositional environment. The second unit consists of heterogenous IHS bodies distributed within the first unit. IHS plays a vital role in the steam chamber development of in-situ processes. The depositional environment is as complex as “Forest deposits of small, Gilbert-type deltas prograding northward into a standing lacustrine or lagoonal body.” (Hassanpour, 2009)

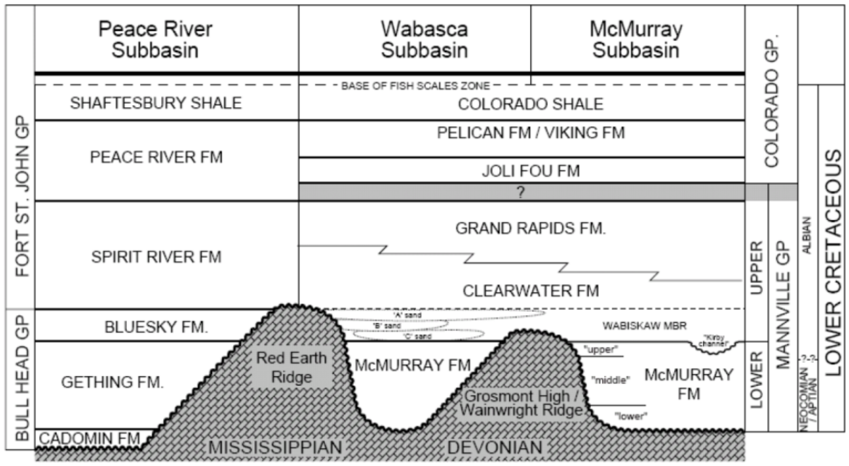

Figure 2.1. Stratigraphy of Northern Alberta (Hassanpour, 2009).

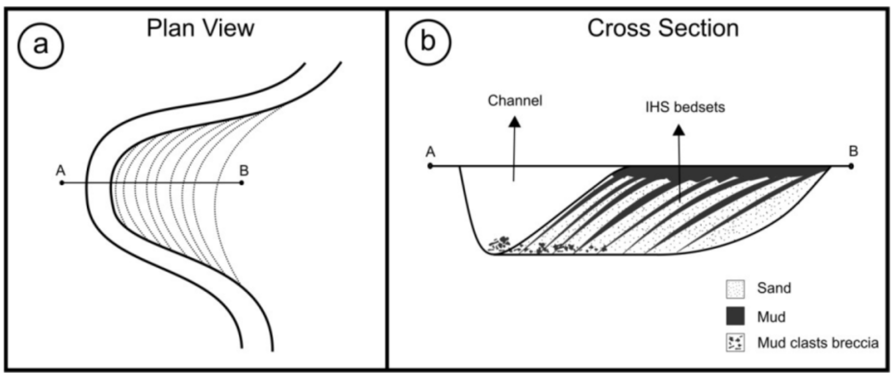

Figure 2.2. Schematic representation of IHS (Hassanpour, 2009).

2.1.2 Geologist Classification of Unconsolidated Particles

Grain size is an essential descriptive factor that reflects weathering and erosion processes. In general, sediments can range in size from boulder to clay size particles. Sedimentologists are interested in grain size measuring techniques, determining particle size distribution, and the use of data to gain perspective about the depositional environment.

Udden-Wentworth modified scale, shown in **Table 2.1**, was proposed by Udden in 1898 and extended by Wentworth in 1922 to classify solid particles. According to this classification, clay size measures less than 1/256 mm. Krumbein made a significant contribution in 1934 by adding logarithmic Phi (ϕ), which enhances representation abilities by using an equal steps scale. Eq. 2.1 shows the mathematical relation of the proposed Phi scale.

$$\boldsymbol{\phi = -\log_2(d)} \qquad \text{(Eq. 2.1)}$$

where (ϕ) is Phi size and (d) is grain diameter in millimetres. It is a common practice in PSD graphs to plot the coarse sizes to the left and the fine sizes to the right. (Boggs, 2006)

There are several techniques used to measure grain size. The selection is based on the objective of the study, range of grain size to be measured, and the degree of consolidation of sediments. Sieving or sieve analysis is considered to have sufficient accuracy for gravel-size to silt-sized particles for unconsolidated sediments. However, sedimentation techniques based on particles' settling velocity provide better accuracy for clay-sized particles compared to coarse-size particles. The reason is the grain shape is measured by such parameters as grain sphericity, affects the settling velocity in large grains as drag forces are size sensitive. However, the technology of associated measurements, which use photo-hydrometer, Sedi-graph, laser-diffractor analyzer, electro-resistance analyzer and image analysis, are costly because they require sophisticated equipment and high experience to run such measurements to produce reliable results. (Boggs, 2009)

Mechanical sieving is considered at the top of the list due to its relatively cheap cost in producing representative measurements. Thin section analysis preparation combined with a reflected-light binocular microscope is recommended to estimate consolidated sediments grain size with minimal disturbance of its original condition. **Table 2.2** summarizes the methods of grain size analysis based on the sample category. (Boggs, 2009)

Table 2.1: Udden-Wentworth Modified Scale (Boggs, 2006).

Millimeters (mm)		Micrometers (µm)	Phi (ϕ)	Wentworth size class	
	4096		-12.0		
				Boulder	Gravel
	256		-8.0		
				Cobble	
	64		-6.0		
				Pebble	
	4		-2.0		
				Granule	
	2.00		-1.0		
				Very coarse sand	Sand
	1.00		0.0		
				Coarse sand	
1/2	0.50	500	1.0		
				Medium sand	
1/4	0.25	250	2.0		
				Fine sand	
1/8	0.125	125	3.0		
				Very fine sand	
1/16	0.0625	63	4.0		
				Coarse silt	Silt
1/32	0.031	31	5.0		
				Medium silt	
1/64	0.0156	15.6	6.0		
				Fine silt	
1/128	0.0078	7.8	7.0		
				Very fine silt	
1/256	0.0039	3.9	8.0		
				Clay	Mud
	0.00006	0.06	14.0		

Table 2.2: Methods of Measuring Sediment Grain Size (Boggs, 2009).

Type of sample	Sample grade	Method of Analysis
Unconsolidated sediment	Boulders	Manual measuremnts of individual clasts
	Cobblers	
	Pebbles	
	Granules	Sieving, settling-tube analysis, image analysis
	Sand	
	Silt	Pipette analysis, sedimentation balances, sedigraph, laser diffractometry, electro-resistance size analysis
	Clay	
Lithified sedimentary rock	Boulders	Manual measuremnts of individual clasts
	Cobblers	
	Pebbles	
	Granules	Thin-section measurement, image analysis
	Sand	
	Silt	Electron microscopy
	Clay	

The measured grain size of a specific sample can be illustrated in a graphical form, which is the most common use in this domain. The graphical representation includes three methods: histogram and frequency curve, cumulative arithmetic curve, and log probability scale cumulative curve, as shown in **Figure 2.3** (Boggs, 2006).

The frequency curve is very similar in appearance to Probability density function (PDF), but it has asymmetric bell-shape. The cumulative curve is a clear representation of the PSD and mathematically corresponds to the cumulative distribution function (CDF), which is defined as the integral of PDF (Soong, 2004). The cumulative arithmetic curve produces S-shape, and the slope of the S-shape is an indicator for size sorting. A good sorting sample exhibits a very steep slope S-shape, whereas a poorly sorted sample exhibits a gentle slope of the S-shape. Furthermore, the evaluation of PSD is a common practice for sand control problems and evaluating PDF would not be hard based on the previously mentioned mathematical relation between CDF and PDF. (Boggs, 2006)

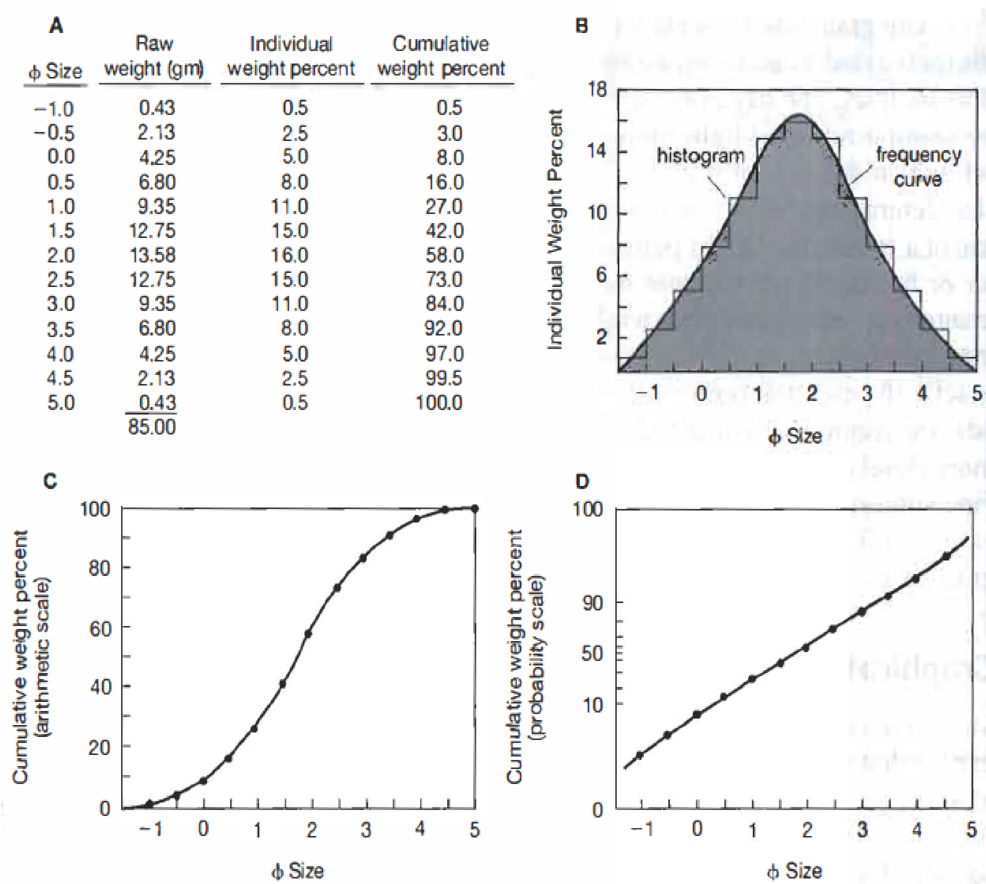

A

ϕ Size	Raw weight (gm)	Individual weight percent	Cumulative weight percent
−1.0	0.43	0.5	0.5
−0.5	2.13	2.5	3.0
0.0	4.25	5.0	8.0
0.5	6.80	8.0	16.0
1.0	9.35	11.0	27.0
1.5	12.75	15.0	42.0
2.0	13.58	16.0	58.0
2.5	12.75	15.0	73.0
3.0	9.35	11.0	84.0
3.5	6.80	8.0	92.0
4.0	4.25	5.0	97.0
4.5	2.13	2.5	99.5
5.0	0.43	0.5	100.0
	85.00		

Figure 2.3. Graphical representation of grain size: A) tabular form, B) frequency curve, C) cumulative arithmetic curve (or PSD), and D) log probability scale cumulative curve (Boggs, 2006).

Mathematical representation of grain size is considered as a better tool compared to the previously mentioned graphical techniques due to providing better understanding and more informative details about a given sample PSD. The definitions and mathematical expressions of a few statistical parameters that are usually reported for a given sample are given next.

Mode size is the most frequently occurring particle size in a sample. The mode is shown as a peak on the frequency curve and the inflection point or the steepest point of a cumulative curve. Median size (ϕ_{50} or D_{50}) is defined as the midpoint of grain distribution. Half of the grains by weight are larger than the median, and the other half are smaller. Arithmetic Mean size is approximated with a graphical mean because it is impractical to count the number of grains in a sample or measure the individual size of each grain to evaluate the arithmetic mean. Graphical Mean (M_z), inclusive graphical standard deviation (σ_i), inclusive graphical skewness (SK_i), and graphical kurtosis (K_G) are all calculated based on the five percentile values shown in **Figure 2.4**. (Boggs, 2006)

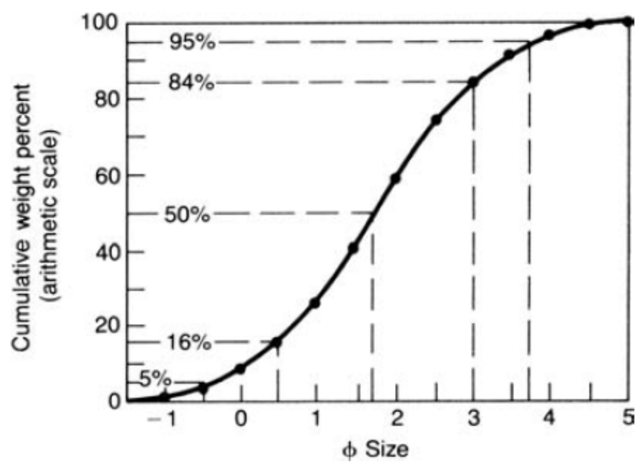

Figure 2.4. Method for calculating percentile values from cumulative curve (Boggs, 2006).

Graphical mean can be estimated using Eq. 2.2 as a function of Phi:

$$M_z = \frac{\phi_{16}+\phi_{50}+\phi_{84}}{3} \quad \text{(Eq. 2.2)}$$

Standard deviation is a unique mathematical expression for grain sorting. However, conventional formulation cannot be used with grain-size data. A graphical-statistical version of inclusive graphical standard deviation (Eq. 2.3) can provide an acceptable approximation and can illustrate the sorting degree that corresponds to each standard deviation. (Boggs, 2006)

$$\sigma_i = \frac{\phi_{84}-\phi_{16}}{4} + \frac{\phi_{95}-\phi_5}{6.6} \quad \text{(Eq. 2.3)}$$

Phi standard deviation	Verbal value expression
< 0.35	very well sorted
0.35 to 0.50	well sorted
0.50 to 0.70	moderately well sorted
0.70 to 1.00	moderately sorted
1.00 to 2.00	poorly sorted
2.00 to 4.00	very poorly sorted
> 4.00	extremely poorly sorted

Skewness is a measure of grain size sorting that reflects the distribution of grain size in the tail of the diagram. It is essential because sand size often yields asymmetric frequency curve or non-perfect bell-shaped curve with positive or negative skewness, as shown in **Figure 2.5**. The numerical value of skewness is obtained using the mathematical representation of inclusive graphical skewness expressed by Eq. 2.4 with the corresponding verbal value expression given below. (Boggs, 2006)

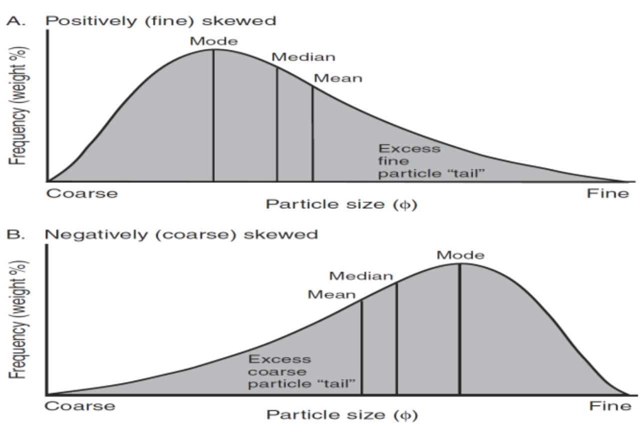

Figure 2.5. Skewed grain size frequency curves (Boggs, 2006).

$$SK_i = \frac{\phi_{84}+\phi_{16}-2\phi_{50}}{2(\phi_{84}-\phi_{16})} + \frac{\phi_{95}+\phi_{5}-2\phi_{50}}{2(\phi_{95}-\phi_{5})} \qquad \text{(Eq. 2.4)}$$

Calculated skewness	Verbal skewness
> +0.30	strongly fine skewed
+0.30 to +0.10	fine skewed
+0.10 to -0.10	near symmetrical
-0.10 to -0.30	coarse skewed
< -0.30	strongly coarse skewed

Kurtosis refers to the sharpness of the frequency curve. It indicates the degree of sorting in the

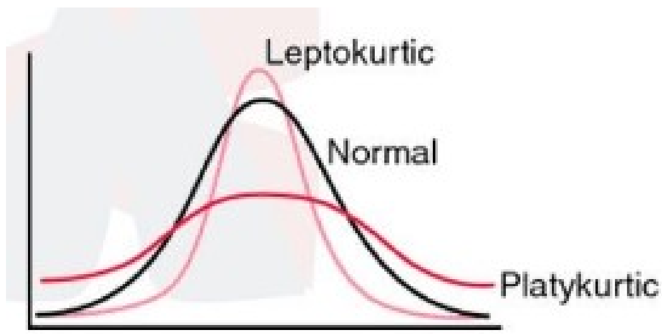

central portion.

Figure 2.6 shows kurtosis for normal distribution compared with a higher and lower kurtosis number.

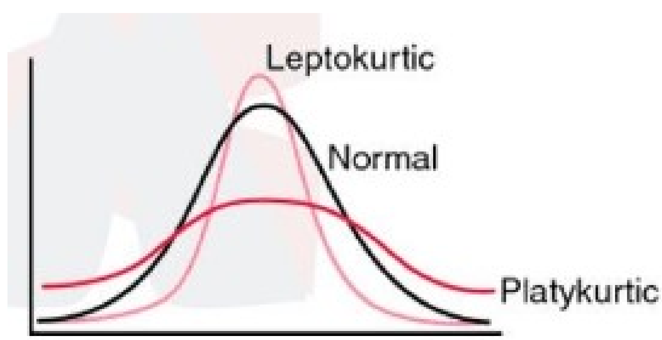

Figure 2.6. Kurtosis of a normal distribution curve.

The mean size ($\bar{x}_\phi$), standard deviation (σ_ϕ), skewness (SK_ϕ), and kurtosis (K_ϕ) of grain size distribution can be calculated without reference to the PSD curve using Eq. 2.5 through Eq. 2.8. A detailed solved example is presented in **Table 2.3**. (Boggs, 2009)

$$\bar{x}_\phi = \frac{\Sigma(fm)}{n} \qquad \text{(Eq. 2.5)}$$

$$\sigma_{\phi} = \sqrt{\frac{\sum f(m-\bar{x}_{\phi})^2}{100}} \quad \text{(Eq. 2.6)}$$

$$SK_{\phi} = \frac{\sum f(m-\bar{x}_{\phi})^3}{100\,\sigma_{\phi}^3} \quad \text{(Eq. 2.7)}$$

$$K_{\phi} = \frac{\sum f(m-\bar{x}_{\phi})^4}{100\,\sigma_{\phi}^4} \quad \text{(Eq. 2.8)}$$

where (*f*) is the weight percentage, Phi (*m*) is the midpoint in each interval, and *(n)* is total number in a sample. *n* =100 when *f* is presented in percentage, as shown in the following example in Table **2.3**.

Table 2.3: Form for Computing Moment Statistics Using ½ Size Classes (Boggs, 2009).

Class interval	midpoint	weight %	product	deviation	deviation squared
( )	m	f	f.m	m-ẋ	(m-ẋ)^2
0 - 0.5	0.25	0.9	0.2	-2.13	4.53
0.5 - 1.0	0.75	2.9	2.2	-1.63	2.65
1.0 - 1.5	1.25	12.2	15.3	-1.13	1.27
1.5 - 2.0	1.75	13.7	24.0	-0.63	0.39
2.0 - 2.5	2.25	23.7	53.3	-0.13	0.02
2.5 - 3.0	2.75	26.8	73.7	0.37	0.14
3.0 - 3.5	3.25	12.2	39.7	0.87	0.76
3.5 - 4.0	3.75	5.6	21.0	1.37	1.88
>4.0	4.25	2.0	8.5	1.87	3.50
total		100	237.8		
Class interval	product	deviation cubed	product	deviation quadrupled	product
( )	f. (m-ẋ)^2	(m-ẋ)^3	f. (m-ẋ)^3	(m-ẋ)^4	f. (m-ẋ)^4
0 - 0.5	4.08	-9.64	-8.67	20.51	18.46
0.5 - 1.0	7.69	-4.31	-12.51	7.02	20.37
1.0 - 1.5	15.52	-1.44	-17.51	1.62	19.75
1.5 - 2.0	5.40	-0.25	-3.39	0.16	2.13
2.0 - 2.5	0.39	0.00	-0.05	0.00	0.01
2.5 - 3.0	3.71	0.05	1.38	0.02	0.51
3.0 - 3.5	9.28	0.66	8.09	0.58	7.05
3.5 - 4.0	10.54	2.58	14.46	3.54	19.84
>4.0	7.01	6.56	13.12	12.28	24.56
total	63.61		-5.09		112.69

2.1.3 Description of McMurry Formation Sands

Statistical parameters, presented in Eq. 2.1 through Eq. 2.8, associated with the Udden-Wentworth modified scale, presented in **Table 2.1**, can describe any unconsolidated formation. However, extensive work was done to categorize Pike 1 project in McMurray formation, and more advanced parameters, presented in **Table 2.4**, were used to describe sand PSD when the range of distribution is narrow. Less than 1% of the McMurray formation particles are larger than the sand size of 2000 μm, and they were discarded from the PSD formulation. (Abram & Cain, 2014)

Table 2.4: PSD Coefficients (Abram & Cain, 2014).

Sorting coefficient, SC	d90/d10
Uniformity coefficient, UC	d60/d10
Devon slope factor, DSF	d65/d35
Percent fines	% volume <44 μm

Abram and Cain (2014) concluded that McMurray formation, especially in Pike 1 site, can be categorized into four primary sand footprints. **Table 2.5** presents the sand footprints along with the PSD coefficient for each sand. Mahmoudi (2017) replicated those characteristics with commercial sand for SRT testing, hence, eliminating the need for field sand core samples.

An essential remark for the notation of PSD percentiles, e.g. d90, d50 and d10, is the small letter d represents the cumulative percentage of passing grain sizes. The capital letter D represents the cumulative percentage of retained grain sizes. **Figure 2.7** represents two identical PSD's analyzed with passing and retained sieving analysis techniques.

Table 2.5: Synthetic Sand-Classes Characteristics (Abram & Cain, 2014).

	Sandprint 1	Sandprint 2	Sandprint 3	Sandprint 4
n	22	28	26	17
Uniformity coefficient	6.5	2.7	2.4	4.5
Sorting coefficient	9.0	3.4	3.1	7.3
Devon Slope Factor	1.5	1.3	1.3	1.8
d90	235	260	315	1,220
d50	145	175	215	570
d10	25	70	100	165
%fines	14.5	7.4	5.4	4.2

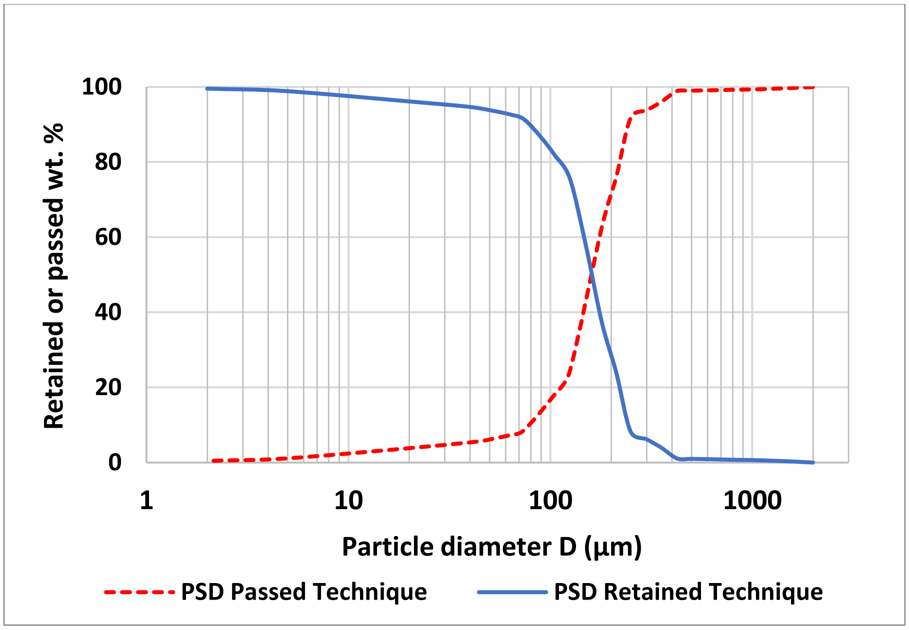

Figure 2.7. Demonstration of cumulative percentage of passing and retained grain sizes.

2.2 Sand Retention Testing for SAGD Application

SRT is a powerful technique to assess SAS and gravel pack performance in laboratory-controlled conditions. However, the results of SRT are prone to artifacts and entirely dependent on experimental conditions. The two dominant testing schemes are slurry and sand pack tests (Ballard & Beare, 2006). The following topics are discussed in this section: SRT description, gravel pack and slot profile impact, SAGD injectors operational conditions, common SRT facilities for SAGD injectors and testing results, and possible scenarios for injector flowback.

2.2.1 Overview of Sand Pack SRT

Sand pack testing with SRT (call pre-pack SRT) has been found to give a proper description for SAGD near-wellbore conditions. The pre-pack SRT is favoured over another SRT type, called Slurry SRT (Montero et al., 2018), in most SRT research for SAGD wells. Schematics of SRT equipment for SAGD producer and injector testing are presented in **Figure 2.8** and **Figure 2.9**, respectively.

The SRT setup consists of a flowback unit or injection unit, sand pack and data acquisition system for axial stress, pressure, and volumetric or mass flow rate. The injection unit in producer SRT has the capacity of three-phase simultaneous injection. The versatile design allows several investigations to be conducted with minor changes to the testing parameters. Brine salinity and pH effects on fines migration (Mahmoudi, 2017), WWS design criteria for SAGD producer (Montero, 2019), steam breakthrough impact (Mahmoudi et al., 2018b), and gravel pack design criteria (Roostaei et al., 2018) are some of the topics investigated by such versatile design.

The results have been analyzed regarding sanding and flow performances. Often, sanding performance is used to identify the upper limit of SAS aperture size, whereas flow performance is used to quantify the associated formation damage due to plugging of formation's pore throat. The optimal goal is to minimize the aperture size as much as possible without inducing severe formation damage (Montero et al., 2019). The assessment of operational testing parameters was based on in-depth understating of the problem.

However, SRT for injector facility schematic was developed to account for, low-steam-quality or compressed-liquid flowback scenario, as proposed by (Mahmoudi et al., 2018a) and, high-steam-quality or saturated-steam flowback scenario, as proposed by (Fattahpour et al., 2018a). The testing results mainly focus on sanding performance only without giving any attention to flow performance. Furthermore, the operational parameters were assigned based on hypothetical assumptions.

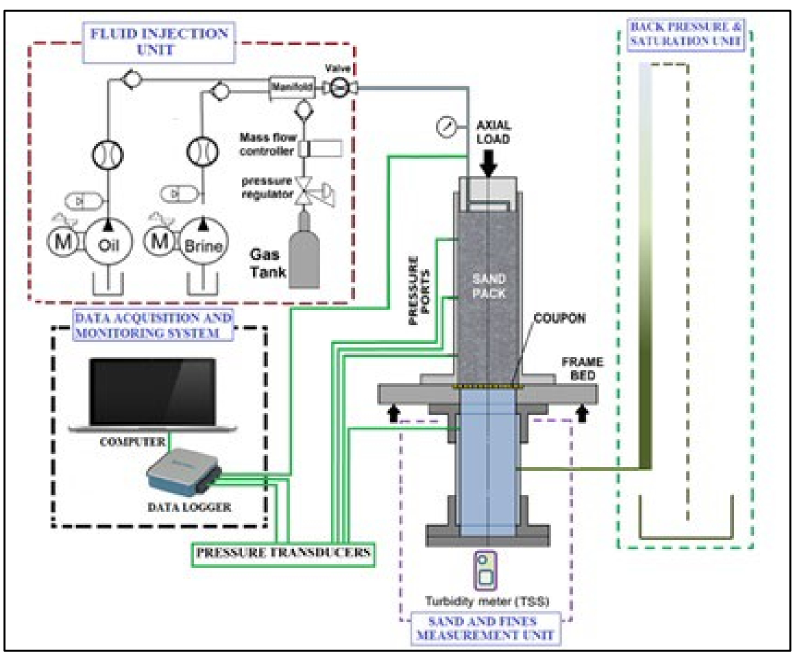

Figure 2.8. SRT facility schematic for SAGD producer (Montero et al., 2019).

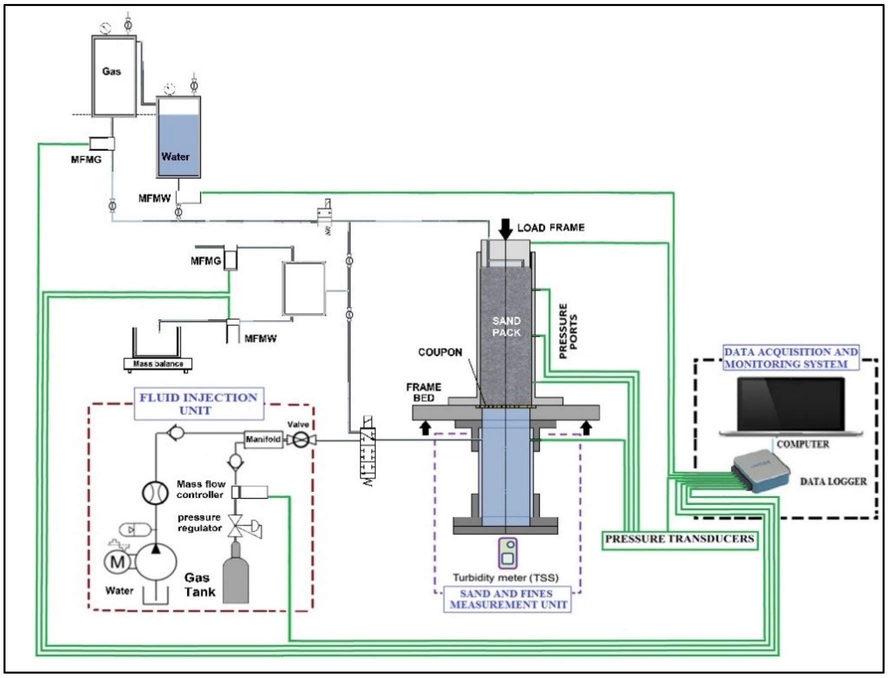

Figure 2.9. SRT facility (2 in 1) schematic for SAGD injector.

2.2.2 Gravel Pack and Slots Profile

Open hole gravel pack (OHGP) is a widely used completion practice in steam drive wells, often associated with SAS. It is well known that the gravel pack creates a higher permeability zone adjacent to the well, which reduces the pressure gradient and ultimately minimizes fines migration. A large-scale SRT facility was used to mimic this type of completion to investigate sand production, absolute pressures, the differential pressure across several sections of the SRT to enable accurate performance assessments of the gravel packs and SLs. The literature is rich with gravel pack design based on designers' perspective to minimize fines invasion to avoid pore plugging of the gravel pack itself (Roostaei et al., 2018). A summary of the gravel pack design based on sand PSD description of either D_{50} or D_{10} is presented in **Table 2.6**.

Table 2.6: Gravel Size and Slot Aperture Design Criteria Summary (Roostaei et al., 2018).

Design	Coberly (1938)	Hill (1941)	Saucier (1974)	Tiffin (1998)
Gravel criteria	(8 to 10) x D_{10}	(8 to 10) x D_{10}	(5 to 6) x D_{50}	(7 to 8) x D_{50}
Screen aperture size	50% to 75% of the smallest gravel size			

Rolled top, Straight and Keystone cuts are the most used slot profiles in manufacturing SLs. A schematic for each cut profile is presented in **Figure 2.10**. The pressure drop across each cut has been modelled based on simplifying assumptions. Results show that straight cut and rolled top slots yield the highest and lowest pressure drop, respectively. However, the pressure drop in the slots, regardless of their profiles, is negligible compared to the pressure drop in the adjacent porous medium. Slots plugging has been investigated based on the slot profile. From a plugging perspective, it was found that slots having rolled top and keystone cuts perform much better than those having straight cut. The produced sand for all three cut profiles was similar, with a slight tendency of the rolled top cut profile to produce more sand than the other two cut profiles. It seems to be wise to use a straight cut profile for SL completion in SAGD injector without any gravel pack because of its relatively lower cost and, most importantly, that injectors will not experience sanding. Reasonable operational condition is dominant in SAGD injectors' lifetime, which prevents sanding by default unless a failure results in uncontrolled flowback. (Roostaei et al., 2018)

Figure 2.10. Schematics of different SL cuts (Roostaei et al., 2018).

2.2.3 Operational Conditions in SAGD Injectors

It is essential to know the initial reservoir conditions and operational parameters for a typical SAGD injector to understand the impact of the shut-in process on the sand control mechanism. Initial reservoir conditions include reservoir thickness, bitumen saturation, temperature, and pore and fracture pressure. Besides, the caprock integrity assessment would result in setting the most suitable operational parameters to optimize the efficiency of the SAGD project and, at the same time to comply with Alberta Energy Regulator (AER) safety and environmental protection standards. Furthermore, operational parameters should include every single detail about the operation, with the most critical parameters in sand control investigation being injection pressure, temperature, steam quality (SQ), and injection rate.

The AER reports indicate that injection pressure varies from 1800 kPa (260 psia) to 4000 kPa (580 psia) during circulation and SAGD mode, where the maximum allowed injection pressure is 7000 kPa (1015 psia). Injection temperature is evaluated based on the corresponding injection pressure to achieve a minimum SQ of 95 % at the wellhead. Temperature varies from 180 °C to 250 °C, which corresponds to a particular injection pressure at formation depth. Injection flow rates are not reported accurately, though the cumulative steam injection per pad is a common term in the AER reports, which makes it difficult to estimate an accurate injection flow rate. The calculated flow rate ranges from 500 to 2000 m^3/day Cold Water Equivalent (CWE) (3145 to 12,580 bbl/D) based on a weighted average of well horizontal lateral and wellbore size. AER rule of thumb is to operate SAGD injection pressure under 80% of the minimum in-situ stress of the caprock, which has a stress gradient of 21 kPa/m or 0.93 psi/ft. (*Canadian Natural Resources Limited (CNRL)*, 2017; *Suncor Energy Inc.*, 2015)

2.2.4 Injection Interruption Possible Scenarios and Consequences

The interruption of the SAGD injector can be classified into two main categories: injector shut-in and injector flowback. Injector shut-in can be subdivided into scheduled shut-in according to maintenance program or emergency shut-in due to natural disasters as what happened in May 2016 referring to Fort McMurray wildfire. However, scheduled shut-in can be described as a step-wise reduction of the injection pressure to reach bottom hole static pressure with minimum pressure disturbance. Emergency shut-in tends to have a very sharp closure rate of the injection wellhead due to unexpected shut-in enforcement. From a reservoir engineering point of view, both shut-ins are resulting in static bottom hole potential greater than or equal to the reservoir potential, which cannot result in reverse flow direction; i.e., fluid flows from the wellbore to the reservoir at any time during shut-in. This process can be described as a fall-off test for a horizontal gas injector well (Chaudhry, 2003). Fall-off tests will not capture any fluids moving towards the injector during the testing period, which eliminates both scheduled and emergency shut-ins from being the cause of sanding in SAGD steam injectors.

On the other hand, injector flowback, which may occur as a result of sudden failure of a mechanical element, reduces the bottom hole potential to a value lower than that of the reservoir, causing flowback. Several possibilities of mechanical failure may occur accidentally, such as immediate pump failure, burst of the injection piping system, or even steam generator failure, yet no such data were released from either manufacture nor operational oil companies. These failures may exhibit a possible flowback scenario for the SAGD injector for a short time until the operator controls wellhead pressure (WHP) to shut-in the well. Technically, the worst flowback scenario takes place when the wellhead pressure is reduced to atmospheric pressure due to the previously mentioned mechanical failures. It results in the lowest possible well BHP from a production engineering point of view (Beggs, 2003; Economides, Hill, & Ehlig-Economides, 2013). Often, subsurface safety valves (SSSV) are used in emergency well closure. Closure time is less than 5 seconds for surface-controlled SSSV and 30 seconds for subsurface-controlled SSSV (Spec, 1998). Accordingly, SAGD injector flowback duration starts with a mechanical failure and terminates with SSSV closure.

It was not possible to find the required data in any publication or even to convince operating oil companies to release such statistics of failure and their causes. Surface equipment mechanical failure seems to be the only possible way of having a differential potential towards the wellbore of the SAGD steam injector that results in flowback and possible transient sanding.

In SAGD injector, sand production is not a problem unless the well undergoes a flowback due to surface equipment failure where the differential potential and its corresponding streamlines are pointing towards the injector. Flowback in an injection well might result in a significant decline of injectivity due to fines mobilization and sand accumulation in the wellbore or even complete loss of injectivity if the accumulated sand filled the wellbore. The aim of sand control in the injector is an essential precaution to prevent any possibility of sanding. Fluidization potential, if it exists, has a significant impact because it reduces the effective stresses for the near-wellbore region. Moreover, the rapid fall of pressure during flowback can result in a large pressure gradient in the vicinity of the wellbore that aggravates the detrimental effects of sanding. Previous researches emphasize the need for clearly defined sand control design criteria for SAGD injector to prevent excessive sanding. As the researches claim, injector design criteria should not be more conservative than that for the producer because injector flowback is not a common practice in the industry. Furthermore, the design criteria should account for a possible worst-case scenario of failure, which results in a severe flowback (Fattahpour et al., 2018a; Mahmoudi et al., 2018a).

However, SAGD injector flowback is not common during regular operation, yet an engineering design should account for the possibility of such possible event, if it occurs, compared to the lifetime of the well due to the ambiguity of its consequences.

Such a scenario is possible, but it is challenging to obtain such data from the industry to guide the design of the SRT facility to simulate flowback conditions in the laboratory. It raises the need to use a numerical model such as the CMG simulator to construct a simplified SAGD model to study the flowback consequences in the SAGD injector during surface equipment failure. This topic will be discussed in Chapter 3.

2.3 Associated Rock and Fluid Properties

Section 2.2 describes the general SRT facilities involved in SAGD injector laboratory testing. Flowback fluids properties and their physical interaction with the porous media, which is the sand pack, has a significant role in this research. SRT results are governed by testing input (Ballard & Beare, 2006); however, assigning testing inputs and interpretation of results are highly linked to rock and fluid properties and Darcy's law, that are discussed in this section.

2.3.1 Darcy's Law for Gases and Klinkenberg Effect

Darcy's law, presented in Eq. 2.9, is used to describe fluid flow in porous media. It accounts for compressible and incompressible fluids in linear, radial and spherical flow geometries. It is applicable under a steady-state laminar flow regime only where Reynold's number is less than one (Pope, 2003). Ideal gas law is incorporated in Darcy's law for compressible fluids, and the discretized form that describes gas flow in a linear flow geometry is presented in Eq. 2.10.

$$q = - \frac{A\,K}{\mu} \frac{\partial \Phi}{\partial x} \qquad \text{(Eq. 2.9)}$$

$$Q_g^{sc} = \frac{\alpha_c\, A\, K_g\, (\Phi_{upstream}^2 - \Phi_{downstream}^2)}{\bar{T}\ \bar{z}\ \overline{\mu_g}\ L} \qquad \text{(Eq. 2.10)}$$

Where (Q_g^{sc}), (α_c), (A) and (Φ) represent gas volumetric flow rate at standard conditions, units conversion factor, cross-sectional area perpendicular to flow, and terminal potential, respectively. Differential potential can be approximated by $\left(P_{upstream}^2 - P_{downstream}^2\right)$ and neglecting the gas gravity term. Moreover, temperature (T), z-factor (z) and gas viscosity (μ_g) should be evaluated at the terminals' average pressure. Furthermore, porous medium permeability for gas (K_g) is not constant and changes due to an electro-kinetic phenomenon known as the Klinkenberg effect (Peters, 2012b; RP40, 1998). **Figure 2.11** demonstrates that the changes in gas permeability (K_g) with respect to average mean pressure and gas type.

However, Eq. 2.10 was derived from Eq. 2.9 based on constant approximation of some gas properties at low pressure. **Figure 2.12** illustrates the range of applicability of the pressure-squared method at 38°C (100°F). To apply Eq. 2.10 with an acceptable marginal error, the average pressure should not exceed 8.3 MPa (1200 psia), 12.1 MPa (1750 psia) and 15.2 MPa (2200 psia) at temperatures of 38°C (100°F), 93°C (200°F) and 149°C (300°F), respectively. In short, laboratory ambient conditions are falling within the applicability range for the pressure-squared method. (Lee, 1996)

Compressible fluid flow in porous media has a non-linear pressure profile along the axis of the core. The nonlinearity in the profile is a function of fluid compressibility, as shown in **Figure 2.13**. It complicates the analysis of the results for gas flow at steady-state conditions. However, gas compressibility is much higher than that of liquid, which results in a dramatic effect on the pressure profile.

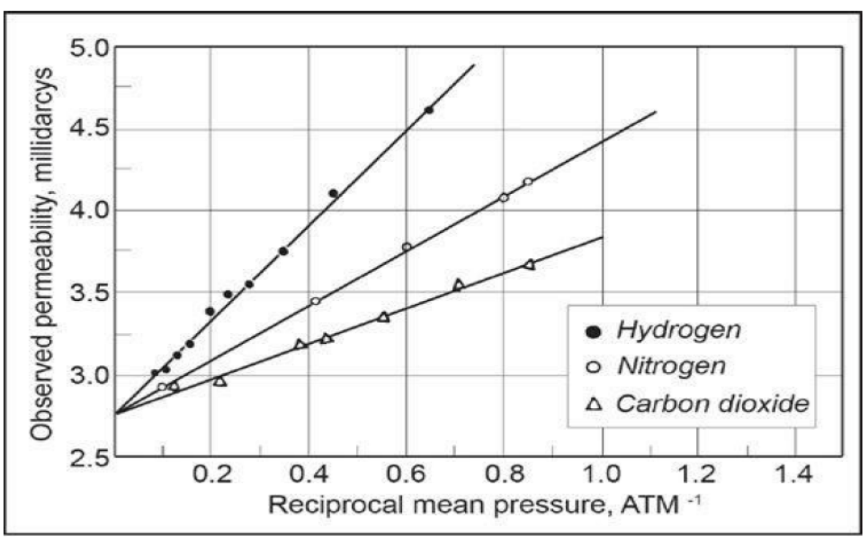

Figure 2.11. Klinkenberg effect (Peters, 2012b).

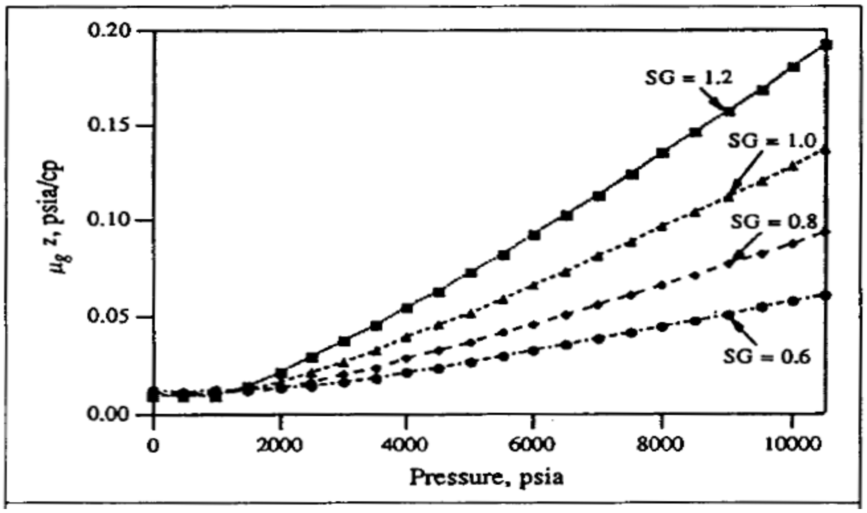

Figure 2.12. Range of applicability of pressure-squared methods at 100°F (Lee, 1996).

Furthermore, the actual volumetric flow rate is determined based on the average pressure and temperature and uses the pressure-squared method. This implies that the volumetric flow rate for compressible fluid is not constant. Slightly compressible fluids can be assumed to have negligible non-linearity in their pressure profile; but such an assumption is not valid for compressible fluids. (Marshall, 2009)

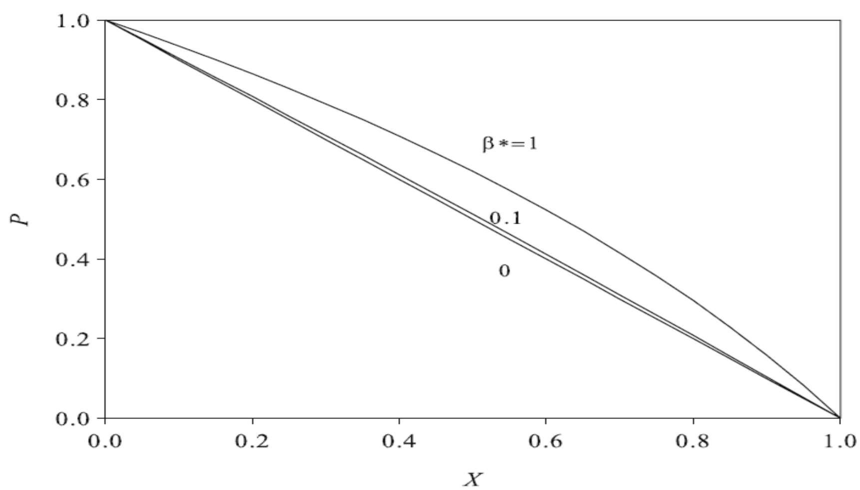

Figure 2.13. Pressure profile changes with compressibility 'normalized P and X, dimensionless β*' (Marshall, 2009).

The wetting phase saturation was found to affect the Klinkenberg effect that produces erroneous results such as negative liquid permeability at high liquid saturations. **Figure 2.14** demonstrates the Klinkenberg effect at different water saturations and the corresponding change in slip factor. (Li & Horne, 2004)

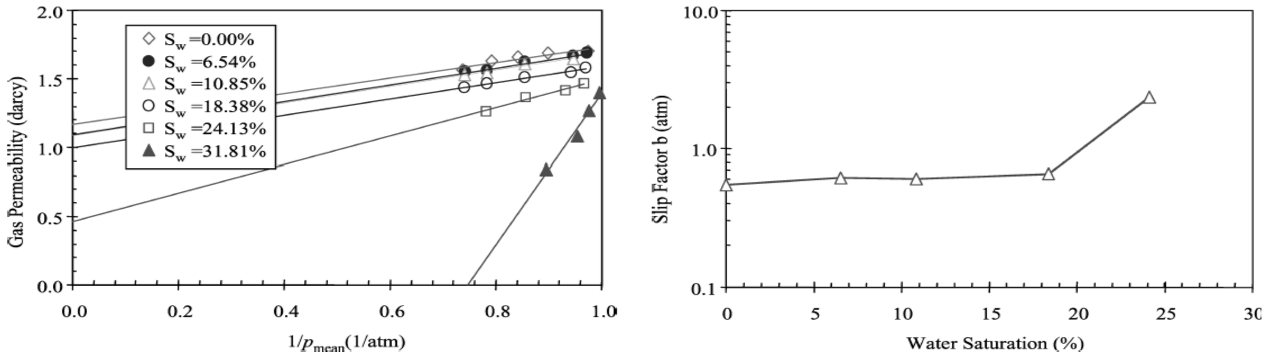

Figure 2.14. Klinkenberg effect 'left' and corresponding slip factor at each saturation 'right' (Li & Horne, 2004).

2.3.2 Surface Tension, Wettability Rock-Fluid Interaction, and Capillary Pressure

Liquid and its vapour interface, under certain circumstances, face a contractile force called surface tension. It governs fluids' behaviour when two or more immiscible fluids co-exist. Its value is inversely proportional to temperature and pressure. The fluid that has the tendency to spread on a solid surface in the presence of other immiscible fluids is known as the wetting phase. Wettability is quantified based on the contact angle, Amott test and USBM wettability index. It has a significant role in multiphase rock-fluid interaction and affects relative permeability, capillary pressure, displacement efficiency and magnitude of irreducible water saturation. Furthermore, it governs the microscopic fluid distribution at the pore scale in porous media. Fluid distribution at the pore scale tends to minimize the specific surface free energy of the system. Accordingly, the wetting phase occupies small pores and coats solid grains surface, whereas the non-wetting phase fills the center of large pores. Table **2.7** demonstrates fluid distribution at pore scale for both oil-wet and water-wet reservoirs in gas cap, oil zone, water zone (aquifer) and oil-gas and oil-water transition zones. Capillary pressure is due to the coexistence of surface tension and wettability phenomena in porous media. Moreover, it is a function of pore size, pore structure, PSD, fluid saturation and fluid saturation history. However, its value is inversely proportional to wetting phase saturation, as shown in **Figure 2.15**. (Peters, 2012a)

Table 2.7: Fluids Distribution at the Pore Scale.

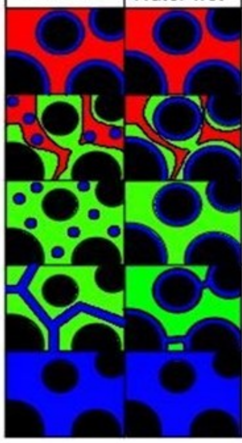

Fluid Distribution			Mobility			Saturation			
Oil wet	Water wet	Zone	Gas	Water	Oil	S_g	S_w	S_o	
		Gas	M	NM	NM	$1-S_{wirr}$	S_{wirr}	ZERO	GOC
		O-G t.z.	M	NM	M	$1-S_o^*-S_{wirr}$	S_{wirr}	$0<S_o^*<1-S_{wirr}$	OGC
		Oil	NM	NM	M	ZERO	S_{wirr}	$S_o = 1-S_{wirr}$	OWC
		W-O t.z.	NM	M	M	ZERO	$S_{wirr}<S_w^*<1$	$S_o = 1-S_w^*$	WOC
		Water	NM	M	NM	ZERO	S_w	ZERO	

Solid   Water   Oil   Gas

M: mobile Phase
NM: immobile Phase

S_{wirr}: Irreducible water Saturation; **S_i^***: Variable fluid (i) saturation with depth, i: o or w; **t.z.**: transition zone
GOC: Gas-Oil Contact; **OGC**: Oil-Gas Contact; **OWC**: Oil-Water Contact; **WOC**: Water-Oil Contact

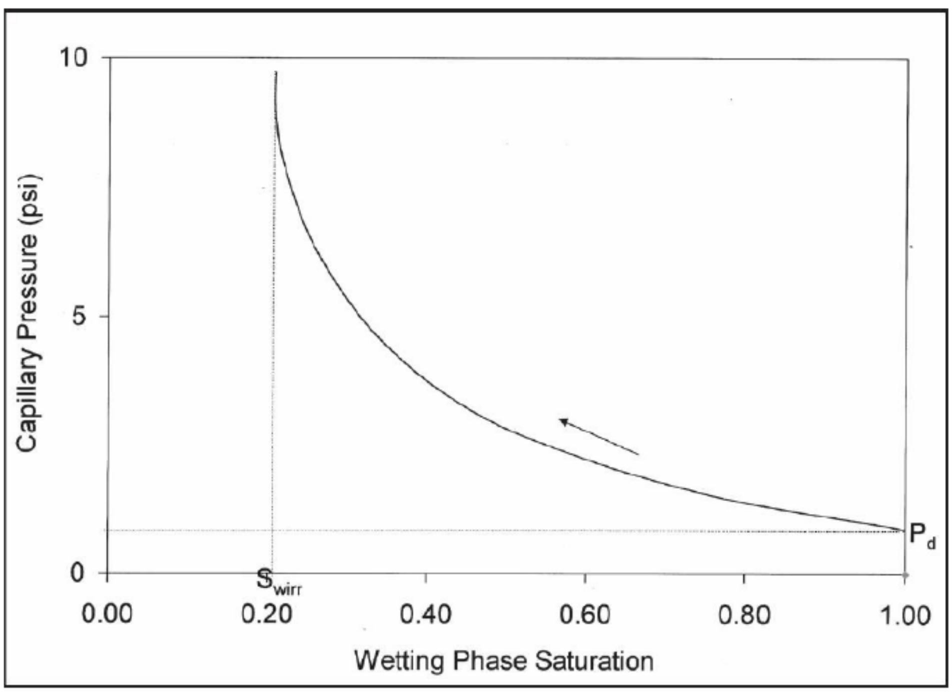

Figure 2.15. A typical drainage capillary pressure curve (Peters, 2012a).

2.4 Thermodynamics and Bernoulli's Equation

It is essential to understand fluid dynamics and thermodynamics because the SAGD injector involves both fluid flow in conduits and heat transfer mechanisms. Considering these concepts and those of fluid flow in porous media, discussed in the previous section, is necessary to come up with suitable problem description and possible solutions. Previous researches ignored involving those concepts as they simplify the problem and overcome the incompleteness of the formulation by relying on hypothetical assumptions for flowback fluids in SAGD injectors (Fattahpour et al., 2018a; Mahmoudi et al., 2018a).

The following topics are discussed in this section: phase behaviour and ideal gas law, the pressure drop in conduits and its application in nodal system analysis.

2.4.1 Phase Behavior and Ideal Gas Law

A pure substance is defined as a homogenous mixture of single or multiple chemical elements or compounds if it has a uniform chemical composition in some physical phases (solid, liquid and gas) at specific temperature and pressure. Pure substance exists in five different forms: solid, solid-liquid mixture, liquid, liquid-vapour mixture, and vapour, as shown in Figure **2.16** and Figure **2.17**, respectively, for substances that contract or expand on freezing.

In petroleum engineering and especially in thermal operations, excluding in-situ combustion, that involve injection of hot material, one is interested in only three forms: liquid, liquid-vapour mixture, and vapour. Thermodynamics divides the three forms into five regions to identify fluid properties at any point on (T-υ) diagram, as presented in Figure **2.18**. In a closed system where the applied pressure of (1 atm) remains constant all the time with heat being continuously added to the system, water is called compressed liquid as long as the temperature is below its boiling temperature (100 °C for deionized water). Water is considered to be a saturated liquid once it reaches the boiling temperature, with at least a single bubble of vapour formed. Adding more heat to the system will vaporize water at constant temperature and results in the coexistence of liquid water and vapour (saturated mixture). Once the last liquid water droplet vaporizes, the phase represents the saturated vapour. Adding more heat to the system will change it into a superheated vapour (steam). These mentioned states are shown in Figure **2.19**.

A similar (T-υ) diagram is obtained at any pressure below the critical pressure and critical temperature. Water properties and states can be identified by knowing at least two independent intensive properties using steam properties tables or by using the Steam Tab software package, which provides more accurate results. The saturated liquid-vapour mixture requires an additional term called steam quality (x or SQ) that is defined as the ratio of the mass of vapour to the mass of the total mixture. It has a value of zero for saturated liquid and one for saturated vapour (Çengel, 2001). High SQ is usually associated with steam injection during SAGD mode.

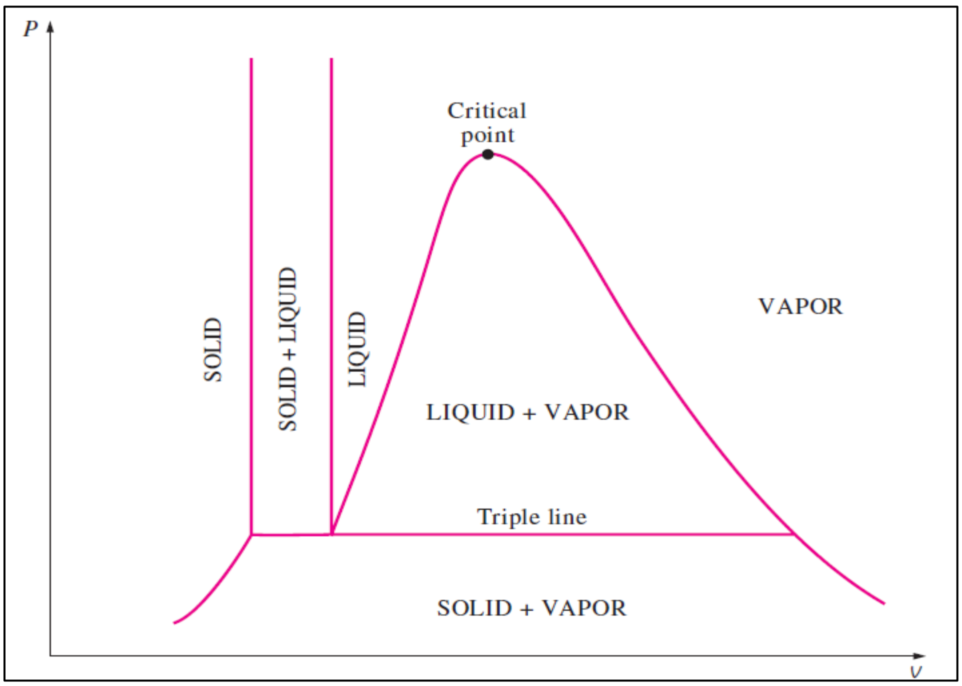

Figure 2.16. P-υ diagram for a substance that contracts on freezing (Çengel, 2001).

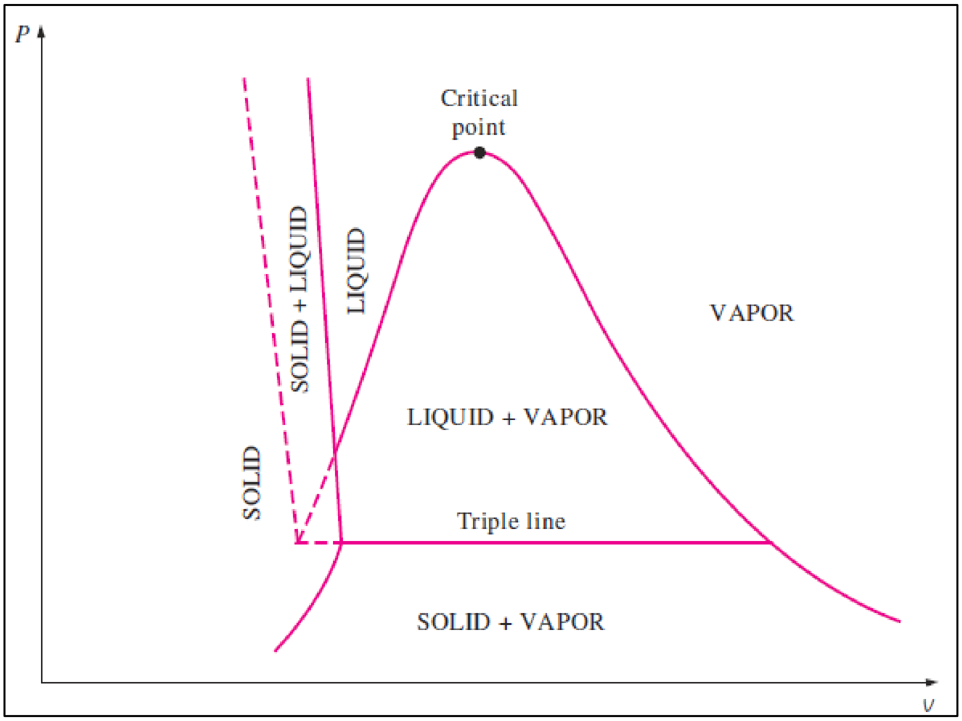

Figure 2.17. P-υ diagram for a substance that expands on freezing (Çengel, 2001).

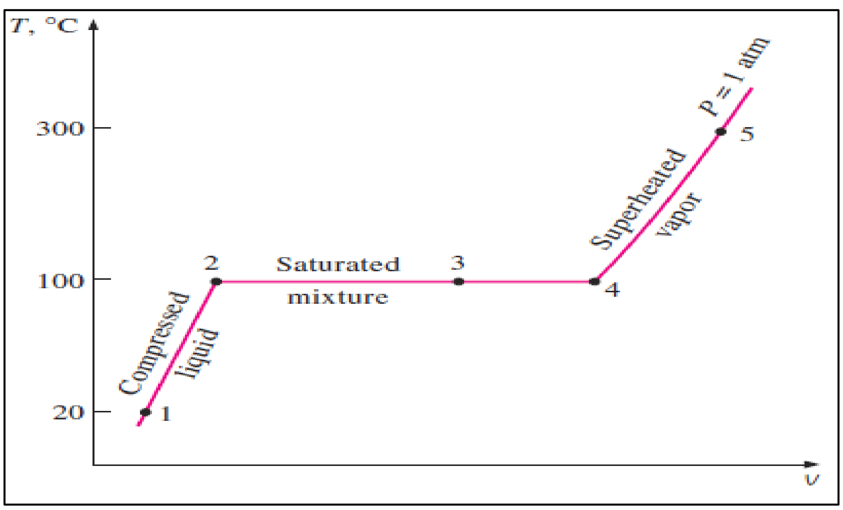

Figure 2.18. T-υ diagram for water molecules (Çengel, 2001).

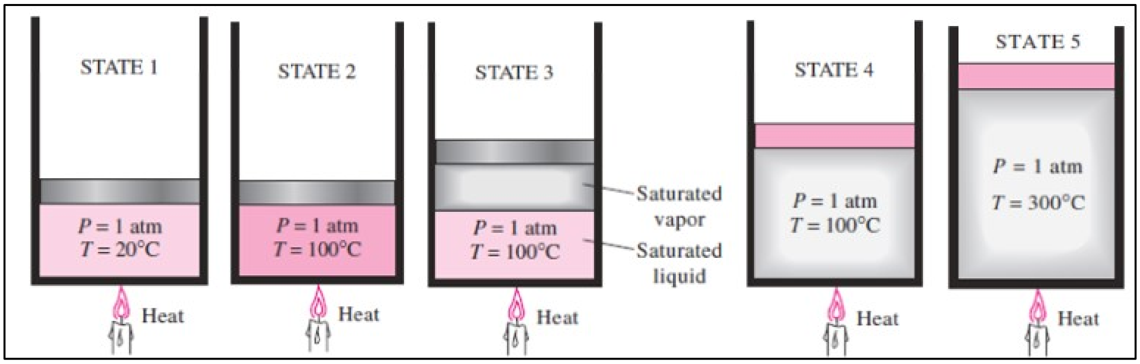

Figure 2.19. State 1: compressed liquid, State 2: saturated liquid, State 3: saturated mixture, State 4: saturated vapour, State 5: superheated vapour (Çengel, 2001).

The ideal gas equation of state describes pressure, temperature and specific volume of a gas if it satisfies the ideal gas assumptions. Ideal gas does not exist, yet the relationship is still applicable to the vast majority of gases by adding compressibility factor (z) as a correction. The z-factor can be determined at any reduced pressure and reduced temperature using Figure **2.20**. It is tough to answer the question of whether water vapour can be treated as an ideal gas or real gas. The errors involved in treating saturated and superheated water vapour as ideal gas is presented in Figure **2.21**. The error is minimal at any pressure below 10 kPa, regardless of temperature, and increases as pressure increases. Moreover, the error is inversely proportional to temperature (Çengel, 2001). This implies that the error in treating superheated water vapour is less than the error for treating saturated water vapour at the same pressure. In conclusion, it is unwise to treat the saturated or superheated water vapour as an ideal gas in SAGD operational conditions.

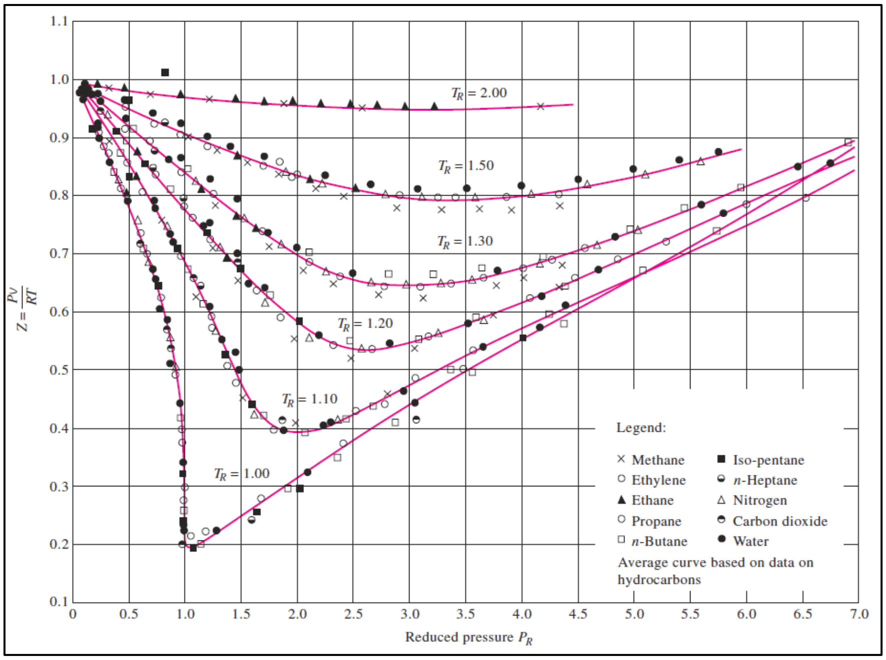

Figure 2.20. Comparison of Z-factor for various gases (Çengel, 2001).

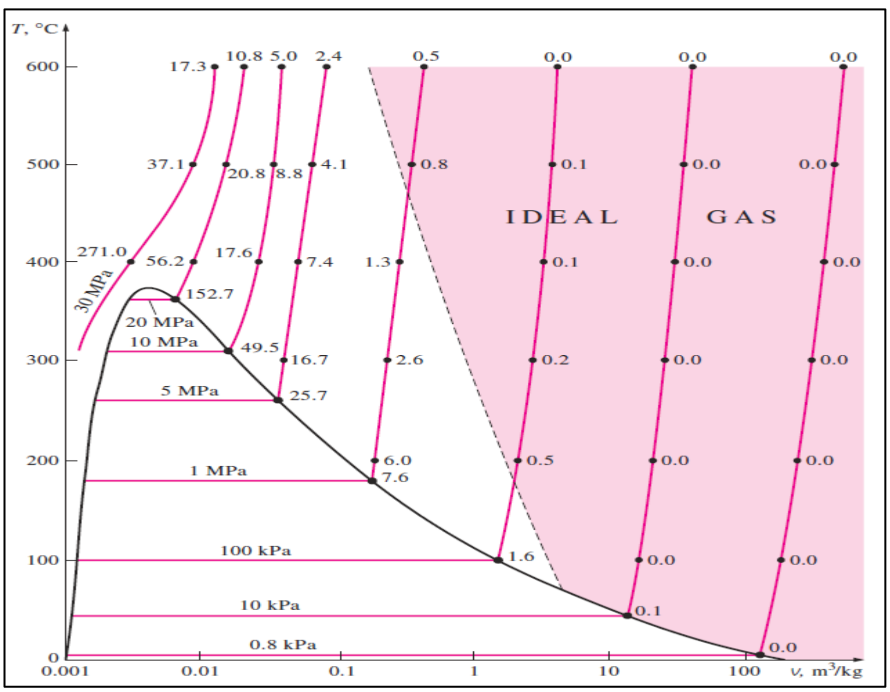

Figure 2.21. The percentage of error involved in assuming steam to be an ideal gas and the shaded region represents the region where the error is less than 1% (Çengel, 2001).

2.4.2 Pressure Drop in Conduits

Bernoulli's equation, shown as Eq. 2.11, expresses the energy balance for incompressible fluid at steady-state flow conditions. It links kinetic, potential, pressure, work and friction terms into a single equation.

$$\alpha\Delta\left(\frac{v^2}{2}\right) + g\,\Delta z + \frac{\Delta P}{\rho} + \omega + \mathcal{F} = 0 \qquad \text{(Eq. 2.11)}$$

The pressure drop of fluid flow in conduits is a function of several factors, including flow regime, fluid properties, conduit dimensions and surface properties. Laminar flow results in a linear pressure profile, whereas a turbulent regime induces excessive pressure drop, which is approximately proportional to the square of flow rate, as shown in Figure **2.22**. Reynolds number, which is a dimensionless parameter defined by Eq. 2.12, is used to identify the flow regime. Moreover, it is the ratio of inertial to viscous forces. The definition of Reynolds number (R_e) in Eq. 2.12 is different from the one used for porous media, discussed in Section 2.3.1 earlier. The common practice in pipe selection criteria is to eliminate turbulence effect unless the flow purpose requires turbulent flow. (Wilkes, 2006)

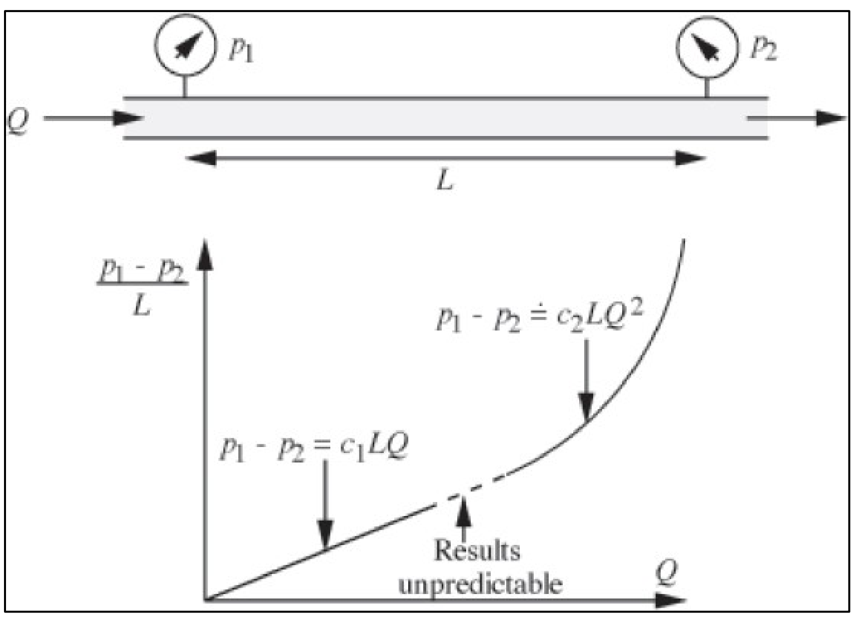

Figure 2.22. Pressure drop profile based on flow regime (Wilkes, 2006).

$$R_e = \frac{\rho v_m D}{\mu} \qquad \text{(Eq. 2.12)}$$

2.4.3 Nodal System Analysis for Gas Wells

The total pressure drop in any production system equals upstream pressure (reservoir pressure) minus the downstream pressure, which is the separator. Often, production wells are equipped with a surface choke that fixes the wellhead pressure, if sonic/critical flow conditions are maintained, regardless of downstream pressure changes. It results in considering wellhead pressure as downstream for NSA. It relies on two fundamental concepts: the inflow equals the outflow at each node, and single pressure value can exist at a node (Beggs, 2003; Guo, Ghalambor, & Lyons, 2007). The well deliverability is defined as the flow rate that satisfies both inflow pressure performance (IPR or WPR) and outflow pressure performance (TPR or CPR), the intersection point, as shown in Figure **2.23**.

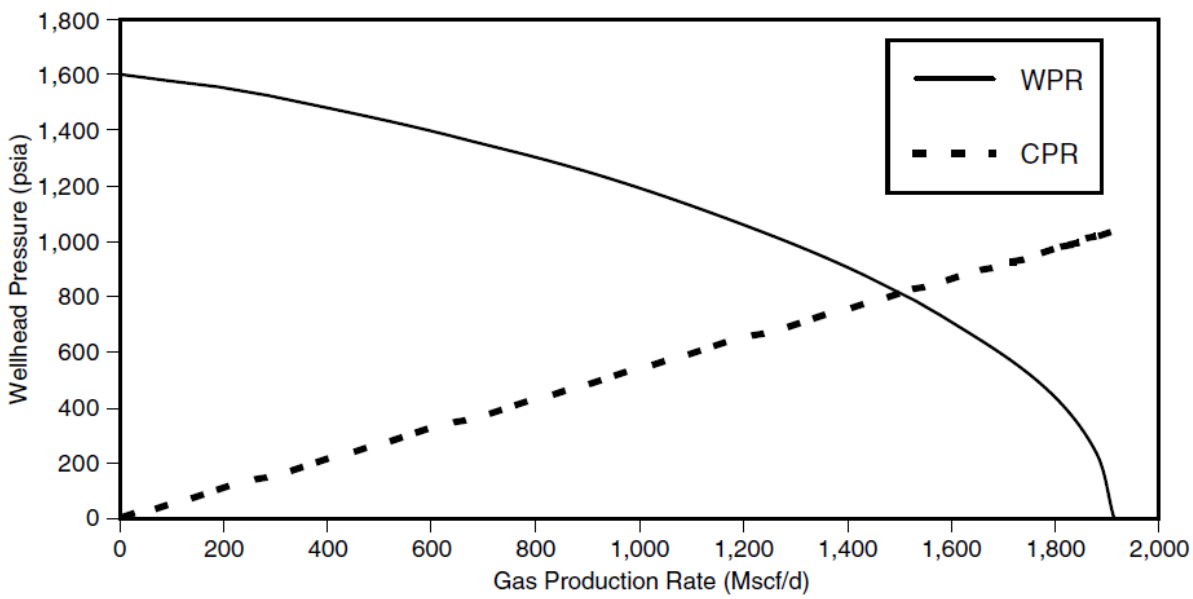

Figure 2.23. Vertical gas well inflow and outflow pressure performances (Guo et al., 2007).

Gas well IPR has a nonlinear trend because of pseudo-pressure (m-function) used to describe the flow. Dry gas and wet gas IPRs are not sensitive functions of pressure, unlike oil and gas retrogrades (gas condensate) IPRs. Gas condensate IPR is governed by dew point pressure and relative permeability if condensates are formed in the reservoir. For a horizontal well, the IPR has a straight-line trend for oil and gas wells. (Beggs, 2003)

Gas well TPR is simply the energy balance equation, Section 2.4.2, associated with a term for internal energy. Temperature prediction along production well can be assumed constant, linear and even nonlinear profile if the required coefficients and parameters are available (Beggs, 2003).

Several empirical correlations were developed for gas well BHP prediction from a known downstream pressure. The average temperature and z-factor method, described in detail in Section 3.2.1, is recommended for shallow gas wells, whereas Poettmann's method was proven to give more reliable results for deeper gas wells assuming isothermal production or injection. Involving the temperature effect on the z-factor in Poettmann's method results in better accuracy, as can be seen from the Cullender and Smith Method. (Lee, 1996)

Chapter 3: **CMG MODEL AND NATURAL GAS FLOW CORRELATION**

This chapter presents the assessment of the operational parameters for SAGD injector SRT laboratory testing. It involves a brief CMG model description and the applicable natural gas flow correlation. This work was done to eliminate the hypothetical assumptions in previous works (Fattahpour et al., 2018a; Mahmoudi et al., 2018a), which are considered to be severe possible artifacts in SRT experiments. (Ballard & Beare, 2006)

3.1 Reservoir Simulation and CMG STARS Model

Reservoir simulation is the most potent tool for reservoir future performance prediction. It has the advantages of eliminating many essential assumptions used in any other prediction technique, considering reservoir geology, and heterogeneity. However, it is the most resource extensive tool that causes investigation overkill in the absence of clear objectives. Input up-scaled data, including porosity, irreducible saturations, permeability, relative permeability, capillary pressure, are the primary quality controller for simulation output. The ultimate goal of using reservoir simulation is to yield relative ranking of several scenarios, e.g. peripheral or pattern injection strategies of several cases (Ertekin, Abou-Kassem, & King, 2001). The CMG STARS model is used in this investigation to simulate thermal EOR processes.

3.1.1 Study Objectives

The governing objective of this model is to mimic SAGD well pairs performance, during SAGD regular operation, to yield reliable results during the flowback in reasonable computational time. Flowback takes place at the most representative time duration of the SAGD operation lifetime. It results in atmospheric SAGD injector wellhead pressure for a short duration of 40 seconds before the SSSV actuation takeover, as discussed earlier in Section 2.2.4. This objective of this study is to get insights into flowback consequences, specifically flowback induced flow rate and associated differential pressure, that guide the SRT facility development. Furthermore, SAGD injector near-wellbore region fluid saturations, flowback fluids ratio, pressure and temperature are given special attention to understand the SAGD injector flowback mechanism. Often, simulation studies are conducted to assess future field development plans (Ertekin et al., 2001), but this study will outline the consequences of SAGD injector flowback.

3.1.2 Model Discretization

The CMG STARS model was used to overcome the problem of data confidentiality and lack of information in this area. The model was developed based on previous work of a team co-worker master's thesis (Sidahmed, 2018). The data were derived from Suncor Energy open source, and all the associated input properties can be found in that thesis. This investigation will not present rock and fluid properties used in the model, yet any model related input can be found in Sidahmed's thesis. However, the focus here will be on the modifications made to that model to fulfill the purpose of this work.

Local grid refinement (LGR) was proven to yield reliable results in line with adequate computational time for SAGD models built by the CMG STARS (Sidahmed, Nouri, Kyanpour, Nejadi, & Fermaniuk, 2018). It serves the purpose of this work by keeping the CMG simulation run in a reasonable time. Accordingly, interpretation of results and experimental SRT will be conducted in a time-efficient manner to accelerate the evaluation process of SLs aperture size performance for SAGD injectors. Moreover, the selected aperture size will be case-specific, based on CMG BHP and corresponding flow rate, to avoid solution generalization as in the proposed sand control design criteria for SAGD producers.

The discretization for the 3D SAGD model, as shown in **Table 3.1**, has 45 thousand grid blocks. **Figure 3.1** represents the well placement location for the injector well that has a 5-meters separation distance from the producer. The producing well was placed 2 meters above the bottom of the reservoir. The active wells length is 900 meters in J-dimension. A cross-sectional view of the I-K plane is shown in **Figure 3.2** and magnified LGR in **Figure 3.3**. Furthermore, gird refinement shown in **Table 3.2** added over 80 thousand child grid blocks to the model.

Table 3.1: 3D Model Gridding Dimensions.

Dimension	Direction	# of Grid Blocks	Grid Block length (m)	Total Length (m)
I	Orthogonal to well	75	1	75
J	Along well axis	20	50	1,000
K	Height axis	30	1	30
Total Coase Grid number		45,000	Total Volume (m^3)	2,250,000

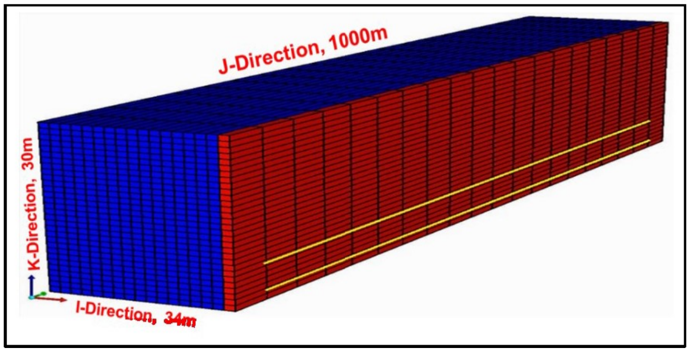

Figure 3.1. SAGD 3D model symmetric half schematic injector and producer placement (Sidahmed, 2018).

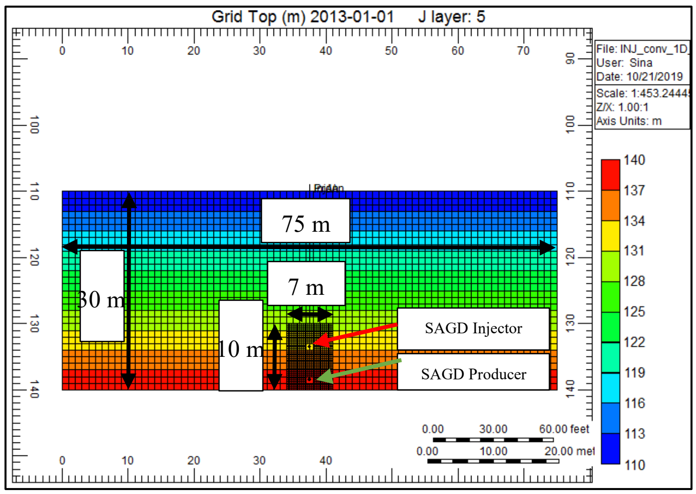

Figure 3.2. 3D model dimensions in the I-K plane (vertical axis K).

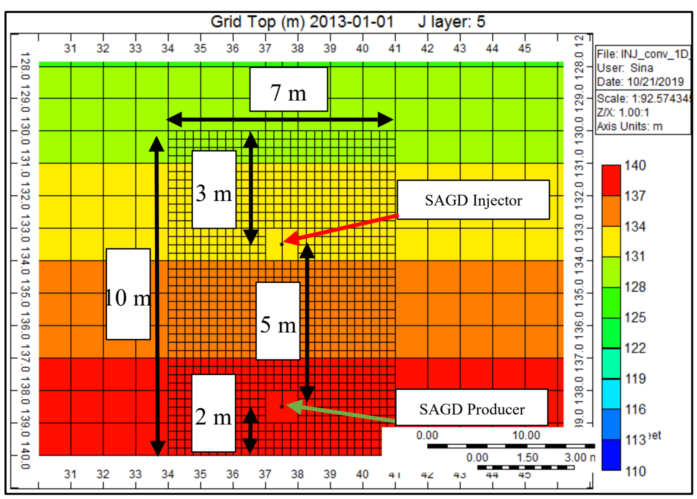

Figure 3.3. Magnified child grids in 3D model I-K plane (vertical axis K).

Table 3.2: Local Grid Refinement Scheme.

Dimension	Visual Schematic	# of Grid Blocks	Grid Block length (m)	Total Length (m)
I	Figure **3.3**	28	0.25	7
J	Figure **3.5**	72	12.5	900
K	Figure **3.3**	40	0.25	10
Total Child Grid Number		80,640	Refined Volume (m^3)	63,000

Figure 3.4 presents part of the cross-sectional view of the J-K plane, and the LGR is magnified in **Figure 3.5**. The refined grid volume fraction to the total model volume is 2.8%, which was proven to accelerate the computational time significantly. (Sidahmed et al., 2018)

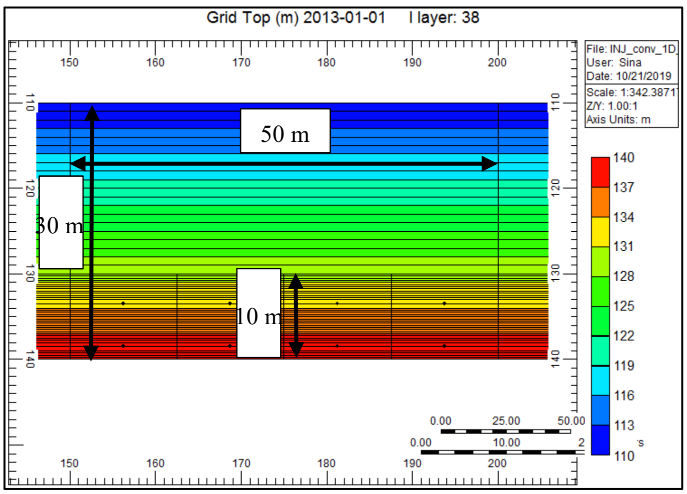

Figure 3.4. 3D model dimensions in the J-K plane (vertical axis K).

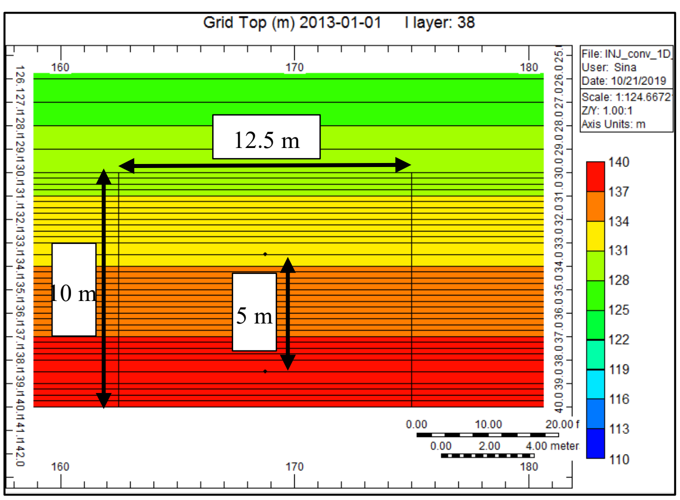

Figure 3.5. Magnified child grids in 3D model J-K plane (vertical axis K).

The initial reservoir model was built and tested by Sidahmed for this project to mimic SAGD behaviour under regular operation. In short, everything other than grid discretization, model volume and well definition is precisely the same as in Sidahmed's thesis. (Sidahmed, 2018)

3.1.3 3D Model Deficiencies

The intention was to precede by coupling a FlexWell model, which accounts for BHP variation along the well, and implementing a tubing model that sets the WHP to atmospheric pressure during the flowback execution. The idea is to create a new production well definition, that handles the flowback operation, located at the same location of the existing injection well placement. The override of the new production well presents the behaviour of the injector during flowback. It was done to avoid CMG technical problems that prevent defined injectors from producing fluid because a well shut-in order will override.

The major drawback in the 3D reservoir model was the long computational time of approximately 17 hours before coupling the FlexWell definition for the wells and surpassing 26 hours per simulation execution after coupling. Furthermore, implementing a simple model that neglects temperature changes or a sophisticated model that accounts for nonlinear temperature profile in the tubing model, to describe fluid flow in tubing during flowback, will further increase execution time. Moreover, the required data to construct the tubing model are not available in public sources and necessitated the need to be assumed. They are essential parameters that may change flow physics due to thermodynamic equilibrium involvement.

Despite the previously mentioned difficulties, the computational time demand contradicts the defined simulation objective of being time efficient. It drastically changes the approach to this problem to minimize the execution time, as discussed next.

3.1.4 2D Model Approximation

The ultimate solution to reduce the execution time is to reduce the number of blocks in the model, yet LGR is proven to yield the least reliable grid number (Sidahmed, 2018). However, homogenous rock and fluid properties along SAGD well pairs, assuming ideal conditions, propose the I-K plane as a plane of symmetry. The 2D model general overview, SAGD wells program, and grid size sensitivity analysis are presented in Appendix A. Moreover, Table **3.3** presents comparison of various grid discretization schemes. The selected model, refined 0.50 m grid size, is based on the criteria that account for the largest grid size model, least grid size output dependency, as shown in Appendix A, and time efficiency.

Table 3.3: Approximate Execution Time for Developed STARS Models.

Model ID	# of Dimensions	Execution time* (hours)
LGR reservoir only	3D (I-J-K)	$\approx \mathbf{17}$
LGR reservoir + FlexWell	3D (I-J-K)	$\approx \mathbf{26}$
LGR reservoir + FlexWell+ tubing	3D (I-J-K)	$\approx \mathbf{26}$**
Base 1.00 m grid size	2D (I-K)	$\approx \mathbf{0.1}$
Refined 0.50 m grid size	2D (I-K)	$\approx \mathbf{1.2}$
Refined 0.25 m grid size	2D (I-K)	$\approx \mathbf{13}$

* Execution time was evaluated with the same personal computer that has an i7 dual-core processor.
** (LGR reservoir + FlexWell+ tubing) model was not developed, and the execution time was estimated to be comparable to (LGR reservoir + FlexWell).

The discretization for the 2D SAGD model, as shown in Table **3.4**, has 9000 grid blocks, and Figure **3.6** represents the model schematic.

Table 3.4: 2D Model Gridding Dimensions.

Dimension	Direction	# of Grid Blocks	Grid Block length (m)	Total Length (m)
I	Orthogonal to well	150	0.5	75
J	Along well axis	1	1	1
K	Height axis	60	0.5	30
Total Coase Grid number		9,000	Total Volume ($\boldsymbol{m^3}$)	2,250

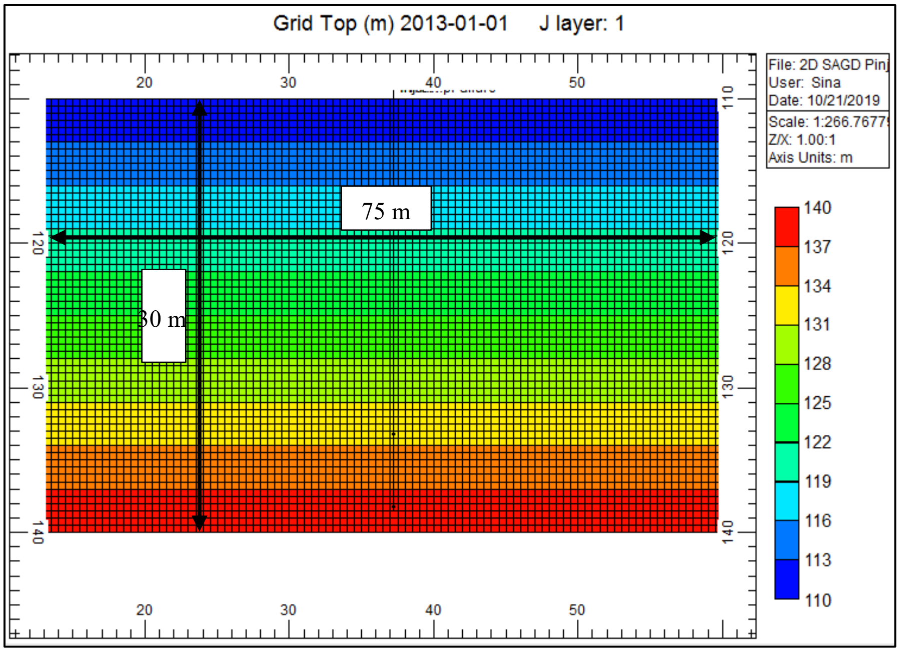

Figure 3.6. 2D model dimensions in I-K plane (vertical axis K).

Temperature and pressure are intensive or volume-independent properties and are not affected in the 2D model. However, evaluating the extensive or volume-dependent properties, and accounting for BHP variation along the well are discussed in Section 3.1.6 with reasonable assumptions.

3.1.5 Related SAGD Simulation Results

This section elaborates on the specific results obtained from the developed 2D SAGD model. Those results will be combined with Section 3.2 to evaluate the injector flowback BHP, which will be presented in Section 4.1. Appendix A presents the performance for SAGD injector and producer during the regular SAGD operation as well as the steam chamber development over time.

The injector near-wellbore region shows three distinct zones over time concerning fluid saturations in the injector well-block, which is the block that contains the well. The first zone represents the heating process or pre-SAGD mode that lasts for 90 days. The second zone shows the early SAGD mode, where near-wellbore fluid saturations are variable over the first year of SAGD mode. The third zone, late SAGD mode, shows stabilized conditions that last for the remaining SAGD mode until terminating the project. The three zones are observed from fluid saturation changes in the SAGD injection well-block shown in Figure **3.7** and block pressure and temperature, and injector BHP during SAGD mode shown in Figure **3.8**. The forth zone represents the induced flowback, which was selected to take place after enough period of steam chamber development, results in stable near-wellbore fluid saturations.

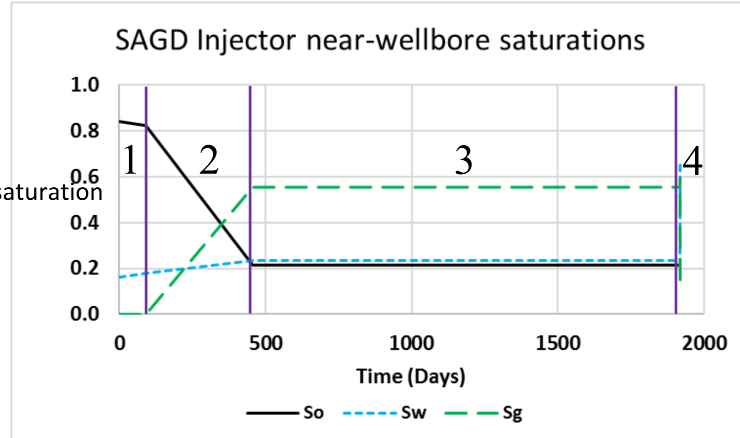

Figure 3.7. SAGD injector well-block fluid saturations during SAGD operation, (1): pre-SAGD mode, (2): early SAGD mode, (3): late SAGD mode, and (4): flowback mode.

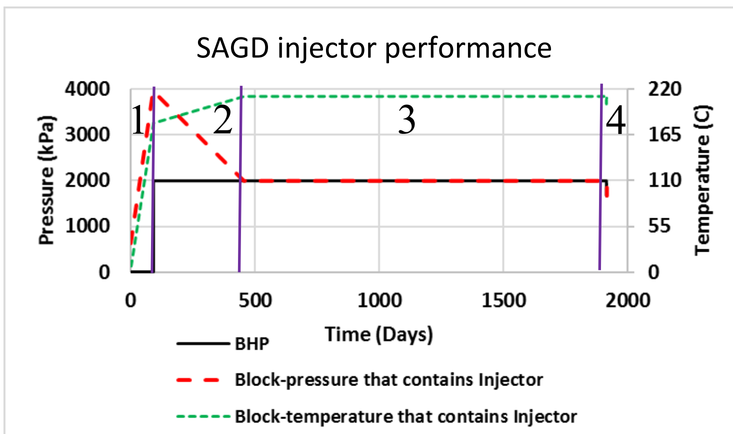

Figure 3.8. SAGD injector BHP, block pressure and temperature during SAGD operation, (1): pre-SAGD mode, (2): early SAGD mode, (3): late SAGD mode, and (4): flowback mode.

The forth zone ensures a mature development of the steam chamber, in other words, maximizing its volume, that corresponds to more severe flowback. It should be mentioned that the injector flowback during the time durations of zones one and two could be discarded because the combined time durations for both zones is less than one-tenth of a regular SAGD operation that could last for a decade; and because the inclusion of block pressure, temperature and saturation variations over time further complicates the SRT experimental investigation. Nevertheless, the engineering design should account for the worst-case scenario regardless of the time ratio. The third zone has the maximum differential pressure towards the injector; in other words, the minimum BHP based on flowback fluid apparent density in tubing pressure losses as will be demonstrated in Section

4.1. Moreover, a technique will be discussed in Section 5.3.1 to overcome this complication and account for the other regions by SRT parameter manipulation.

The well-block saturations profile reveals a dramatic change during the injector extended shut-in during the first 24 hours following the injector closure after the induced flowback, as shown in **Figure 3.9**. However, fluids saturation was monitored during flowback, as shown in Figure **3.10**, and shockingly water saturation drops below the irreducible water saturation. It seems to violate a fundamental principle of fluid flow in porous media; however, the confusion was eliminated by accounting for well-block intensive properties. **Figure 3.11** demonstrates well-block pressure, temperature, and injector-flowback BHP during flowback. Considering thermodynamics in the analysis explains that phase change of liquid water to superheated steam at flowback BHP maintains equilibrium, which justifies well-block water saturation fall during flowback duration, yet it is a logical justification, and Section 4.2.2 presents a mathematical proof of phase change based on average saturation calculation.

The pressure profile was captured after the flowback injector shut-in, as shown in **Figure 3.12**, which has a similar response to gas well buildup test (Lee, 1996). It shows well-block pressure builds up after shut-in due to supplied fluids from neighbouring blocks until pressure stabilizes after 80 seconds from the well shut-in. Finally, flowback fluids were detected in their standard condition equivalent flow rates, as shown in **Figure 3.13**, which indicates CWE is the primary fluid followed by traces of oil and gas (methane). The flow rates correspond to a one-meter SAGD horizontal well interval, which is the 2D model well length, and Section 3.1.6 will handle this issue. It is vital to understand the reservoir simulation formulation to deal with the discrete flow rates reading. In short, well flow rate formulation is either implicit or explicit, as shown in **Figure 3.14**. Yet in either case, it is strictly constant in between the time steps if finite-difference formulation is used to describe the flow in the simulator (Ertekin et al., 2001).

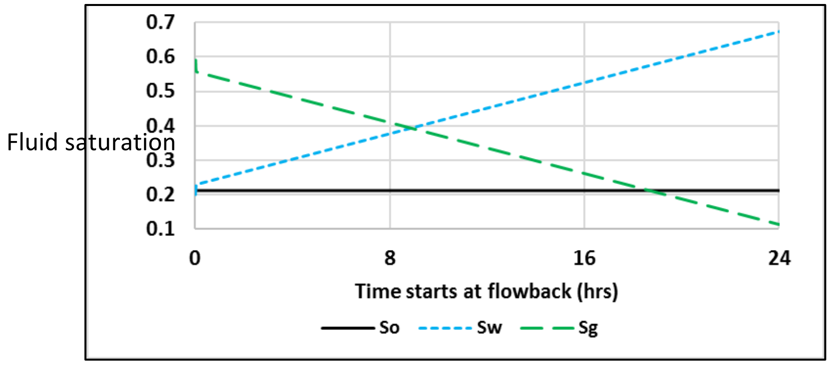

Figure 3.9. SAGD injector-flowback well-block fluid saturations during one day of shut-in after and during flowback.

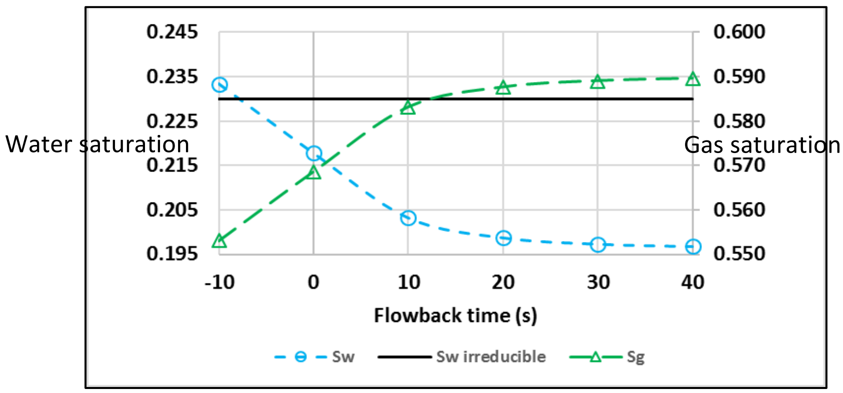

Figure 3.10. SAGD injector-flowback well-block fluid saturations during flowback.

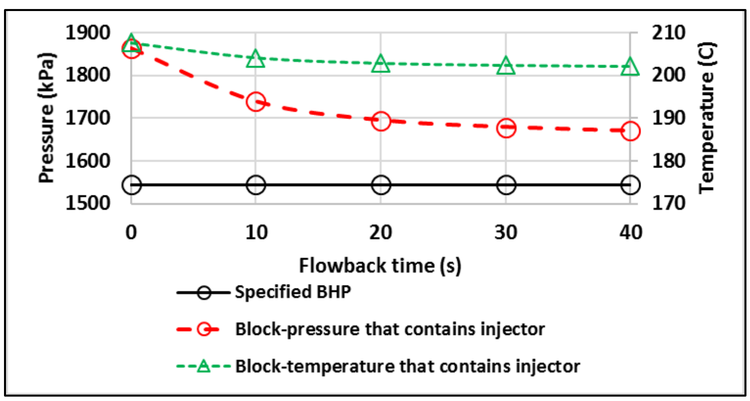

Figure 3.11. Injector-flowback at 1545 kPa BHP and well-block pressure and temperature during flowback.

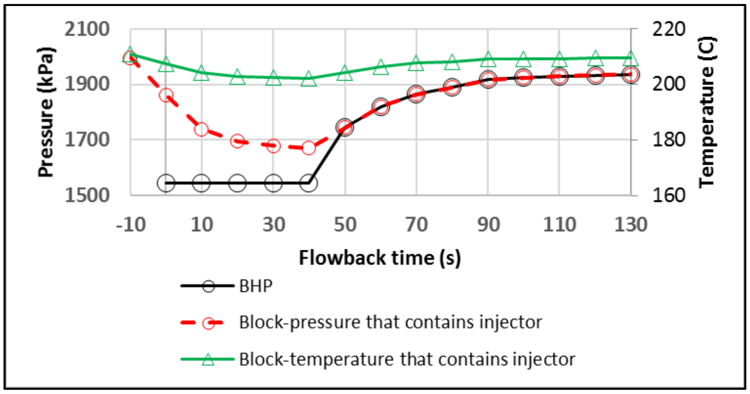

Figure 3.12. Injector-flowback at 1545 kPa BHP and well-block pressure and temperature before, during, and after flowback.

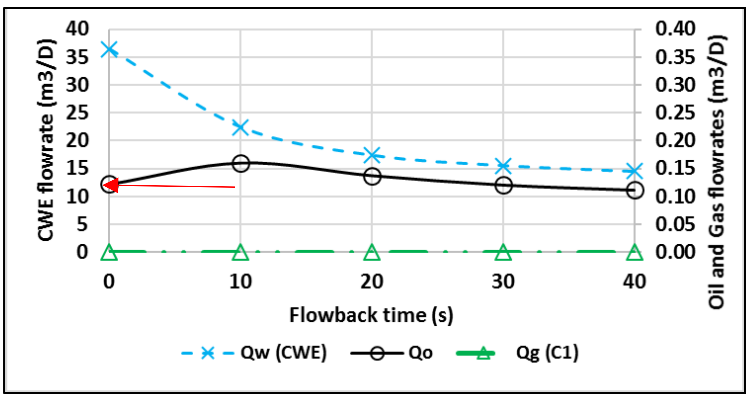

Figure 3.13. Injector-flowback rates for oil (bitumen), water, and gas (methane) during flowback at 1545 kPa BHP.

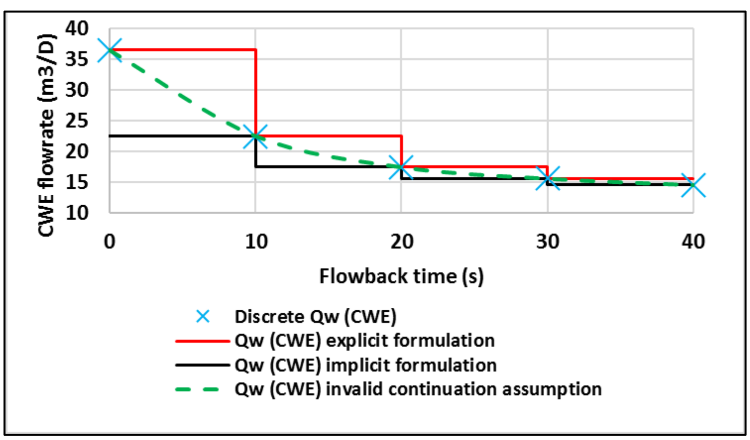

Figure 3.14. Explicit 'red' and implicit 'black' treatment of well flowrate in simulator.

3.1.6 2D Model Associated Problem

The 2D model solves the long computation time issue yet creates other technical problems. It eliminates the possibility of coupling FlexWell, yields unrepresentative actual SAGD flowback flow rates, and prevents deploying tubing model to predict the flowback BHP at atmospheric

WHP. Solving these problems is crucial to rely on the 2D model output results based on reliable assumptions.

Nevertheless, deploying FlexWell helps to predict pressure profile along the horizontal section of the well based on section in-flow rates, as shown in **Figure 3.15**, for homogenous formation along SAGD well during the production phase, which is similar to SAGD injector flowback conditions.

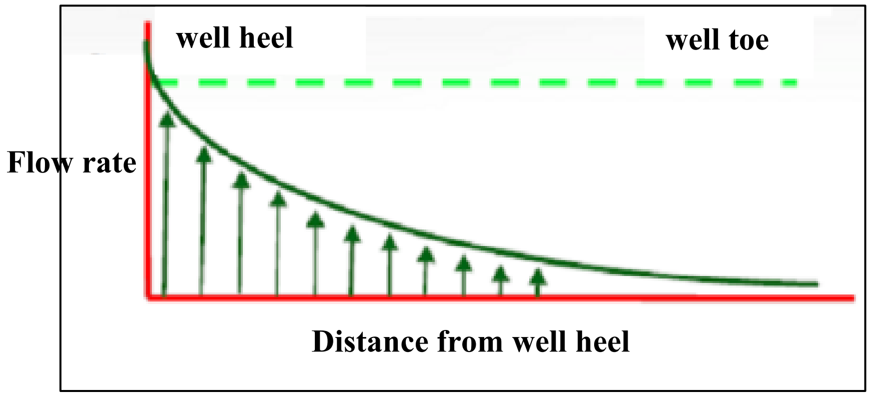

Figure 3.15. SAGD production rate along the well in homogenous formation (Sidahmed, 2018).

It is wise to conclude that well heel pressure is lower than well toe pressure as they are inversely proportional to in-flow rates. Accordingly, assuming well flow rate to be constant, at well heel maximum flow rate, along the SAGD well represents the maximum flow rate. It maximizes the differential pressure and its gradient towards the SAGD injector wellbore during flowback, which enhances sanding possibility along the entire well; in other words, it adds more safety factor to the obtained operational parameters. Moreover, the 2D model flow rates are unrepresentative, yet assuming superposition in space using Eq. 3.1 solves the problem for any flowback fluid (i), including CWE (steam), oil (bitumen) and gas (methane).

$$Q_i^{well} = Q_i^{2D\ model} \times \left(\frac{well\ horizontal\ length}{Length_{j-dricetion}^{2D\ model}}\right) \qquad \text{(Eq. 3.1)}$$

Furthermore, the implementation of tubing model in the current 2D model yields misleading results because of using model flow rate ($Q_i^{2D\ model}$) in tubing model, whereas it should calculate pressure drop in tubing based on the entire well flow rate (Q_i^{well}). Moreover, it gives the option to modify the well specifications based on the required well length and SL diameter without changing the CMG model. SAGD wells length varies between 800 (2625 ft) to 1200 (3937 ft) meters and injector SL diameter ranges from 17.8 (7 in) to 24.5 (9 $^5/_8$ in) centimetres, and even it could go up to 27.3 centimetres (10 ¾ in) in some sections, (*Canadian Natural Resources Limited (CNRL)*, 2017; *Suncor Energy Inc.*, 2015). However, using natural gas flow correlation, which is a separate interactive excel sheet, to predict the pressure drop in the vertical tubing section is possible based on reliable simplified assumptions. It allows the incorporation of different well specifications with minor changes, as discussed in Section 3.2.

Finally, the simulation objectives were met by providing a time-efficient simulation process and maintaining representative results based on the previous stated argument and assumptions. It will help in reducing the overall investigation time for commercial usage of SAGD SL aperture size by reducing individual task performing time, as presented in Table **3.3**.

3.2 Natural Gas Flow Correlation

Petroleum flow correlations are considered one of the most effective techniques to predict BHP from a specified downstream pressure, e.g. WHP, flow restriction device, or separator, in the absence of BHP field measurements as discussed in Section 2.4.3. Often, it involves iterative pressure computations along with tubing component, vertical flow. Yet, some correlations were made to predict pressure losses in slanted or even horizontal conduits such as Beggs and Brill method. Furthermore, correlation can be classified, based on fluid phases causing pressure drop, into single and multiphase flow regimes to account for most of petroleum production fluids. The average temperature and z-factor method demonstrates an effective, simple and the least demanding technique for BHP prediction strictly in shallow, up to slightly under one kilometre (3,000 ft), gas wells as discussed in Section 3.2.1. (Lee, 1996)

3.2.1 Average Temperature and Z-Factor Method

The technique relies on depth and density to predict changes in BHP. It uses the computed z-factor and temperature, as constants, at wellhead and wellbore arithmetic average pressure and temperature. Furthermore, it approximates the differential equation integral by the exponential method based on the stated assumptions. An iterative procedure is used until the solution converges. The BHP is equivalent to bottom hole flowing pressure (BHFP) though out this thesis, whereas bottom hole static pressure is abbreviated as BHSP. Figure **3.16** represents a schematic of slanted well geometry and Eq. 3.2 is used to approximate the first guess; then iterations start using Eq. 3.3 through Eq. 3.6.

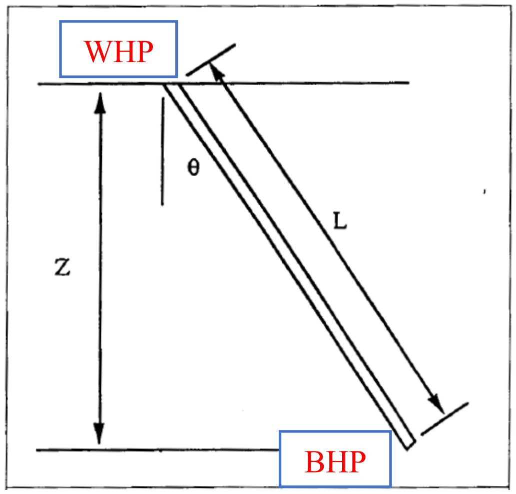

Figure 3.16. Schematic of well geometry (Lee, 1996).

$$BHP \approx WHP + 0.25 \times \left(\frac{WHP}{100}\right) \times \left(\frac{L\ \cos\theta}{100}\right) \quad \text{(Eq. 3.2)}$$

$$S = \frac{0.0375 \times \gamma_g \times L \times \cos\theta}{\bar{z} \times \bar{T}} \quad \text{(Eq. 3.3)}$$

$$N_{Re} = \frac{20 \times \gamma_g \times Q_g}{\overline{\mu_g} \times ID_{tubing}} \quad \text{(Eq. 3.4)}$$

$$f = 4 \times [\,2.28 - 4 \times log_{10}(\frac{0.0023}{ID_{tubing}} + \frac{21.25}{N_{Re}^{0.9}})\,]^{-2.0} \quad \text{(Eq. 3.5)}$$

$$BHP = [\,(WHP^2 \times e^S\,) + (\frac{6.67\times10^{-4} \times Q_g^2 \times f \times \bar{T}^2 \times \bar{Z}^2}{ID_{tubing}^5 \times \cos\theta}) \times (e^S - 1)]^{0.5} \quad \text{(Eq. 3.6)}$$

Correlations use field units in most petroleum applications. Accordingly, pressure (psia), temperature (R), length (ft), gas flow rate, Q_g^{well} , (scf/D), gas viscosity (cp), and inner-tubing diameter, ID_{tubing} (in) should be used in the above equations. However, such correlations were developed to predict BHP for natural gas wells only. The next section will emphasize the similarities between superheated steam and natural gas. Nevertheless, the composition of dry natural gas varies between 80% to 99% methane, which is wise to approximate methane physical properties for natural gas properties. (Lee, 1996)

3.2.2 Similarity Between Superheated Steam and Natural Gas Properties

The correlation discussed in the preceding section was developed for dry natural gas single-phase flow. Similarly, superheated steam exists in a single gaseous, and its properties are a function of pressure and temperature. The assumption here is that natural gas flow correlation can be implemented to predict BHP only if the physical properties of the two fluids are comparable. The comparison considers three different temperatures at 127°C, 227°C and 327°C, as demonstrated in Table **3.5**, Table **3.6**, and Table **3.7**, respectively, that fall within the thermal EOR techniques (Green, 1998). Furthermore, the pressure associated with the SAGD injection procedure is a function of depth, as discussed in Section 2.2.3, can be around (20 bar) for injectors having 140 meters of true vertical depth (TVD) as used in 2D CMG model as described earlier in Section 3.1. However, SAGD injector wellhead may encounter atmospheric pressure (1 bar) during the flowback. Also, the middle-pressure point in between those two values was added to ensure a representative and consistent comparison.

The comparison between dynamic methane viscosity obtained from ("Methane Dynamic and Kinematic Viscosity," Oct. 28, 2019), Superheated Steam (SHS) dynamic viscosity and specific weight from ("Superheated Steam Table," Oct. 28, 2019), and methane density were obtained from ("Methane Density and Specific Weight," Oct. 28, 2019). Methane and SHS viscosities and densities are compared at the previously mentioned pressures and temperatures. Those properties were the crucial factors in the comparison because Eq. 3.3 through Eq. 3.6 rely on them to predict the BHP or BHFP. (Lee, 1996)

Table 3.5: Methane and Superheated Steam (SHS) Properties at 400K (127°C, 260°F).

Pressure	Methane Viscosity	SHS Viscosity	Methane Density	SHS Density
bar (psia)	mPa·s (cp)	mPa·s (cp)	Kg/m^3	Kg/m^3
1.00 (14.50)	0.01418	0.01328	0.483	0.548
10.0 (145.0)	0.01428		4.845	
20.0 (290.1)	0.01448*	N/A	11.430*	N/A
50.0 (725.2)	0.01487		24.60	

* linear interpolation

Table 3.6: Methane and Superheated Steam (SHS) Properties at 500K (227°C, 440°F).

Pressure	Methane Viscosity	SHS Viscosity	Methane Density	SHS Density
bar (psia)	mPa·s (cp)	mPa·s (cp)	Kg/m^3	Kg/m^3
1.00 (14.50)	0.01692	0.01726	0.386	0.435

10.0 (145.0)	0.01704	0.01704	3.859	4.535
20.0 (290.1)	0.01716*	0.01680	8.996*	8.586
50.0 (725.2)	0.01741	N/A	19.27	N/A

* linear interpolation

Table 3.7: Methane and Superheated Steam (SHS) Properties at 600K (327°C, 620°F).

Pressure	Methane Viscosity	SHS Viscosity	Methane Density	SHS Density
bar (psia)	mPa·s (cp)	mPa·s (cp)	Kg/m^3	Kg/m^3
1.00 (14.50)	0.01941	0.02140	0.322	0.362
10.0 (145.0)	0.01948	0.02132	3.210	3.688
20.0 (290.1)	0.01958*	0.02124	7.450*	7.544
50.0 (725.2)	0.01977	0.02105	15.93	20.40

* linear interpolation

The conclusion is that natural gas flow correlations could be used to represent SHS properties due to the similar physical properties at various temperatures that may be encountered in SAGD operation and for pressures up to (50 bar) which is the critical methane pressure ("Air Dynamic and Kinematic Viscosity," Oct. 28, 2019). The assumption of using natural gas flow correlation to predict BHP of SAGD injector during flowback may be valid as long as the properties are in the same order of magnitude, as shown in **Table 3.5** through **Table 3.7**.

Chapter 4: ASSESSMENT OF OPERATIONAL PARAMETERS

This chapter describes the procedure used in the coupling of CMG STARS model results with empirical correlations for gas flow. The aim is to assign BHP during flowback and interpret the model output to assign representative testing variables for the SRT laboratory scale testing.

4.1 BHP Evaluation During Flowback

BHP evaluation was achieved using an iterative procedure that couples the 2D CMG model with average temperature and z-factor correlation, as shown in Figure **4.1**.

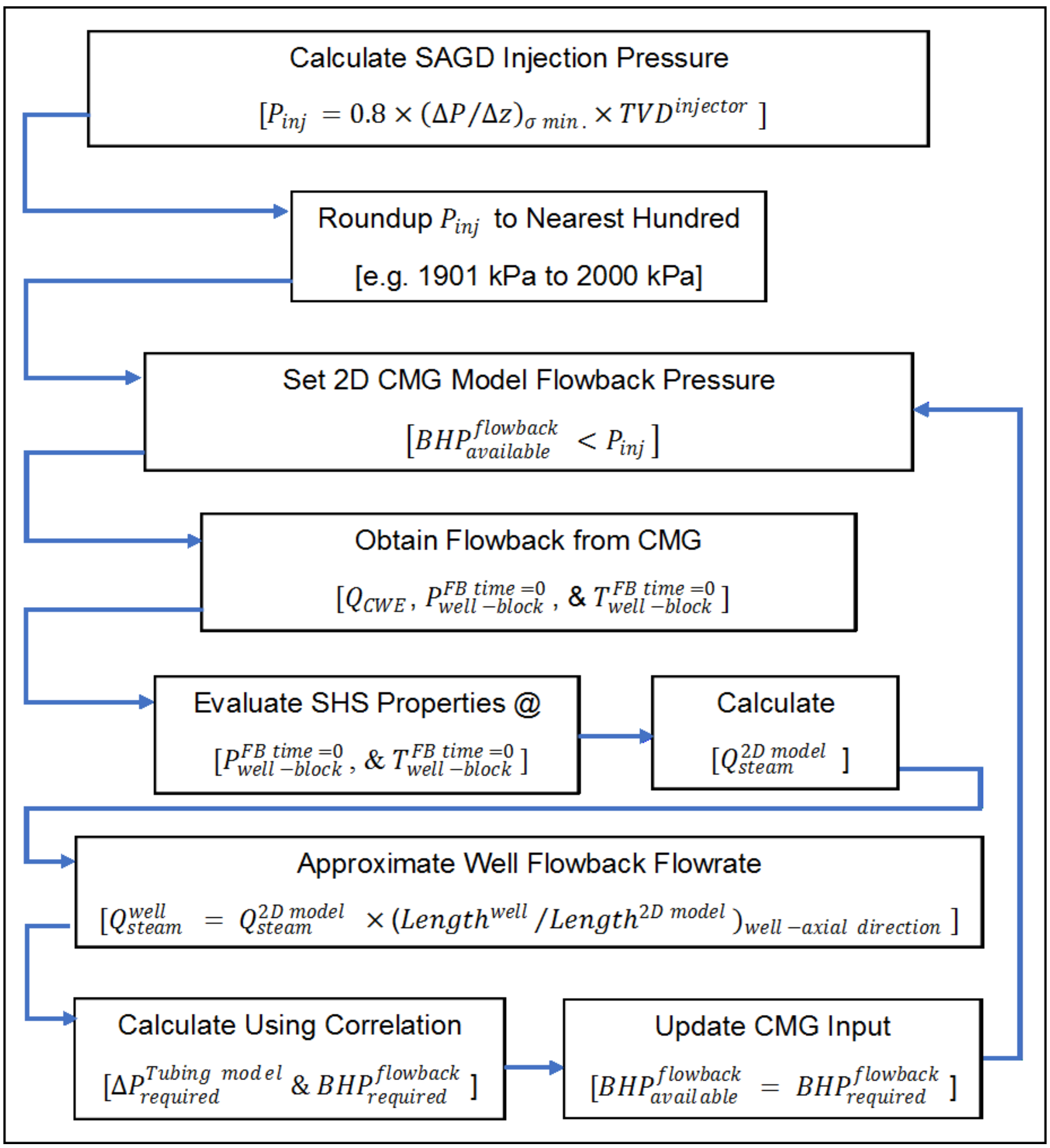

Figure 4.1. BHP assessment flowchart.

The procedure uses the CMG model to predict CWE flow rate (Q_{CWE}) at any specified ($BHP_{available}^{flowback}$) during SAGD injector flowback. Moreover, well-block pressure ($P_{well-block}^{FB\ time=0}$) and temperature ($T_{well-block}^{FB\ time=0}$) can be obtained from CMG to convert the (Q_{CWE}) to steam flow rate ($Q_{steam}^{2D\ model}$) at wellbore thermodynamic equilibrium conditions. The calculated ($Q_{steam}^{2D\ model}$) for the 2D model will be used to approximate the well flow rate (Q_{steam}^{well}) using Eq. 3.1, which will be used in natural gas flow correlation to evaluate ($\Delta P_{required}^{Tubing\ model}$) and ($BHP_{required}^{flowback}$). Finally, iterations continue until ($BHP_{required}^{flowback}$) converges to ($BHP_{available}^{flowback}$) with an absolute difference of 10 kPa (1.5 psi).

The methodology, described in Figure **4.1**, requires a precisely defined tubing model with general assumptions to clearly identify the future improvement areas in this procedure and overcome uncertainties due to approximations made, which are outside the scope of this research, as will be discussed in Section 7.2. Moreover, Appendices C and D demonstrate the SRT set-up equipment and the final SRT standard operational procedure (SOP), respectively, based on extensive laboratory testing.

4.1.1 Essential Assumptions and Tubing Specifications

The following list shows the assumptions used in the BHP evaluation procedure during flowback to guide the design of the SRT facility based on calculated parameters.

- SAGD injector may exhibit at least one uncontrolled shut-in "failure" during late SAGD mode that results in flowback before subsurface safety valve (SSSV) closure. Injector flowback duration ranges from 5 to 30 seconds based on the SSSV controlling mechanism. (Spec, 1998)
- SAGD injector WHP will be reduced to atmospheric pressure 101.3 kPa (14.7 psia), instantly, due to any surface facility failure near the wellhead, which includes but not limited to the possibility of pipe rapture, compressor dysfunction, steam generator interruption, or wellhead assembly severe leakage.
- Pressure wave transmitting speed equals sonic wave speed in any medium, including SHS.
- Instant thermodynamic equilibrium is expected at each simulation time-step during flowback.

- SHS properties are comparable to natural gas, as discussed in Section 3.2.2, which permits the applicability of natural gas flow correlations for SHS.
- SAGD injector will be treated as a sink-source well, which has a single BHP value along the well. BHP value is a function of injection pressure and TVD. In addition, homogeneous formation properties along SAGD injector result in the same flowback rate from all I-K planes, shown in **Figure 3.6**, which satisfies Eq. 3.1.
- Flowback transient flow rate will be treated as a steady-state flow rate at the initial flowback time ($FB^{time=0}$) to apply nodal system analysis (NSA), that will be used to evaluate pressure losses in the tubing component from a known WHP.
- Well flow rate used in the NSA is equal to the numerically calculated flow rate in the finite-difference explicit formulation.
- Flowback proposed scenario represents a static system without pressure wave pulsation.

The tubing model specifications and data used in the natural gas flow correlation to estimate pressure losses in the tubing are listed in Table **4.1** for the base case that has a cap rock depth of 110 meters. Moreover, tubing inner diameter (ID) was selected based on the average SAGD injector slotted linear outer diameter (OD) completion (*Canadian Natural Resources Limited (CNRL)*, 2017; *Suncor Energy Inc.*, 2015). SHS specific gravity was calculated based on SHS to air density ratio at atmospheric pressure at 100°C. ("Air Density at Varying Temperature and Constant Pressure," Oct. 31, 2019; "Superheated Steam Table," Oct. 28, 2019)

Table 4.1: Tubing Model Input Data.

Parameter	value	unit
Cap rock bottom TVD	110	m
Reservoir thickness	30	m
SAGD injector height from reservoir bottom	6	m
SAGD injector TVD	134	m
Min. in-situ stress gradient $(\Delta \boldsymbol{P} \,/\, \Delta \boldsymbol{z})_{\boldsymbol{\sigma\, min.}}$	21	kPa/m
Calculated min. stress $(\boldsymbol{\sigma_{min.}})$	2411	kPa
Max. injection Pressure AER allowance	0.8	Fraction of $(\boldsymbol{\sigma_{min.}})$
Calculated injection pressure	1930	kPa
CMG injection pressure $(\boldsymbol{P_{inj}})$	2000	kPa
SHS specific gravity $(\boldsymbol{\gamma_g})$	0.62	---
Wellhead flowback pressure (WHP)	101	kPa
Wellhead flowback temperature (WHT)	equal to BHT	°C
Tubing vertical section length	134 (440)	m (ft)
SAGD horizontal lateral	1000	m
Tubing ID	22 (8-5/8)	cm (in)
Liquid water density	1000	$\mathrm{Kg/m^3}$

4.1.2 Base Case Technique Results

The $(\boldsymbol{BHP^{flowback}_{available}})$ was varied between 1000 to 1600 kPa in different CMG runs during the investigation for SAGD injector flowback. Bottom hole flowing temperature $(\boldsymbol{BHT^{FB}_{available}})$ and the corresponding flowback flow rate $(\boldsymbol{Q^{2D\,model}_{CWE}})$ was determined for the 2D model that has a length of one meter. Steam density was evaluated at corresponding bottom hole pressure and temperature using SteamTab software. Equivalent steam flow rate $(\boldsymbol{Q^{2D\,model}_{steam}})$ was calculated using Eq. 4.1. Finally, SAGD injector flow rate $(\boldsymbol{Q^{well}_{steam}})$ was approximated using Eq. 3.1. The previously mentioned procedure is presented in **Table 4.2** in SI units.

$$Q_{steam}^{2D\ model} = Q_{CWE}^{2D\ model} \times \left(\frac{\rho_{water(CWE)}}{\rho_{steam}^{@(BHP\ \&\ BHT)}} \right) \qquad \text{(Eq. 4.1)}$$

Table 4.2: Base-Case Injector Flowback BHP Solution for Cap Rock TVD 110 m (361 ft).

$BHP_{available}^{FB}$	$BHT_{available}^{FB}$	$Q_{CWE}^{2D\ model}$	$\rho_{steam}^{@(BHP\ \&BHT)}$	$Q_{steam}^{2D\ model}$	Q_{steam}^{well}
kPa	°C	m^3/D	Kg/m^3	m^3/D	m^3/D
1000	207.1	96.8	4.763	20,329	20,329,204
1500	207.5	41.0	7.374	5,555	5,554,651
1525	207.6	38.4	7.508	5,120	5,120,272
1540	207.6	36.9	7.590	4,866	4,866,140
1545*	207.6	36.4	7.617	4,783	4,782,723
1550	207.6	35.9	7.644	4,700	4,700,026
1600	207.8	30.9	7.915	3,904	3,903,853

* NSA BHP solution

However, most natural gas flow correlations, especially in petroleum engineering, were developed in United States Customary Units (USCU). The ($BHP_{available}^{flowback}$) and ($Q_{steam}^{well}$) were converted to USCU. Pressure and temperature were evaluated at the average value of the wellbore and wellhead as the average temperature, and z-factor as the method requires (Lee, 1996). Furthermore, average z-factor ($Z_{average}^{(Pavg.,Tavg.)}$) was evaluated using SteamTab software at average pressure and temperature, whereas SHS viscosity was evaluated at the average temperature only because it shows a weak dependency on pressure ("Steam Viscosity," Nov. 4, 2019). Table **4.3** summarizes the calculated values for the parameters in USCU, which will be used in average temperature and z-factor correlation to predict pressure drop in tubing due to SHS well flow rate during flowback.

Table 4.3: Base-Case Injector Flowback BHP Solution for Cap Rock TVD 110 m (361 ft).

$BHP^{FB}_{available}$	Q^{well}_{steam}	$T^{(BHT,WHT)}_{average}$	$P^{(BHP,WHP)}_{average}$	$Z^{(Pavg.,Tavg.)}_{average}$	$\overline{\mu}^{(Tavg.)}_{SHS}$
psia	M SCF/D	R	psia	---	cP
145	717,824	864.8	79.9	0.972	0.016
218	196,135	865.5	116.1	0.959	0.016
221	180,797	865.7	117.9	0.958	0.016
223	171,823	865.7	119.0	0.958	0.016
224*	168,878	865.7	119.4	0.958	0.016
225	165,958	865.7	119.8	0.957	0.016
232	137,845	866.0	123.4	0.956	0.016

* NSA BHP solution

The average temperature and z-factor method equations, presented in Section 3.2.1, were used to evaluate the correlation parameter (S), Reynolds number (N_{Re}), and friction factor (f), as shown in **Table 4.4**. Moreover, the ($BHP^{FB}_{required}$) was determined using Eq. 3.6 and the difference between the calculated BHP and input ($BHP^{FB}_{available}$) was computed as ($\Delta BHP_{available-required}$). The correlation solution converges for the two values, as shown in Table **4.4**, at BHP around 223 psia (1545 kPa).

Table 4.4: Base-Case Flowback BHP Solution for Cap Rock TVD 110 m; Solution at [Δ**BHP** = 1 psi].

$BHP^{FB}_{available}$	S (Eq. 3.3)	N_{Re} (Eq. 3.4)	f (Eq. 3.5)	$BHP^{FB}_{required}$	$\Delta BHP_{available-required}$
psia	---	---	---	psia	psi
145	1.217E-02	6.46E+07	1.458E-02	951	-806
218	1.233E-02	1.76E+07	1.463E-02	259	-42
221	1.234E-02	1.63E+07	1.464E-02	239	-18
223	1.234E-02	1.55E+07	1.464E-02	227	-4
224*	1.234E-02	1.52E+07	1.464E-02	223	1
225	1.235E-02	1.49E+07	1.464E-02	219	6
232	1.236E-02	1.24E+07	1.466E-02	182	50

* NSA BHP solution

The graphical representation of NSA solution is shown in **Figure 4.2**. The IPR was created using the CMG results; however, the TPR was constructed based on average temperature and z-factor correlation. Furthermore, the intersection between IPR and TPR represents the well deliverability, which represents the only possible solution based on the total pressure drop in the production system. The NSA solution shows well flow rate of steam (Q_{steam}^{well}) has a value about (170 $Mscf/D$) based on the ($BHP_{available}^{FB}$) CMG input value of 224 psia, whereas the ($BHP_{required}^{FB}$) the correlation output has a value of 223 psia, which represents a converged solution based on the set criterion for convergence.

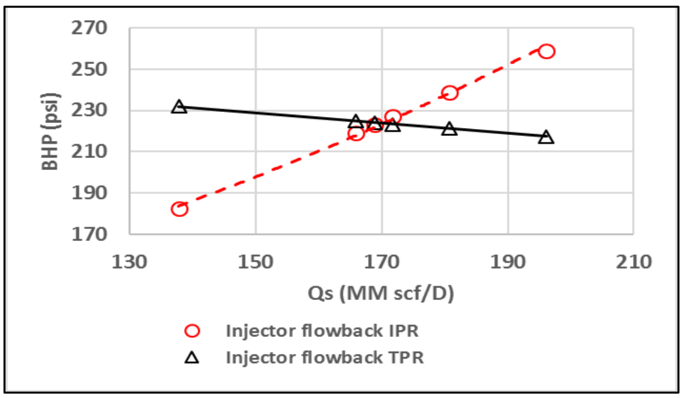

Figure 4.2. SAGD injector well deliverability during flowback for the base-case.

Finally, for the solution point in the NSA, which represents a unique CMG 2D model. The near-wellbore properties were investigated in detail using the solution as an example of SAGD related results in Section 3.1.5. Furthermore, **Table 4.5** shows that the well-block pressure ($P_{well-block}^{FB}$) has a value of 270 psia and results in 47 psi differential pressure ($\Delta P_{towards\ well}^{FB}$) towards the injector during flowback. However, the ($BHP_{solution}^{FB}$) of 223 psia shows a thermodynamic phase-equilibrium at saturation temperature ($T_{Steam}^{saturation}$) of 391°F ("Superheated Steam Table," Oct. 28, 2019) yet the well-block temperature ($T_{well-block}^{FB}$) has a higher value of 406°F, as shown in Table **4.6**. It is a clear evidence that SHS is the flowback fluid, which supports the conclusion that only SHS can exist at the wellbore sand face.

Table 4.5: Base-Case Flowback BHP and Differential Pressure in USCS.

$\boldsymbol{TVD^{CR}}$	$\boldsymbol{TVD^{injector}}$	$\boldsymbol{BHP_{solution}^{FB}}$	$\boldsymbol{P_{well-block}^{FB}}$	$\boldsymbol{T_{well-block}^{FB}}$	$\boldsymbol{\Delta P_{towards\ well}^{FB}}$

ft	ft	psia	psia	°F	psi
361*	440	223	270	406	47

* 361 ft represents the base-case of 110 m cap rock TVD.

Table 4.6: Base-Case Flowback Fluid Phase and Associated Medium Sonic Velocity in USCS.

$\boldsymbol{TVD^{CR}}$	$\boldsymbol{TVD^{injector}}$	$\boldsymbol{BHP^{FB}_{solution}}$	$\boldsymbol{T^{FB}_{well-block}}$	$\boldsymbol{T^{saturation}_{Steam}}$	FB Fluid Phase	$\boldsymbol{v^{sonic}}$
ft	ft	psia	°F	°F	Liquid/Gas	ft/s
361*	440	223	406	391	SHS	1680

* 361 ft represents the base-case of 110 m cap rock TVD.

Nevertheless, liquid oil will be present near the wellbore at residual oil saturation. Finally, the sonic velocity at SHS was evaluated using SteamTab software and has a value of 1680 ft/s. The sonic velocity indicates that SAGD injector well heel will start to experience flowback after 0.3 seconds from the surface equipment failure time, discussed in Section 2.2.4, based on the time for the pressure wave to reach ($TVD^{injector}$) of 440 ft. The flowback will at least last for 5 seconds before the closure of the SSSV if surface controlled SSSV was installed or around 30 seconds for subsurface controlled SSSV (Spec, 1998). However, it proves the validity of the SAGD injector flowback assumption listed in Section 4.1.1.

4.1.3 SAGD Injector Flowback BHP Changes with TVD

The constructed 2D CMG model was used to investigate the flowback relative severity in terms of (Q^{well}_{steam}) and ($BHP^{FB}_{solution}$) for deeper TVD of SAGD injector. The injection pressure (P_{inj}) during regular SAGD operation was set to the maximum approved pressure by AER for 3 cases. The depth was increased in equal steps of 100 meters to reach a maximum cap rock depth of 410 meters, which was encountered in the Pike project (Hassanpour, 2009). However, injection temperature was not intentionally matched with the base-case, but the injection SQ was kept constant at 0.95, and the CMG simulator will calculate the corresponding temperature to achieve consistent SQ in all cases. The same procedure used in Sections 4.1.1 and 4.1.2 was followed, and the results of NSA, presented in Appendix B, are shown in Figure **4.3** for $210\ m(TVD^{CR})$, Figure **4.4** for $310\ m(TVD^{CR})$, and Figure **4.5** for $410\ m(TVD^{CR})$. NSA results show direct proportionality trend between the depth of the injector ($TVD^{injector}$) and the converged solution of ($BHP^{FB}_{solution}$), which indicates that flowback injector is case-specific problem and cannot be generalized for SRT.

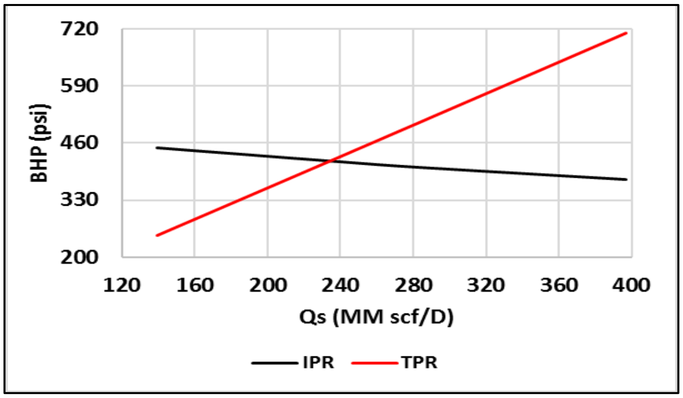

Figure 4.3. SAGD injector well deliverability during flowback for caprock 210 m TVD.

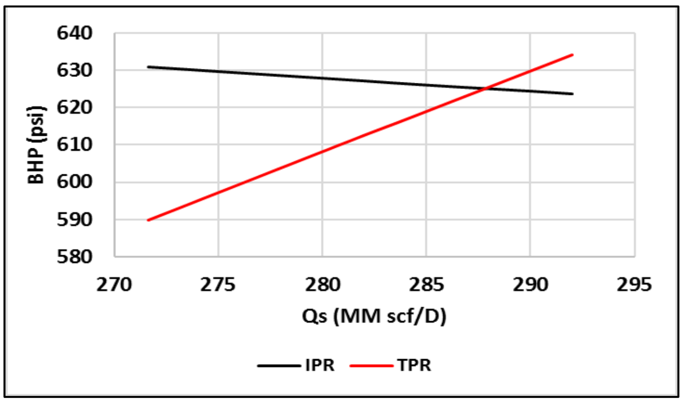

Figure 4.4. SAGD injector well deliverability during flowback for caprock 310 m TVD.

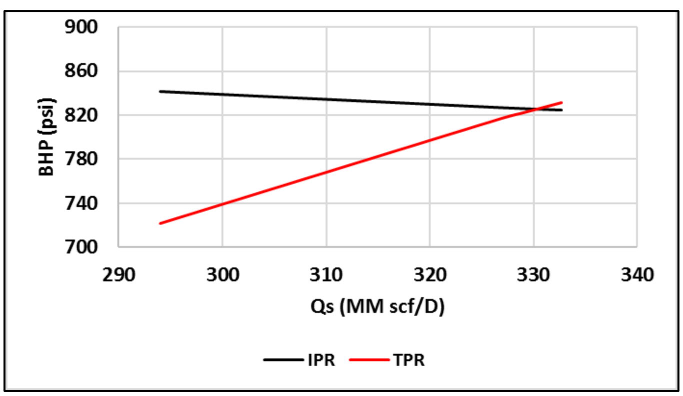

Figure 4.5. SAGD injector well deliverability during flowback for caprock 410 m TVD.

Furthermore, the results for well-block pressure $(P^{FB}_{well-block})$ and differential pressure $(\Delta P^{FB}_{towards\ well})$ towards the injector during flowback for the four cases, including the base-case, are presented in Table **4.7** in SI units and Table **4.8** in USCU.

However, the $(BHP^{FB}_{solution})$ shows a similar thermodynamic phase-equilibrium to be lower than well-block temperature $(T^{FB}_{well-block})$ that emphasizes and confirms that SHS is the only possible flowback fluid to exist and flow during flowback ("Superheated Steam Table," Oct. 28, 2019). The results are presented for the four cases in Table **4.9** in SI units and Table **4.10** in USCU.

The focus of the present research on the base-case scenario is to develop a representative SRT scheme. An objective is to upgrade the SRT facility to mimic the flowback occurrence in SAGD injectors. These details are further discussed in the next section.

Table 4.7: Flowback BHP and Summary of Differential Pressures for Various Depths in SI Units.

TVD^{CR}	$TVD^{injector}$	$BHP^{FB}_{solution}$	$P^{FB}_{well-block}$	$T^{FB}_{well-block}$	$\Delta P^{FB}_{towards\ well}$
m	m	kPa	kPa	°C	kPa
110*	134	1538	1862	208	324
210	234	2903	3448	241	545
310	334	4309	5095	264	786
410	434	5702	6695	282	993

* Base-case

Table 4.8: Flowback BHP and Summary of Differential Pressures for Various Depths in USCS.

TVD^{CR}	$TVD^{injector}$	$BHP^{FB}_{solution}$	$P^{FB}_{well-block}$	$T^{FB}_{well-block}$	$\Delta P^{FB}_{towards\ well}$
ft	ft	psia	psia	°F	psi
361*	440	223	270	406	47
689	774	421	500	466	79
1017	1102	625	739	508	114
1345	1430	827	971	539	144

* Base-case

Table 4.9: Flowback Fluid Phase Identity and Associated Medium Sonic Velocity in SI Units.

TVD^{CR}	$TVD^{injector}$	$BHP^{FB}_{solution}$	$T^{FB}_{well-block}$	$T^{saturation}_{Steam}$	FB Fluid Phase	v^{sonic}
m	m	kPa	°C	°C	Liquid/Gas	m/s
110*	134	1538	208	199	SHS	512
210	234	2903	241	232	SHS	515
310	334	4309	264	255	SHS	513
410	434	5702	282	272	SHS	509

* Base-case

Table 4.10: Flowback Fluid Phase Identity and Associated Medium Sonic Velocity in USCS.

TVD^{CR}	$TVD^{injector}$	$BHP^{FB}_{solution}$	$T^{FB}_{well-block}$	$T^{saturation}_{Steam}$	FB Fluid Phase	v^{sonic}
ft	ft	psia	°F	°F	Liquid/Gas	ft/s
361*	440	223	406	391	SHS	1679
689	768	421	466	450	SHS	1688
1017	1096	625	508	491	SHS	1683
1345	1424	827	539	522	SHS	1670

* Base-case

4.2 Base Case Set-Up Operational Parameters Requirements

This section demonstrates the usage of the proposed technique results to implement those parameters into SRT laboratory testing. The objective is to simplify SRT testing to the point that it can be widely used to assess optimum SL aperture size, performance and its interaction with the porous medium. It involves comparison of some possible testing schemes to mimic the SAGD injector flowback described in Section 4.1. Moreover, it includes the possibility of conducting high-pressure SRT using a large facility. The complication associated with using SHS in the lab that requires the need for a safer SRT technique. Air is suggested as a good alternative, due to comparable SHS properties, at SAGD injection temperatures up to 227°C (440°F) to air properties in terms of dynamic viscosity at laboratory temperature 21°C (70°F) at every pressure step as shown in Table **4.11**. The air density at laboratory temperature is significantly different from SHS density at SAGD injection temperature. However, properties at laboratory temperature of Nitrogen **Table 4.12**, Carbon-dioxide **Table 4.13**, Oxygen **Table 4.14**, and Methane **Table 4.15** are comparable to SHS properties at SAGD injection temperature. Even though methane provides the optimum match for SHS density, it does not match SHS viscosity, which is a crucial factor in Darcy's law. Furthermore, methane and carbon-dioxide were eliminated from being possible options due to the associated safety hazards. However, the final decision was to use air to simulate SHS flowback due to relatively lower cost compared to other investigated safe options when it comes to extensive SRT that requires massive volumes of flowback fluid.

Table 4.11: SHS Properties at 227°C (440°F) and Air Properties at 21°C (70°F) at Different Pressures ("Air Properties Calculator ", Nov. 4, 2019; "Superheated Steam Table," Oct. 28, 2019).

Pressure	Air Viscosity	SHS Viscosity	Air Density	SHS Density
bar (psia)	mPa·s (cP)	mPa·s (cP)	$\mathrm{Kg/m^3}$	$\mathrm{Kg/m^3}$
1.00 (14.50)	0.01829	0.01726	1.185	0.435
10.0 (145.0)	0.01840	0.01704	11.883	4.535
20.0 (290.1)	0.01853	0.01680	23.836	8.586

Table 4.12: SHS Properties at 227°C (440°F) and Nitrogen Properties at 21°C (70°F) at Different Pressures ("Nitrogen Properties Calculator ", Nov. 5, 2019; "Superheated Steam Table," Oct. 28, 2019).

Pressure	Nitrogen Viscosity	SHS Viscosity	Nitrogen Density	SHS Density
bar (psia)	mPa·s (cp)	mPa·s (cp)	$\mathrm{Kg/m^3}$	$\mathrm{Kg/m^3}$
1.00 (14.50)	0.01765	0.01726	1.146	0.435
10.0 (145.0)	0.01777	0.01704	11.486	4.535
20.0 (290.1)	0.01792	0.01680	23.012	8.586

Table 4.13: SHS Properties at 227°C (440°F) and Carbon-Dioxide Properties at 21°C (70°F) at Different Pressures ("Carbon-Dioxide Properties Calculator ", Nov. 5, 2019; "Superheated Steam Table," Oct. 28, 2019).

Pressure	CO2 Viscosity	SHS Viscosity	CO2 Density	SHS Density
bar (psia)	mPa·s (cp)	mPa·s (cp)	$\mathrm{Kg/m^3}$	$\mathrm{Kg/m^3}$
1.00 (14.50)	0.01474	0.01726	1.808	0.435
10.0 (145.0)	0.01483	0.01704	19.016	4.535
20.0 (290.1)	0.01500	0.01680	40.556	8.586

Table 4.14: SHS Properties at 227°C (440°F) and Oxygen Properties at 21°C (70°F) at Different Pressure ("Oxygen Properties Calculator ", Nov. 5, 2019; "Superheated Steam Table," Oct. 28, 2019).

Pressure	O2 Viscosity	SHS Viscosity	O2 Density	SHS Density
bar (psia)	mPa·s (cp)	mPa·s (cp)	$\mathrm{Kg/m^3}$	$\mathrm{Kg/m^3}$
1.00 (14.50)	0.02043	0.01726	1.309	0.435
10.0 (145.0)	0.02053	0.01704	13.17	4.535
20.0 (290.1)	0.02066	0.01680	26.507	8.586

Table 4.15: SHS Properties at 227°C (440°F) and Methane Properties at 21°C (70°F) at Different Pressure ("Methane Properties Calculator ", Nov. 5, 2019; "Superheated Steam Table," Oct. 28, 2019).

Pressure	CH4 Viscosity	SHS Viscosity	CH4 Density	SHS Density
bar (psia)	mPa·s (cp)	mPa·s (cp)	$\mathrm{Kg/m^3}$	$\mathrm{Kg/m^3}$
1.00 (14.50)	0.01103	0.01726	0.657	0.435
10.0 (145.0)	0.01117	0.01704	6.680	4.535
20.0 (290.1)	0.01133	0.01680	13.607	8.586

4.2.1 SRT Terminals Pressure and Differential Pressures

SRT variables, presented in **Figure 4.6**, or more explicitly testing operational parameters, should be carefully selected to match the proposed iterative procedure results. These are discussed in Section 4.1.2 for the base-case SAGD injector flowback scenario. The procedure applies to other testing variables, but the purpose of this research is to come up with justified operational parameters based on calculated values not based on assumptions. It does not mean that the assumptions, listed in Section 4.1.1, are invalid or do not require further improvements. Section 7.2.1 describes possible procedure improvements, yet those assumptions were used to facilitate the technique to calculate the operational parameters. They were derived based on a systematic procedure, the proposed iterative technique discussed in Section 4.1, which includes coupling the developed CMG model, natural gas flow correlations, and thermodynamic equilibrium concepts to eliminate the possibility of assigning subjective operational parameters. This contradicts the previous researches (Fattahpour et al., 2018a; Mahmoudi et al., 2018b; Mahmoudi et al., 2018a), which involve simulating steam breakthrough in SAGD producers and SAGD injector flowback SRT based on hypothetical assumptions of the operational parameters themselves, which seems to be biased and subjective. Despite the misleading technical assumptions concerning thermodynamic equilibrium, the objectives of this research extend to enhance SAGD injector flowback SRT and emphasize the importance of involving thermodynamics, reservoir engineering, production engineering and SRT experience. They help to increase the chances of getting representative SRT results.

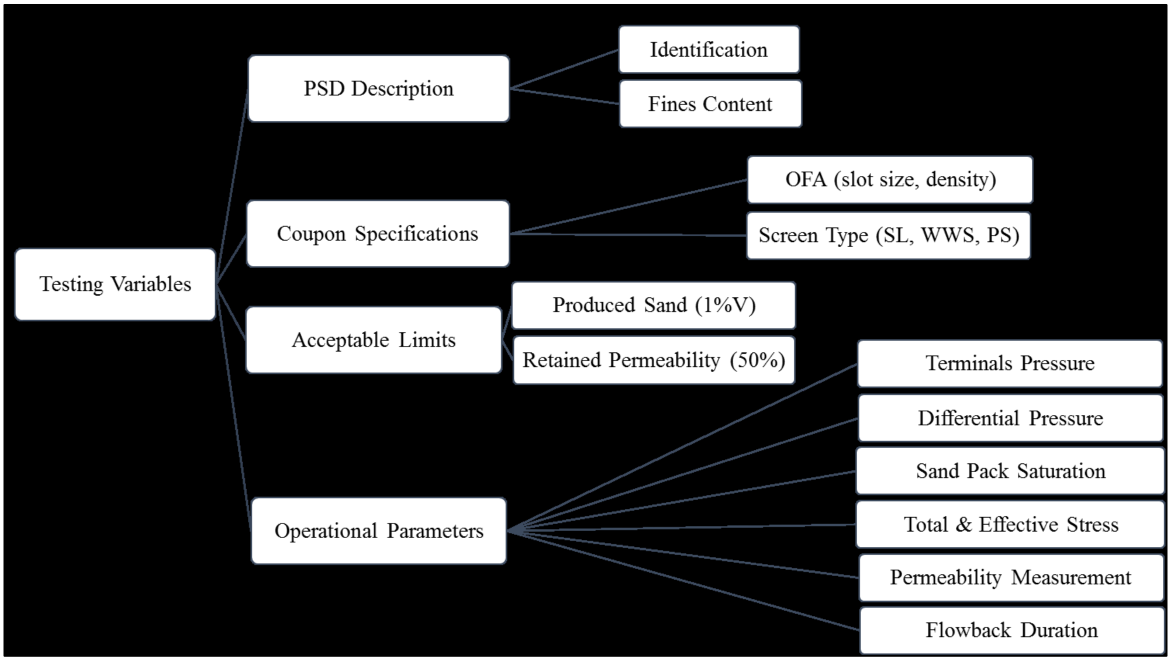

Figure 4.6. Sand retention testing (SRT) variables.

The investigation, discussed in Section 4.1.2, results in a representative set of SRT operational parameters summarized in **Table 4.16**. The parameters can be translated into laboratory testing as follows. At this point, it is wise to emphasize that those parameters are influenced by the CMG model input properties, strictly limited to SAGD injector at the specified (TVD^{CR}) and ($TVD^{injector}$), and can not , under any circumstances, represent a different ($TVD^{injector}$). They cannot be generalized by any form because the problem and its solution are case-specific.

Furthermore, the following sections will use USCS units for all related laboratory testing parameters and equipment specifications.

Average well-block pressure ($P^{FB}_{well-block}$) and well bottom hole pressure ($BHP^{FB}_{solution}$), presented in Table **4.16**, can be assigned to SRT injection pressure at 270 psia and outlet pressure at 223 psia, respectively, because they are intensive properties. However, they exceed the maximum permissible pressure limit of 200 psig set by RGL Reservoir Management Inc., the SRT aluminum cell provider. Differential pressure ($\Delta P^{FB}_{towards\,well}$) at 47 psi will be matched as a solution for equipment limitation for this research. However, using lower terminals pressure to match the differential pressure instead of actual terminal pressures will influence the measured core permeability and stress-strain diagram (Shafer, Boitnott, & Ewy, 2008), yet it will be used to lower the cost of this project as it represents a first step only. However, the research will discuss the influence and improvements in results for using High-Pressure facility (HP-SRT) in Section 7.2.3.

Table 4.16: SAGD Injector Flowback Base-Case SRT Operational Parameters Summary in USCS Units.

<table>
<tr><td>TVD^{CR}</td><td>$TVD^{injector}$</td><td>$BHP^{FB}_{solution}$</td><td>$P^{FB}_{well-block}$</td><td>$T^{FB}_{well-block}$</td><td>$\Delta P^{FB}_{towards\ well}$</td></tr>
<tr><td>ft</td><td>ft</td><td>psia</td><td>psia</td><td>°F</td><td>psi</td></tr>
<tr><td rowspan="4">361*</td><td rowspan="4">440</td><td rowspan="4">223</td><td>270</td><td>406</td><td>47</td></tr>
<tr><td>$T^{FB}_{well-block}$</td><td>$T^{saturation}_{Steam}$</td><td>FB Fluid Phase</td></tr>
<tr><td>°F</td><td>°F</td><td>Liquid/Gas</td></tr>
<tr><td>406</td><td>391</td><td>SHS</td></tr>
</table>

* 361 ft represents the base-case for 110 m cap rock TVD.

Similarly, High-Temperature (HT-SRT) laboratory application is not favourable due to associated safety hazards, yet Section 7.2.4 presents the HT-SRT as a more representative facility to SAGD injector flowback SRT applications. The ultimate set-up improvement will be discussed in Section 7.2.4 for High-Pressure-High-Temperature (HP/HT-SRT) facility, which considers both HP-SRT and HT-SRT set-ups.

4.2.2 Fluid Saturation and Saturation Distribution

Fluid saturation, as discussed in Section 2.3, is affected by the capillary pressure curve of a given porous media. A mercury pump injection test should measure capillary pressure and is cross-checked by the centrifugal method to ensure reliable results in core analysis according to API standards (RP40, 1998). Moreover, the techniques require a consolidated rock specimen of the porous medium, which is nearly impossible to achieve when dealing with loose sand particles found in oil sand porous medium. However, unpublished research was done by the research team co-workers to approximate the sand pack capillary pressure and relative permeability curves based on multi-phase fluid flow at steady-state condition. Despite the involved error in such approximation, it remains a cost reliable technique to quantify unknown parameters in the absence of exact values. Constructed relative permeability curves indicate the irreducible water saturation to be around 0.30 for all Pike 1 project sand replica with commercial sands, as discussed earlier in Section 2.1.3.

Well-block saturation during CMG model flowback, presented in Figure **3.10**, can be justified mathematically, knowing that CMG saturation represents the average block saturation. Moreover, Table **4.17** presents the saturation values shown in Figure **3.10**.

Table 4.17: Well-Block Average Saturations Just Before and During Flowback.

Flowback time (s)	S_w	S_o	S_g^*
-10	0.2333	0.2136	0.5531
0	0.2178	0.2136	0.5686
10	0.2032	0.2136	0.5832
20	0.1988	0.2136	0.5870
30	0.1974	0.2136	0.5890
40	0.1968	0.2136	0.5896

S_g^*: Simulators represent water vapour (steam) and hydrocarbon gas combined saturation.

Average saturation (S_g^*), expressed by Eq. 4.2, was used to estimate the volume of an SHS cylinder around the SAGD injector during flowback, as shown in **Figure 4.7**.

$$S_g^* = \ (S_g^{SHS} \times V^{SHS} + S_g'' \times V) \,/\, (V^{SHS} + V'') \qquad \text{(Eq. 4.2)}$$

It is wise to assume that unaffected volume (V'') has a gas saturation (S_g'') equals to average block gas saturation before flowback ($S_g^{FB\ t=-10}$). Keeping the third dimension fixed for both cylinders, reduces the weighted volume average saturation to the area-weighted average saturation, as presented by Eq. 4.3. Moreover, combining Eq. 4.3 with the total area ($A^* = 0.25\, m^2 = A^{SHS} + A''$) and rearranging variables yield Eq. 4.4. Finally, solving for (A^{SHS}) yields Eq. 4.5. Besides, residual oil saturation in injector (S_{or}) is constant which implies that the increase in (S_g^*) equals the decrease in (S_w).

$$S_g^* = \ (S_g^{SHS} \times A^{SHS} + S_g'' \times A'') \,/\, (A^{SHS} + A'') \qquad \text{(Eq.4.3)}$$

$$S_g^* \times A^* \ = S_g^{SHS} \times A^{SHS} + S_g'' \times (A^* - A^{SHS}) \qquad \text{(Eq.4.4)}$$

$$A^{SHS} = A^* \times \left[S_g^* - S_g'' \right] / \left[S_g^{SHS} - S_g'' \right] \qquad \text{(Eq.4.5)}$$

The SHS zone gas saturation (S_g^{SHS}) can be calculated using Eq. 4.6 at each time step with liquid water saturation (S_w^{SHS}) equal to zero at SHS conditions. However, gas saturation (S_g'') is constant at each time step.

$$S_g^{SHS} = 1 - S_o - S_w^{SHS} \qquad \text{(Eq.4.6)}$$

The calculated SHS zone radius propagation, presented in **Table 4.18**, is shown graphically for sink-source well in **Figure 4.8**. It is a clear indication that SHS is the only mobile fluid near the wellbore, which has comparable size to the SRT facility. Nevertheless, the presence of residual oil in the near region of flowback well will be taken into consideration in the SRT sand pack.

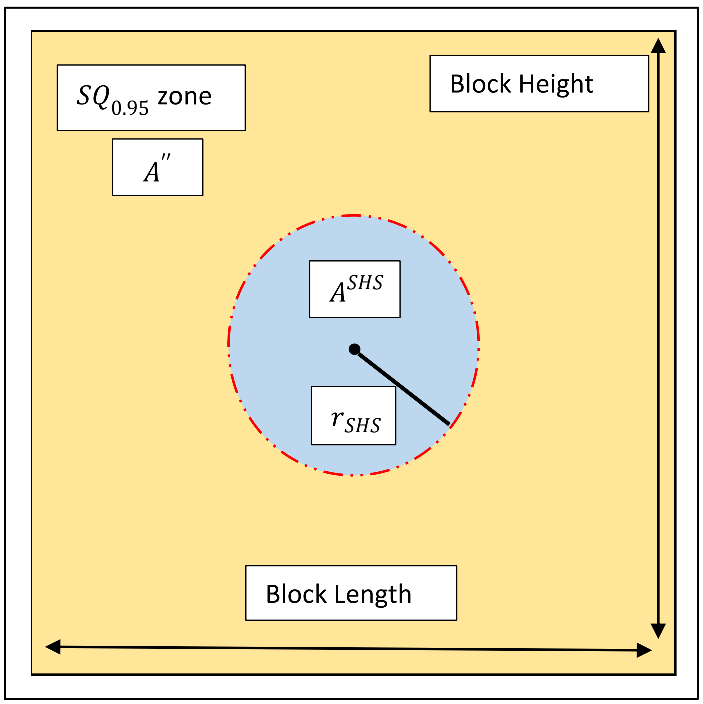

Figure 4.7. SAGD injector well-block during flowback (sink-source).

Table 4.18: SHS Zone Radius ($\boldsymbol{r_{SHS}}$) Propagation Near the SAGD Injector Wellbore During Flowback.

FB time	S_w	S_o	S_g^*	S_g''	S_g^{SHS}	A^{SHS}	r_{SHS}	r_{SHS}
s	---	---	---	---	---	m^2	m	cm
0	0.2178	0.2136	0.5686	0.5531	0.7864	0.01661	0.073	7.3
10	0.2032	0.2136	0.5832	0.5531	0.7864	0.03225	0.101	10.1
20	0.1988	0.2136	0.5870	0.5531	0.7864	0.03633	0.108	10.8
30	0.1974	0.2136	0.5890	0.5531	0.7864	0.03847	0.111	11.1
40	0.1968	0.2136	0.5896	0.5531	0.7864	0.03911	0.112	11.2

Note that S_w represents the average well-block water saturation not (S_w^{SHS}) that equals zero in Eq. 4.6.

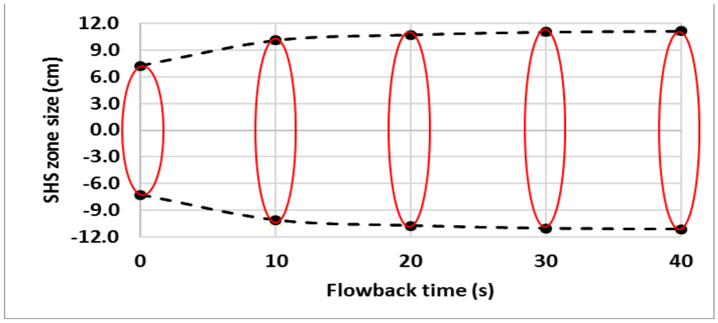

Figure 4.8. SHS zone radius propagation around the flowback well (sink-source represented at y = 0).

The present research intends to match the fluid saturation based on the previous argument and to match fluid distribution at the pore scale, discussed in Section 2.3.2, to select the best representation of the SAGD injector flowback SRT. However, matching fluid distribution at the pore scale requires thermodynamic equilibrium to take place, which requires the HT-SRT facility. However, a new technique will be presented in Section 5.3.1 to overcome this complication to use the regular SRT facility.

In this research, Sections 5.1 and 5.2 will consider matching near well saturation during flowback in SRT testing, and Section 5.3 will present a reasonable approximation for fluid distribution at the pore scale, which will be used in SRT development.

4.2.3 Recommended Ambient Conditions Testing Operational Parameters

There are two possible scenarios of SAGD injector SRT using laboratory facilities, discussed in Section 2.2.4, based on flowback duration that ranges from 5 to 30 seconds depending on the selected SSSV controlling mechanism (Spec, 1998). Moreover, simulation results, discussed in Section 3.1.5, shows three regions for SAGD injector flowback based on near-wellbore fluid saturations.

Furthermore, the base-case SAGD ($TVD^{injector} = 440ft$), which was discussed in Section 4.1.2, will be used to assign the SRT operational parameters. This research intends to investigate the SAGD injector flowback possibility and mimic the flowback with a simple SRT set-up to evaluate SLs sand control efficiency. Accordingly, the 5 seconds flowback duration was selected to minimize the overall cost of the required equipment because 30 seconds flowback requires customized expensive compressors to deliver extra-large required flow rates. Although simulating the 5 seconds flowback requires the same sophisticated compressor, the impact can be approximated by discharging compressed air from a known volume tank.

A commercial 30.2-litre tank and its compressor [Campbell Hausfeld 8 Gallon Air Compressor 200-psi] will be used to induce the flowback effect on the sand pack in the SRT cell. The tank volume is approximately 8 to 12 times the sand pore volume (PV), depending on the sand replica type discussed in Section 2.1.3. The SRT flowback differential pressure across the SRT cell should be at least equal to ($\Delta P^{FB}_{towards\ well} = 47\ psi$) as discussed in Section 4.2.1. However, the developed iterative technique has some uncertainty based on the CMG input data, SHS approximation to natural gas in the correlation, and other unconsidered factors. The solution to overcome such uncertainty is to specify a design factor that will be considered to set the differential pressure across the cell to the maximum allowable operating pressure for both the flowback tank and SRT aluminum cell, according to Eq. 4.7.

$$\Delta P^{FB}_{SRT\ cell} = DF \times \Delta P^{FB}_{towards\ well} \qquad \text{(Eq. 4.7)}$$

Furthermore, the theoretical value ($\Delta P^{FB}_{SRT\ cell}$) should be 200 psi in ideal conditions, yet it is not the case in laboratory conditions, as will be discussed in Section 5.1. However, the design factor will be calculated based on the measured values of the maximum differential pressure ($\Delta P^{FB\ max}_{SRT\ cell}$) during the flowback. The flowback duration will be controlled based on tank specifications and tank discharge time models of isothermal and adiabatic processes ("Discharge Tank Calculation Software," Nov. 7, 2019), as shown in **Figure 4.9**.

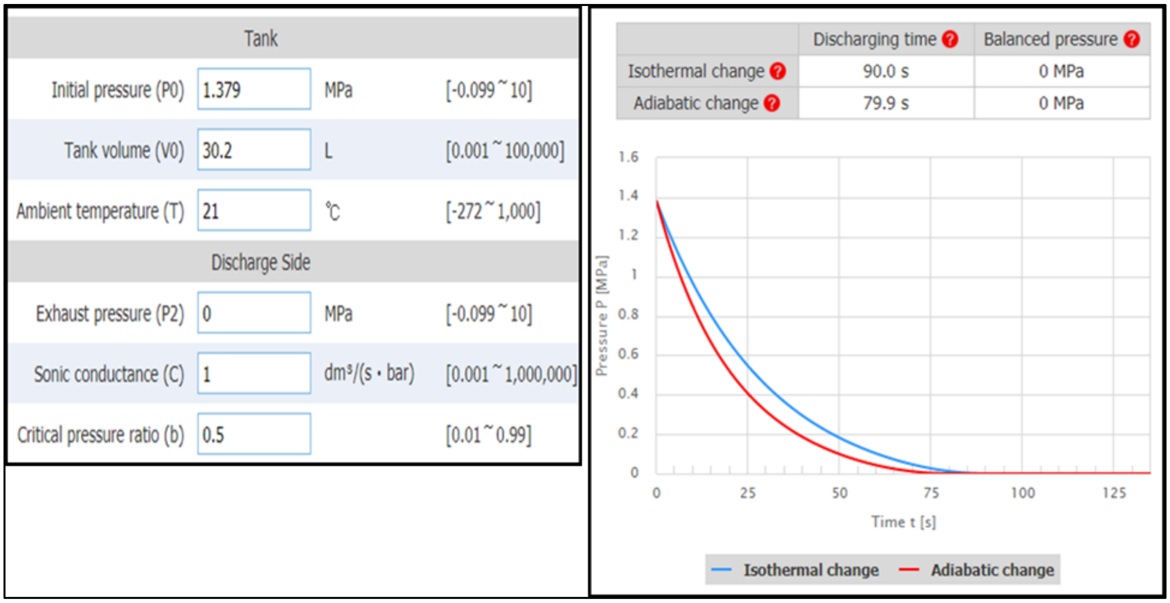

Figure 4.9. Flowback tank discharge time based on isothermal and adiabatic models ("Discharge Tank Calculation Software," Nov. 7, 2019).

The remaining SRT operational parameters, according to **Figure 4.6**, are stress and permeability measurement. Effective stress ($\boldsymbol{\sigma_i'}$) is a function of total stress ($\boldsymbol{\sigma_i}$), pore pressure (P) and Biot's coefficient ($\boldsymbol{\alpha}$), as presented in Eq. 4.8, that represents certain fluids and solids of a porous medium. Moreover, researchers show that loose sand ($\boldsymbol{\alpha}$) approaches unity (Alam et al., 2010). Furthermore, it is possible to simplify matching effective stress during SRT flowback with effective stress during SAGD injector flowback by neglecting thermal-induced stresses.

$$\sigma_i' = \sigma_i - \boldsymbol{\alpha} \times P \qquad \text{(Eq. 4.8)}$$

Table 4.19: Total and Effective Stress Evaluation for SAGD Injector and SRT Cell During Flowback.

Parameter	Symbol	Magnitude	Unit
SAGD injector depth	$\boldsymbol{TVD^{injector}}$	440	ft
Vertical stress gradient	$\boldsymbol{\partial P/\partial z}$	0.92	psi/ft
Total vertical stress	$\boldsymbol{\sigma_{v\,,well\ inj}}$	410	psi
Loose sand Biot's coefficient	α	1.00	---
Injection pressure	$\boldsymbol{P_{well\,inj}}$	290	psia
Injection phase effective stress	$\boldsymbol{\sigma'_{v\,,well\ inj}}$	120	psi
Flowback BHP	$\boldsymbol{BHP^{FB}_{solution}}$	223	psia
Flowback phase effective stress	$\boldsymbol{\sigma'_{v\,,well\,FB}}$	187	psi
SRT axial applied 'total' stress	$\boldsymbol{\sigma_{v\,,SRT}}$	200	psi
SRT effective stress after loading	$\boldsymbol{\sigma'^{\,initial\,L}_{v\,,SRT\,FB}}$	200	psi
SRT pressure at flowback start	$\boldsymbol{P^{FB\,,start}_{SRT}}$	200	psi
SRT effective stress after pressurizing	$\boldsymbol{\sigma'^{\,initial\,P}_{v\,,SRT\,FB}}$	200	psi

The exception in effective stress calculation in SRT sand pack ($\sigma'^{\,initial}_{v\,,SRT\,FB}$), which does not follow Eq. 4.8. The reason is using a fixed displacement piston to apply the force on the sand at zero gauge pore pressure for safety purposes in laboratory testing. Using fixed displacement piston results in approximately fixed effective stress ($\sigma'^{\,initial\,L}_{v\,,SRT\,FB} \cong \sigma'^{\,initial\,P}_{v\,,SRT\,FB}$) even after increasing the pore pressure ($P^{FB\,,start}_{SRT}$) of the sand, as shown in Table **4.19**. Furthermore, it helps to match the effective stress for SAGD well ($\sigma'_{v\,,\boldsymbol{well\,FB}}$) during flowback with sand pack ($\sigma'^{\,initial\,\boldsymbol{P}}_{v\,,SRT\,FB}$) during SRT. Further improvements for effective stress matching SAGD well and SRT sand pack at all times, including before and during flowback will be discussed in Section 7.2.3.

In previous research for SAGD flowback injector SRT testing, permeability measurements were not carried out (Fattahpour et al., 2018a; Mahmoudi et al., 2018a). However, the influence of retained permeability is as important as sand production when it comes to performance evaluation of SLs, even other mechanical screens, in SRT. Compressible fluid flow in porous media complicates permeability measurements by injecting the fluid from near the screen side, bottom to top injection is common practice, which could lead to erroneous permeability results. Meanwhile, top to bottom injection or injection from the side away from the screen may disturb the sand particles near the screen unless very small flow rates were injected. A rotameter, [Omega rotameter model 044-40-CA, max. 200 psig and 60 L/min], was used to evaluate the approximate volumetric flow rates to apply Darcy's law in permeability determination before and after the flowback to obtain the retained permeability. A more accurate flow rate device measurement will be discussed in Section 7.2.2.

The last topic that is discussed in this section is the number of flowback cycles per SRT. Previous researches tend to apply several cycles in an incremental differential pressure trend across the sand pack. However, the produced sand and retained permeability, if measured, were given in terms of a single value for all flowback cycles. Figure **4.10** shows the SRT cell pressure during eight cycles of compressible fluid flowback to mimic the high SQ SAGD injector flowback scenario (Fattahpour et al., 2018a). Figure **4.11** shows 20 cycles of incompressible fluid flowback that represents low SQ flowback fluids (Mahmoudi et al., 2018a).

Despite the inconsistency of the suggested flowback fluids in SAGD injector in those two tests concerning basic principles of thermodynamics, as discussed in Section 2.4.1, the effect of each flowback cycle was not isolated or quantified for each cycle, which may lead to inaccurate conclusions. Also, flowback volumes were often variables (not constant) that further complicates the evaluation of SLs performance. Moreover, the number of cycles themselves is purely subjective in those two pieces of research. Nevertheless, they formed the drive for initiating present investigation.

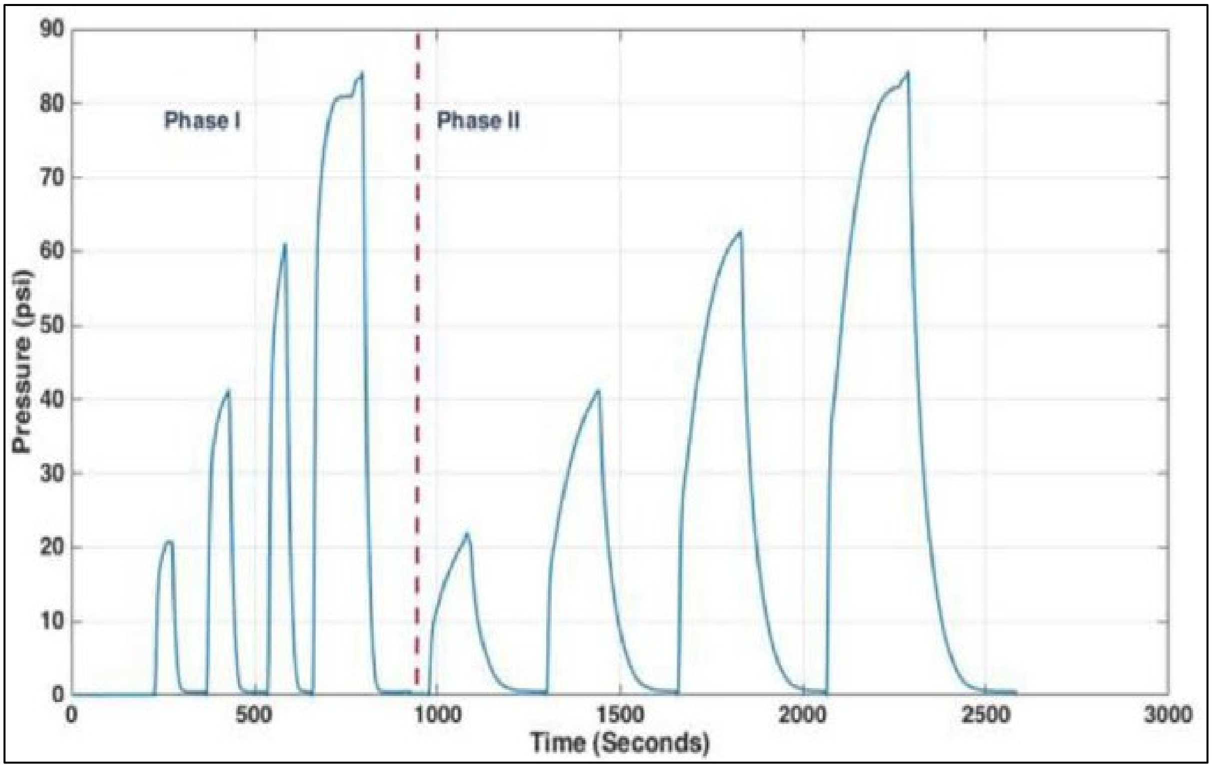

Figure 4.10. SAGD injector flowback SRT using compressible fluid (Fattahpour et al., 2018a).

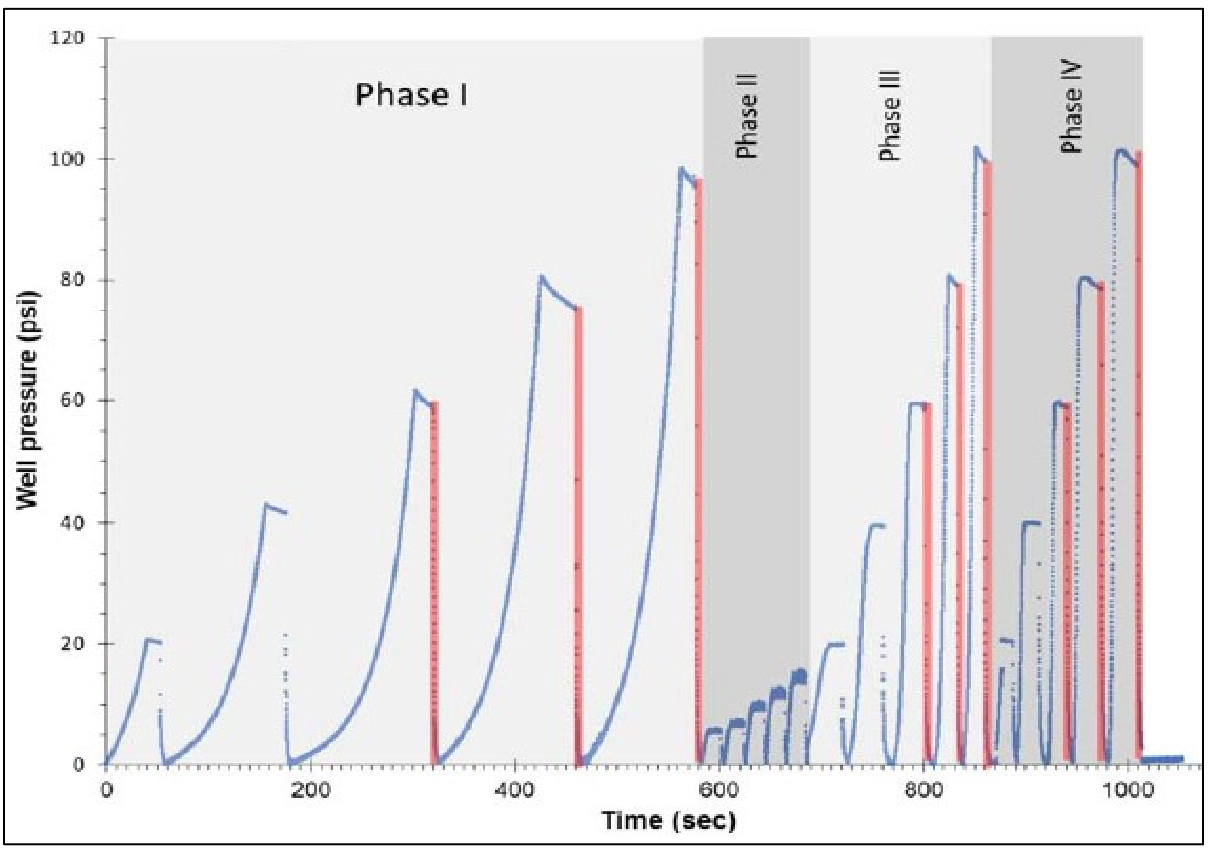

Figure 4.11. SAGD injector flowback SRT using incompressible fluid (Mahmoudi et al., 2018a).

Chapter 5: **DESIGN OF EXPERIMENTAL SET-UP AND TESTING PROCEDURE**

The purpose of SRT experiments is to evaluate the deployed SAS performance in SAGD producer and injector. The SAS performance evaluation is based on sand production and retained permeability, as discussed earlier in Section 2.2.1. (Fattahpour et al., 2018a; Fattahpour et al., 2018b; Mahmoudi, 2017; Mahmoudi et al., 2018b; Mahmoudi et al., 2018a; Montero, 2019; Montero et al., 2019)

This research went through several stages of improvements and enhancements for both SRT facility and operational parameters. The lack of research and released data in this specific area of interest required the study to consider all possible scenarios, as discussed in Section 2.2.4 and to obtain a representative set of SRT operational parameters, as discussed in Section 4.2.3. However, the required testing equipment and the final SOP are based on intensive improvements of SRT laboratory experiments, which will be discussed in this chapter. This chapter demonstrates the major development stages of the SRT facility, which yields the most representative experimental testing to the SAGD injector flowback scenario.

5.1 Initial Testing Set-Up (SRT-I)

Initial set-up (SRT-I) was inspired by the previous research of (Fattahpour et al., 2018a). The set-up schematic diagram is presented in Figure **5.1** and Table **5.1**. The intention was to reproduce the results of the previous research and upgrade the equipment to deliver the proposed operational parameters during the SRT experiment. Despite the process cons of being resource-intensive, the investment was worthy because most of the research findings in the experimental SRT were in the form of set-up re-design and mandatory upgrades to best mimic SAGD injector flowback. However, the operational parameters, discussed in Sections 4.1 and 4.2, contradict the possibility of liquid flowback scenario suggested by Mahmoudi et al. (2018a) in SAGD and narrow the SRT possible upgrades to mimic single-phase compressible fluid flowback scenario proposed by (Fattahpour et al., 2018a). Therefore, the present research proposed a single flowback scenario in the SRT that avoids being subjective and, at the same time, in line with the stated assumptions in Section 4.1.1.

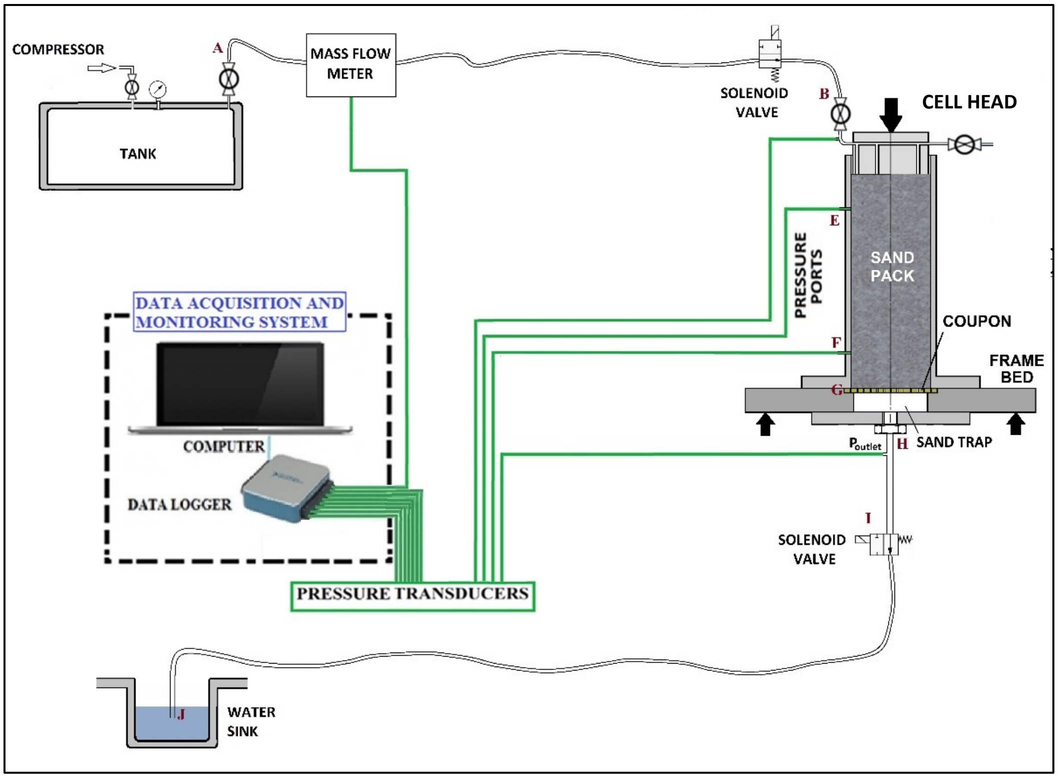

Figure 5.1. Initial testing set-up (SRT-I).

Table 5.1: SRT-I Diagram Specifications.

Start Point (SP)	SP Description	End Point	Flow Media	Length (in)	D (in)
A	FB tank outlet	B	Flexible tube	≅ 120	1/8
B	Cell head inlet	E	Sand	≅ 4	6
E	Top port	F	Sand	10	6
F	Bottom port	G	Sand	2	6
G	Sand pack end	H	Conduit	≅ 4	6
H	Trap outlet	I	Flexible tube	12	1/8
I	Solenoid inlet	J	Flexible tube	≅ 120	1/8

5.1.1 Specifications and Mechanical Components

A commercial compressor was used to pressurize the flowback tank. The flowback process was controlled by two solenoid valves to enhance testing repeatability, eliminate human interference and capture the entire flowback duration as recommended by Fattahpour et al. (2018a). Gas mass flowmeters (MFMG) were part of the design, as shown in Figure **5.1**, yet they were not available at the preliminary stages of present research. A technique will be proposed in Section 5.2 to replace the MFMG and maintain research feasibility. Absolute pressure transducers were used to record the pressure at the SRT cell outlet just after the SL coupon (P_{outlet}^{SRT-I}), 2 inches from the SL (P_{bottom}^{SRT-I}), in the porous medium, and 12 inches (P_{top}^{SRT-I}) from the SL in the porous medium, as shown in Figure **5.1**. The outlet line was directed to a nearby sink away from personnel for safety proposes.

5.1.2 Testing Scheme

The testing program can be summarized in few steps, including initial permeability measurement, pressurizing the flowback tank and the SRT cell, initiate the flowback by opening the outlet valve, and final permeability measurement to quantify the effect of flowback on sand permeability.

In short, the SRT test procedure consists of a few steps to check the functionality of the set-up in delivering the intended testing operational parameters across the sand pack. A SL coupon was used in the SRT-I facility functionality test. The coupon specifications are (10 thou, 10 thousandths of an inch or 0.010") of aperture size or slot width (SW) and slots density of 216 slots per foot (SPF), which is equivalent to 54 slots per column (SPC).

The commercial sand print one replica (DC-1), discussed in Section 2.1.3., was mixed with de-ionized liquid water (DI-water) volume equivalent to 30% PV as the irreducible water saturation. The DI-water used in mixing the sand was not intended to match the liquid water saturation in the SAGD injector near-wellbore during flowback because thermodynamic equilibrium proves the impossibility of liquid water existence. However, it was intended to mimic the effect of residual oil saturation, discussed in Section 3.1.5, in near-wellbore of SAGD injector during flowback for practicality.

Moist tamping method was used to pack the sand in the SRT cell as the common SRT practice by the research team. SRT-I pressure gradients were comparable to the SRT facility results proposed by Fattahpour et al., (2018a), yet the differential pressure across the sand pack during flowback was problematic and not justifiable as is discussed in the next section.

5.1.3 Associated Problems and Deficiencies

The experiments conducted by SRT-I setup were comparable to Fattahpour et al. (2018a) SRT in terms of the operational parameters, sand pack properties and SRT cell specifications. DC-1 sand pack has percentiles (D10, D50 and D90), which are comparable to PSD (C) used by Fattahpour et al. (2018a) SRT. However, some minor differences were encountered in pressure gradients across the sand pack ($\Delta P/\Delta x$ Top-Outlet), shown in Figure **5**.**2**, and near-coupon region ($\Delta P/\Delta x$ Bottom-Outlet) which represents the 2 inches of porous medium away from the coupon shown in Figure **5**.**3**.

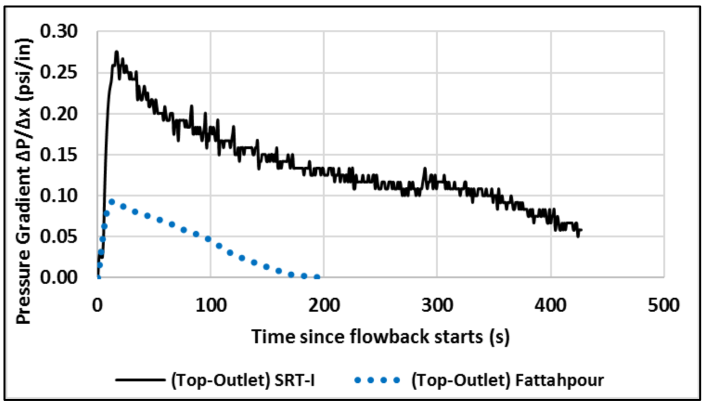

Figure 5.2. Pressure gradient across the sand pack during flowback in SRT-I and Fattahpour's SRT.

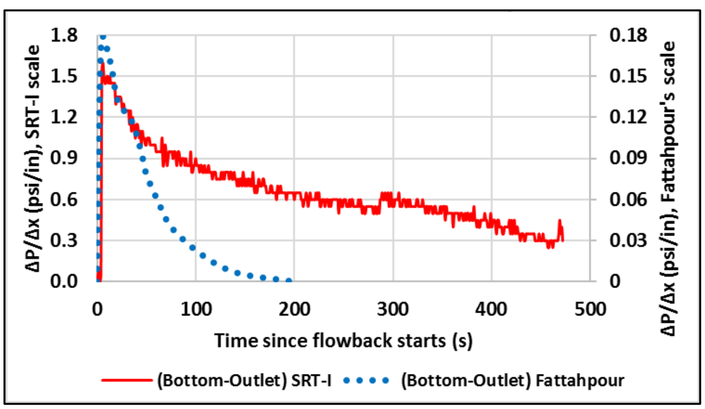

Figure 5.3. Pressure gradient near-coupon during flowback in SRT-I and Fattahpour's SRT.

The SRT-I flowback duration lasted for 480 seconds, whereas it lasted 200 seconds in Fattahpour's flowback. The difference shown in Figure **5**.**4** could be attributed to differences in initial pressure values, pressure profiles during flowback, and flowback tank sizes. Moreover, the long flowback duration was justified by a newly invented term "dissipation time," which is a function of sand pack properties and SL specifications (Fattahpour et al., 2018a). Nevertheless, the flowback duration for the SRT-I experiment was about six times longer than the expected ideal tank discharge time, shown in Figure **5.5**, evaluated by ("Discharge Tank Calculation Software," Nov. 7, 2019). Moreover, Mechanical equipment flow restriction can be quantified by Bernoulli's equation discussed in Section 2.4.2. Furthermore, it eliminates the need for the "dissipation time" ambiguous term to justify the flowback duration; meanwhile, it strictly emphasizes a mechanical restriction in the SRT-I flow system. Moreover, it replaces solenoid valves by manual valves to initiate flowback as long as they do not influence the test.

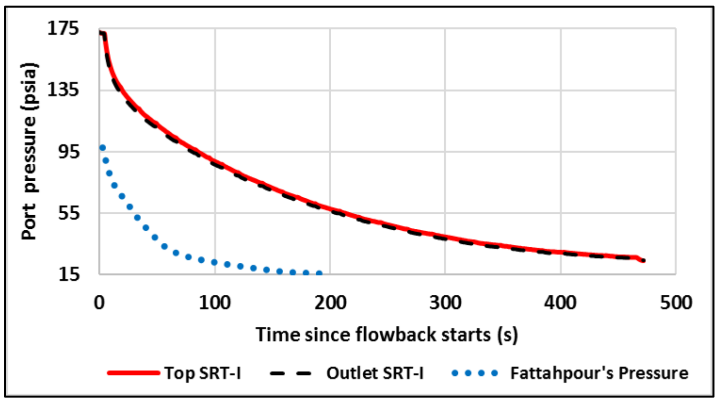

Figure 5.4. Pressure during flowback in SRT-I and Fattahpour's SRT.

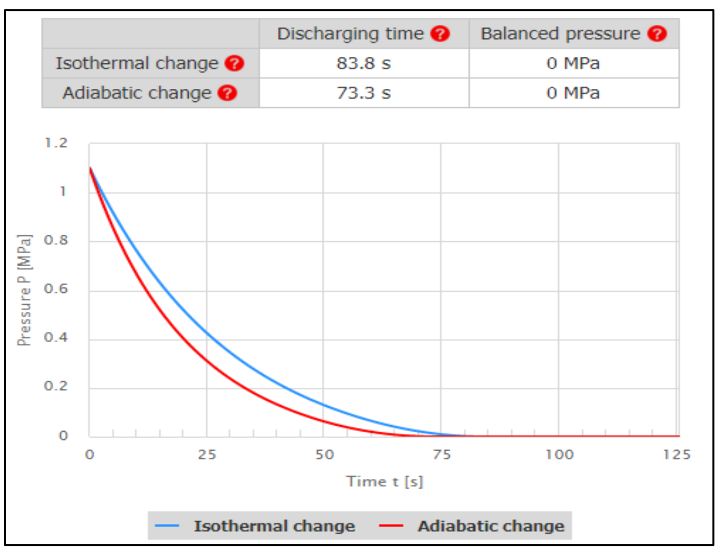

Figure 5.5. Flowback tank discharge time based on isothermal and adiabatic models for SRT-I at flowback initial pressure of 175 psia ("Discharge Tank Calculation Software," Nov. 7, 2019).

It is suggested to evaluate SRT-I set-up efficiency based on the differential pressure across the sand pack ratio to total system differential pressure, as presented in Eq. 5.1 to Eq. 5.3. Efficiency evaluation of the SRT-I set-up, shown in Figure **5.6**, clearly indicates a considerable flow-restriction that yields 96% pressure losses out of the component of interest, which is the sand pack. The solutions to improve the ultra-low SRT-I efficiency set-up, which is less than 4%, is discussed in the next section to come up with a modified version of the SRT set-up (SRT-II).

$$\Delta P^{SRT\ cell} = P(t)^{Top}_{measured} - P(t)^{Outlet}_{measured} \quad \text{(Eq. 5.1)}$$

$$\Delta P^{system} = P(t)^{Top}_{measured} - P(t)^{Outlet}_{ideal\ atmospheric} \quad \text{(Eq. 5.2)}$$

$$Efficiency^{SRT\ cell} = \Delta P^{SRT\ cell} / \Delta P^{system} \quad \text{(Eq. 5.3)}$$

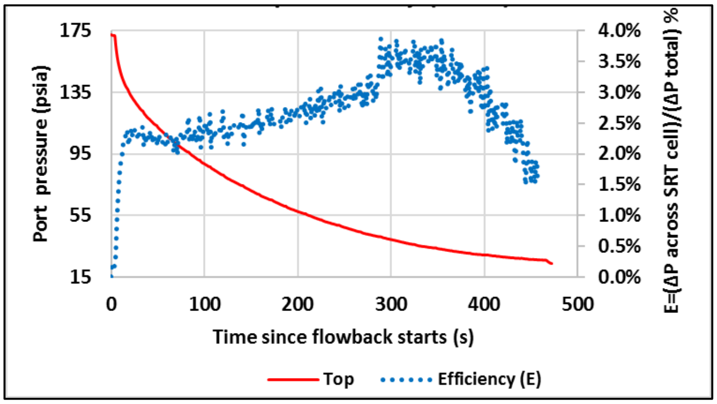

Figure 5.6. SRT-I set-up efficiency.

5.2 Modified Testing Set-Up (SRT-II)

SRT-I, as discussed earlier, has two significant drawbacks. It has enormous pressure losses in the mechanical component of the set-up and no feasible device (mass flow meter) to quantify the flowback rates. Mass flowmeters (MFM) are accurate devices to estimate the volumetric flow rate, yet their efficiency is dictated by the device's operation range at a relatively constant flow rate ("How Does Mass Flow Meter Work?," Nov. 14, 2019). The transient flow rate encountered during SRT-I requires at least two MFM to capture high and low flow rates accurately.

The MFM issue was resolved by changing the measurement techniques for the flow rate. It combines a mass-balance (ULINE Deluxe Counting Scale H-5822, ±1g accuracy) and real-time measurement of absolute pressure through the ideal gas law to approximate the volumetric flow rate of the flowback fluid during SRT. Moreover, a rotameter was used in SRT-II set-up to predict retained permeability by sperate measurements before and after flowback at steady-state flow conditions by applying Darcy's law as discussed in Section 2.3.1. Despite the simplicity of the idea, yet previous researches (Fattahpour et al., 2018a; Mahmoudi et al., 2018a) intended to evaluate permeability during the flowback transient flow, but no reliable results were obtained. Accordingly, the retained permeability was not calculated. The implemented modifications on SRT-II are illustrated in **Figure 5.7** and Table **5.2** to emphasize the upgrades to SRT-I shown in Figure **5.1**.

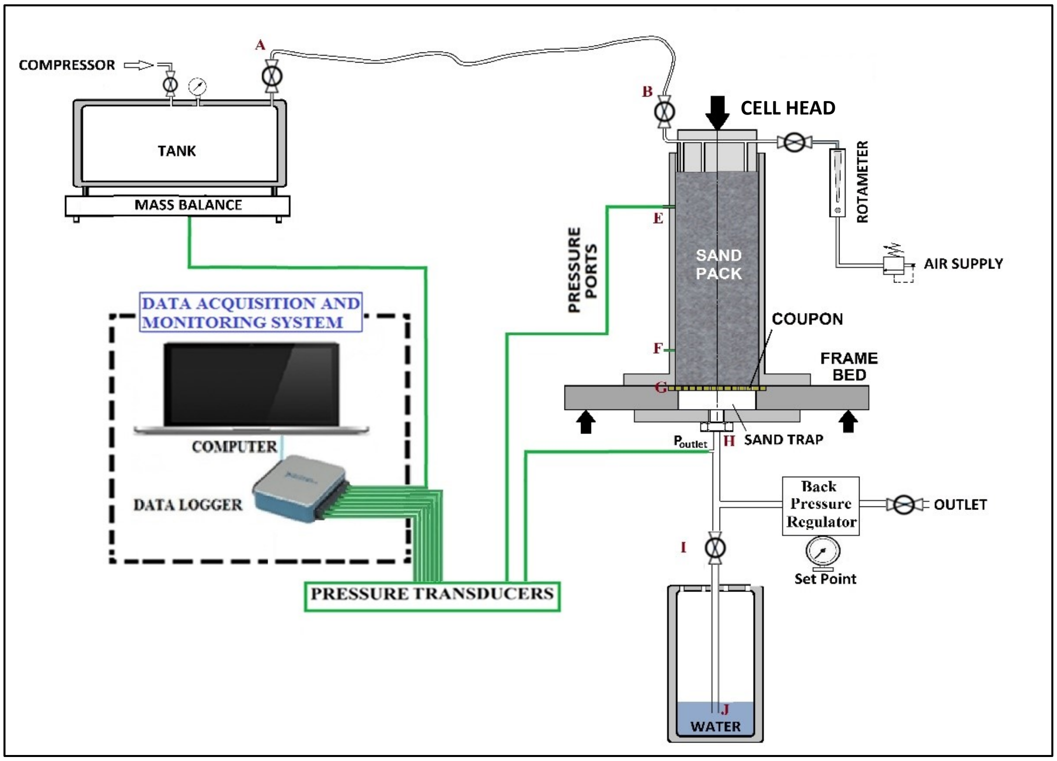

Figure 5.7. Modified testing set-up (SRT-II).

Table 5.2: SRT-II Diagram Specifications.

Start Point (SP)	SP Description	End Point	Flow Media	Length (in)	D (in)
A	FB tank outlet	B	Flexible tube	≅ 120	1/8
B	Cell head inlet	E	Sand	≅ 4	6
E	Top port	F	Sand	10	6
F	Bottom port	G	Sand	2	6
G	Sand pack end	H	Conduit	≅ 4	6
H	Trap outlet	I	Flexible tube	12	1/2*
I	Solenoid inlet	J	Flexible tube	≅ 36*	1/2*

* represents the changes compared to SRT-I

5.2.1 Influence of SRT-II Upgrades

The modifications, discussed in the previous section, have a significant difference in the top and outlet pressures of SRT-II, as shown in **Figure 5.8**, compared to **Figure 5.4** for SRT-I. SRT-II pressure drop, presented in **Figure 5.9**, is around 80 psi across the sand pack. Accordingly, it results in relatively high-pressure gradients, close to 7 psi/in, as illustrated in **Figure 5.10**, which is equivalent to almost 20 times larger than the SRT-I pressure gradient across the sand pack shown in **Figure 5.2**.

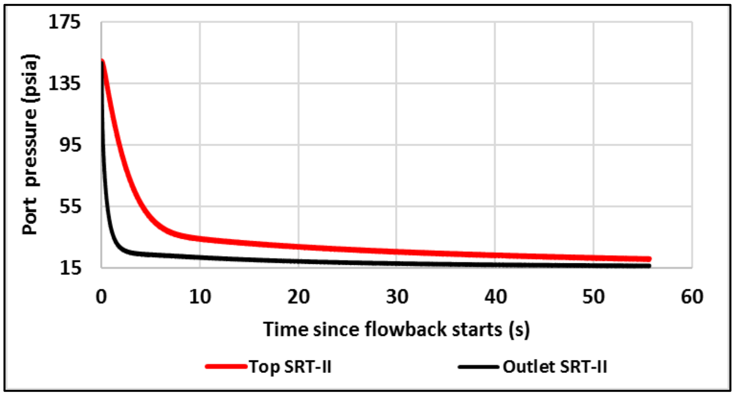

Figure 5.8. Pressure during flowback in SRT-II set-up.

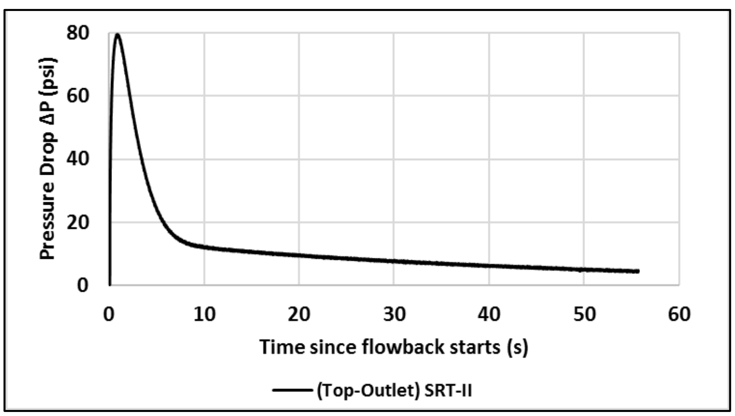

Figure 5.9. Pressure drop across the sand pack during flowback in SRT-II set-up.

Figure **5.11** shows the set-up efficiency, which has a maximum magnitude of 70%, evaluated using Eq. 5.3. This is a dramatic improvement over SRT-I efficiency of 4%, shown in Figure **5.6**. According to the previous arguments, it was concluded that the significant problems of SRT-I were attributed to pressure losses in small size flow lines. Moreover, they highlight the importance of SRT set-up, minimizing the pressure drops in the input and output lines, which was not considered by previous researches.

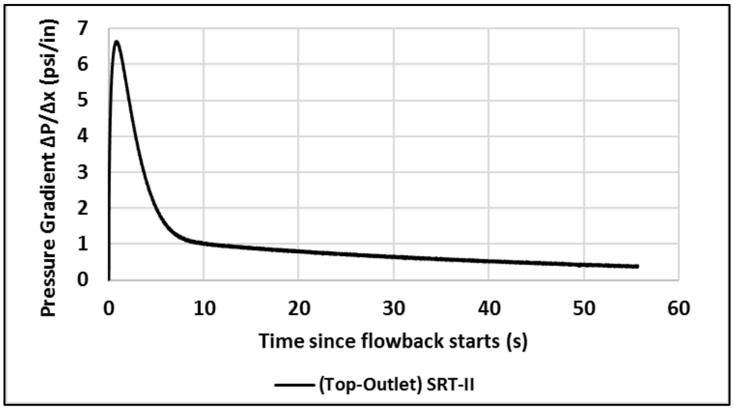

Figure 5.10. Pressure gradient during flowback in SRT-II set-up.

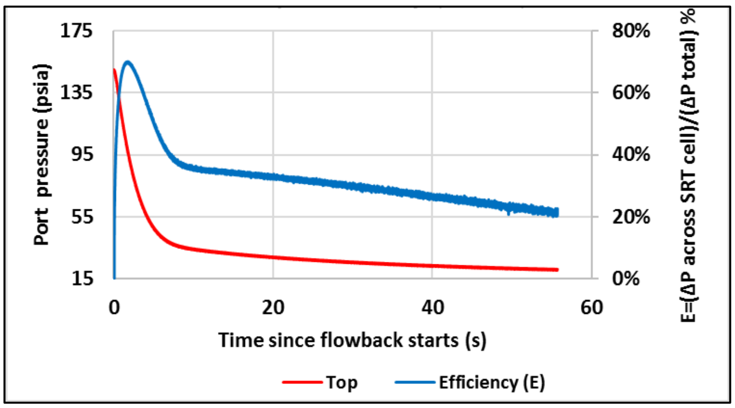

Figure 5.11. SRT-II set-up efficiency.

However, pressure drops in **Figure 5.12** show an exciting trend, especially at the early time of initiating the flowback. It shows that the maximum pressure drop was reached after one second from opening the outlet valve. It helps to support the hypothesis that solenoid valves will not affect the flowback, even at the initial flowback time, because the opening time (4 milliseconds) is three orders of magnitude less than the required time to initiate the flowback at maximum differential pressure capacity. It contradicts the belief of previous researches (Fattahpour et al., 2018a; Mahmoudi et al., 2018a) that solenoid valves would affect the SRT results. However, it helps to eliminate solenoid valves from the SRT-II set-up, which reduces the initial investment of the cell. Nevertheless, it seems to contradict the theory of fluid flow in porous media by having time to initiate the flow, where the theory assumes an instant outlet pressure reduction to atmospheric pressure. However, previously mentioned results were purely experimental where the outlet pressure takes time to be reduced to atmospheric as long as there are frictional losses in the downstream of the outlet. Moreover, outlet pressure is a continuous function, as shown in **Figure 5.8**, that is consistent with theory. It cannot jump to atmospheric pressure instantly.

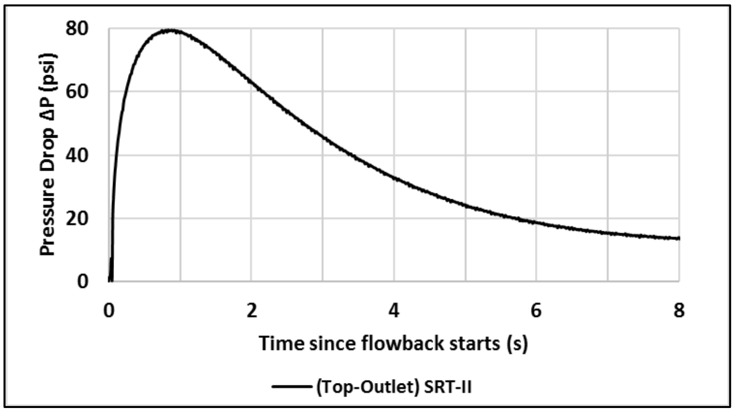

Figure 5.12. Magnified peak of pressure drop in SRT-II.

By adding a rotameter and a back-pressure regulator at the outlet during steady-state air injection, as shown in the SRT-II set-up diagram in Figure **5.7**, SRT-II will have more advantages over SRT-I. It is important to emphasize that the rotameter and the back-pressure regulator used in SRT-II are manually controlled by the operator, which involves adequate bias associated with uncertainty, which requires further investigation using automated devices to eliminate induced human error. Nevertheless, they were used to reduce the initial investment of SRT-II set-up cost and predict the feasibility of involving more sophisticated equipment.

The calibration table for Rotameter, as presented by the manufacturer, is brought in Appendix C. Tables that are used to construct Figure **5.13** and Figure **5.14** are shown in Appendix D with associated equations. The back-pressure regulator was used to control the outlet pressure at 0, 50 and 80 psig to account for Klinkenberg effect, discussed in Section 2.3.1 by three permeability measurements before and after flowback to construct initial permeability (initial K DC-1 SRT-II) and final permeability (final K DC-1 SRT-II), respectively. However, it was nearly impossible to match precisely the pressure drop across the sand pack during steady-state injection because of using a manually controlled equipment. Nevertheless, an attempt to match rotameter reading (Q_g^* in rcf/D), which results in a significant difference in equivalent flow rates at standard condition (Q_g in scf/D) but comparable differential pressures across the sand pack, as shown in Figure **5.13**. It shows that sand pack permeability to liquid is 1300 md comparable to (Montero, 2019) absolute permeability for DC-1. It seems to be incorrect because the relative permeability, after the pressure correction for the flow rates, should be lower than the absolute permeability of the same sand.

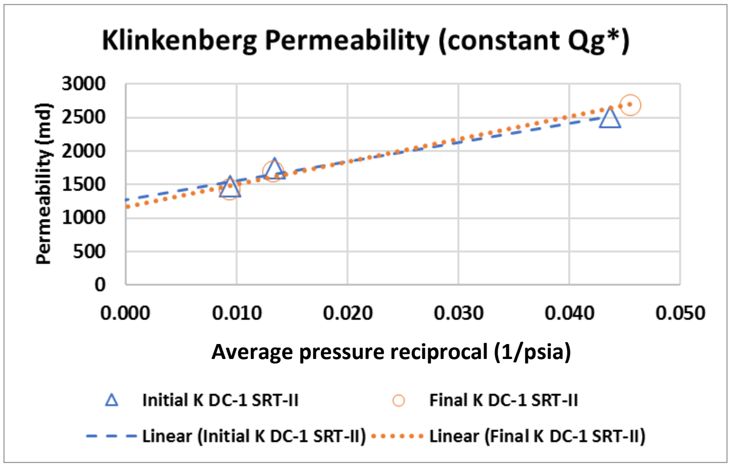

Figure 5.13. SRT-II Klinkenberg permeability at constant rotameter reading (see Appendix D).

However, another attempt was made by matching the standard conditions equivalent flow rates (Q_g in SCF/D), as illustrated in Figure **5.14**, by changing the (Q_g^* in rcf/D) according to rotameter exit pressure, which is comparable to SRT-II cell top port pressure. Klinkenberg permeability using Q_g shows a similar trend for a previous work (Li & Horne, 2004), discussed in Section 2.3.1, which emphasizes the complication of relative permeability to gas (k_{rg}) in the presence of mobile liquid saturation.

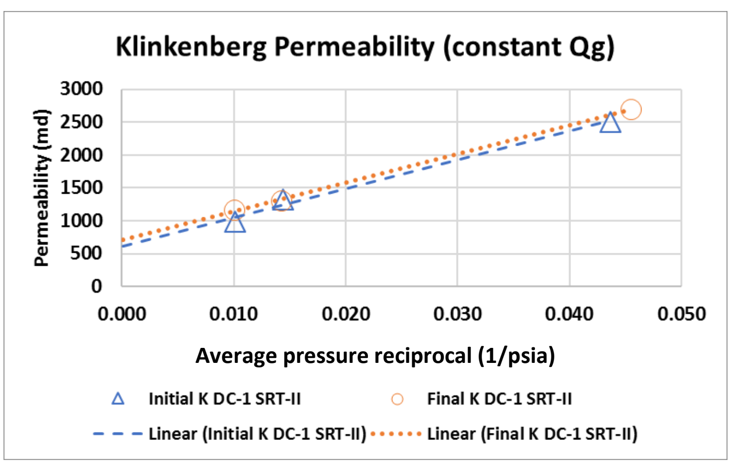

Figure 5.14. SRT-II Klinkenberg permeability at constant standard conditions equivalent flow rate.

Accordingly, the internal unpublished work for oil-water relative permeability, which indicates the irreducible water saturation to be around 30%, cannot be used in the gas-water system. **Figure 5.14** highlights the inconsistency of quantifying the actual (representative) sand effective permeability (k_g) to gas in the presence of irreducible water in the gas-water system. Nevertheless, it is evident from **Figure 5.13** and **Figure 5.14** that initial and final permeability magnitudes are comparable, which indicates no detectable changes in permeability, regardless of the permeability inconsistency issue due to flowback.

However, the present permeability deals with the sand pack as a single core. Yet in SRT practices, researches tend to describe the section permeability as the top, middle and bottom permeabilities. Section's permeability, shown in Figure **5.15**, was developed based on single permeability value (K1) presented in Appendix D, where the pressure of each section was monitored during steady-state injection. It seems that the sand pack permeability is heterogonous because permeability changes with location. Yet, understanding the difference between compressible fluid flow and incompressible fluid flow in porous media removes the confusion.

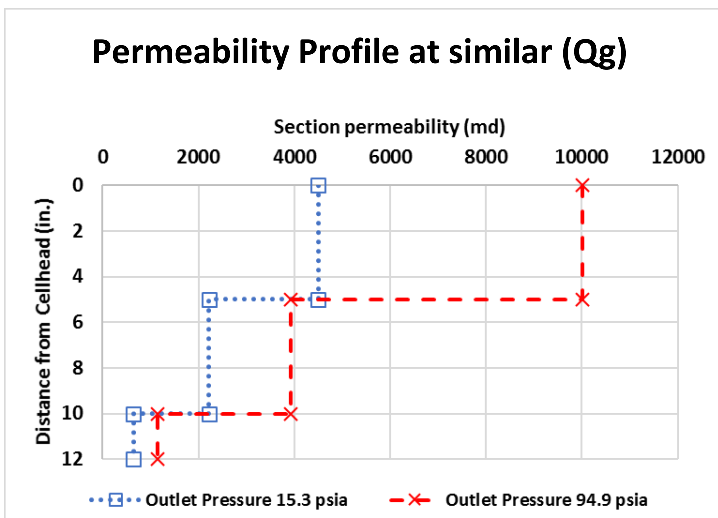

Figure 5.15. Permeability profile across the sand pack.

The sand pack permeability is calculated based on the weighted average permeability calculated from permeabilities at different intervals. Moreover, average permeability in the series was developed based on two fundamental concepts: the actual flow rate is the same in all sections, and the total pressure drop is the algebraic sum of the pressure drops in all sections (Pope, 2003). Those concepts are perfectly met for incompressible fluids where the fluid compressibility is zero. Yet, some real liquids, like water and dead oil, are considered to have an incompressible behaviour in laboratory conditions at low pressure (Marshall, 2009). On the other hand, gases, by default, are compressible fluids, and their compressibility cannot be assumed zero under any circumstances. It implies that the actual flow rate (Q_g^* in rcf/D) in each section cannot be equal as pressure across the sand pack is declining towards the outlet, as shown in Figure **5.16** at low mean cell pressure at the same atmospheric equivalent flow rate (Q_g in scf/D).

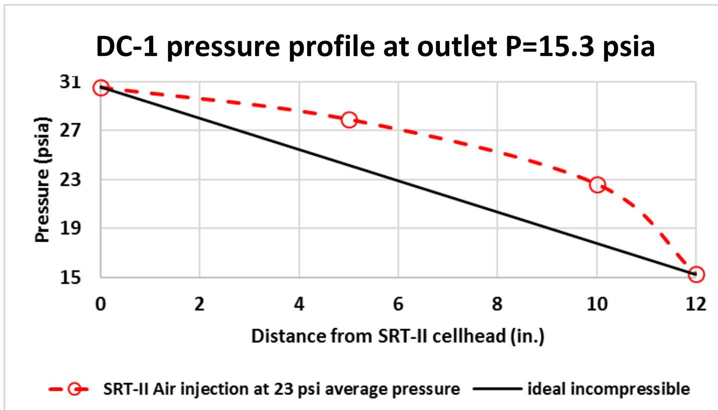

Figure 5.16. Pressure profile across the sand pack at low average pressure.

Figure 5.16 and **Figure 5.17** are presenting low and high mean cell pressure at a comparable atmospheric equivalent flow rate (Q_g in scf/D), respectively. They justify the permeability variation across the sand pack, shown in Figure **5.15**. However, the pressure gradient, which represents the slope of the pressure profile, increases towards the cell outlet, which is a fundamental trend for gases in a linear flow system. It clarifies the previously mentioned confusion of variation in permeability across the cell shown in Figure **5.15**.

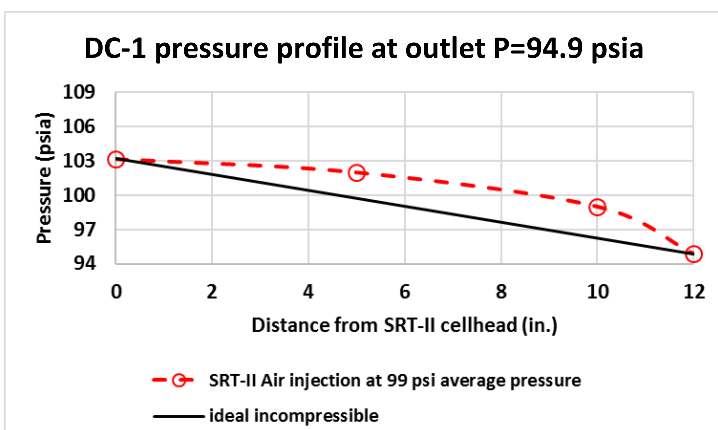

Figure 5.17. Pressure profile across the sand pack at high average pressure.

5.2.2 Associated Problems with Set-up Modifications

This section discusses a few problems associated with SRT-II. They include technical difficulties in flowback rates, permeability evaluation technique, Klinkenberg associated issues, and produced sand due to flowback. These topics are discussed in terms of lessons learnt to inform designing the final set-up (SRT-III).

SRT-II uses a flexible steel tube to transmit flowback fluid from the flowback tank to the cell head, as shown in Figure **5.7**. The flexible tube vibration was so noisy, which results in ineffective balance reading. However, permeability evaluation during steady-state air injection requires more improvement to eliminate uncertainty in measurements.

Furthermore, the Klinkenberg effect is used to determine liquid permeability using gas, yet it is difficult to match the outlet pressure using the manual pressure regulator, and presence of liquid water saturation adds further complications (Li & Horne, 2004). Moreover, the permeability evaluation was not to predict the slippage factor of Klinkenberg effect but to quantify the permeability induced change due to flowback.

The permeability induced change or reduction in retained permeability is attributed to fines migration, which results in porous media pore throat plugging. It was noticed that retained permeability was approaching unity all the time, which can be due to the presence of water as a wetting phase. All those topics were directly affecting the SRT set-up design and SOP. The solutions for those problems which enhance SRT are discussed in Section 5.3. On the other hand, the SRT-II produced particles were orders of magnitude less than the acceptable industry limit, $0.12 - 0.15\ lb/ft^2$ (Fattahpour et al., 2018a; Mahmoudi et al., 2018a), even at extra-large slots aperture, as shown in Figure **5.18**, which may not be considered as a possible candidate in SAGD completion.

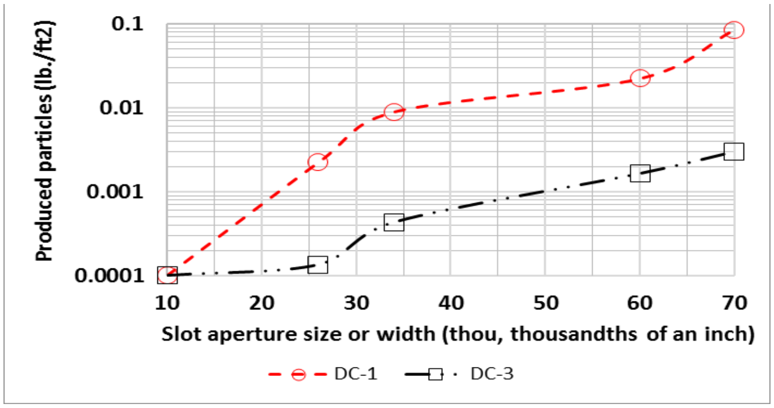

Figure 5.18. SRT-II produced particles.

5.3 Final Testing Set-Up (SRT-III)

The final testing set-up developed in this research is SRT-III, shown in **Figure 5.19** and presented in **Table 5.3**. SRT-III overcomes most problems encountered in SRT-II. Recommendations for further upgrades will be presented in Section 7.2.2.

The major resolved technical problems for SRT-II can be summarized in the following aspects as a problem-solution orientation. (1) A significant difficulty was the noisy balance reading to estimate flowback rates due to the vibration of the flexible tubing. One possible solution would be to replace the tube with a solid pipe that absorbs most of the vibration. (2) Permeability measurements during steady-state injection through the rotameter for a single flow rate can be enhanced by measuring permeability using multiple flow rates, through the graphical form of Darcy's law instead of a single point calculation. (3) Klinkenberg effect is essential to estimate the liquid permeability. However, for this research, the accurate measurement of the change in permeability is more critical to assess the impact of flowback. (4) The manual back pressure regulator, removed in SRT-III, induces a significant impact on Klinkenberg permeability.

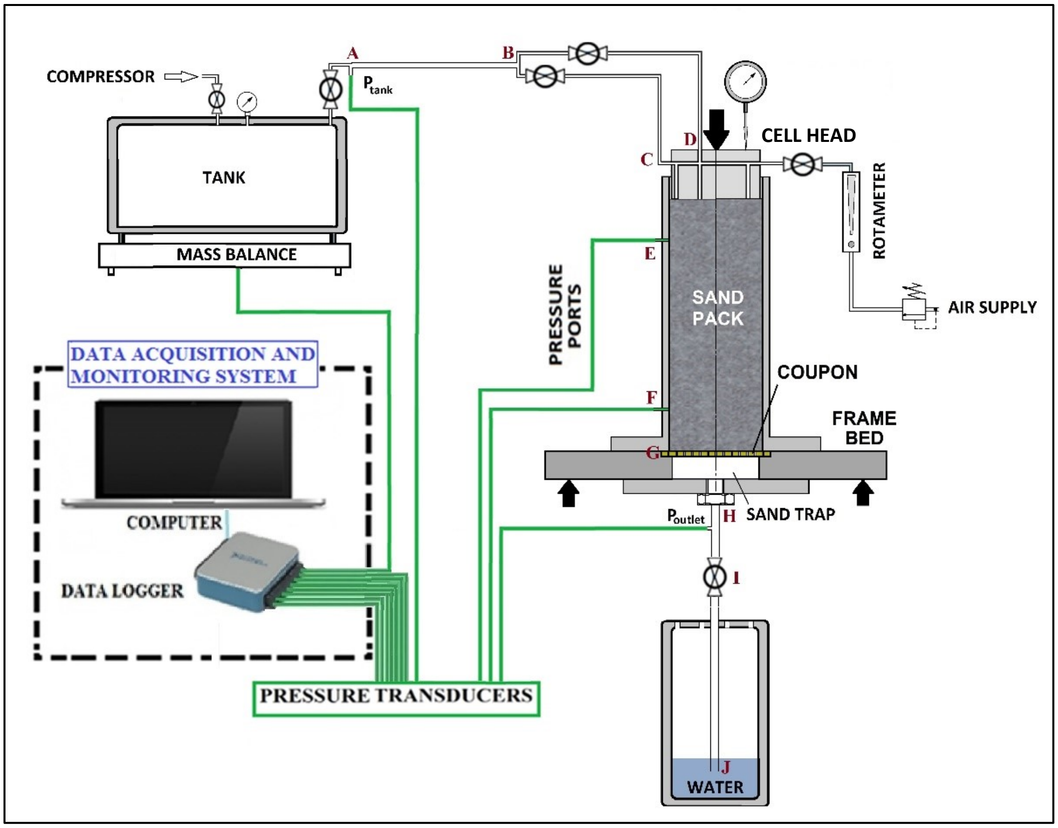

Figure 5.19. Final testing set-up (SRT-III).

Table 5.3: SRT-III Diagram Specifications.

Start Point (SP)	Start Point (SP) Description	End Point	Flow Media	Length (in)	D (in)
A	FB tank outlet	B	Steel pipe*	≅ 36*	1/2*
B	T-connection	C*	Flexible tube	≅ 6	1/8
B	T-connection	D*	Flexible tube	≅ 6	1/8
C and D	Injection ports (1 and 2)	E	Sand	≅ 4	6
E	Top port	F	Sand	10	6
F	Bottom port	G	Sand	2	6
G	Sand pack end	H	Conduit	≅ 4	6
H	Trap outlet	I	Flexible tube	12	1/2
I	Solenoid inlet	J	Flexible tube	≅ 36	1/2

* represents the changes compared to SRT-II

The elimination of the back-pressure regulator permits the measurement of porous medium permeability at atmospheric outlet pressure, which is relatively constant under controlled laboratory conditions. It yields more comparable results at the same Klinkenberg mean pressure. Nevertheless, one major associated problem with SAGD injector SRT was the extremely low produced particles even at high differential pressure across the cell with extra-large aperture slots. Previous research (Fattahpour et al., 2018a; Mahmoudi et al., 2018a) considered the industry practices classify it as extremely conservative, especially for SAGD injectors SLs small aperture selection. Although this claim seems to be logical, yet there is a possibility of the SRT to be unrepresentative of field conditions, which results in this misconception, as discussed in the next section.

5.3.1 Implications of Matching Fluid Saturation Match and Optimal Saturation

In this research, previous set-ups, SRT-I and SRT-II used the moist tamping method to place the sand pack as previous research (Fattahpour et al., 2018a; Mahmoudi et al., 2018a) claims to be the most representative for SAGD injector near-wellbore zone. Moreover, the used water content was determined to be 30% PV, which corresponds to irreducible water saturation, as discussed earlier. The used technique can easily match fluid saturations as a bulk term without rock-fluid wettability interactions, which results in relatively high capillary pressure as it is inversely proportional to fluid saturations, as discussed in Section 2.3.3. However, this claim does not take into consideration the fundamentals of thermodynamic equilibrium and fluid distribution at the pore scale, which may make it invalid.

The fluid distribution at pore scale of SAGD injector near-wellbore was investigated before and during flowback for the water-wet porous medium, is presented in Table **5.4**, as Alberta oil sands exhibit a unique water wet characteristic ("Oil Sand Geology & the Properties of Bitumen," Sep. 23, 2019). Moreover, it magnifies the detrimental effects of human artifacts' role in neglecting the thermodynamic equilibrium of SAGD injector flowback SRT, which determines the quality of testing results. (Ballard & Beare, 2006)

Table 5.4: Fluid Distribution at Pore Scale of Water Wet Porous Medium System.

SAGD phase	Larger pores fluid content	Smaller pores fluid content
Late SAGD mode	residual oil + steam at injection SQ	water in liquid form at injection SQ
Flowback mode	residual oil + SHS	SHS

The investigation, presented in **Table 5.4**, shows that liquid water content found in the small pores should be transferred into SHS during flowback leaving smaller pores filled with non-wetting phase in SHS and residual oil system. However, replicating such fluid distribution in laboratory SRT is not possible using the air-water system because of missing the thermodynamic equilibrium interference in ambient SRT experiments. Moreover, Section 7.2.4 presents a possible solution that accounts for this effect using HT-SRT facility.

Nevertheless, it seems to justify the ultra-low particle production during SRT experiments, shown earlier in Figure **5.18**, due to the capillary pressure. Yet, there is no possible laboratory technique to place the non-wetting phase in smaller pores in the presence of a wetting phase. However, a useful trick was used to remove the wetting phase from the system, and accordingly, the packing technique used dry pouring method instead of moist tamping method to eliminate the effect of the capillary pressure in SRT-III.

5.3.2 Influence of Additional Modifications and Flowback Description

Up to this point, this chapter describes the effects of significant modifications that resulted in the development of SRT-III. This section elaborates on the remaining features of SRT-III. Theoretically, removing the wetting phase from porous media should maximize the impact of flowback on fines migration, which was not detected in SRT-II experiments. Moreover, sand permeability was under different axial stress as shown in Figure **5.20**, with details in Appendix E. Dramatic permeability change was detected in the first loading cycle especially bellow 150 psi axial stress, yet there is no significant permeability difference in higher stresses and the second loading cycle as shown in Figure **5.21**.

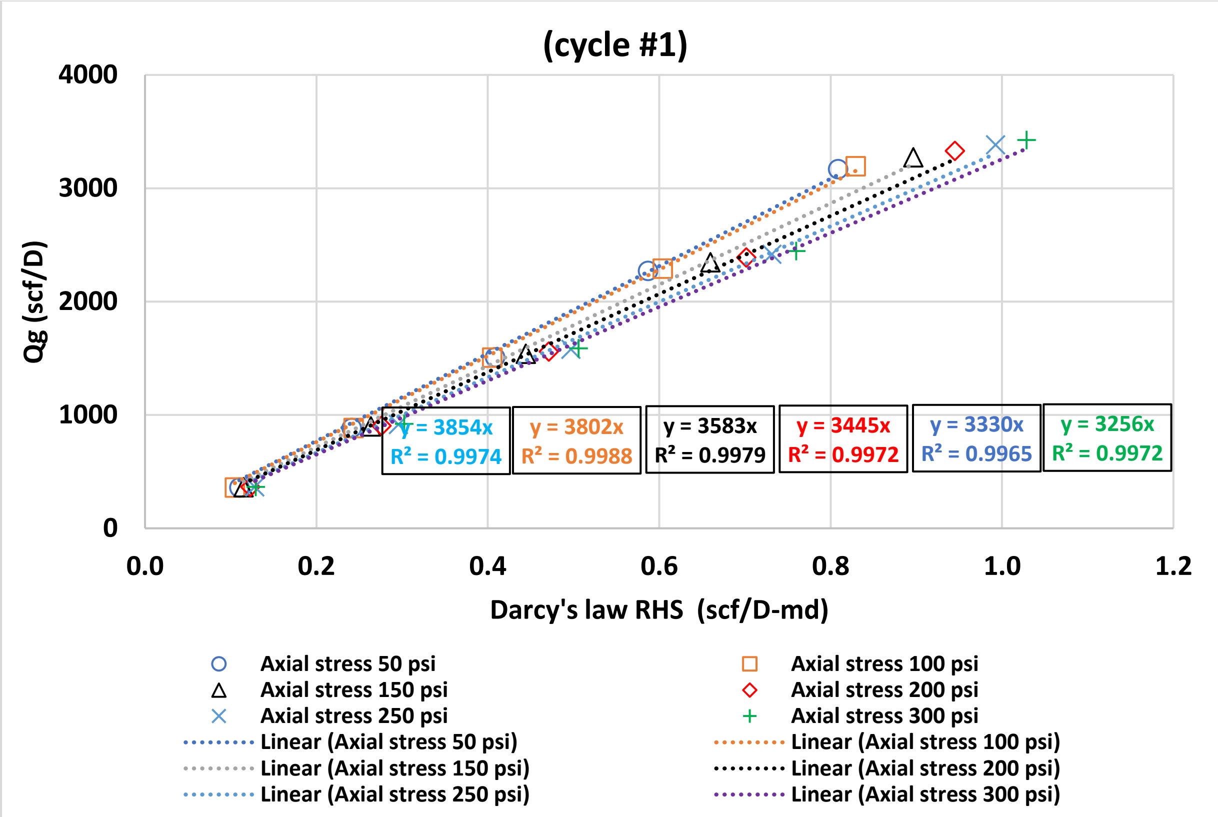

Figure 5.20. SRT-III permeability measurements under different axial stresses (1st cycle).

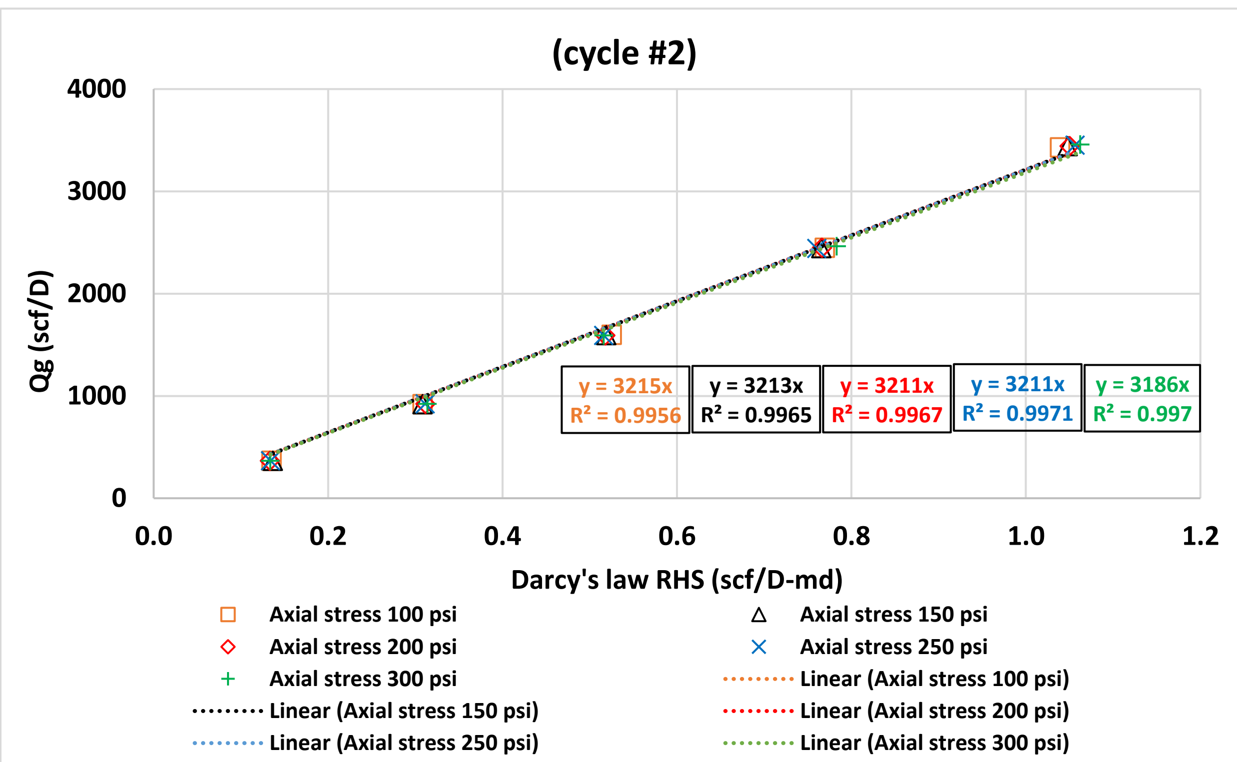

Figure 5.21. SRT-III permeability measurements under different axial stresses (2nd cycle).

It indicates that loose sand permeability is independent of low applied stress up to 300 psig during the second loading cycle. This conclusion helps to minimize the axial applied stress to the lowest possible stress to meet both safety regulation and expected stress calculated near the wellbore of SAGD injector discussed in Section 4.2.3. However, all those improvements were meant to reduce the SAGD injector flowback SRT subjectivity, yet the remaining challenge was testing reproducibility (repeatability) criteria.

5.3.3 SRT-III Set-up Reproducibility Criteria

In general, SRT reproducibility criteria were controlled by the moist tamping method packing technique (Fattahpour et al., 2018a; Mahmoudi et al., 2018a; Montero et al., 2019; Roostaei et al., 2018). The technique counts on packing several layers that each has a specific height that corresponds to specified targeted porosity based on the sand type and water content, which in return controls the sand pack properties, especially permeability. However, the moist tamping method cannot be used in SAGD injector flowback SRT to match fluid distribution at the pore scale, as discussed earlier in Section 5.3.1. Dry sand pouring requires implementing unique repeatability criteria for SAGD injector flowback SRT, which seem to emphasize that almost all current SRT practices for SAGD producers will fail to mimic SAGD injector flowback.

The proposed reproducibility criteria for SRT include computing fundamental properties of the sand pack based on preliminary measurements to decide whether the test is representative or not. It includes the stress-displacement diagram, stress-strain diagram, porosity changes due to applied stress and initial permeability measurement. Two identical SRT experiments were compared, and their reproducibility criteria were illustrated in this section. However, the stress-displacement error bars, shown in Figure **5**.**22**, were added based on used devices minimum precision, which is ten psi for the axial stress piston gauge and 0.01 inch for displacement gauge. However, the stress-displacement diagram is dependent on sample initial intact length, which can be controlled by pouring the exact weight of sand for each sand type during sand pack preparation. Nevertheless, the stress-strain diagram, shown in Figure **5**.**23**, was used to generalize the producibility criterion to account for initial sample length variation if it exists. The associated error bars for stress are ten psi for the axial stress piston gauge, whereas strain error is a lump sum of 5% to account for error involved in sample length and displacement gauge measurements. The stress-strain diagram was developed to quantify sand pack properties match from geomechanics point of view.

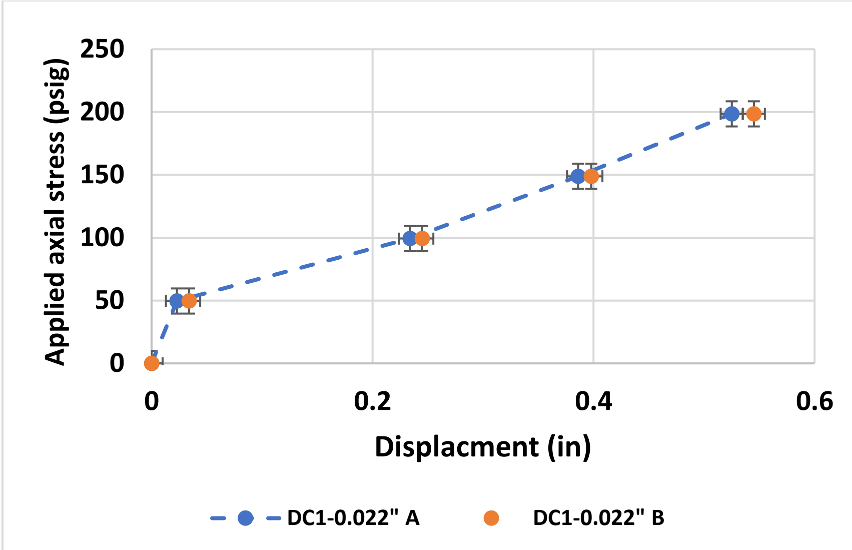

Figure 5.22 Stress-displacement curve (SRT-III).

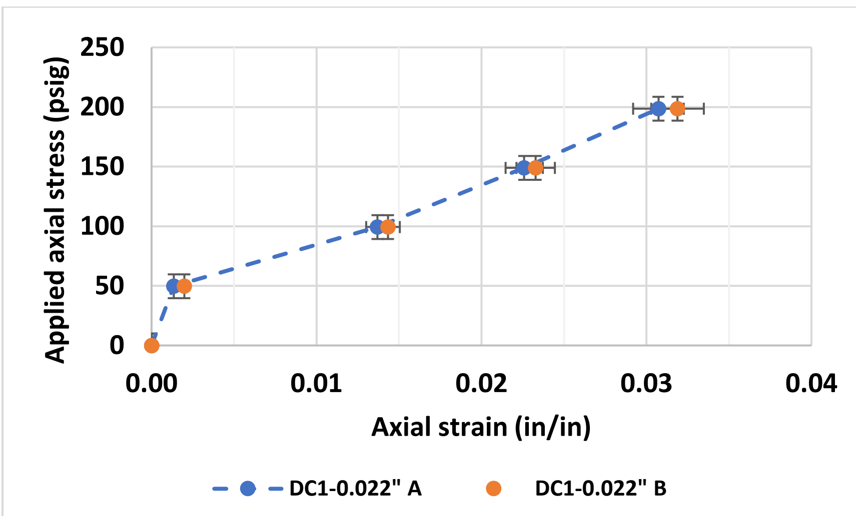

Figure 5.23 Stress-strain curve (SRT-III).

Besides, stress-porosity reduction and initial permeability measurement, shown in Figure **5.24** and Figure **5.25**, were considered to quantify petrophysical properties repeatability. However, the stress-porosity reduction diagram associated with the stress-strain diagram should be evaluated immediately after packing to check the reproducibility criteria. In case the experimental differences were acceptable, then the SRT will be resumed; but if the differences were significant, the sand should be repacked. This technique saves the investigators' time and effort. The porosity reduction acceptable criterion limit was set to 5%., which incorporates errors involved in sample length measurement, displacement gauge, sand pack weight, and particle density variation.

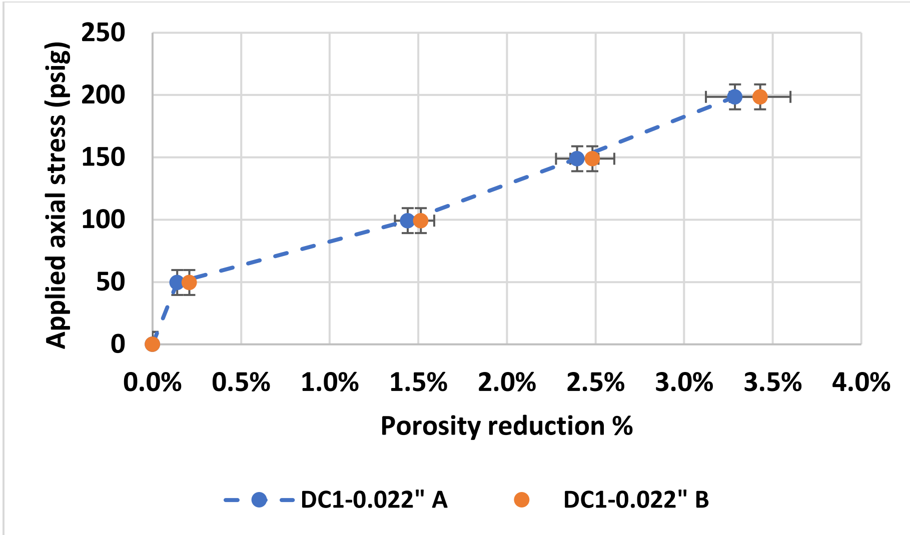

Figure 5.24 Stress-porosity reduction curve (SRT-III).

Finally, the last reproducibility measure is the initial permeability measurement, which should be conducted using five different flow rates and use Darcy's law in graphical form as shown in Figure **5**.**25**. The slope of the fitted line that passes by (0, 0) represents the packed sand permeability. The acceptable difference was set to 5% for both axes and slope.

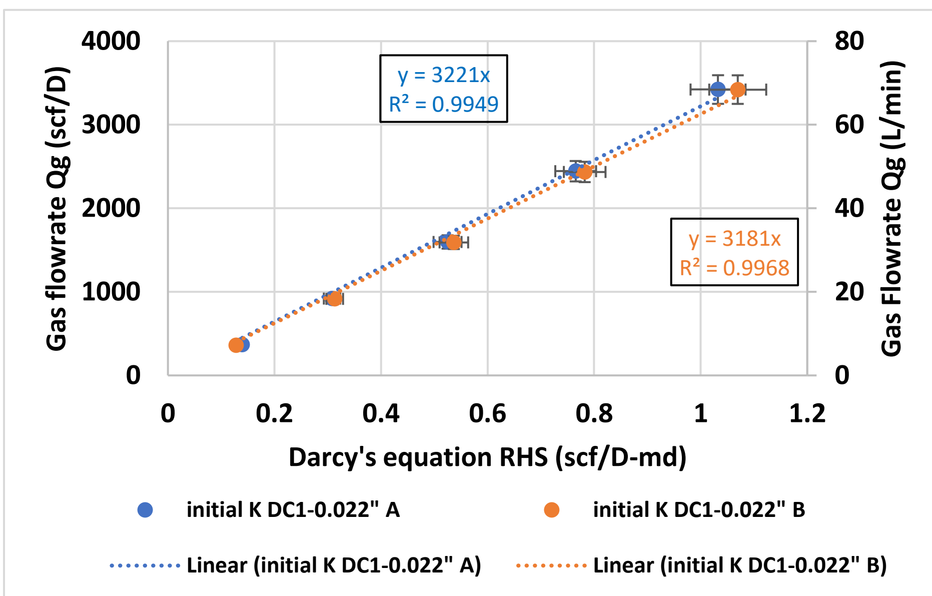

Figure 5.25 Initial sand permeability (SRT-III).

Chapter 6: EXAMINATION OF CURRENT INDUSTRY PRACTICES

This chapter explores industry practices in selecting the appropriate aperture size for SLs for SAGD producers and injectors based on SRT experiments. Moreover, it elaborates on the practical application of the proposed SRT-III set-up to assess the performance of SL during the SAGD injector flowback. The SRT is used to examine whether the industry practices are reliable or conservative as previous research claims (Fattahpour et al., 2018a; Mahmoudi et al., 2018a). Furthermore, brief insights into the dependency of SRT results on sand pack PSD is presented.

6.1 Industry Selection Practices

The literature is rich with multiple proposed SL design criteria for SAGD production wells. However, SRT designed for SAGD producer takes into consideration some measurable factors to specify suitable aperture size, whereas SRT for SAGD injector seems to rely on industry experience or rules of thumb. This section investigates the SRT design criteria for the SAGD producer, which may yield comparable criteria for the SAGD injector.

6.1.1 Criteria for SL Aperture Size in SAGD Producer

SL performance through SRT is evaluated on two measurable fronts, sanding and flow performances. Sanding acceptable limit is an arbitrary percentage equals to 1% sand volume to liner volume (Mahmoudi, 2017). The specified percentage was translated into sand weight per liner's unit area, which is expressed as 0.12 to $0.15\ \mathrm{lb/ft^2}$. Those numbers were calculated for a seven-inch liner diameter and associated apparent sand density. Moreover, the produced sand does not account for fines weight by assuming the fines to be continuously carried out during SAGD fluids production. However, the retained permeability minimum acceptable limit was arbitrarily chosen to be 50% to maintain sufficient well productivity. Retained permeability is linked to fines migration across the sand pack during the SRT experiment (Fattahpour et al., 2018b; Mahmoudi et al., 2018b; Montero et al., 2019; Roostaei et al., 2018). Often, the sanding criterion dictates the slot aperture upper limit, whereas flow performance determines aperture lower limit as described in the traffic light system (TLS), that was first introduced by (Mahmoudi, 2017) shown in Figure **6.1**. The TLS is a powerful tool to demonstrate SRT design criteria visually, where green, yellow, and red colours represent safe, moderate, and failure conditions, respectively. It is used to assess SAS performance for SRT applications. (Mahmoudi et al., 2018c)

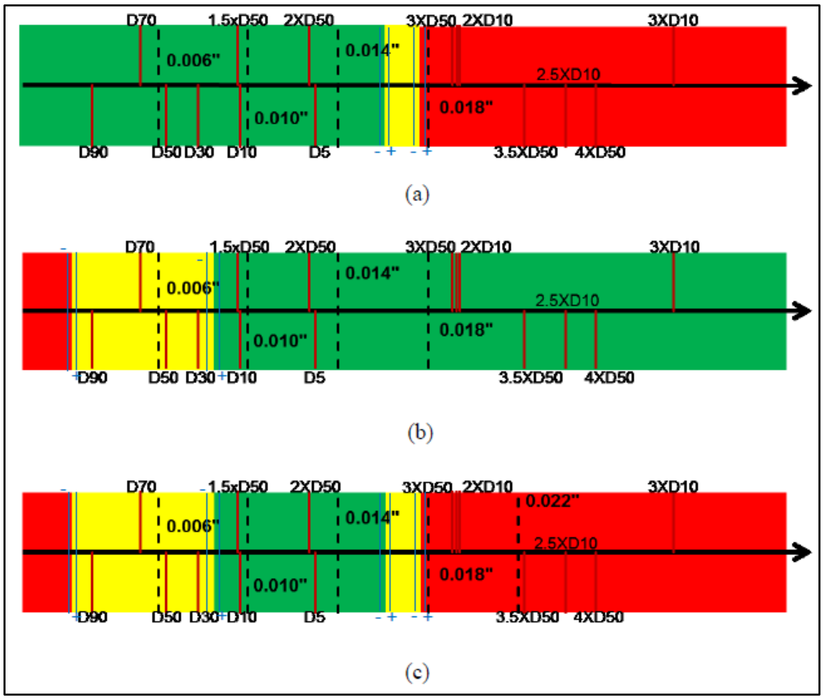

Figure 6.1. TLS technique, (a) sanding performance, (b) flow performance, (c) combined design window (Montero, 2019).

6.1.2 SAGD Injector SL Aperture Size Standards

In contrast with SAGD producer SL performance by SRT, SAGD injector performance receives minimal attention from a sand prevention point of view except for very few previous pieces of research, yet it shares half of the capital investment of the SAGD well pairs. The industry seems to rely upon “the narrower aperture size, the better the design” rule of thumb, which supports the conservative claim of research based on SAGD producers TLS (Fattahpour et al., 2018a; Mahmoudi et al., 2018a). However, the industry prefers to maximize the open-to-flow area by selecting the maximum available slots density in a SL.

This research will modify the existing acceptability criteria slightly to represent SAGD injector flowback SRT, yet it is recommended to come up with a new approach to assess such parameters, which is beyond the scope of this research as will be discussed in Section 7.2.1.

Produced particles were used instead of produced sand because fluids will not be produced to the surface intentionally in SAGD injector flowback. It implies that both fines and sand will accumulate in the injector wellbore in case of flowback. However, a separate investigation should be performed to assess the acceptable reduction limit in injectivity based on produced particle volume, which is not necessarily equal to 1% volume fraction when a normal injection process is resumed after a flowback.

On the other hand, retained permeability will be more precisely defined to account for fines migration that causes pore throat plugging, which can be expressed by permeability changes only, not by change of fines distribution along the sand pack. Nevertheless, aperture selection criteria require improvement to interpret the SRT results, which are dictated by the SRT testing program and considered to be a significant artifacts source (Ballard & Beare, 2006). The testing program for the SAGD producer SRT will be discussed and used to create a similar program for the SAGD injector flowback SRT.

6.2 SRT Program

Section 6.2.1 sheds some light on the standard SRT practices by different researchers to understand testing program objectives and use similar objectives in Section 6.2.2 that yields a SAGD injector representative SRT program. The constant terminal pressure (CTP) and the constant terminal rate (CTR) are the primary injection schemes in core flooding practices (RP40, 1998). An SRT program lends itself more towards the CTR technique because of its relative simplicity in implementation and ease of determining the operational parameters, yet it is associated with problems that will be discussed in the next section. Nevertheless, the SRT sand pack size, applied stress, and SL coupon arrangement of single or multi-slots are testing variables, which vary among 15 different SRT researches (Montero et al., 2018). Furthermore, some researches use $39\ \text{in}^3$ sand pack volume, $500\ \text{psi}$ applied axial stress, and single slot coupon arrangement of SRT experiments. However, others use a relatively larger sand pack volume of $561\ \text{in}^3$, one order of magnitude lower axial stress of $60\ \text{psi}$, and multi-slots SRT coupons (Kotb, 2018). Although researches start with the same assumption of a SAGD well, that has the same length, SL diameter and production rates, yet their SRT operational parameters are dependant on specifications of testing facility, which seem to introduce a considerable subjectivity (Ballard & Beare, 2006). The discrepancies will be discussed in the next section to amplify its impact on the SRT program for SAGD producers. Moreover, some researches stated valid matching points, yet no current SRT research accounts for those crucial factors. The factors include oil viscosity change due to bitumen structure change and in-situ emulsions formation, mineralogy change due to injected heat, associated silica dissolution or precipitation, and rock wettability alteration. (Romanova, Ma, Piwowar, Strom, & Stepic, 2015)

6.2.1 SAGD Producer SRT Program

This section will focus on the variation of SRT injection programs for SAGD producer testing, which indeed induces a degree of testing subjectivity or human artifacts (Ballard & Beare, 2006). There is a joint agreement in SRT that single, two-phase, and three-phase flow should be conducted to mimic oil, oil with liquid water, and steam breakthrough scenarios, respectively. However, the agreement ends there because different researches assign different number of stages for each fluid injection, and the duration of injection of each stage varies. Moreover, the injected flow rate, in each stage, varies dramatically from one research to another, as can be seen in Table **6.1** (Kotb, 2018). The assigned flow rate differences are orders of magnitude, which should severely affect the SRT results and the corresponding discussion made, despite the involved speculation in the properties of the used fluid (Montero et al., 2018). However, the SRT injection rates vary amongst the same research from one scenario to another, as expressed clearly in the standard rate, low rate and reverse rate SRT injection programs. (Devere-Bennett, 2015)

Another factor that introduces the SRT flow rates variation is referred to as the slots plugging tendency. Researches assume that flow rates should be multiplied by a design factor of from 50% to 90% to account for plugging, which by itself introduces human interference to assign plugging excess flow rates (Kotb, 2018).

Moreover, the SRT produced sand acceptance limit is expressed as the cumulative produced sand (Montero, 2019), as shown in **Figure 6.2**, whereas the incremental produced sand (Devere-Bennett, 2015) limit is used as illustrated in **Figure 6.3**.

Table 6.1: SRT Program for SAGD Producer for Two Different Researches (Kotb, 2018; Montero, 2019).

	U of A SRT injection				Weatherford standard SRT injection		
Stage	Oil rate	Water rate	Gas rate	Stage	Oil rate	Water rate	Gas rate
#	cm^3/hr			#	cm^3/hr		
Oil injection at irreducible water saturation							
1	2900	0	0	1	40	0	0
2	4300	0	0	2	80	0	0
3	7200	0	0	3	120	0	0
				4	160	0	0
Oil and water simultaneous injection (variable water cut)							
4	1450	1450	0	5	160	80	0
5	2150	2150	0	6	160	160	0
6	3600	3600	0	7	160	240	0
7	1800	5400	0	8	160	320	0
8	0	7200	0				
Oil, water and gas simultaneous injection (constant water cut, variable SLR)							
9	1450	1450	15000	9	160	320	10000
10	1450	1450	30000	10	160	320	20000
				11	160	320	30000

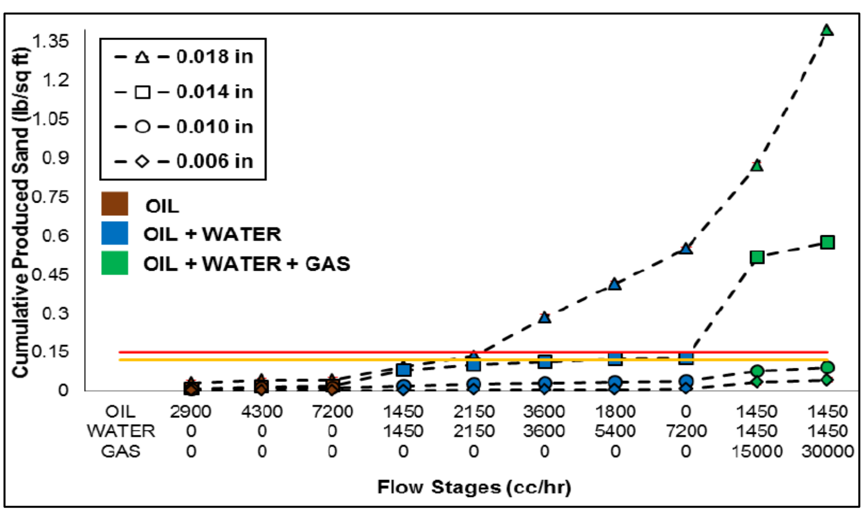

Figure 6.2. Sample of results for cumulative produced sand during SRT stages (Montero, 2019).

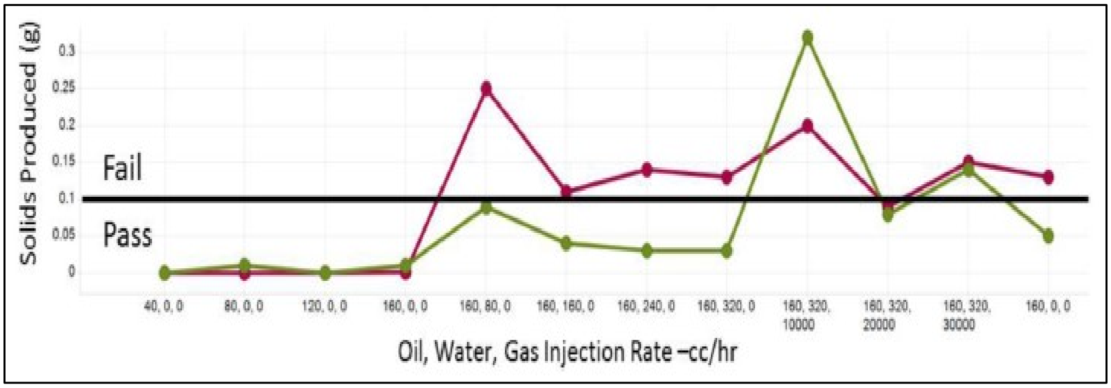

Figure 6.3. Sample of results for incremental produced sand during SRT stages (Devere-Bennett, 2015).

The assigned flow rates by different researches are the primary controller of the associated pressure gradients, based on Darcy's law, and drag forces, based on geomechanics, on the adjacent coupon sand, which is reflected in the variation of the produced sand. However, the associated total pressure drop across the sand pack varies from one stage to another even during the same SRT because either the flow rate is changed, or another fluid phase is introduced. Changing the total pressure drop has a tangible influence on the associated axial effective stress during gas injection. Gas injection is used to simulate steam breakthrough, and the effect is more severe in the researches that use a low value of applied axial stress. The effect can be observed in the associated effective stress reduction based on changes of the pore pressure, which should change the produced sand magnitude, theoretically. On the other hand, researches that use high axial stress will avoid such problematic situations, where the pore pressure is orders of magnitude lower than the axial stress, which has dramatic retention of the sand particles due to the enormous frictional forces due to the high effective stress. This discussion does not intend to criticize previous researches, but to learn how to avoid such inconsistency in present research, which will be discussed in the next section for SAGD injector flowback SRT.

The last topic that is discussed in this section is the relation between different coupon arrangement, single or multi-slots, and their impact on flow convergence. Multi-slots coupon has the potential to capture the interaction between the slots, yet it drastically minimizes the possibility of detecting flow convergence's effect compared to the single-slot coupon (Kotb, 2018). The flow convergence or "rate-dependent skin" is defined as the pressure drop increment because of the reduction in the flowing area, that can be attributed to the mechanical component restriction or an SAS presence (Guo et al., 2007). It is like Bernoulli's equation, discussed in Section 2.4.2 when it describes the increment of velocity as area shrinks as a result of extra pressure drop in a conduit to hold the energy balance equation.

6.2.2 SAGD Injector SRT Program

The discussion in Section 6.2.1 emphasizes the importance of a systematic and objective procedure to develop an SRT program, which should yield comparable SRT operational parameters by different researches. A possible technique is to assess SRT facility independent operational parameters, which is impossible using CTR because of matching flow rate, which is an extensive property, based on the area ratio. On the other hand, the CTP technique matches an intensive property like pressure, which technically should yield the same operational parameters if sand pack length is matched regardless of the sand pack diameter, coupon slots arrangement, and plugging tendency.

The SRT operational parameters were evaluated to overcome the challenge of data confidentiality for SAGD injector flowback through the methodology described in Chapters 4 and 5. However, the same methodology can be used to assign the SRT producer operational parameters to minimize what seems to be testing subjectivity discussed in the previous section. Moreover, it helps to avoid a generalized solution for a case-specific problem. The generalization comes from the average SAGD production rate used by different researches, that did start with comparable well flow rates to end up with orders of magnitude difference in the SRT operational parameters. Furthermore, pressure-controlled SRT or CTP helps match the effective stress rather than applied stress, which varies orders of magnitude among different researches, as discussed earlier.

Finally, the SAGD injector flowback SRT operational parameters were discussed in detail in Section 4.2.3. It should be mentioned that the differential pressure was matched instead of the actual pressure due to set-up limitations, yet it can be considered as one-step towards the solution of more specific operational parameters.

6.3 SAGD Injector Flowback SRT-III Results

This section categorizes the SRT-III experimental results into two groups. The results will be presented for steady-state gas injection flow to quantify the sand pack permeability in Section 6.3.1 and transient flow to mimic the flowback in Section 6.3.2. However, only six tests were conducted using SRT-III to verify the set-up performance capability to achieve the objectives of this research. Two PSDs, DC-1 and DC-3 discussed in Section 2.1.3, were used in the testing matrix with two coupons aperture sizes of 10 and 22 thou.

6.3.1 Steady-State Flow Measurements

DC-1 sand type with a coupon slots aperture of 10 thou was used as the primary PSD and testing coupon throughout this research. Its stress-strain diagram during the entire SRT test is shown in Figure **6.4**.

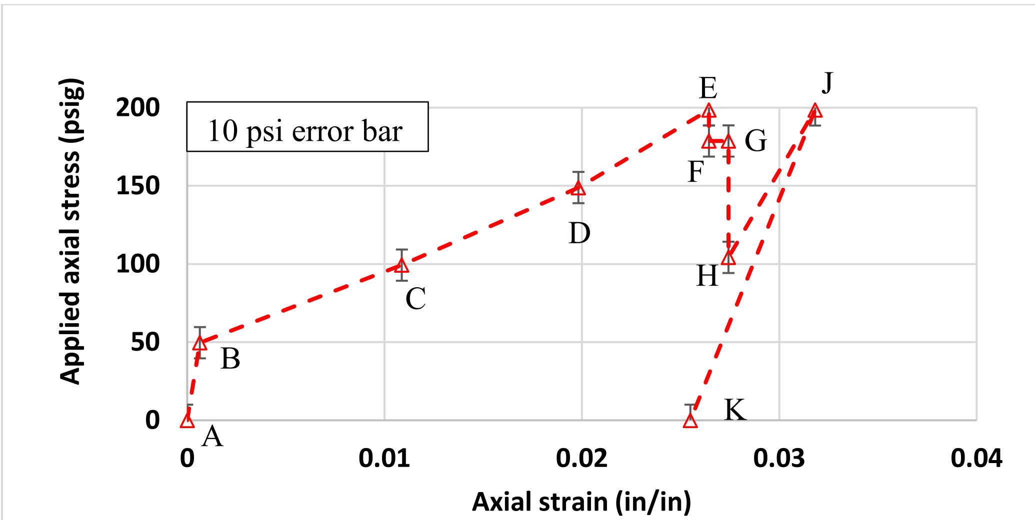

Figure 6.4. Stress-strain diagram for DC-1 at slot width 0.010".

Points (A) to (E), in **Figure 6.4**, represent the axial loading from 0 to 200 psi in incremental steps of 50 psi. Point (E) represents the stress at the start of the initial permeability measurement, whereas point (F) shows the final stress reading by the end of steady-state gas injection. Moreover, point (G) shows a slight strain increment over point (F) due to sand trap removal for cleaning before the flowback. The stress reduction because of the flowback impact is illustrated in point (H). However, the applied stress is increased to point (J) to perform the final permeability measurement. Also, point (K) shows the sand pack residual strain. However, the associated error bars represent the minimum precision of a dial gauge of 10 psi.

Nevertheless, the stress-strain diagram shows a slight horizontal shift for the same PSD at larger slots aperture of 22 thou, as illustrated in **Figure 6.5**, which can be misinterpreted to an alteration of sand geomechanical properties due to coupon slots aperture changes. However, the horizontal shift of stress-strain diagram is attributed to the higher possibility of sand passing through the large slots of 22 thou while the sand is being axially loaded, whereas the same sand has lower possibility to pass through the narrower slots of 10 thou.

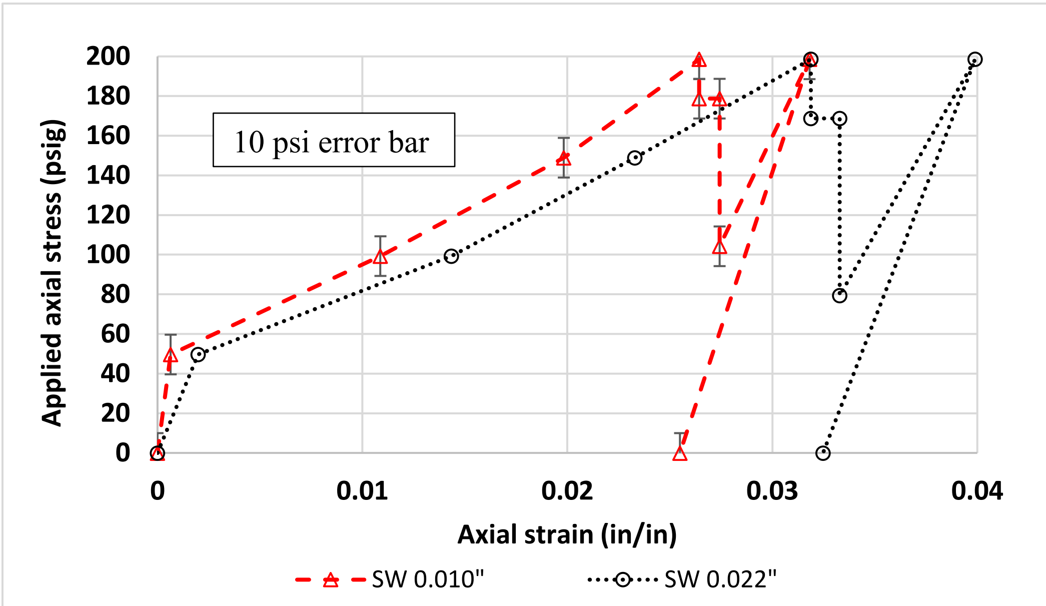

Figure 6.5. Stress-strain diagram for DC-1 at 0.010” or 0.022” aperture slot size.

The horizontal shift in the stress-strain diagram decreases with larger grain sizes, as shown in **Figure 6.6,** for DC-3. Moreover, it seems that strain is inversely proportional to PSD size as for DC-1 maximum observed strain was around 0.04, whereas it is shy below 0.02 for DC-3 at the same axial loading of 200 psi. **Figure 6.7** shows a lower stress reduction due to flowback, points (G) to (H) in Figure **6.4**, in DC-3 compared to DC-1. However, the larger slot aperture shows more reduction in stress due to flowback at the same PSD, which confirms that stress reduction is due to sand production. Moreover, the analogy supports the justification for the horizontal shift in the stress-strain diagram at larger aperture sizes, which was discussed earlier.

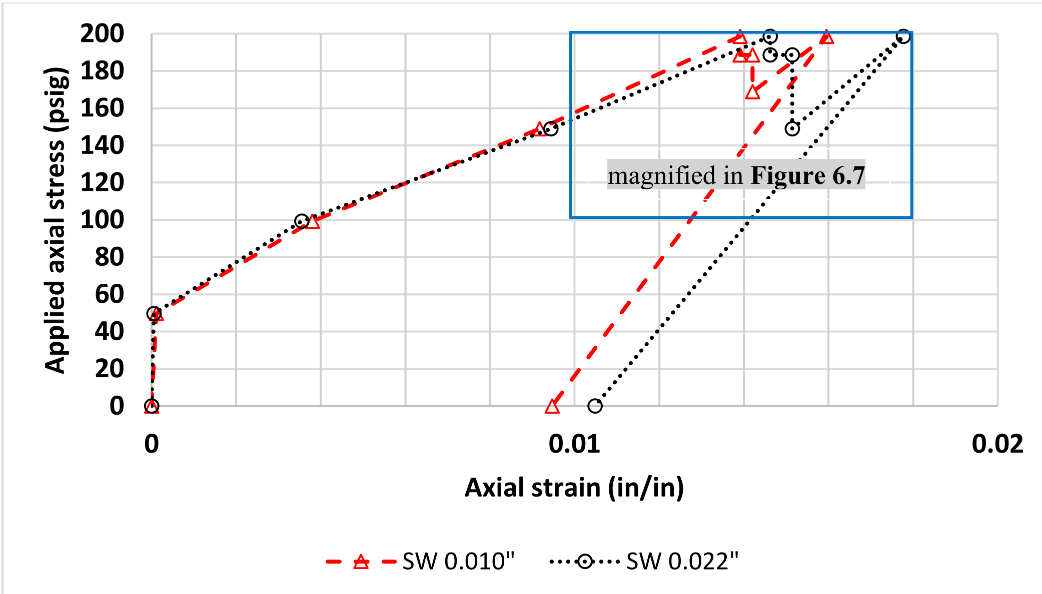

Figure 6.6. Stress-strain diagram for DC-3 at 0.010” or 0.022” aperture slot size.

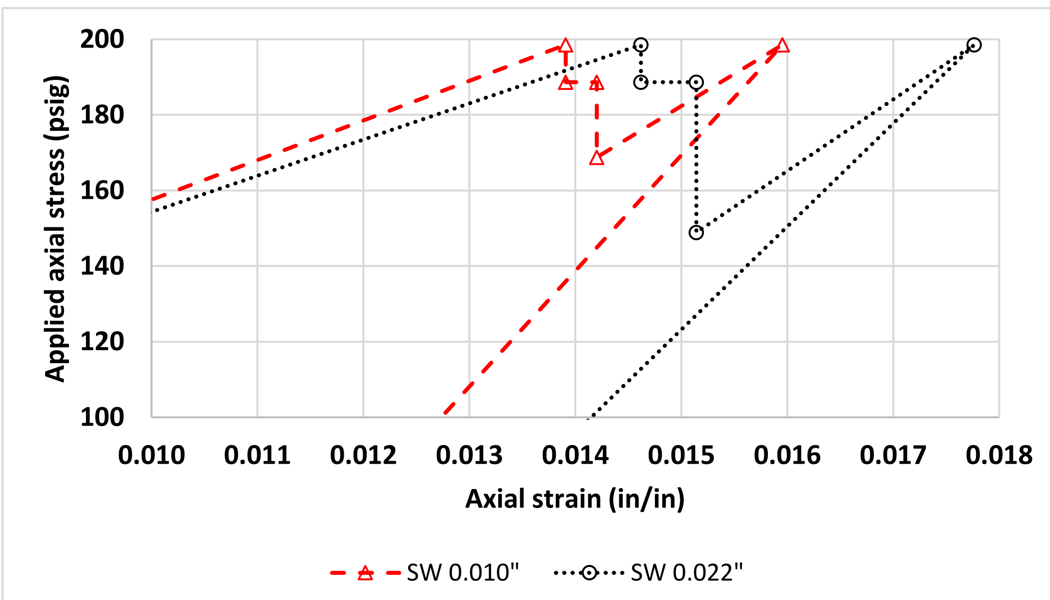

Figure 6.7. Magnified stress-strain diagram for DC-3 at 0.010” or 0.022” aperture slot size.

The next sections will demonstrate the initial and the final permeability measurements, at points (E) and (J) in Figure **6.4**, respectively, to quantify the flowback impact on retained permeability due to fines migration and pore throat plugging discussed in Section 6.1.2.

The permeability will be measured in terms of sand pack apparent permeability to gas at atmospheric outlet pressure using five different flow rates. The pressure will be measured at the same spatial location if the produced sand volume and its corresponding height reduction, due to flowback, are neglected. Moreover, it is assumed that the added stress to reach point (J) does not influence the final permeability for the range of used stresses as shown in Figure **5.21**. However, the sand pack sections permeabilities, presented in Section 5.2.1, will not be included due to the impracticality of applying Darcy's law in series for compressible fluids, as discussed earlier.

6.3.1.1 SRT-III Retained Permeability for DC-1

The initial and final sand pack permeability measurements for DC-1 at 10 thou slot aperture, shown in **Figure 6.8**, are based on Darcy's law graphical form plotted for five different flow rates. The straight line represents the permeability in millidarcy, and curves were developed in a similar approach presented in Appendix E. However, permeability change is less than 3%, based on slope percentage difference, due to SRT-III flowback. It indicates that the permeability reduction is insignificant even for small slots with aperture size of 10 thou. Accordingly, the retained permeability approaches unity, which indicates that fines migration did not cause any detectable pore throat plugging.

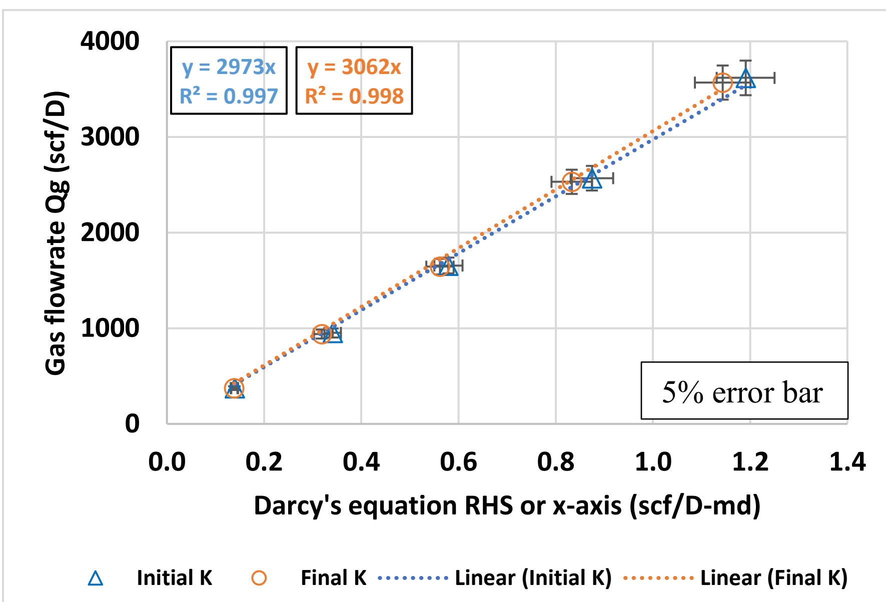

Figure 6.8. DC-1 sand pack permeability before and after flowback at 10 thou slot aperture.

Darcy's law was used to construct **Figure 6.8** for compressible fluids in a linear system using the pressure-squared method. Moreover, initial permeability measurement is listed in Table **6.2**, whereas Table **6.3** represents the final permeability measurements.

Table 6.2: DC-1 Initial Permeability Measurements in **Figure 6.8** at Slot Aperture of 10 thou.

Rotameter	Qg*	Qg	x-axis	Top Pressure	Outlet Pressure	Average Pressure
units	rcf/D	scf/D	scf/D-md	psia	psia	psia
20	331.7	373.4	0.139	16.55	14.62	15.59
40	735.3	950.9	0.341	19.01	14.64	16.83
60	1129.1	1656.0	0.579	21.56	14.67	18.12
80	1550.0	2568.9	0.874	24.36	14.73	19.54
100	1965.5	3617.4	1.191	27.06	14.80	20.93

Table 6.3: DC-1 Final Permeability Measurements in **Figure 6.8** at Slot Aperture of 10 thou.

Rotameter	Qg*	Qg	x-axis	Top Pressure	Outlet Pressure	Average Pressure
units	rcf/D	scf/D	scf/D-md	psia	psia	psia
20	331.7	373.7	0.138	16.56	14.65	15.61
40	735.3	939.0	0.319	18.77	14.67	16.72
60	1129.1	1643.9	0.562	21.40	14.70	18.05
80	1550.0	2531.0	0.833	24.00	14.74	19.37
100	1965.5	3568.5	1.143	26.69	14.82	20.75

However, the sand pack permeability may seem to be general and not representative for the near-coupon sand permeability alteration due to flowback. Moreover, the impracticality of applying the sectional permeability due to compressible fluid flow implies the need for an additional indicator for permeability change. The average pressure gradient across the sand pack and near the coupon region was evaluated before and after flowback during permeability measurements to detect any possible changes in permeability, as presented in **Table 6.4**.

Table 6.4: Pressure Gradient Before and After the Flowback Across the Sand Pack and Near the Coupon.

	Pressure Gradient Across the Sand Pack			Pressure Gradient Near the Coupon		
Rotameter	Initial ($\Delta P/\Delta x$)	Final ($\Delta P/\Delta x$)	Absolute Difference	Initial ($\Delta P/\Delta x$)	Final ($\Delta P/\Delta x$)	Absolute Difference
units	psi/in		%	psi/in		%
20	0.161	0.159	1.03	0.827	0.825	0.34
40	0.364	0.342	5.98	1.040	1.026	1.31
60	0.574	0.559	2.64	1.289	1.284	0.39
80	0.803	0.772	3.90	1.589	1.562	1.72

100	1.021	0.989	3.17	1.900	1.867	1.74

The absolute difference in the pressure gradients shows insignificant changes due to flowback, which confirms that the sand pack permeability results presented in **Figure 6.8**. Furthermore, the fines content distribution profile across the sand pack was quantified as shown in Figure **6.9**. The negligible changes in permeability and pressure gradient confirm the absence of clear evidence of fines migration.

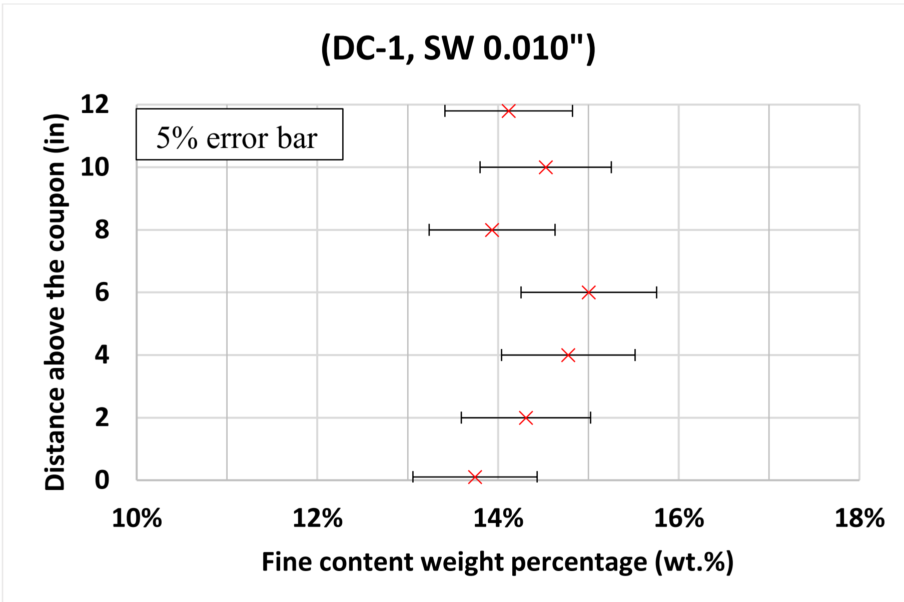

Figure 6.9. Fines content distribution across the sand pack after flowback.

Similarly, the initial and the final permeabilities were measured for the same sand but with larger slots having aperture of 22 thou as shown in **Figure 6.10**. It confirms the insignificance of permeability reduction due to flowback. However, initial and final permeabilities measured for 22 thou coupon slots aperture has a slight tendency to be higher than the permeabilities for 10 thou slot by 6%. It can be attributed to the flow convergence effect, which causes a slightly higher pressure drop for narrower slots. The claim of flow convergence was not investigated, yet this is considered as a logical justification because the used flow rates are significantly higher compared to conventional liquid flow rates used in SRT for SAGD producer. However, it requires further investigation, which is beyond of the scope of this research. The difference can be simply due to using imprecise rotameter to measure permeability.

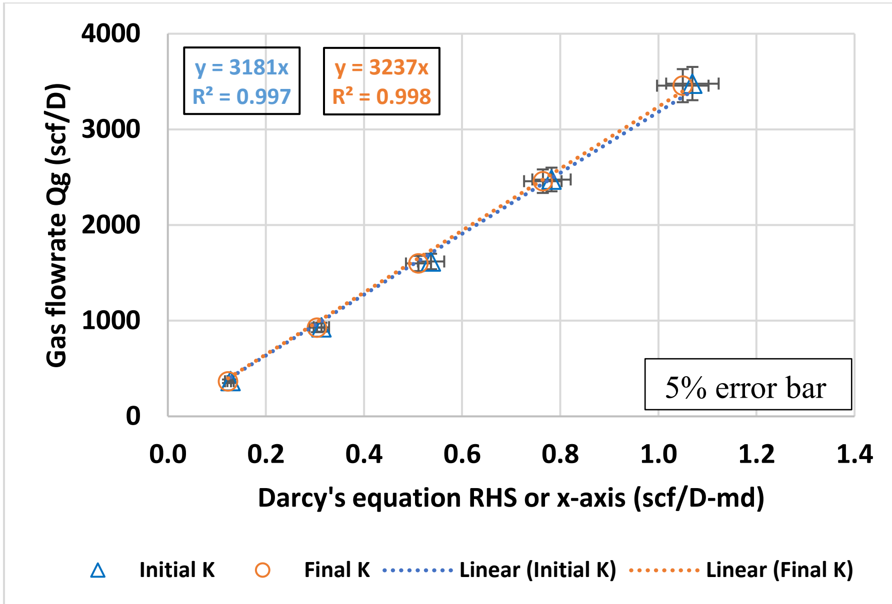

Figure 6.10. DC-1 sand pack permeability before and after flowback at 22 thou slot aperture.

6.3.1.2 SRT-III Retained Permeability for DC-3

The initial and final permeabilities were evaluated for DC-3 sand pack with 10 thou slots aperture, as shown in Figure **6.11**. The figure indicates insignificant changes in permeability due to flowback. This is expected because DC-3 fines content is much lower compared to that in DC-1, whereas the permeability magnitude is much higher than DC-1. Moreover, the retained permeability approaches unity for DC-3. Furthermore, Table **6.5** and Table **6.6** were used to estimate the initial and the final permeabilities (slopes of lines) in Figure **6.11**.

The pressure drops, presented in Table **6.5** and Table **6.6**, for DC-3 are lower than the corresponding pressure drops associated with DC-1. The permeability is the primary factor, yet not the only one. The secondary factor can be seen in the standard equivalent flow rate (Qg), which is relatively higher for DC-1 at the same rotameter reading (Qg*). Moreover, the standard equivalent flow rate is a function of rotameter outlet pressure or cell top pressure, which is determined based on the pressure drop across the sand pack due to its permeability. There is no feasible way to isolate those two factors because of the inadequate precision of the manual rotameter used, yet this observation seems to be interesting for future work.

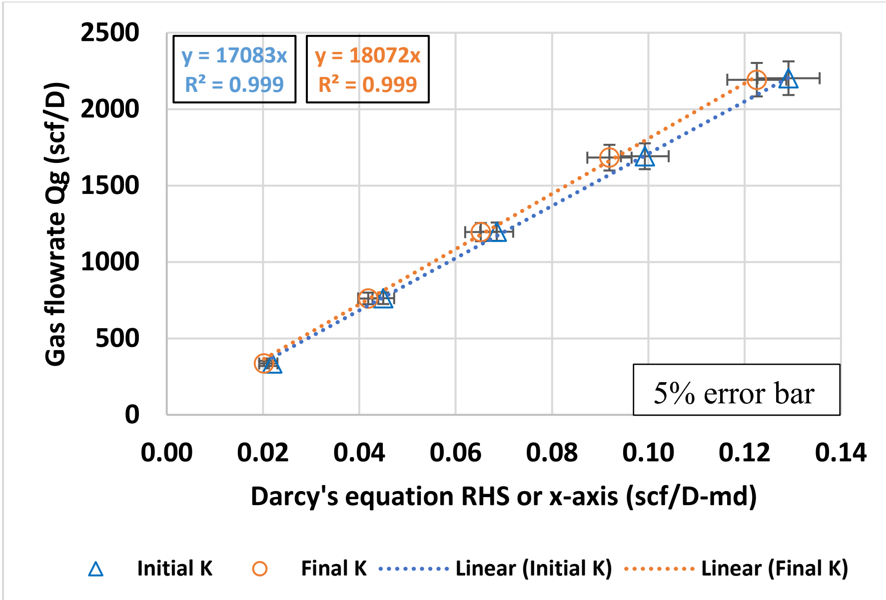

Figure 6.11. DC-3 sand pack permeability before and after flowback at 10 thou slot aperture.

Table 6.5: DC-3 Initial Permeability Measurements in **Figure 6.11** at Slot Aperture of 10 thou.

Rotameter	Qg*	Qg	x-axis	Top Pressure	Outlet Pressure	Average Pressure
units	rcf/D	scf/D	scf/D-md	psia	psia	psia
20	331.7	336.4	0.022	14.91	14.59	14.75
40	735.3	762.9	0.045	15.25	14.60	14.93
60	1129.1	1198.2	0.069	15.60	14.62	15.11
80	1550.0	1691.8	0.099	16.04	14.65	15.35
100	1965.5	2202.4	0.129	16.47	14.69	15.58

Table 6.6: DC-3 Final Permeability Measurements in **Figure 6.11** at Slot Aperture of 10 thou.

Rotameter	Qg*	Qg	x-axis	Top Pressure	Outlet Pressure	Average Pressure
units	rcf/D	scf/D	scf/D-md	psia	psia	psia
20	331.7	336.2	0.020	14.90	14.60	14.75
40	735.3	761.5	0.042	15.22	14.62	14.92
60	1129.1	1195.2	0.065	15.56	14.63	15.09
80	1550.0	1682.4	0.092	15.96	14.66	15.31
100	1965.5	2192.7	0.123	16.40	14.70	15.55

DC-3 sand pack initial and final permeabilities were evaluated for the larger 22 thou slot aperture, yet it again confirms the retained permeability approaching unity. Moreover, it shows 6 %, on average, permeability increment due to larger slots aperture as noticed and discussed earlier for DC-1.

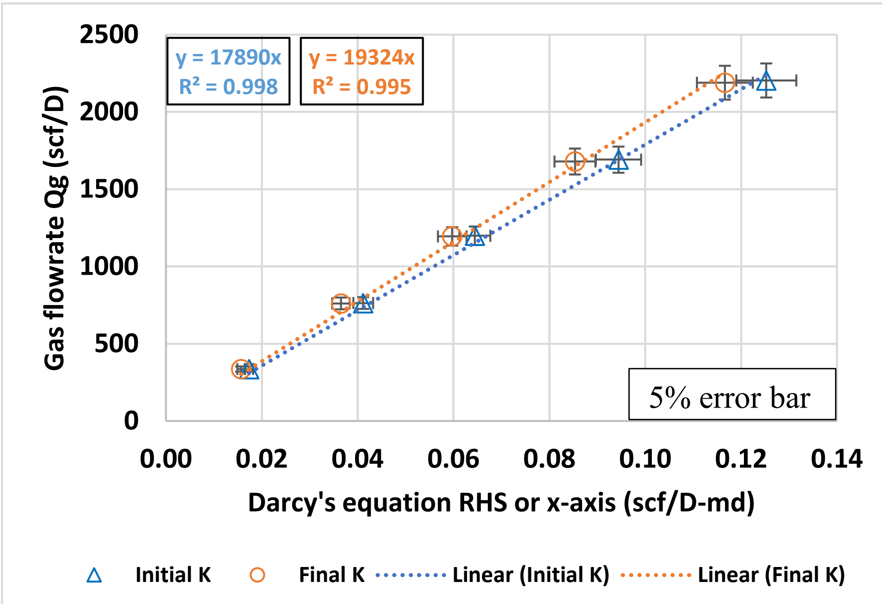

Figure 6.12. DC-3 sand pack permeability before and after flowback at 22 thou slot aperture.

Nevertheless, the insignificant (or the minor undetectable) permeability changes due to flowback was the key finding of this section, which results in retained permeability approaching unity. It proves that the lower limit for SRT does not exist for SAGD injector flowback testing. Accordingly, the claim of previous research that classifies the industry selection practices for narrower aperture slots to be conservative (Fattahpour et al., 2018a; Mahmoudi et al., 2018a), is merely invalid for SAGD injectors because lower limit, or permeability reduction, does not exist in the first place.

The next section will elaborate on transient flow measurements, which represent flowback to ensure SRT-III experiments are representative of the expected operational parameters specified in Section 4.2.3.

6.3.2 SRT-III Transient Flow Measurements for DC-1

The SRT-III Set-up efficiency, shown in Figure **6.13**, shows an improvement over the SRT-II set-up efficiency, presented in Figure **5.11**, discussed earlier in Section 5.2.1. The efficiency improvement was noticed over the entire flowback duration (about 120 seconds). Moreover, SRT-III flowback duration was compared to the ideal tank discharge model, which has a shorter period of 80 to 90 seconds ("Discharge Tank Calculation Software," Nov. 7, 2019) depending on adiabatic or isothermal processes, respectively, as shown in Figure **6.14**.

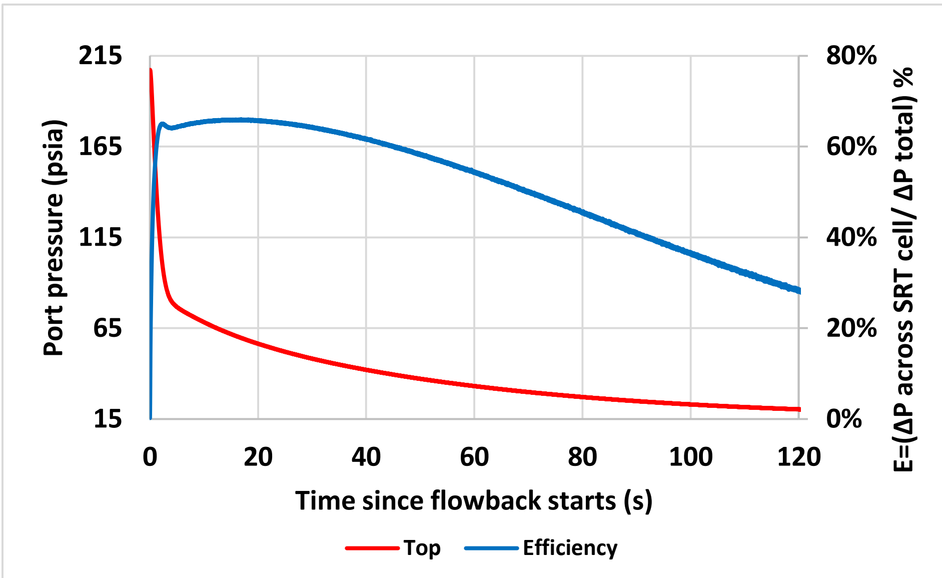

Figure 6.13. SRT-III set-up efficiency for the entire flowback duration.

The SRT-III flowback time shows, on average, an excess of 30% required time over the ideal tank discharge time because of the presence of actual mechanical flow restrictions in the set-up. However, it is acceptable because the area of interest of this research is to study the impact during the first 5 seconds of the flowback, as proposed earlier in Section 4.2.3, to mimic the actual SAGD injector flowback. The scenario suggests a differential pressure equals at least 47 psi across the SRT cell was achieved as shown in the shaded area in Figure **6.15**

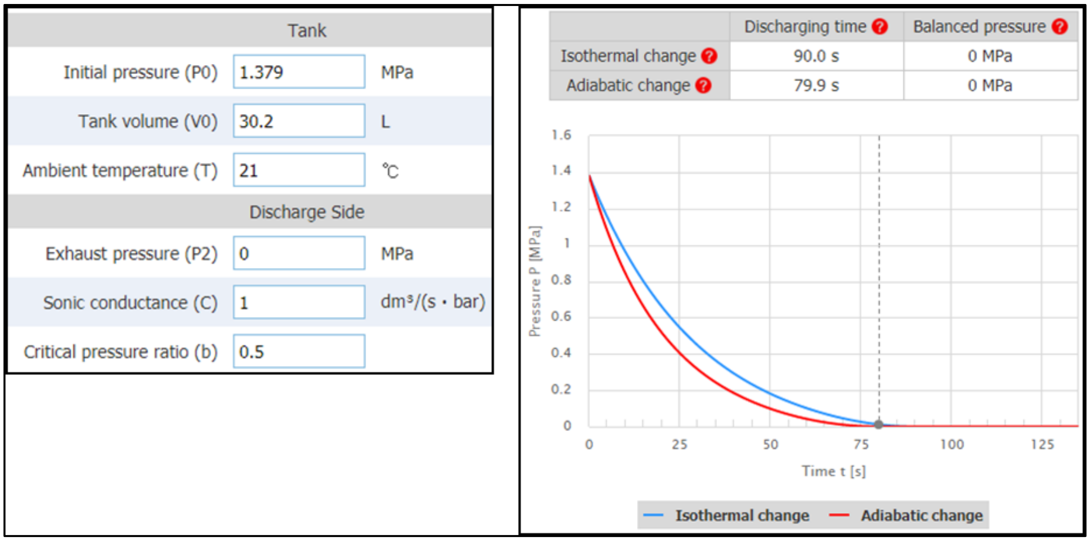

Figure 6.14. Flowback tank discharge time based on isothermal and adiabatic models for SRT-III at flowback initial pressure of 215 psia ("Discharge Tank Calculation Software," Nov. 7, 2019).

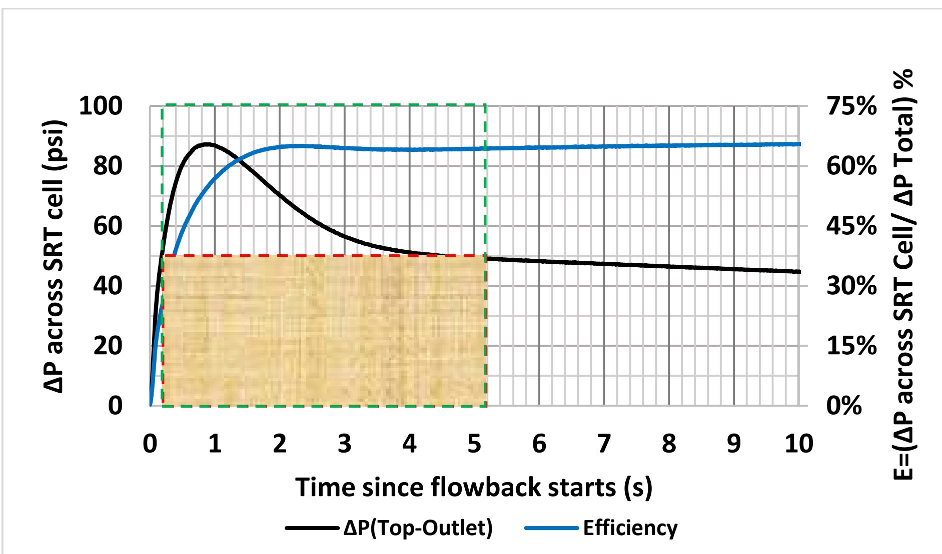

Figure 6.15. SRT-III ΔP across the cell and set-up efficiency for the 1st ten seconds of flowback.

Although the designated differential pressure was delivered during the SRT-III flowback, yet it took about 0.2 seconds and was not instant. The delay was attributed to mechanical flow restrictions at the outlet, which prevents the outlet pressure from being reduced to atmospheric instantly, as shown in Figure **6.16**. Moreover, it confirms the decision to eliminate the solenoid valves from SRT-III because the outlet pressure required more time to reach atmospheric pressure compared to the sharp opening time of the solenoid.

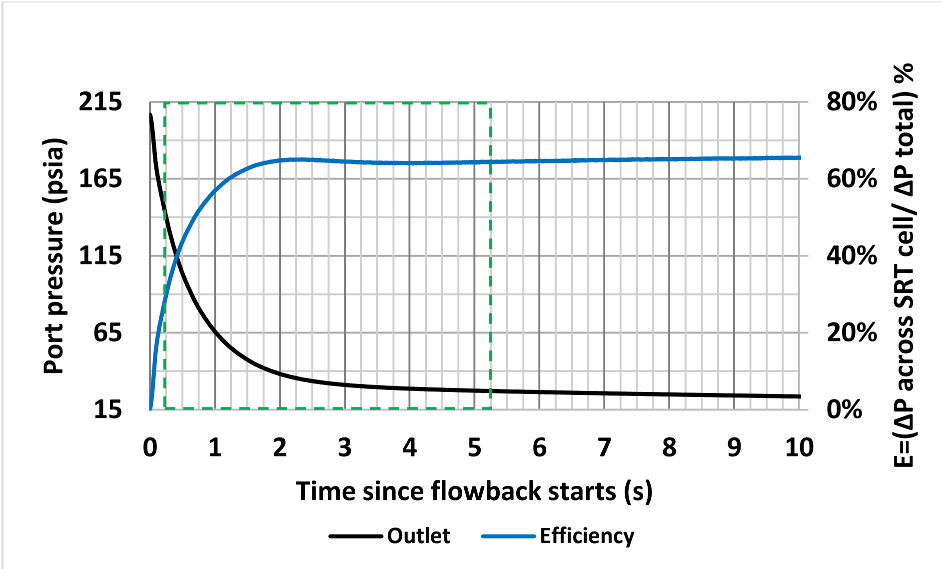

Figure 6.16. SRT-III outlet pressure of the cell and set-up efficiency for the 1st ten seconds of flowback.

However, these findings were accessible through the absolute pressure measurements and not by analyzing the differential pressure. It raises the importance of analyzing absolute pressures and their corresponding gas flow rates during flowback, which will be discussed in the following sections.

6.3.2.1 Pressure and Pressure Gradient Profiles

The absolute pressures of the SRT-III cell were monitored during flowback, as shown in Figure **6**.**17**, because of the previously mentioned advantage to troubleshoot the system problems. It seems that using differential transducers only during SRT is not a wise decision.

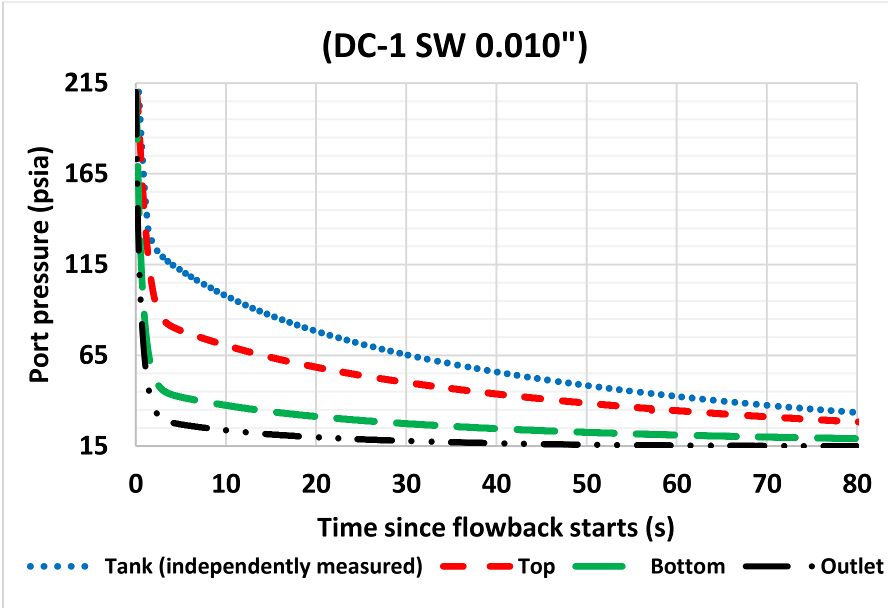

Figure 6.17. Pressure during flowback.

The corresponding differential pressures estimated during flowback are consistent with the theory of compressible fluid flow in porous media. Over 30% of the total pressure drop across the sand pack was consumed in the last 2 inches near the coupon region (T-Outlet) as shown in Figure **6.18** for the peak point. Nevertheless, the corresponding average pressure gradients ($\Delta P/\Delta x$) for the near coupon region reach 15 psi/in and 7 psi/in across the sand pack as shown in Figure **6.19**. These values are two orders of magnitude of those reported by a previous research for a similar flowback scenario (Fattahpour et al., 2018a).

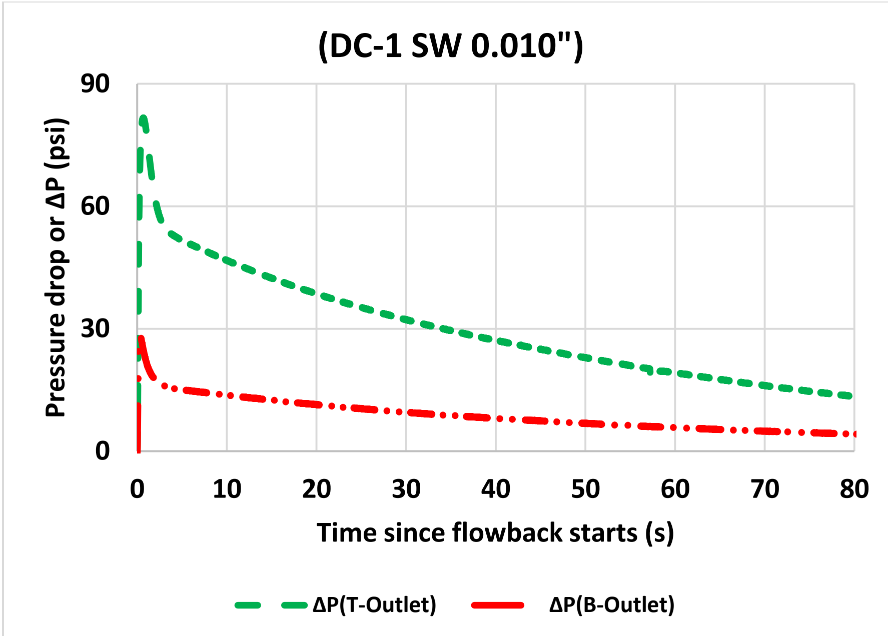

Figure 6.18. Differential pressure across the sand pack and near-coupon.

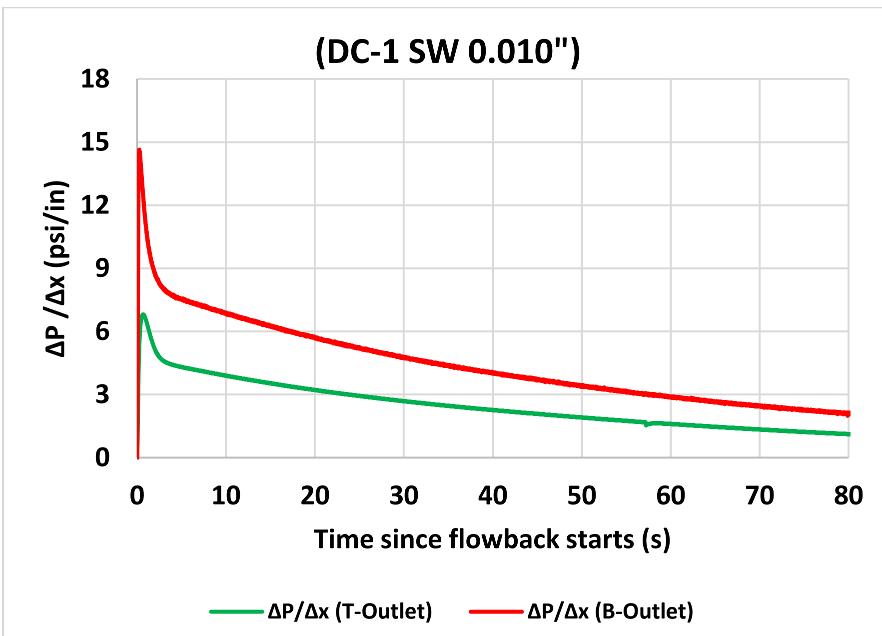

Figure 6.19. Pressure gradient across the sand pack and near-coupon.

Pressure gradients across the cell were comparable for DC-1 sand pack for the two different coupon slot apertures of 10 and 22 thou, as illustrated in Figure **6.20**.

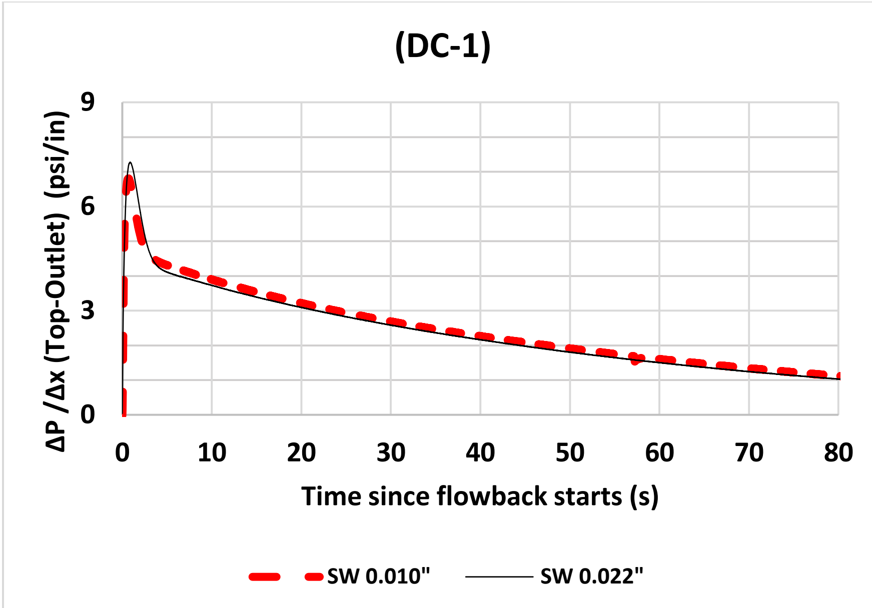

Figure 6.20. Pressure gradient across the sand pack at different coupon slot widths.

However, pressure gradients near the coupon region for the two tests differ by 20% at the peak point in Figure **6.21**, which is attributed to the outlet pressure variation shown in Figure **6.22**.

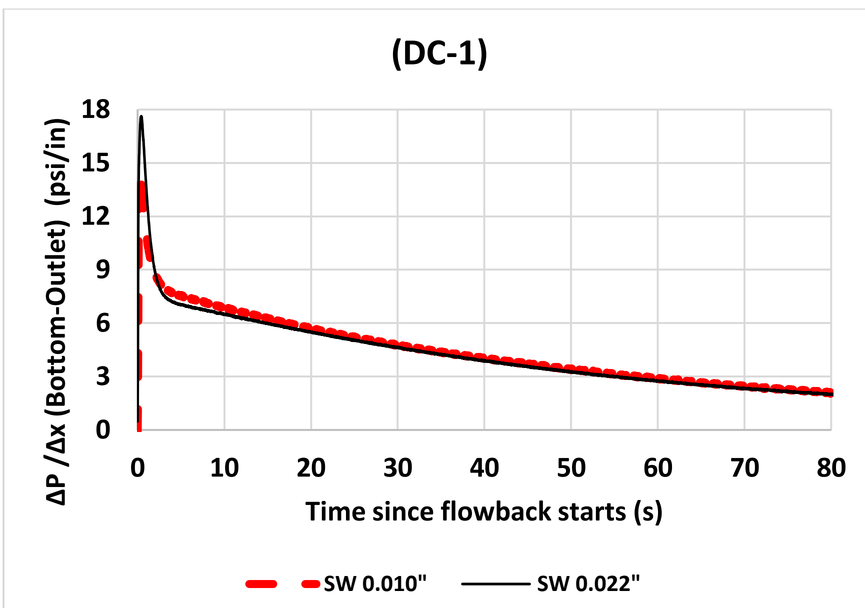

Figure 6.21. Pressure gradient near the coupon region at different coupon slot widths.

The outlet pressure variation for the two tests, shown **Figure 6.22**, was due to additional flow restriction that took place at the outlet arrangement; but not due to slot aperture variation, which will be disused later in Section 6.3.2.3.

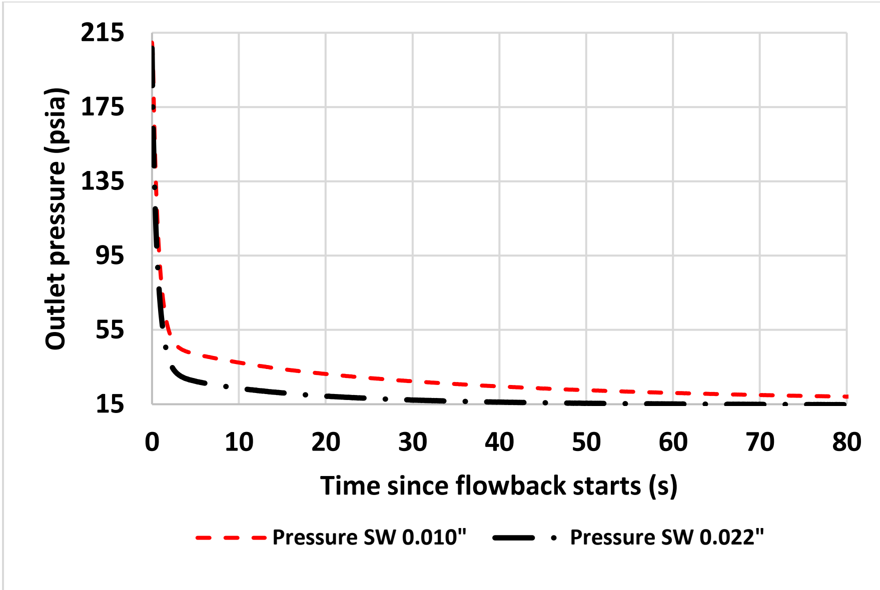

Figure 6.22. Outlet cell pressure during the flowback for DC-1 at different slot widths.

6.3.2.2 Evaluation of Mass Flow Rate

The mass flow meter was replaced in the set-up by a flowback tank having known size and weight, as discussed in Sections 5.2 and 5.3, to maintain a moderately cost-effective SRT facility. This section presents the method used to evaluate mass flow rate based on understanding the involved physics associated with an appropriate mathematical formulation.

The flowback tank was placed on a sensitive electronic scale to measure the gas mass inside the tank or the net gas mass remaining (NGMR) during flowback, which is shown in **Figure 6.23**. The existing gas mass (EGM), presented in **Figure 6.24**, was evaluated based on this mathematical relation [$EGM(t) = NGMR(t = 0) - NGMR(t)$]. The mass flow rate is defined as the rate of mass change per unit time, which represents the function derivative with respect to time, expressed by Eq 6.1. Accordingly, the estimated flowback mass rate is shown in **Figure 6.25**. Although the pipe that connects the flowback tank to the cell head was firmly fastened, yet the mass flowrate shows oscillation as can be seen in **Figure 6.25**.

$$\frac{d\,(EGM)}{dt} = \frac{EGM(t^{n+1}) - EGM(t^{n})}{t^{n+1} - t^{n}} \qquad \text{(Eq. 6.1)}$$

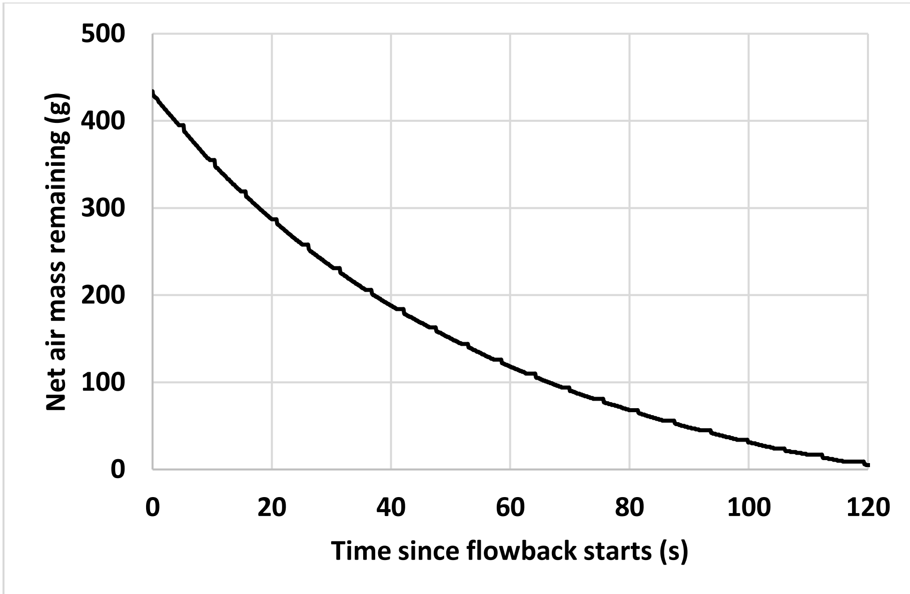

Figure 6.23. Electronic scale raw data reading during flowback.

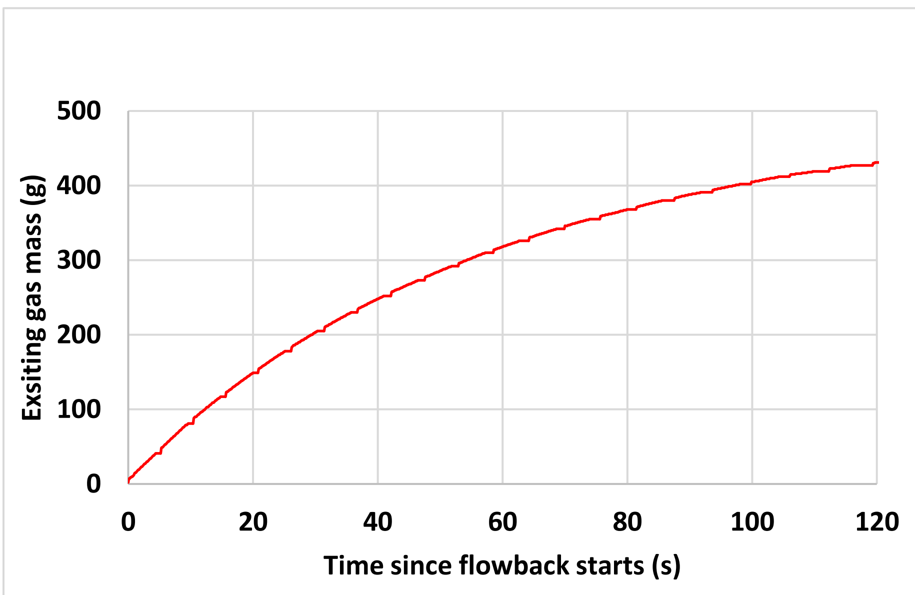

Figure 6.24. EGM, calculated from scale raw data, during flowback.

However, the oscillation magnitude and frequency, as shown in **Figure 6.26**, were visually comparable to the calculated mass flow rates, which introduce significant uncertainty in flow rate estimation using Eq. 6.1. The suggested solution was to find the best fit for the EGM and compute its corresponding derivative, which may yield representative flow rates during flowback.

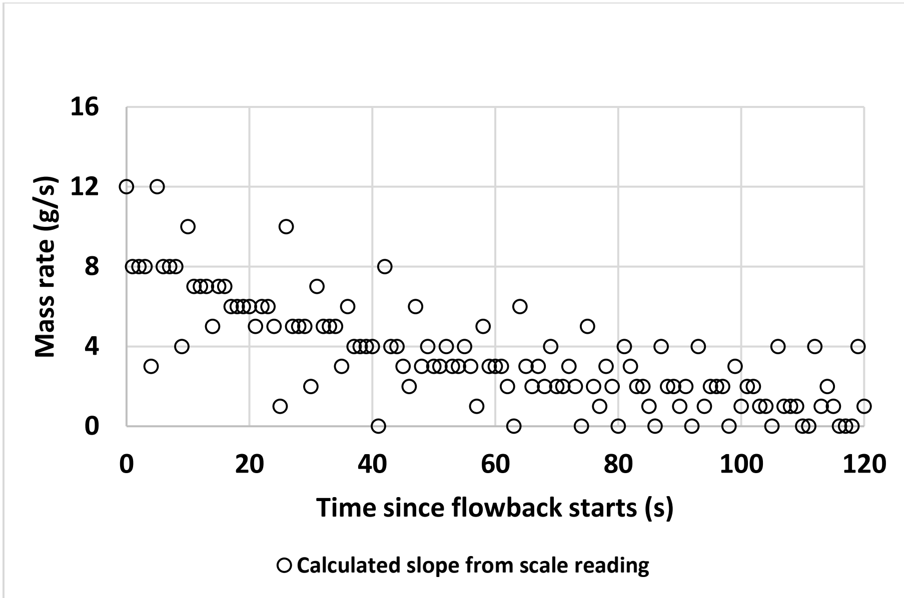

Figure 6.25. Mass rate, calcuated from scale raw data, during flowback.

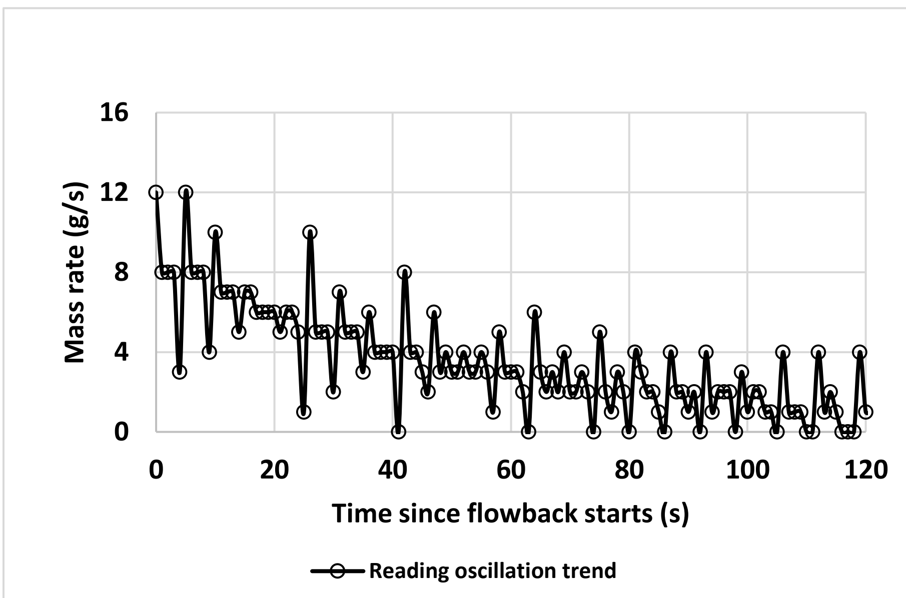

Figure 6.26. Mass rate oscillation trend.

The EGM, shown in **Figure 6.24**, look like a logarithmic function, yet a logarithmic fit shows considerable deviation, especially in the first few seconds that follow the initiation of flowback as shown in **Figure 6.27**.

However, the slope of the fit does not represent the flow rate. Therefore, a polynomial is tried next as the fitting function.

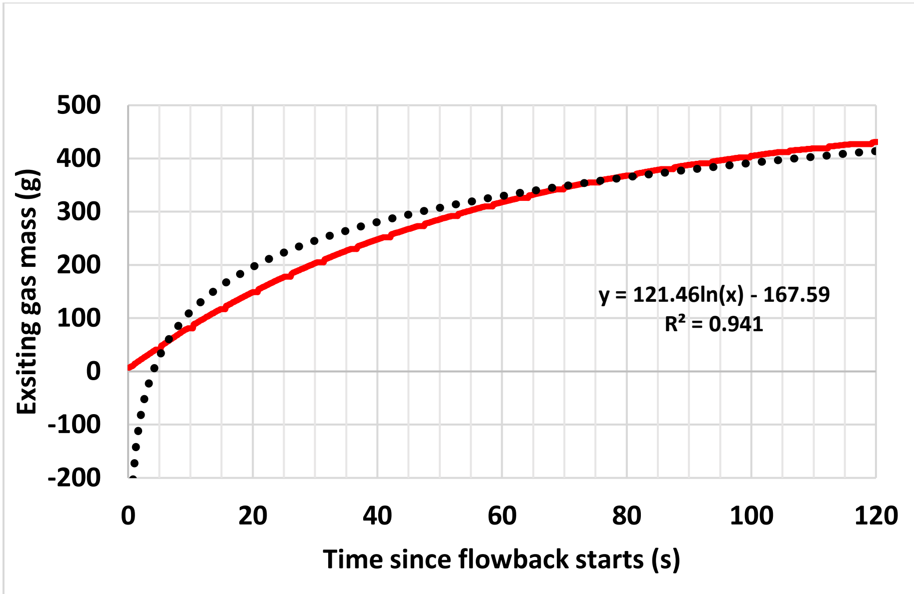

Figure 6.27. EGM, calcuated from scale raw data, and its logarithmic fit during flowback.

The polynomial fit for the EGM, shown in **Figure 6.28**, was intended to use a simple fitting function, yet a sophisticated fitting technique may result in better precision, but this is beyond the scope of this research because the objective of this study is to demonstrate the used concepts.

The EGM fit was forced to pass through the origin point as it represents the initial condition of flowback, as presented by the fit equation and shown in **Figure 6.28**. The computed mass flow rates from the polynomial fit and Eq. 6.1 were graphically illustrated in **Figure 6.29**.

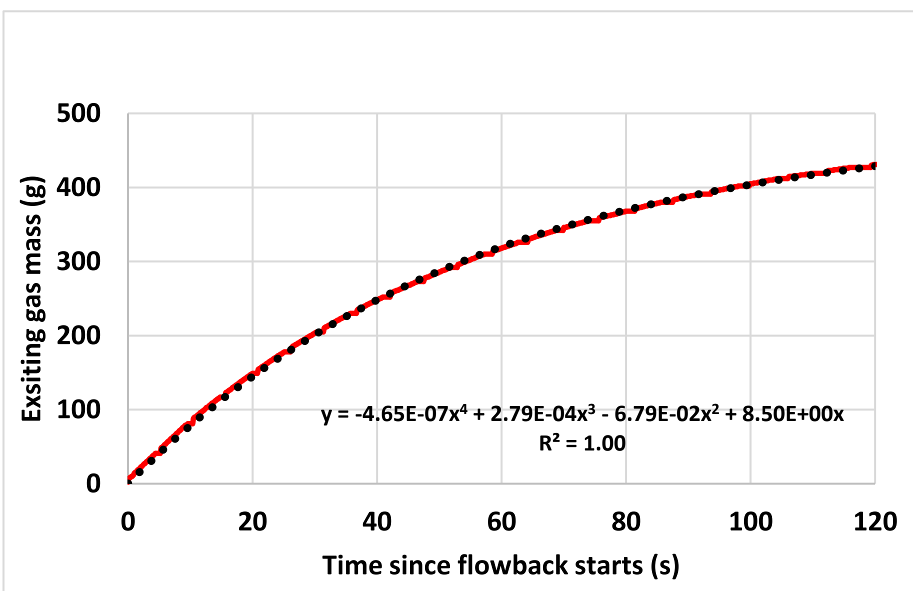

Figure 6.28. EGM, calcuated from scale raw data, and its polynomial fit during flowback.

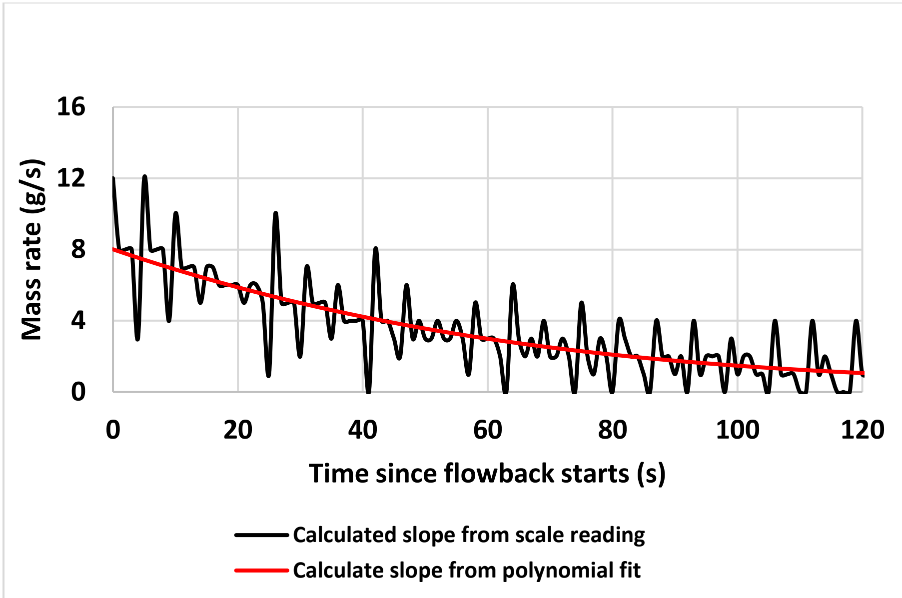

Figure 6.29. Comparison between the mass rates calculated from EGM and derevative of polynomial fit.

It should be mentioned that the calculated mass flow rates from the scale reading of EGM, shown in **Figure 6.29**, were taken for points separated by one second time interval to enhance visibility, yet the polynomial fit accounts for all scale readings at ten readings per second.

The EGM computed for DC-1 in SRT-III experiments for both 10 and 22 thou slots aperture, as shown in **Figure 6.30**, are used to estimate the mass flow rates presented in **Figure 6.31**.

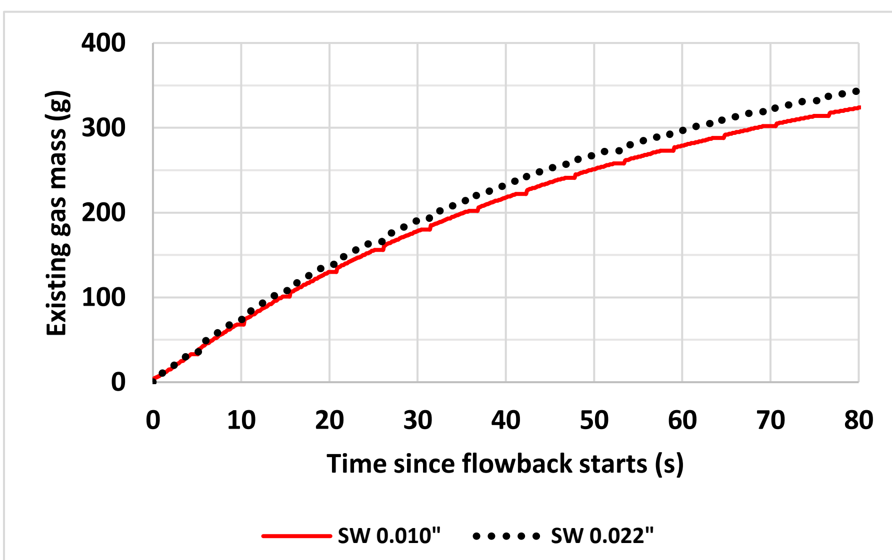

Figure 6.30. EGM, calcualted from scale raw data, during the flowback for DC-1 at 0.010" and 0.022" slot widths.

Although the EGM seems to diverge after 40 seconds of flowback as shown in **Figure 6.30**, their corresponding slopes, which represent the mass flow rates, are converging after 40 seconds as shown in **Figure 6.31**. The divergence in the calculated mass flow rate in the first 40 seconds of flowback is discussed in the next section.

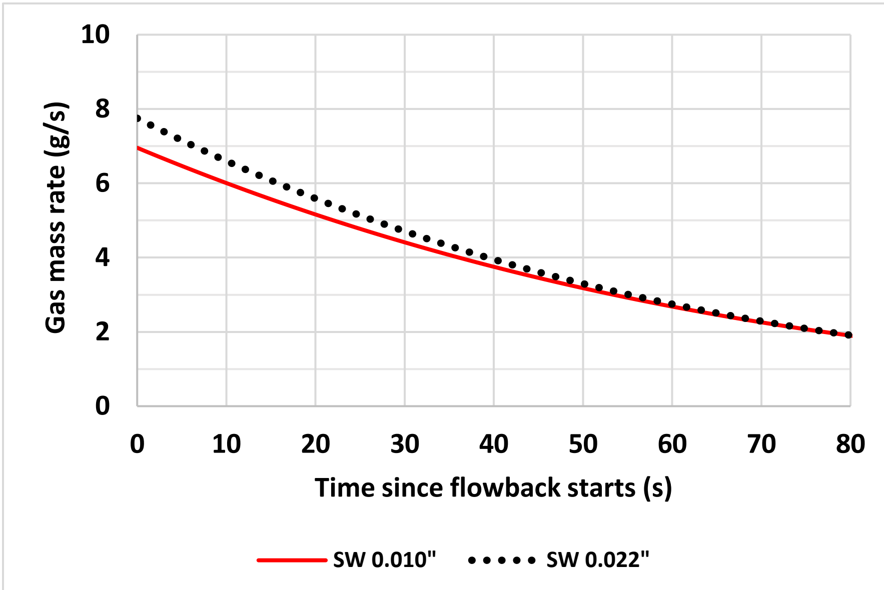

Figure 6.31. Mass rates, calculated from polynomial fit, during DC-1 flowback at 0.010" and 0.022" slot widths.

6.3.2.3 Evaluation of Gas Volumetric Flow Rate

The calculated mass flow rates combined with the pressure measurements presented in Section 6.3.2.1, and ideal gas law yield the volumetric flow rates.

The gas volumetric flow rate at the outlet for DC-1's tests, shown in **Figure 6.32**, resolves the mass flow rate divergence confusion discussed earlier. The used volumetric flow rate (Q_g^*) is evaluated at the outlet pressure, which is not necessarily atmospheric pressure throughout the entire flowback duration, as discussed in Section 6.3.2. Furthermore, the standard conditions equivalent flow rate (Q_g) was not used because it had the same magnitude across the cell regardless of the location of pressure.

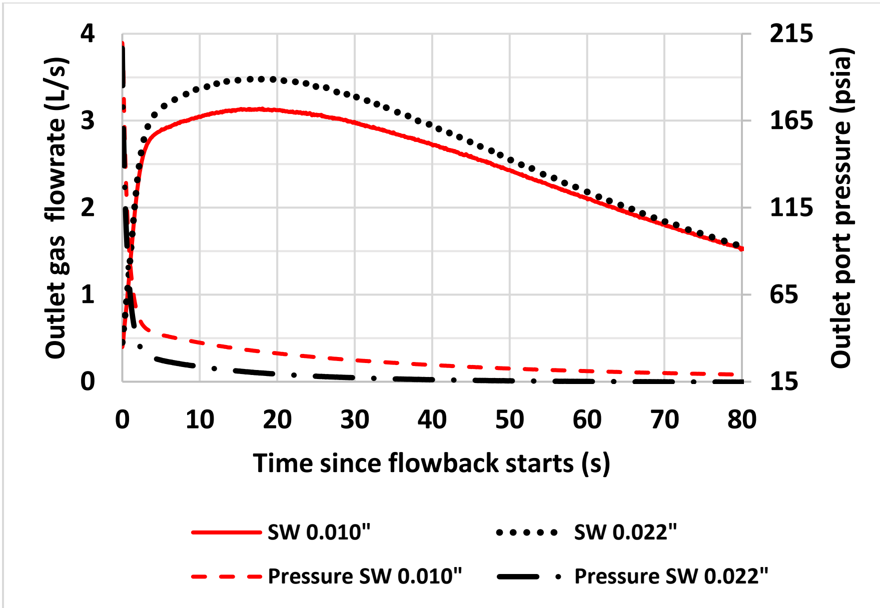

Figure 6.32 In-situ outlet volumetric flow rates and corresponding outlet pressures during DC-1 flowback at 0.010" and 0.022" slot widths.

Eq. 6.2 and Eq. 6.3 are used to evaluate the actual flow rate (Q_g^*) at any pressure measurement location across the SRT cell.

$$m \;= \rho \,.V \qquad \text{(Eq. 6.2)}$$

$$\rho_g = m \,/\, V \;=\; P\, M_{wt.}/z\, R\, T \qquad \text{(Eq. 6.3)}$$

Figure 6.33 and **Figure 6.34** show the actual volumetric flow rate (Q_g^*) at the outlet, bottom, and top pressures for DC-1 with 10 thou and 22 thou slots aperture, respectively. The volumetric flow rate, in both figures, shows a considerable match between the bottom and top flow rates because of similar gas density at these two locations. Moreover, it seems that these flow rates are relatively constant at around 1.0 L/s (3.0 M rcf/D). However, the actual outlet flow rate dramatically changes during the flowback to reach a maximum of around 3.0 L/s (9 M rcf/D) in **Figure 6.33** and a slightly higher maximum of 3.5 L/s (10.5 M rcf/D) in **Figure 6.34**. The difference between the outlet flow rates is attributed to the outlet pressure differences discussed earlier and shown in **Figure 6.32.**

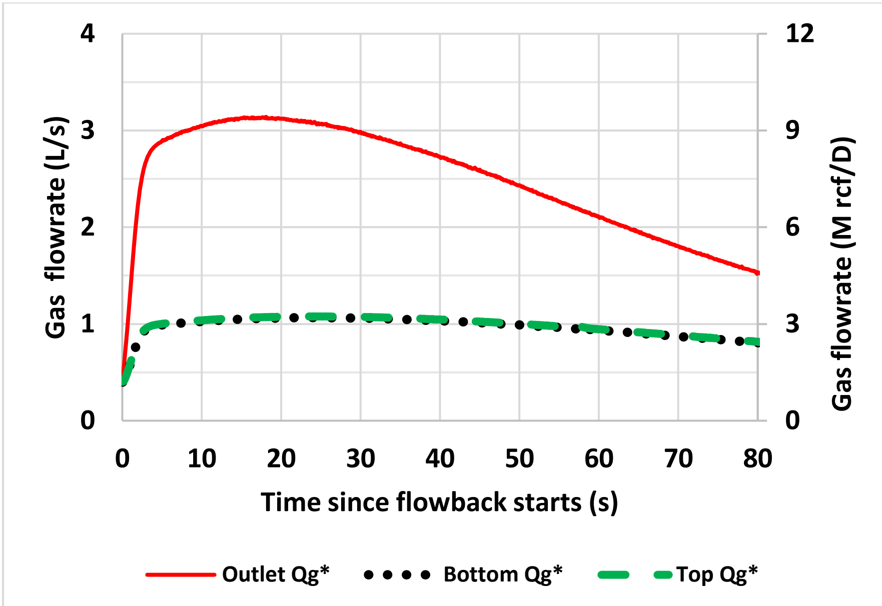

Figure 6.33. In-situ volumetric flow rates during DC-1 flowback at 0.010" slot width at the pressure of outlet, bottom and top ports.

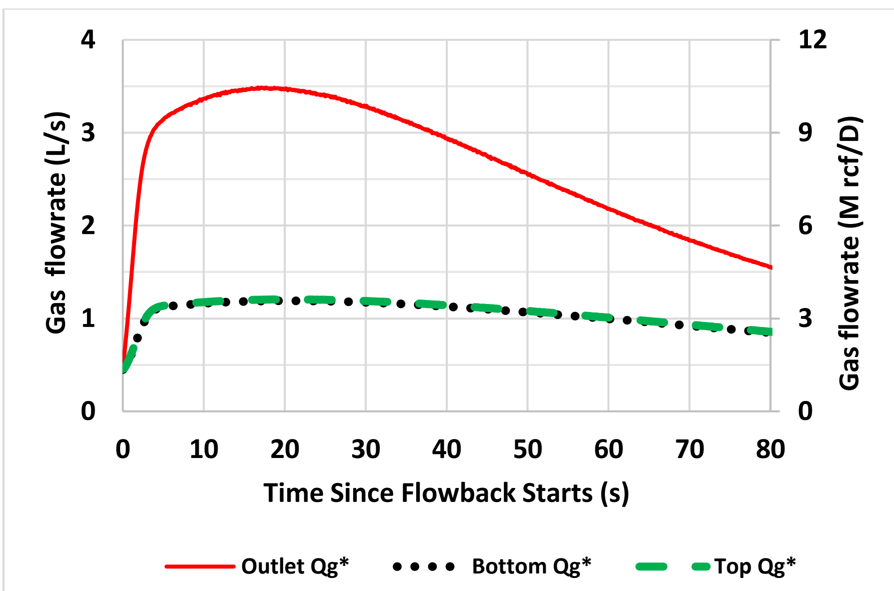

Figure 6.34. In-situ volumetric flow rates during DC-1 flowback at 0.022" slot width at the pressure of outlet, bottom and top ports.

6.4 Result Dependency on Particle Size Distribution (PSD)

This section highlights the results of the SRT-III flowback dependency on PSD, if any, whereas Section 6.3.2 elaborated on pressure, pressure gradient, mass and volumetric flow rates evaluation for DC-1. The same procedure was followed for DC-3 experiments with SRT-III set-up, where the steady-state injection was discussed in Section 6.3.1.2 for DC-3. This section presents comparison of aperture size effect on steady-state injection based on the PSD effect and DC-3 flowback results.

The initial sand pack permeability for DC-1 and DC-3, presented in **Figure 6.35**, confirms the difference in sand petrophysical properties, discussed in Section 2.1.3, for McMurry formation. Although the presented permeability is the apparent porous media permeability at near atmospheric outlet pressure, the inlet pressure is determined at each injection rate based on sand pack permeability. It does not represent the liquid-equivalent permeability due to complications associated with Klinkenberg effect evaluation using the manually controlled equipment.

Moreover, permeability evaluation using Darcy's law based on five different flow rates shows that the SL effect is negligible during the permeability measurement for the injection stage even at high gas flow rates. The slope was determined based on high root mean square (RMS or R^2), which confirms linear Darcy's flow during the measurement. Darcy's law was plotted in the Semi-log graph, shown in **Figure 6.36**, which shows an order of magnitude difference between DC-1 and DC-3 apparent permeability.

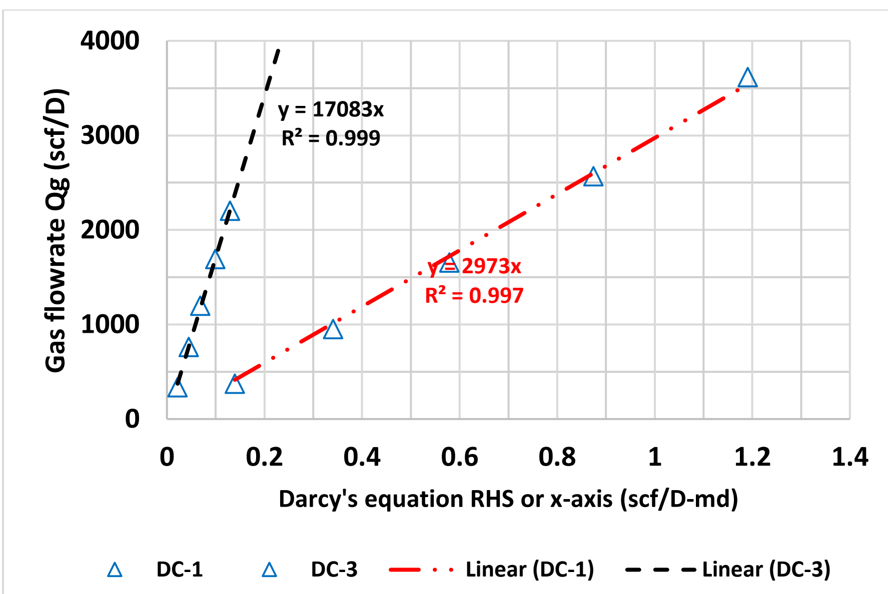

Figure 6.35. Initial permeability measurements for DC-1 and DC-3 at 0.010" slot width plotted using cartesian scale.

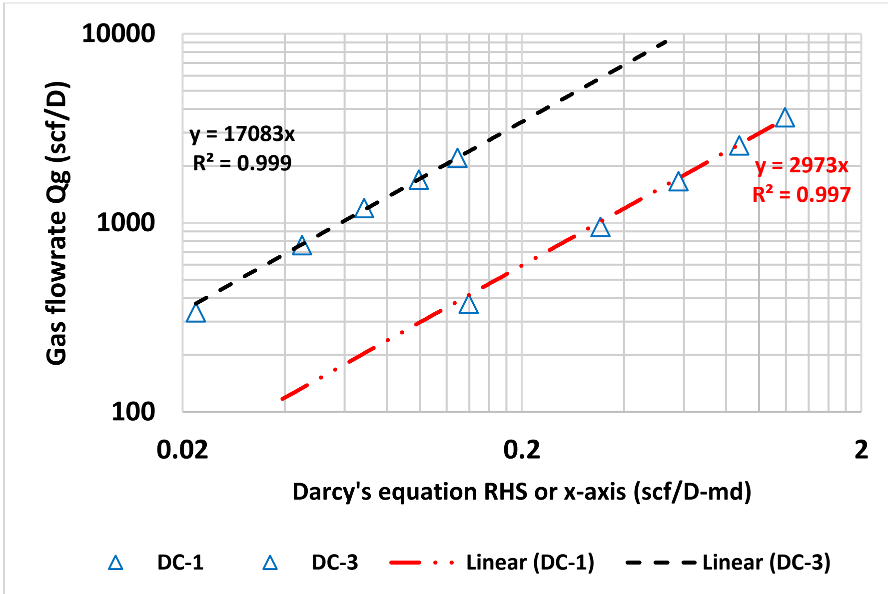

Figure 6.36. Initial permeability measurements for DC-1 and DC-3 at 0.010" slot width plotted using logarithmic scale.

The EGM was evaluated for DC-3 during flowback for slot aperture of 10 and 22 thou, as shown in **Figure 6.37**, and they were identical for both flowback experiments. EGM seems to be independent of the slot aperture.

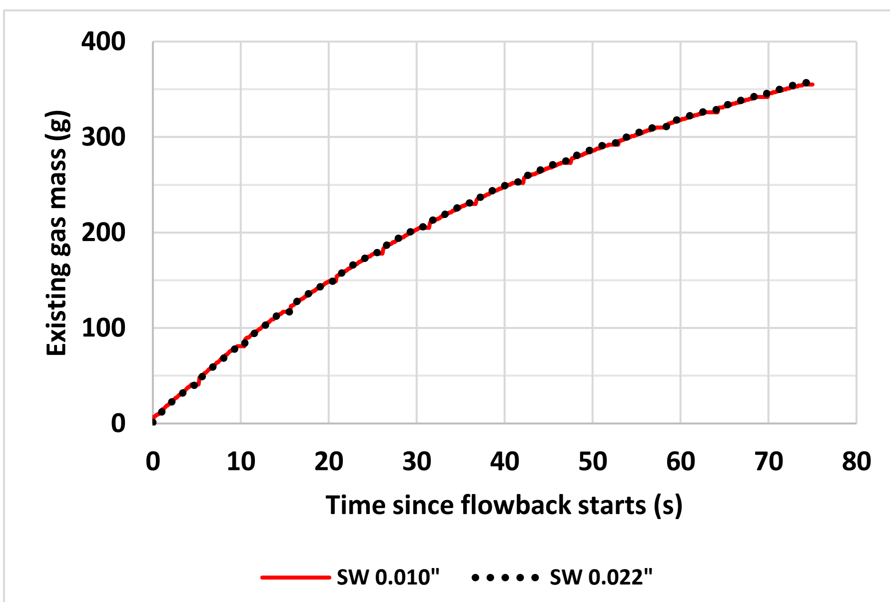

Figure 6.37. EGM, calculaed from scale raw data, during flowback for DC-3 at 0.010" and 0.022" slot widths.

Moreover, the gas mass flow rate, shown in **Figure 6.38**, was evaluated for the two tests, using a similar approach to that presented in Section 6.3.2.2, which shows a better match over DC-1 mass flow rates. However, the match was due to the outlet pressure consistency during the two flowback experiments in DC-3 experiments, as shown in **Figure 6.39**.

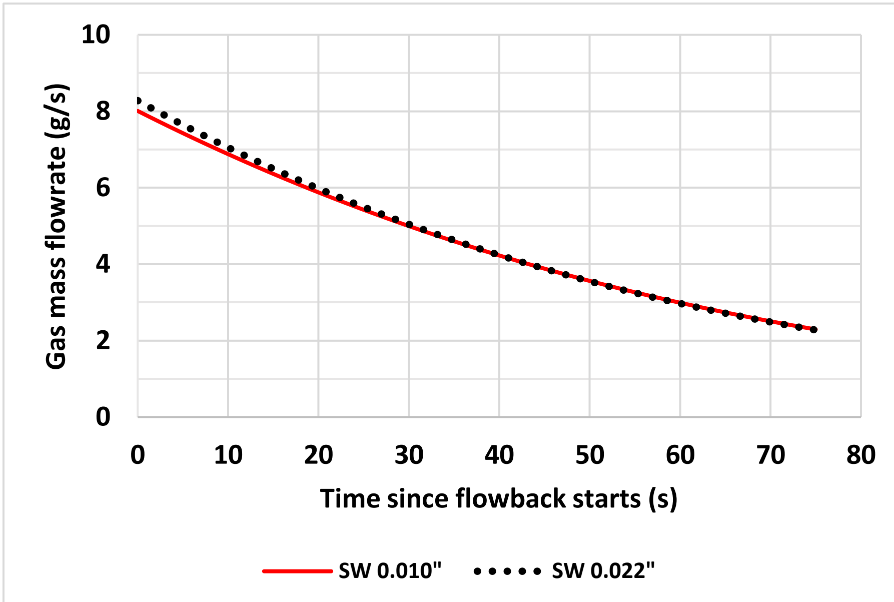

Figure 6.38. Mass rates, calculated from polynomial fit, during DC-3 flowback at 0.010" and 0.022" slot widths.

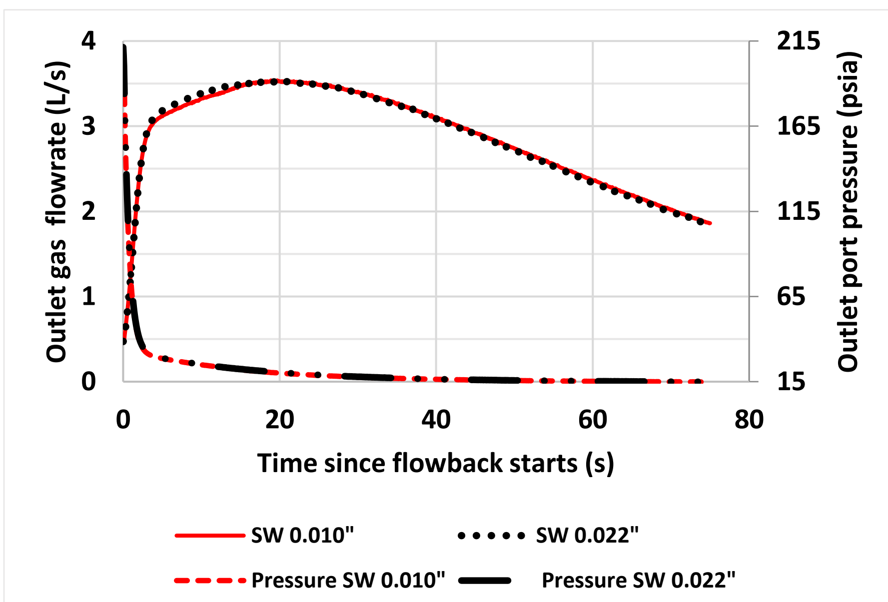

Figure 6.39. In-situ outlet volumetric flow rates and their corresponding outlet pressures during DC-3 flowback at 0.010" and 0.022" slot widths.

The volumetric flow rate was evaluated at the top, bottom and outlet ports, as shown in **Figure 6.40** for DC-3 with 10 thou and in **Figure 6.41** for DC-3 with 22 thou. The actual outlet flow rates for DC-3 flowback experiments match the outlet flow rate for DC-1 with 10 thou slots aperture. It indicates that the actual outlet flow rate is PSD independent, like the EGM. It proves the "dissipation time" term introduced by previous research (Fattahpour et al., 2018a) is not valid . Gas flow rate reaches a comparable maximum flowback rate of 3.5 L/s (10.5 M rcf/D) for DC-1, as presented earlier in Section 6.3.2.3. However, the actual bottom and top flow rates were matching for DC-3 flowback as shown in **Figure 6.40** and **Figure 6.41** and reach a maximum value at 2.5 L/s (7.5 M rcf/D). It indicates the PSD dependancy on the actual bottom and top flow rates because of the different permeabilities in DC-1 and DC-3, that dictate the pressure of bottom and top ports.

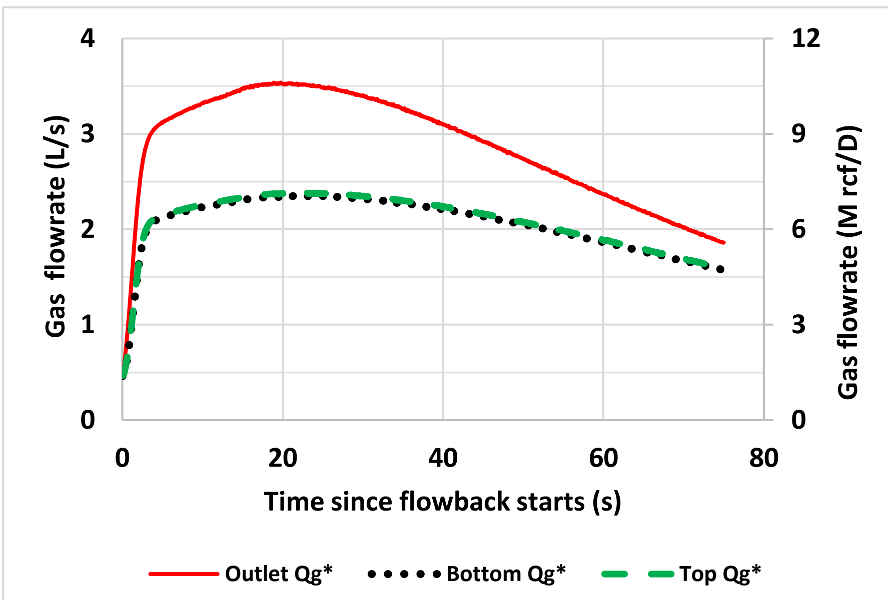

Figure 6.40. In-situ volumetric flow rates during DC-3 flowback at 0.010" slot width at the pressure of outlet, bottom and top ports.

Finally, the produced particles due to SRT-III flowback, presented in **Figure 6.42**, show a dramatic increase in particle production compared to SRT-II shown earlier in **Figure 5.18**. It reveals a substantial justification for the industry practice where the decision for smaller aperture slot size is favourable in SAGD injector. Moreover, this argument should clarify the confusion in previous researches that claim that the industry selection is conservative, which is not the case. However, it indicates that the decision made in Section 5.3.1, by matching the fluid distribution at the pore scale rather than saturation, has a significant influence on the SRT results. It confirms that SRT should take into consideration reservoir engineering, production engineering, and thermodynamics to yield representative laboratory testing. Accordingly, the moist tamping method should not be used in sand pack preparation in SRT dedicated to the SAGD injector flowback scenario.

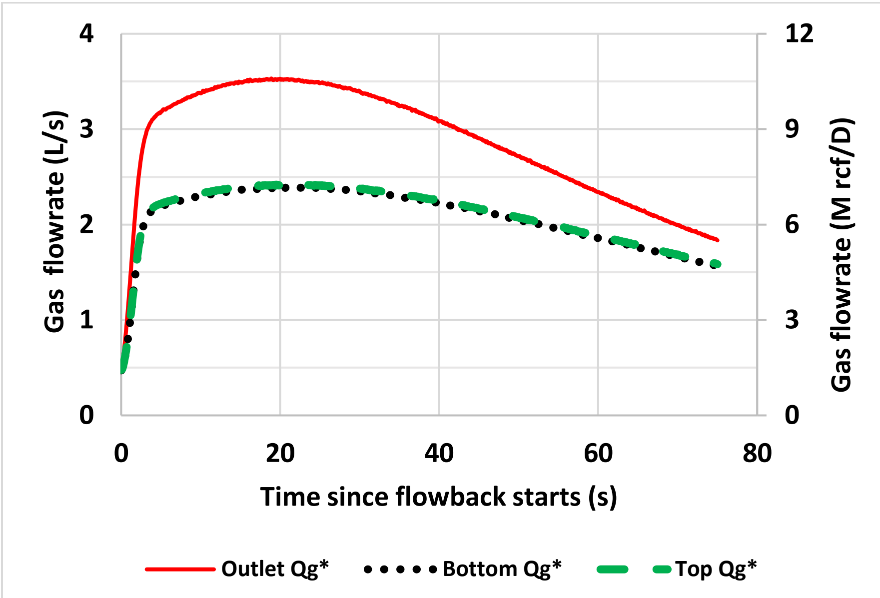

Figure 6.41. In-situ volumetric flow rates during DC-3 flowback at 0.022" slot width at the pressure of outlet, bottom and top ports.

Figure 6.42. SRT-III produced particles.

Chapter 7: CONCLUSIONS AND FUTURE WORK RECOMMENDATIONS

This chapter consists of two sections: conclusions of the present research (Section 7.1) and recommendations for future work (Section 7.2) to fill the current remaining gaps. These include: (1) the enhancement of SRT operational parameters to eliminate assumptions listed in Section 4.1.1 to yield more reliable testing variables (Section 7.2.1); (2) upgrades of the current SRT-III facility to mimic the SAGD injector flowback scenario using relatively lower testing costs (Section 7.2.2); and (3) suggestions to overcome the SRT-III limitations by using more sophisticated SRT facilities (Sections 7.2.3 and 7.2.4).

7.1 Conclusions

This section summarizes the SAGD injector flowback SRT investigation. It includes the research problem, milestones and focal points, and a brief description of this research contribution in petroleum engineering related to well completion or more precisely in sand control evaluation using an SRT facility.

7.1.1 Problem Statement Revision

This research aimed at evaluating SAGD injector flowback using laboratory SRT facility to assess SAS performance based on several testing variables obtained from possible failure consequences. Moreover, the objective of this research was to propose a systematic methodology to evaluate and downscale testing variables from field to laboratory scale. The industry practices by oil companies, were contradicting designs proposed by previous research (Fattahpour et al., 2018a; Mahmoudi et al., 2018a) that result in considering the industry practices to be conservative when it comes to SAGD injector SAS. The SRT facility design was used to estimate SAS sanding and flow performances to examine the current industry aperture size selection.

7.1.2 Research Findings

This research fulfils the anticipated objectives on several fronts. SAGD injector flowback scenario was mimicked using scientific methodology, presented in Chapter 3, to calculate case-specific operational parameters by the developed SRT-III facility. The key findings in the assessment of operational parameters were related to flowback fluids associated with SAGD injector, which relies on reservoir engineering, production engineering, simulation engineering, geomechanics and thermodynamics fundamental concepts as described in Chapter 4. Moreover, SRT facility design should align with mechanical engineering fundamentals to minimize set-up pressure losses outside the component of interest, as discussed in Chapter 5.

The industry practices for SAS aperture size selection were investigated, in Section 6.1, and the importance to tune SAGD producers, to result in more clearly defined acceptable limits, for SAGD injector were discussed. Nevertheless, the CTP technique yields a better representation at laboratory scale due to the induced consistency in matching intensive properties. On the other hand, CTR results in evident discrepancies among researches, as discussed in Section 6.2.

SAGD injector flowback results were split into two major categories in Section 6.3. The SRT-III experiments show the retained permeability approaches unity in Section 6.3.1. It indicated the insignificance of fines migration even for the smallest tested coupon at 10 thou slot aperture size. SRT-III flowback results emphasized the capacity to perform SRT with essential equipment at low experimental cost; meanwhile, adequate results were maintained. Moreover, flowback duration was confirmed to be dependent on flowback tank pressure, size and associated pressure previously invented term of "dissipation time" was automatically excluded from the flowback duration.

Finally, the importance of using a small slot aperture size to prevent sanding was discussed in Section 6.4. It clarified the confusion that led previous research to unfairly classify the industry selection of SAS apertures size selection as conservative.

7.1.3 Research Contribution

This research went through a few significant focal points. Although the objective was to examine the industry aperture size selection for SAGD injector using SRT, it developed a general methodology for a case-specific problem. The developed methodology worked for SAGD injector and, theoretically, it should work for different producers and injectors. The proposed methodology has changed the orientation of this research from being a particular problem-solution case into a general solution to solve a specific problem. The methodology may help SRT researchers to start deviating from design or parametric analysis into a more scientific approach and standardized procedure for laboratory SRT.

However, the remaining valid question would be, "Is it worth to develop sand control design criteria for SAGD injector for SAS using laboratory SRT?". There is no simple answer because it is tightly dependent on the investigation's purpose. There is no need to develop design criteria to examine industry practices. Moreover, SRT experiments should be conducted based on a case-specific approach for industrial purposes, which was illustrated throughout this research. Nevertheless, the continuous passion will drive researchers more towards developing sand control design criteria for different SAS. Their purpose is to understand the involved physics and mechanisms in sanding and dependency of flow performance on SAS specifications.

7.2 Future Work

This section elaborates on the enhancement of SRT operational parameters and facility upgrades to better represent the actual field SAGD injector flowback scenario. These modifications were not implemented in this research to maintain cost-effective preliminary research in a reasonable time. They would help to eliminate a number of the assumptions stated in Section 4.1.1.

7.2.1 SRT Enhanced Operational Parameters and Selection Criteria

The SAGD well pairs simulation using the CMG 2D-model shows three different regions as discussed in Section 3.1.5 and more precisely illustrated in Figure **3**.**7** and Figure **3**.**8**. This research relied on apparent flowback fluid density to conclude that the late SAGD mode resulted in the highest differential pressure. The assumption should be revised and validated by the actual BHP evaluation for each region. The used technique, in Section 5.3.1, eliminated the capillary forces by removing the wetting phase. It resulted in the worst-case theoretical scenario, yet it is recommended to match fluids saturation and fluid distribution at the pore scale, as suggested in Section 7.2.4.

Furthermore, the natural gas flow correlation, used in NSA in Sections 3.2 and 4.1, was developed for steady-state gas flow in tubing. However, there are other gas flow correlations to predict pressure losses in conduit for transient flow, which better describe the SAGD injector flowback, yet they were not used because, on top of their complexity, they are extremely data demanding. The decision was made to minimize the overall number of assumptions in this research and present the proposed methodology in a simple form.

The pressure drop along the axial SAGD well trajectory was neglected to simplify BHP computation during flowback. Accordingly, when flow rates in the 2D-model were assumed to be equal along the well length, as evaluated in Section 4.1, resulted in an overestimated well flow rate, that overrated tubing pressure drops. It resulted in an overestimated flowback BHP that reduced the differential pressure across the SRT cell. The SAGD injector flowback rates should be revised to match Figure **3.15** trend to yield a closer approximation of required differential pressure across the sand pack (or SRT cell).

Moreover, flowback tank size, referred to in Chapter 5, was arbitrarily chosen based on maximum allowable pressure, which automatically dictated the flowback duration based on tank pressure. Flowback duration is a crucial factor in SRT because it governs sanding and flow performances, which technically considered as unintended subjectivity. Nevertheless, such subjectivity should be eliminated because it has a significant influence on SRT results. Testing results would represent the SAGD injector performance if SRT flowback duration and volumes were matched with field scenarios based on the type of SSSV. However, matching the flowback volumes only would result in an acceptable approximation using SRT-III set-up, as will be discussed in the next section.

On the other hand, SAS selection criteria, discussed in Section 6.1.2, should be developed with new acceptable limits based on reduction in injectivity due to sanding and fines migration, if it occurs. Sanding and retained permeability conclusions were presented in Sections 6.3, based on the five seconds flowback duration for a SAGD well equipped with a surface-controlled SSSV. However, sub-surface controlled SSSV closure time is 30 seconds, which affects the injector flowback duration, as discussed in Section 2.2.4. Although the 30 seconds flowback has a much severe impact, the limitations in carrying out a cost-effective investigation was not possible. Moreover, the goal was to present the proposed methodology throughout this work, as mentioned earlier.

Eventually, CTP used core flooding technique described in Section 6.2, that by default ignores plugging tendency due to matching intensive properties. However, plugging tendency should be fully investigated to find a feasible way to account for SRT using the CTP if necessary.

7.2.2 Testing Facility Upgrade Limitations

This section elaborates on possible upgrades to SRT-III will yield enhanced and cost-effective laboratory testing set-up. The upgrades have not received enough attention because this research is considered as a preliminary investigation to evaluate the research potential in this topic.

SRT-III set-up uses three absolute pressure and two differential pressure transducers, yet the differential pressure during flowback across any neighbouring ports in SRT-III exceeded the limit for differential transducers. However, it is recommended to use at least one absolute transducer with differential transducers during steady-state injection to evaluate more accurate pressure drops used in permeability estimation.

The rotameter used in SRT-III to approximately quantify the volumetric flow rate during steady-state injection can be replaced by a gas mass flow controller (GMFC). GMFC will help to match flow rates accurately at different outlet pressures to evaluate the Klinkenberg effect. However, the GMFC should be used with an automated back pressure regulator to yield reproducible permeability measurements. The used equipment in this research was controlled manually.

All the developed SRT-I, SRT-II and SRT-III set-ups use a flowback tank to mimic the SAGD injector flowback by the transient flow that produces comparable differential pressures in the 2D-model. The used technique to evaluate the volumetric flowback rates that was affected by equipment oscillation, as discussed in Section 6.3.2, induces uncertainty. One possible solution is to add a gas mass flow meter (GMFM) to reduce the associated uncertainty.

However, by using a customized air compressor, one would be able to match flowback volumes and duration in the 2D-model. In addition, it allows the SRT investigation to account for the extended 30 seconds flowback duration, which is nearly impossible to achieve using the flowback tank and its associated transient flow. The flowback would be conducted under steady-state flow conditions, which eases the implementation of the test and eliminates the need for a separate permeability measurement phase.

The used cell head in SRT-III was designed to deliver relatively lower liquid flow rates in SRT experiments. Changing the cell head configuration to allow higher flow rates at lower pressure drop is essential. Moreover, the configuration should produce a linear instead of a conical-shape flow regime. The conical-shape flow regime was assumed to become linear by using four inches of porous media as a porous disk, but it was not proven. A separate study should be conducted to determine the minimum length of porous media required to produce linear flow from the conical-shape flow regime.

Pressure losses optimization is essential, as discussed throughout Chapter 5. The trial and error techniques were used to minimize pressure losses, in this research's set-ups, using the larger diameter and shorter connection lines. Ideal tank discharge time was computed using an SMC online calculator, whereas other pressure losses were neglected. However, proper optimizing pressure losses or pressure drop across the system components, except for the porous media, should be performed. Pressure losses evaluation can be conducted numerically by applying the Navier-Stokes equation or analytically by using Bernoulli's equation.

It is essential to highlight the unavoidable laboratory SRT limitations in this work. The change of SL aperture size due to corrosion and scaling are not incorporated. Accordingly, the results of this research are useful in laboratory results prediction and require validation using field data before judging the industry selection at the field scale.

All the previous recommendations are considered as minor upgrades for SRT-III. Developing more powerful SRT facilities to account for high pressure (HP), high temperature (HT) or even HP-HT applications have pros and cons in SRT, which will be discussed in the next sections.

7.2.3 High-Pressure Set-Up Upgrade

The SRT-III set-up was developed in Section 5.3 to match the differential pressure of SAGD injector during flowback at a laboratory scale. However, matching the differential pressure but not the actual terminal pressures resulted in a significant difference in petrophysical properties, as discussed in Section 4.2.1. HP-SRT set-up would be able to minimize such differences, yet it comes with its own cost. Despite matching the pressure of the terminal using HP-SRT, it automatically matches the effective stress before and during the laboratory flowback, which was not feasible using SRT-III. It is recommended to validate SRT-III results, which depend on matching the differential pressure instead of actual pressures by using HP-SRT at matched terminal pressures to rely on reliable SRT conclusions.

However, SRT-III mechanical equipment specifications may not work for the HP-SRT, which highlights the importance of optimizing pressure losses for any SRT facility during the design phase.

7.2.4 High-Temperature Set-Up Upgrade

The importance of thermodynamics equilibrium was discussed in Sections 2.4 and 4.1and the SRT operational parameters were evaluated accordingly. Although the thermodynamic calculation is solid proof on its own, yet more representative SRT results will be accomplished if the temperature is involved in laboratory testing. HT-SRT is proposed to mimic the in-situ forming of SHS near the SAGD injector wellbore during flowback, as described in Section 4.2.2. Moreover, it simultaneously matches sand pack fluids saturation and fluids distribution at the pore scale in the porous media due to the wettability effect discussed in Section 2.3.2. Steam, water and bitumen should replace air or water-air systems, which were used throughout this research. The HT-SRT associated drawbacks are its high cost and safety considerations, which can be managed to validate SRT-III testing results.

HP-HT SRT facility combines the pros and cons of HP and HT-SRTs at a time, yet it should not be built before the previous two set-ups. Associated problems with such facilities are countless, but certainly, SRT understanding will improve. It can merely reveal whether current SRT practices are reliable or not, and validate the assumptions made in ambient condition SRT and their corresponding results.

REFERENCES

Abram, M., & Cain, G. (2014). Particle-Size Analysis for the Pike 1 Project, McMurray Formation. *Journal of Canadian Petroleum Technology, 53*(06), 339-354. doi:10.2118/173890-PA

Air Density at Varying Temperature and Constant Pressure. (Oct. 31, 2019). *The Engineering Toolbox.* Retrieved from https://www.engineeringtoolbox.com/air-density-specific-weight-d_600.html

Air Dynamic and Kinematic Viscosity. (Oct. 28, 2019). *The Engineering Toolbox.* Retrieved from https://www.engineeringtoolbox.com/air-absolute-kinematic-viscosity-d_601.html

Air Properties Calculator (Nov. 4, 2019). *Peace Software.* Retrieved from https://www.peacesoftware.de/einigewerte/luft_e.html

Alam, M. M., Borre, M. K., Fabricius, I. L., Hedegaard, K., Røgen, B., Hossain, Z., & Krogsbøll, A. S. (2010). Biot's coefficient as an indicator of strength and porosity reduction: Calcareous sediments from Kerguelen Plateau. *Journal of Petroleum Science and Engineering, 70*(3-4), 282-297.

Ballard, T., & Beare, S. P. (2006). *"Sand Retention Testing: The More You Do, the Worse It Gets"*. Paper presented at the SPE International Symposium and Exhibition on Formation Damage Control, Lafayette, Louisiana, USA. https://doi.org/10.2118/98308-MS

Beggs, H. D. (2003). ***Production optimization : using NODAL analysis***. In (2nd ed., pp. 1-7, 20, 37, 54, 58-63, 81-82, 96-97). Tulsa, Okla.: OGCI.

Boggs, S. (2006). ***Principles of sedimentology and stratigraphy***. In (4th ed., pp. 51-71). Upper Saddle River, N.J.: Pearson Prentice Hall.

Boggs, S. (2009). ***Petrology of sedimentary rocks***. In (2nd ed., pp. 3-7, 28-33). New York, USA.: Cambridge University Press.

Canadian Natural Resources Limited (CNRL). (2017). Retrieved from Alberta Energy Regulator (AER): https://www.aer.ca/documents/oilsands/insitu-presentations/2017AthabascaCNRLKirbySAGD11475.pdf

Carbon-Dioxide Properties Calculator (Nov. 5, 2019). *Peace Software.* Retrieved from https://www.peacesoftware.de/einigewerte/co2_e.html

Çengel, Y. A., Boles, M. A. (2001). ***Thermodynamics: an engineering approach***. In (6th ed., pp. 112-132, 139-142). Boston: McGraw-Hill Higher Education.

Chaudhry, A. U. (2003). ***Gas well testing handbook***. In (pp. 102-122). Amsterdam: Elsevier/Gulf Professional Publisher.

Devere-Bennett, N. (2015). *Using Prepack Sand-Retention Tests (SRT's) to Narrow Down Liner/Screen Sizing in SAGD Wells*. Paper presented at the SPE Thermal Well Integrity and Design Symposium, Banff, Alberta, Canada. https://doi.org/10.2118/178443-MS

Discharge Tank Calculation Software. (Nov. 7, 2019). *SMC Design Support Software.* Retrieved from https://mssc.smcworld.com/cdtcs/index.php/cdtcs/app?isReturn=1

Economides, M. J., Hill, A. D., & Ehlig-Economides, C. (2013). ***Petroleum production systems***. In (2nd ed. ed., pp. 57-79). Upper Saddle River, NJ: Prentice Hall.

Ertekin, T., Abou-Kassem, J. H., & King, G. R. (2001). ***Basic applied reservoir simulation***. In (pp. 190, 308-325). Richardson, TX: Society of Petroleum Engineers.

Fattahpour, V., Mahmoudi, M., Roostaei, M., Wang, C., Kotb, O., Nouri, A., . . . Fermaniuk, B. (2018a). *"Sand Control Testing for Steam Injection Wells"*. Paper presented at the SPE

Canada Heavy Oil Technical Conference, Calgary, Alberta, Canada. https://doi.org/10.2118/189766-MS

Fattahpour, V., Mahmoudi, M., Wang, C., Kotb, O., Roostaei, M., Nouri, A., . . . Sutton, C. (2018b). *"Comparative Study on the Performance of Different Stand-Alone Sand Control Screens in Thermal Wells"*. Paper presented at the SPE International Conference and Exhibition on Formation Damage Control, Lafayette, Louisiana, USA. https://doi.org/10.2118/189539-MS

Green, D. W., Willhite, G. P. (1998). ***Enhanced oil recovery***. In (pp. 301-329). Richardson, TX: Henry L. Doherty Memorial Fund of AIME, Society of Petroleum Engineers.

Guo, B., Ghalambor, A., & Lyons, W. C. (2007). ***Petroleum production engineering : a computer-assisted approach***. In (pp. 60-77). Burlington, MA: Gulf Professional Publisher.

Hassanpour, R. M. (2009). *A Review of McMurray Formation Geology in Athabasca Oil Sands* (paper 201). Retrieved from CCG Annual Report 11: http://www.ccgalberta.com/ccgresources/report11/2009-201_mcmurray_formation_geology.pdf

How Does Mass Flow Meter Work? (Nov. 14, 2019). *OMEGA Engineering.* Retrieved from https://www.omega.com/en-us/resources/thermal-mass-flow-meters

In-situ Bitumen Extraction. (Sep. 23, 2018). *Oil Sands Magazine.* Retrieved from http://www.oilsandsmagazine.com/technical/in-situ

Kotb, O. (2018). *An Investigation into Present Sand Control Testing Practices for SAGD Wells.* (Master of Science). University of Alberta,

Lee, J., Wattenbarger, R. A. (1996). ***Gas reservoir engineering***. In (pp. 58-65, 84-85, 131-138, 168-170). Richardson, TX: Henry L. Doherty Memorial Fund of AIME, Society of Petroleum Engineers.

Li, K., & Horne, R. N. (2004). Experimental Study of Gas Slippage in Two-Phase Flow. *SPE Reservoir Evaluation & Engineering, 7*(06), 409-415. doi:10.2118/89038-PA

Mahmoudi, M. (2017). *New Sand Control Design Criteria and Evaluation Testing for Steam Assisted Gravity Drainage (SAGD) Wellbores.* (PhD). University of Alberta,

Mahmoudi, M., Fattahpour, V., Roostaei, M., Kotb, O., Wang, C., Nouri, A., . . . Fermaniuk, B. (2018b). *"An Experimental Investigation into Sand Control Failure Due to Steam Breakthrough in SAGD Wells"*. Paper presented at the SPE Canada Heavy Oil Technical Conference, Calgary, Alberta, Canada. https://doi.org/10.2118/189769-MS

Mahmoudi, M., Fattahpour, V., Velayati, A., Roostaei, M., Kyanpour, M., Alkouh, A., . . . Nouri, A. (2018c). *Risk Assessment in Sand Control Selection: Introducing a Traffic Light System in Stand-Alone Screen Selection*. Paper presented at the SPE International Heavy Oil Conference and Exhibition, Kuwait City, Kuwait. https://doi.org/10.2118/193697-MS

Mahmoudi, M., Fattahpour, V., Wang, C., Kotb, O., Roostaei, M., Nouri, A., . . . Sutton, C. (2018a). *"A Large-Scale Sand Retention Test Facility for Evaluation and Selection of Optimal Standalone Sand Screen for Injection Wells in Thermal Operations"*. Paper presented at the SPE International Conference and Exhibition on Formation Damage Control, Lafayette, Louisiana, USA. https://doi.org/10.2118/189557-MS

Marshall, S. L. (2009). Nonlinear pressure diffusion in flow of compressible liquids through porous media. *Transport in Porous Media, 77*(3), 431.

Methane Density and Specific Weight. (Oct. 28, 2019). *The Engineering Toolbox.* Retrieved from https://www.engineeringtoolbox.com/methane-density-specific-weight-temperature-pressure-d_2020.html

Methane Dynamic and Kinematic Viscosity. (Oct. 28, 2019). *The Engineering Toolbox.* Retrieved from https://www.engineeringtoolbox.com/methane-dynamic-kinematic-viscosity-temperature-pressure-d_2068.html

Methane Properties Calculator (Nov. 5, 2019). *Peace Software.* Retrieved from http://www.peacesoftware.de/einigewerte/methan_e.html

Montero, J. D. (2019). *Design Criteria and Performance Evaluation of Wire-Wrapped Screens for Steam Assisted Gravity Drainage (SAGD) Wellbores.* (Master of Science). University of Alberta,

Montero, J. D., Chissonde, S., Kotb, O., Wang, C., Roostaei, M., Nouri, A., . . . Fattahpour, V. (2018). *A Critical Review of Sand Control Evaluation Testing for SAGD Applications*. Paper presented at the SPE Canada Heavy Oil Technical Conference, Calgary, Alberta, Canada. https://doi.org/10.2118/189773-MS

Montero, J. D., Wang, C., Nouri, A., Haftani, M., Mahmoudi, M., & Fattahpour, V. (2019). *"Assessment of Existing Design Criteria for Wire-Wrapped Screens in Thermal Wells"*. Paper presented at the 53rd U.S. Rock Mechanics/Geomechanics Symposium, New York City, New York.

Nitrogen Properties Calculator (Nov. 5, 2019). *Peace Software.* Retrieved from http://www.peacesoftware.de/einigewerte/stickstoff_e.html

Oil Sand Geology & the Properties of Bitumen. (Sep. 23, 2019). *Oil Sands Magazine.* Retrieved from http://www.oilsandsmagazine.com/technical/properties

Oxygen Properties Calculator (Nov. 5, 2019). *Peace Software.* Retrieved from https://www.peacesoftware.de/einigewerte/o2_e.html

Peters, E. J. (2012a). ***Advanced petrophysics***. In (1st ed., Vol. 2, pp. 153-156, 190-197, 204-206, 254-160). Austin, TX: Live Oak Book Company.

Peters, E. J. (2012b). ***Advanced petrophysics***. In (1st ed., Vol. 1, pp. 213-219). Austin, TX: Live Oak Book Company.

Pope, G. A. (2003). ***Fluid flow through permeable media*** PGE 323 course note. Department of Petroleum and Geosystems Engineering. University of Texas at Austin.

Romanova, U. G., Ma, T., Piwowar, M., Strom, R., & Stepic, J. (2015). *Thermal Formation Damage and Relative Permeability of Oil Sands of the Lower Cretaceous Formations in Western Canada*. Paper presented at the SPE Canada Heavy Oil Technical Conference, Calgary, Alberta, Canada. https://doi.org/10.2118/174449-MS

Roostaei, M., Kotb, O., Mahmoudi, M., Fattahpour, V., Wang, C., Nouri, A., & Fermaniuk, B. (2018). *"An Experimental Investigation into Gravel Pack Performance in Steam-Drive Operations"*. Paper presented at the SPE Western Regional Meeting, Garden Grove, California, USA. https://doi.org/10.2118/190125-MS

RP40, A. P. I. (1998). Recommended practices for core analysis. *Feb*, pp. 117-133.

Shafer, J. L., Boitnott, G. N., & Ewy, R. T. (2008). *"Effective Stress Laws For Petrophysical Rock Properties"*. Paper presented at the SPWLA 49th Annual Logging Symposium, Austin, Texas.

Sidahmed, A. K. (2018). *Optimization of Outflow Control Devices Design in Steam-Assisted Gravity Drainage Models with Wellbore Trajectory Excursions.* (Master of Science). University of Alberta, Sidahmed, A. K., Nouri, A., Kyanpour, M., Nejadi, S., & Fermaniuk, B. (2018). *"Optimization of Outflow Control Devices Placement and Design in SAGD Wells with Trajectory Excursions"*. Paper presented at the SPE International Heavy Oil Conference and Exhibition, Kuwait City, Kuwait. https://doi.org/10.2118/193773-MS

Soong, T. T. (2004). ***Fundamentals of probability and statistics for engineers***. In (1st ed., pp. 196-200). Chichester, England: John Wiley & Sons.

Spec, A. P. I. (1998). 14A. *Specification for Subsurface Safety Valve Equipment, American Petroleum Institute*, pp. 57 & 73.

Steam Viscosity. (Nov. 4, 2019). *The Engineering Toolbox.* Retrieved from https://www.engineeringtoolbox.com/steam-viscosity-d_770.html

Suncor Energy Inc. (2015). Retrieved from Alberta Energy Regulator (AER): https://www.aer.ca/documents/oilsands/insitu-presentations/2015AthabascaSuncorFirebagSAGD8870.pdf

Superheated Steam Table. (Oct. 28, 2019). *TLV: A Steam Specialist Company.* Retrieved from https://www.tlv.com/global/TI/calculator/superheated-steam-table.html

Wilkes, J. O. (2006). ***Fluid mechanics for chemical engineers*** In (3rd ed., pp. 120-129). Upper Saddle River, NJ: Prentice Hall Professional Technical Reference.

Appendix A: 2D CMG model

Table A.1: General STARS Model (Base-Case) Input Data.

property	value	unit	property	value	unit
Cap rock bottom height	110	m	S_{wir}	23%	
Reservoir thickness	30	m	S_{gc}	5%	
Porosity	32%		$S_{or}@k_{row}$	20%	
Horizontal k	1500	md	$S_{or}@k_{rog}$	16%	
Vertical k	825	md	Well pre-heating temperature	220	°C
Bitumen mole fraction	99.99%		Well pre-heating duration	90	day
(C1) mole fraction	0.01%		Injection pressure	2000	kPa
Initial reservoir pressure	1500	kPa	Injection steam quality (SQ)	0.95	
Initial reservoir temperature	7	°C	Production steam-trap temp.	25	°C

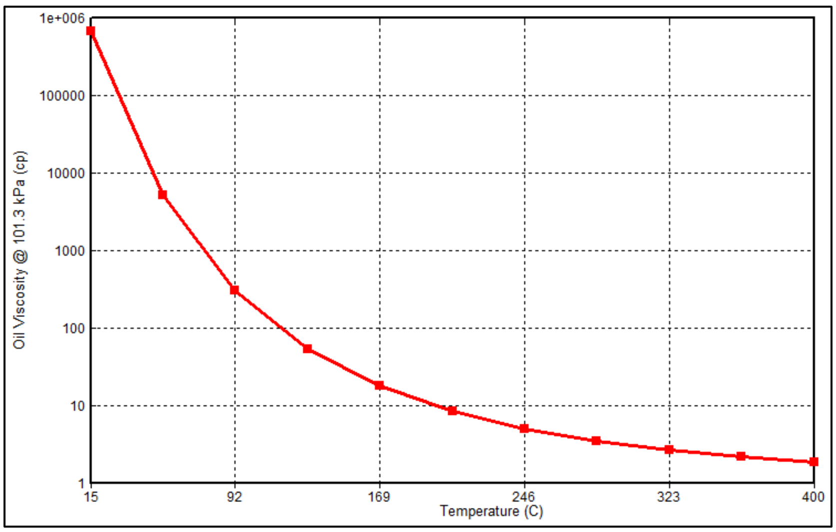

Figure A.1. Oil viscosity versus temperature.

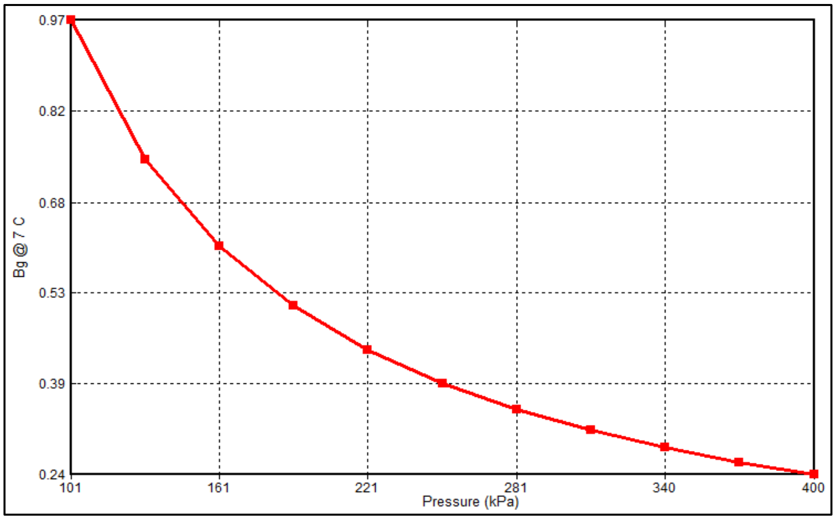

Figure A.2. Gas formation volume factor versus pressure.

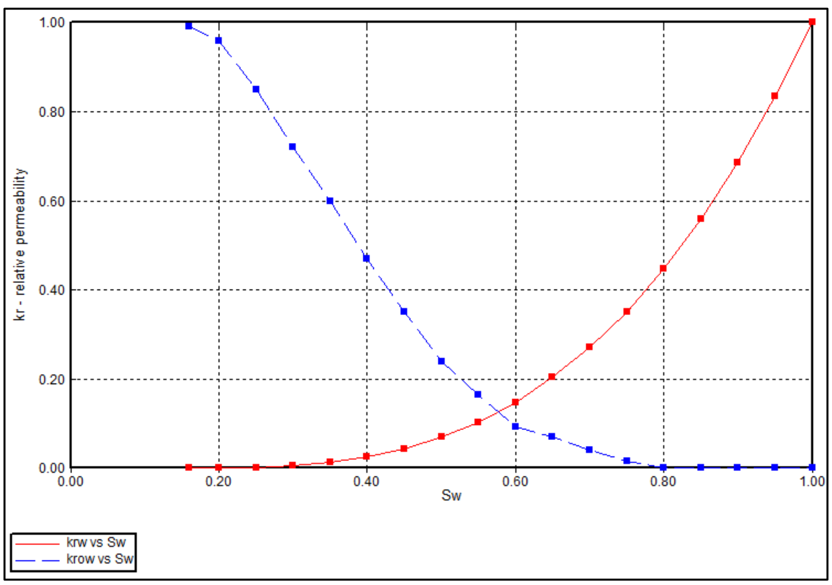

Figure A.3. Oil-water relative permeability curves.

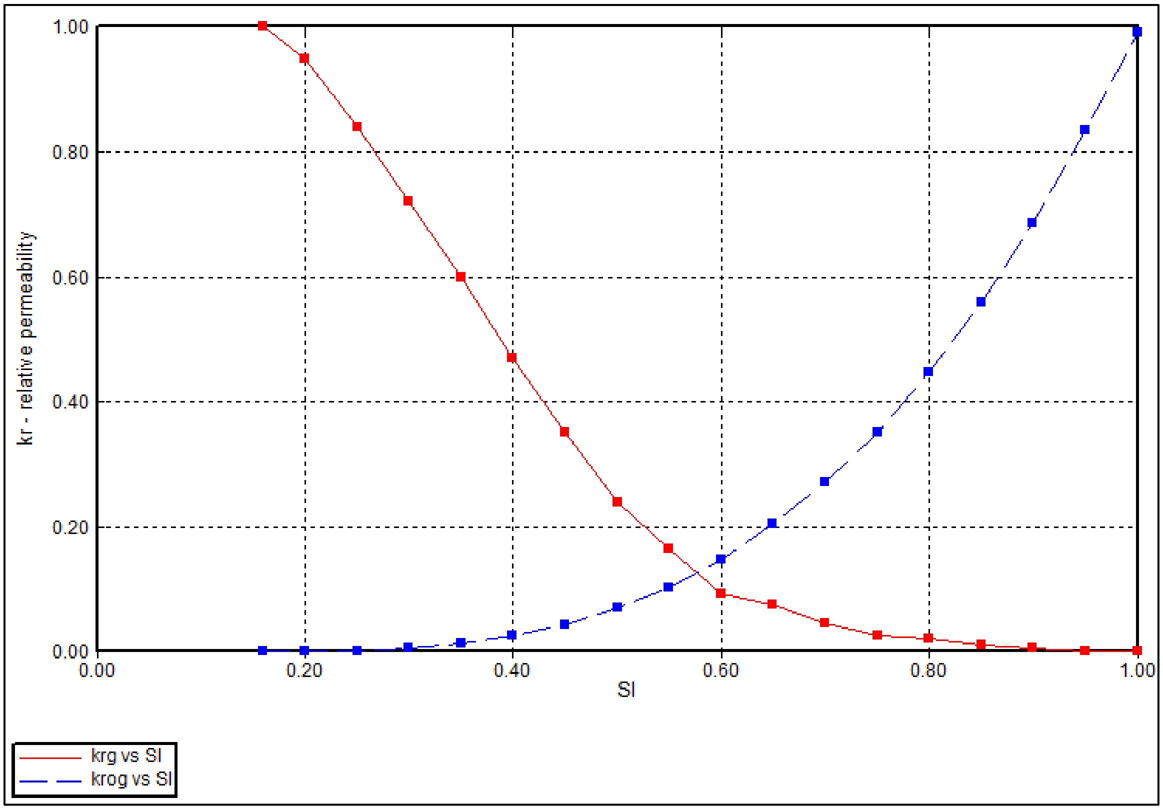

Figure A.4. Oil-gas relative permeability curves.

Table A.2: Injector Well Program During Normal SAGD Operation (2D model).

CMG well definition	Fluid injection
Location [I, J, K]	(75, 1, 47)
Date	Operation/s
January 1, 2013	Created/ start heating
April 1, 2013	Stop heating/ start injection at specified BHP
April 1, 2018	Shut-in

Note: The simulation time step was selected automatically without user interference.

Table A.3: Injector Well Program During SAGD Injector Flowback Operation (2D model).

CMG well definition	Fluid production
Location [I, J, K]	(75, 1, 47)
Date	Operation/s
January 1, 2013	Created/ shut-in
April 1, 2013	Shut-in
April 1, 2018	start production at specified BHP/track changes
April 1, 2018 + 40 seconds	Shut-in/track changes
April 1, 2018 + 150 seconds	Stop changes manual tracking
April 2, 2018	Terminate simulation Run

Note: The simulation time step was selected automatically without user interference until April 1, 2018. Parameters* including the block that contains the well pressures, temperatures, oil, gas, and water block average saturations were monitored until after-flow effects had vanished. Furthermore, oil, gas, and water flow rates, during the 40 seconds flowback, were monitored at 10 seconds time step.

<u>2D model grid (block) size sensitivity analysis</u>

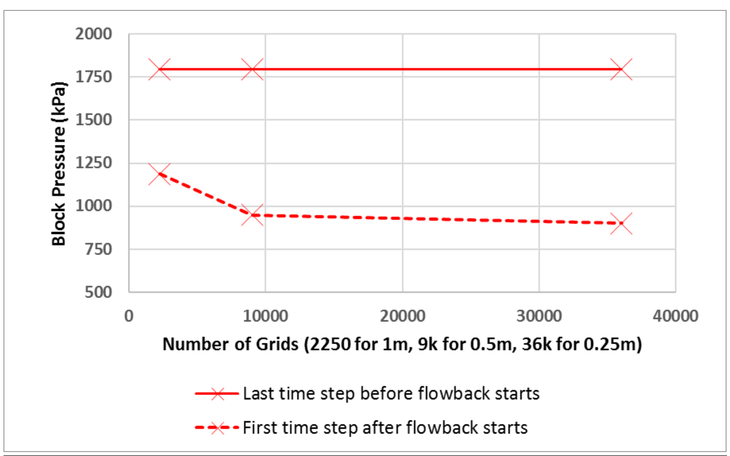

Figure A.5. Effect of number of grids on well-block pressure (BHP of 100 kPa).

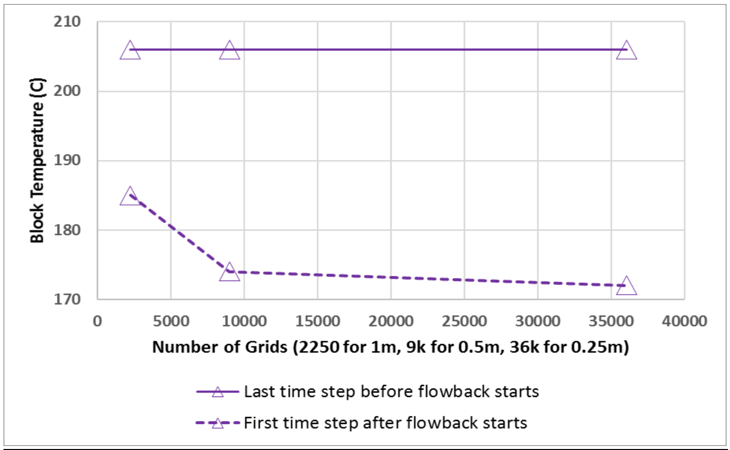

Figure A.6. Effect of number of grids on well-block temperature (BHP of 100 kPa).

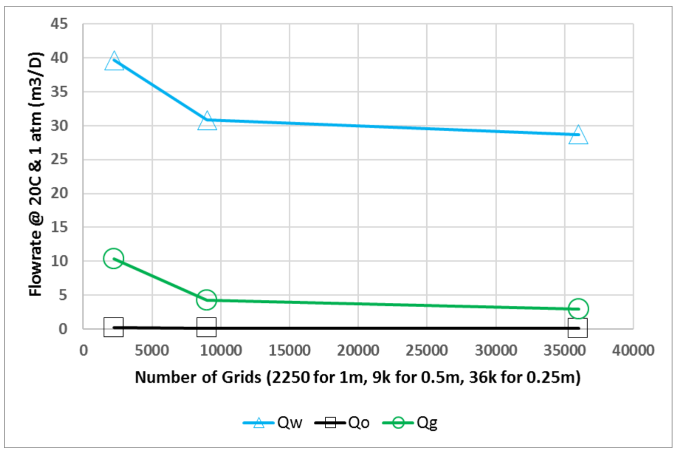

Figure A.7. Effect of number of grids on flow rate during flowback (BHP of 100 kPa).

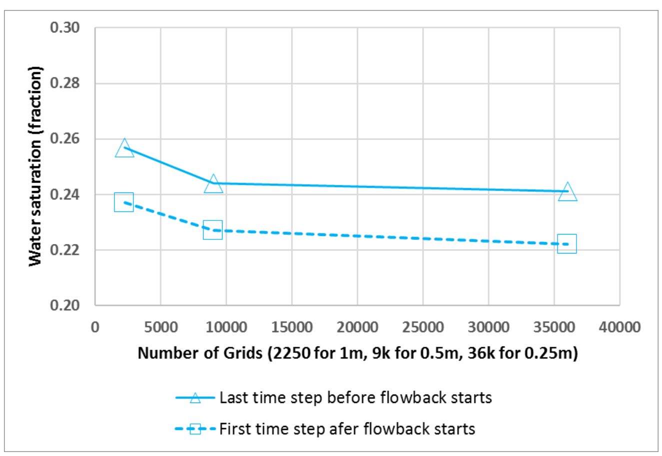

Figure A.8. Effect of number of grids on well-block water saturation (BHP of 100 kPa).

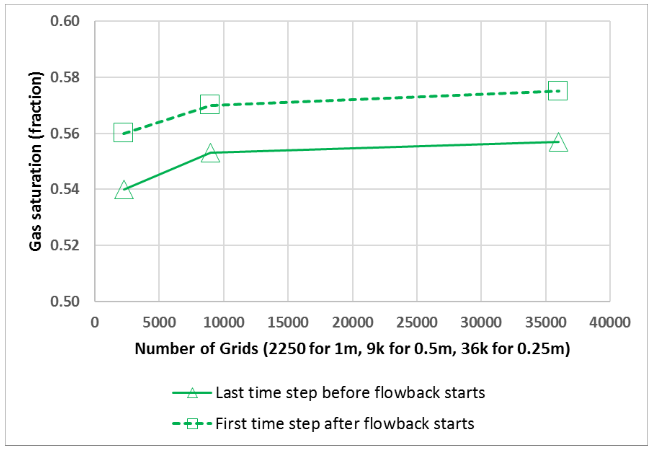

Figure A.9. Effect of number of grids on well-block gas saturation (BHP of 100 kPa).

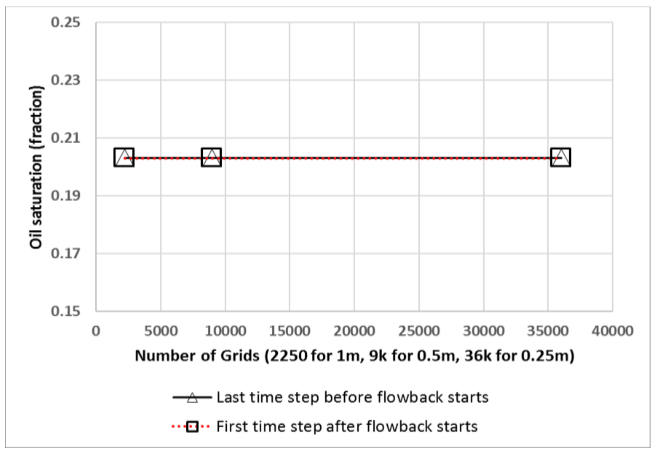

Figure A.10. Effect of number of grids on well-block oil saturation (BHP of 100 kPa).

<u>2D model SAGD operation performance</u>

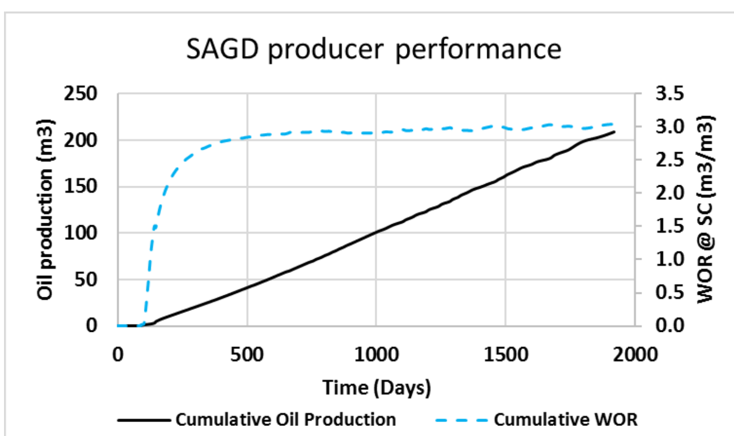

Figure A.11. Cumulative oil production and producing WOR.

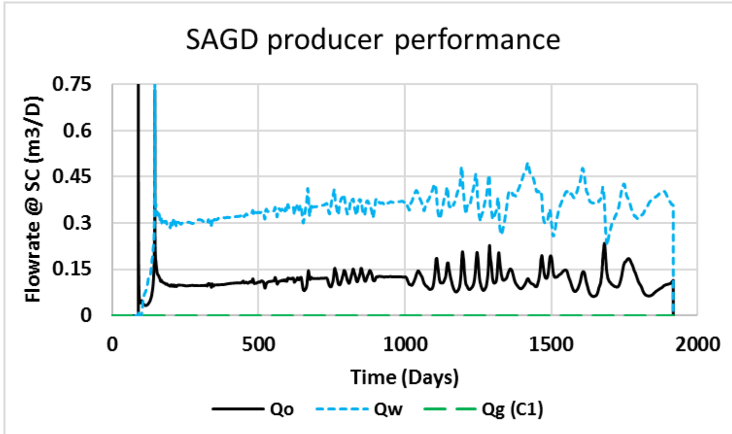

Figure A.12. Oil (bitumen), water and gas (methane) production rates.

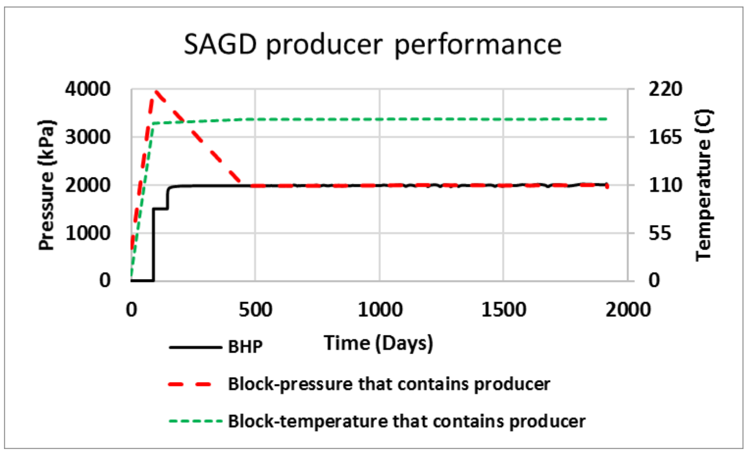

Figure A.13. Producer BHP and well block pressure and temperature.

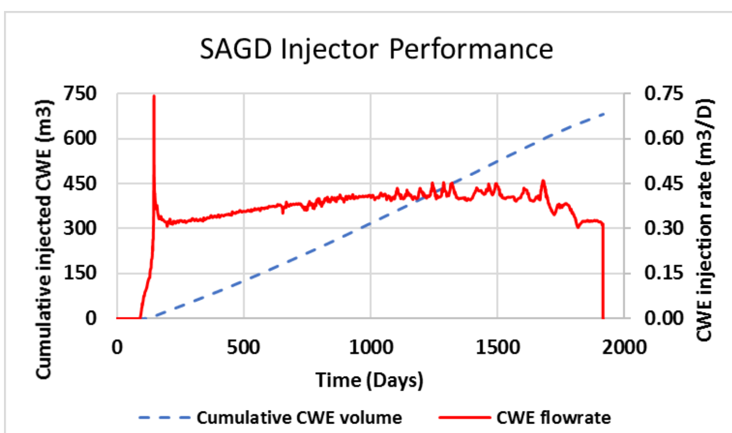

Figure A.14. CWE injection rate and cumulative injected volume.

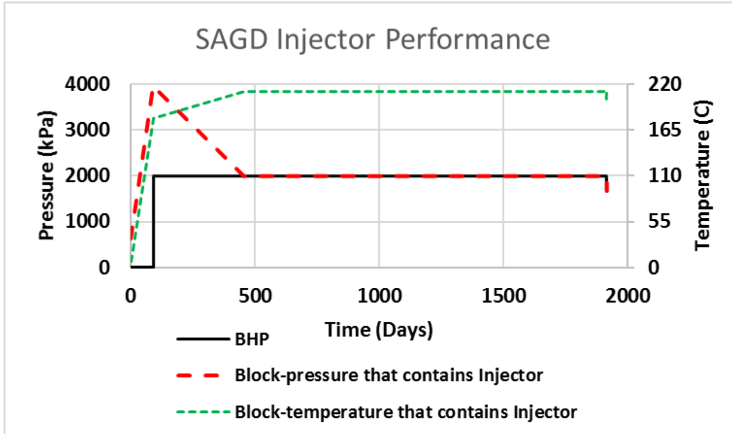

Figure A.15. Injector BHP and well-block pressure and temperature.

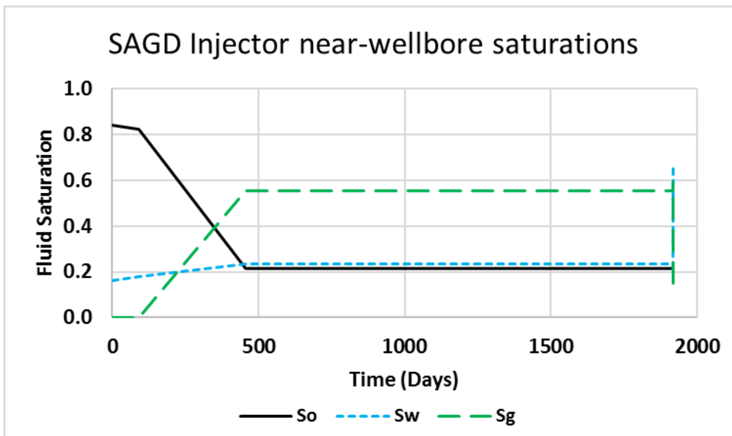

Figure A.16. Injector well-block oil, water and gas saturations.

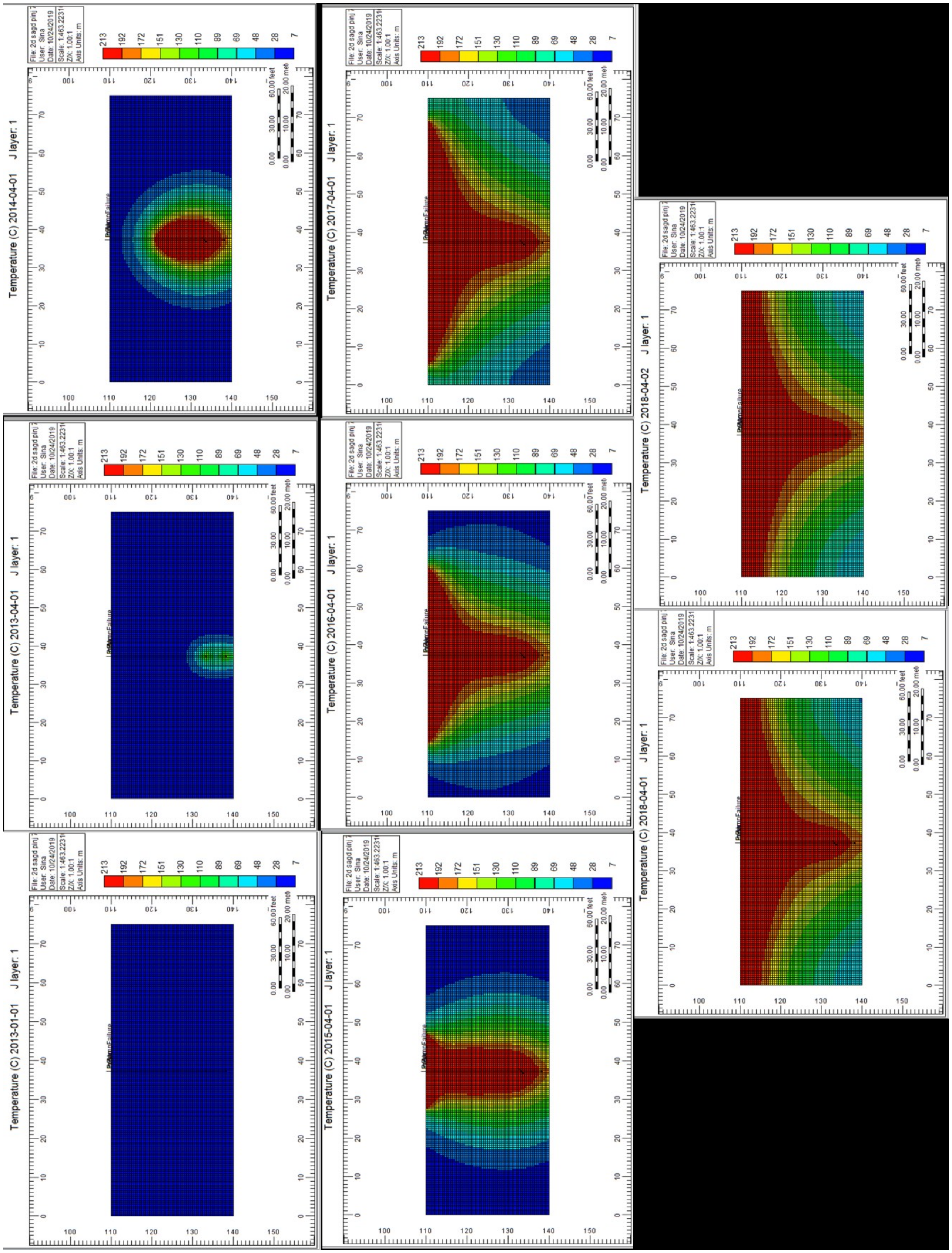

Figure A.17. 2D model steam chamber development over time (date is mentioned on top of each picture).

Appendix B: 2D model flowback BHP in varying injector depth

Table B.1: Injector Flowback BHP Solution for Cap Rock TVD 210 m.

$BHP_{available}^{FB}$	$BHT_{available}^{FB}$	$Q_{CWE}^{2D\ model}$	$\rho_{steam}^{@(BHP\ \&BHT)}$	$Q_{steam}^{2D\ model}$	Q_{steam}^{well}
kPa	°C	$\mathrm{m^3/D}$	$\mathrm{Kg/m^3}$	$\mathrm{m^3/D}$	$\mathrm{m^3/D}$
2600	240.3	139.0	12.376	11231	1,1230,688
2800	240.8	106.3	13.468	7893	7,893,006
2875	241.0	95.2	13.880	6862	6,861,527
2890	241.0	93.0	13.970	6659	6,659,055
2895	241.0	92.3	13.998	6593	6,593,085
2900	241.1	91.6	14.022	6529	6,529,240
3100	241.3	59.9	15.173	3950	3,950,438

Table B.2: Injector Flowback BHP Solution for Cap Rock TVD 210 m.

$BHP_{available}^{FB}$	Q_{steam}^{well}	$T_{average}^{(BHT,WHT)}$	$P_{average}^{(BHP,WHP)}$	$Z_{average}^{(Pavg.,Tavg.)}$	$\bar{\mu}_{SHS}^{(Tavg.)}$
psia	M scf/D	R	psia	---	cP
377	396,556	924.5	195.9	0.946	0.018
406	278,702	925.4	210.4	0.942	0.018
417	242,281	925.8	215.8	0.940	0.018
419	235,131	925.8	216.9	0.940	0.018
420	232,802	925.8	217.3	0.940	0.018
421	230,547	926.0	217.6	0.940	0.018
450	139,490	926.3	232.2	0.936	0.018

Table B.3: Injector Flowback BHP Solution for Cap Rock TVD 210 m; Solution at [$\Delta \mathbf{BHP}$ = -2 psi].

$BHP^{FB}_{available}$	S (Eq. 3.3)	N_{Re} (Eq. 3.4)	f (Eq. 3.5)	$BHP^{FB}_{required}$	$\Delta BHP_{available-required}$
psia	---	---	---	psia	psi
377	2.043E-02	3.17E+07	1.460E-02	710	-333
406	2.050E-02	2.23E+07	1.462E-02	499	-93
417	2.053E-02	1.94E+07	1.462E-02	433	-16
419	2.053E-02	1.88E+07	1.463E-02	421	-2
420	2.053E-02	1.86E+07	1.463E-02	417	3
421	2.053E-02	1.84E+07	1.463E-02	413	8
450	2.061E-02	1.12E+07	1.467E-02	250	200

Table B.4: Injector Flowback BHP Solution for Cap Rock TVD 310 m.

$BHP^{FB}_{available}$	$BHT^{FB}_{available}$	$Q^{2D\ model}_{CWE}$	$\rho^{@(BHP\ \&BHT)}_{steam}$	$Q^{2D\ model}_{steam}$	Q^{well}_{steam}
kPa	°C	$\mathrm{m^3/D}$	$\mathrm{Kg/m^3}$	$\mathrm{m^3/D}$	$\mathrm{m^3/D}$
4300	264.7	171.6	20.757	8269	8,269,066
4305	264.7	170.8	20.788	8214	8,214,403
4310	264.7	169.7	20.818	8151	8,150,975
4315	264.7	168.6	20.848	8088	8,087,730
4320	264.7	167.7	20.879	8030	8,030,078
4325	264.8	166.7	20.901	7976	7,976,173
4350	264.8	162.0	21.053	7693	7,692,870

Table B.5: Injector Flowback BHP Solution for Cap Rock TVD 310 m.

$\boldsymbol{BHP^{FB}_{available}}$	$\boldsymbol{Q^{well}_{steam}}$	$\boldsymbol{T^{(BHT,WHT)}_{average}}$	$\boldsymbol{P^{(BHP,WHP)}_{average}}$	$\boldsymbol{Z^{(Pavg.,Tavg.)}_{average}}$	$\boldsymbol{\bar{\mu}^{(Tavg.)}_{SHS}}$
psia	M scf/D	R	psia	---	cP
623.6	291,981	968.5	319.2	0.925	0.019
624.4	290,051	968.5	319.5	0.925	0.019
625.1	287,811	968.5	319.9	0.925	0.019
625.8	285,578	968.5	320.3	0.925	0.019
626.5	283,542	968.5	320.6	0.925	0.019
627.3	281,639	968.6	321.0	0.925	0.019
630.9	271,635	968.6	322.8	0.924	0.019

Table B.6: Injector Flowback BHP Solution for Cap Rock TVD 310 m; Solution at [Δ**BHP** = 0 psi].

$\boldsymbol{BHP^{FB}_{available}}$	S (Eq. 3.3)	$\boldsymbol{N_{Re}}$ (Eq. 3.4)	$\boldsymbol{f}$ (Eq. 3.5)	$\boldsymbol{BHP^{FB}_{required}}$	$\Delta \boldsymbol{BHP_{available-required}}$
psia	---	---	---	psia	psi
623.6	2.847E-02	2.21E+07	1.462E-02	634.1	-10
624.4	2.847E-02	2.20E+07	1.462E-02	629.9	-6
625.1	2.847E-02	2.18E+07	1.462E-02	625.0	0
625.8	2.847E-02	2.16E+07	1.462E-02	620.2	6
626.5	2.847E-02	2.15E+07	1.462E-02	615.8	11
627.3	2.847E-02	2.13E+07	1.462E-02	611.7	16
630.9	2.850E-02	2.06E+07	1.462E-02	589.7	41

Table B.7: Injector flowback BHP Solution for Cap Rock TVD 410 m.

$BHP_{available}^{FB}$	$BHT_{available}^{FB}$	$Q_{CWE}^{2D\ model}$	$\rho_{steam}^{@(BHP\ \&BHT)}$	$Q_{steam}^{2D\ model}$	Q_{steam}^{well}
kPa	°C	m^3/D	Kg/m^3	m^3/D	m^3/D
5685	281.6	261.6	27.771	9421	9,420,583
5690	281.6	260.4	27.804	9365	9,364,912
5695	281.6	259.1	27.837	9309	9,309,301
5700	281.7	257.9	27.857	9258	9,258,176
5800	281.9	233.0	28.491	8179	8,178,934
5900	283.2	241.3	28.986	8324	8,324,087
6000	283.4	214.8	29.630	7250	7,250,186

Table B.8: Injector flowback BHP Solution for Cap Rock TVD 410 m.

$BHP_{available}^{FB}$	Q_{steam}^{well}	$T_{average}^{(BHT,WHT)}$	$P_{average}^{(BHP,WHP)}$	$Z_{average}^{(Pavg.,Tavg.)}$	$\bar{\mu}_{SHS}^{(Tavg.)}$
psia	$\mathbf{M\ scf/D}$	R	psia	---	cP
824.5	332,641	998.9	419.6	0.912	0.019
825.2	330,675	998.9	420.0	0.912	0.019
826.0	328,711	998.9	420.3	0.912	0.019
826.7	326,906	999.1	420.7	0.912	0.019
841.2	288,798	999.4	427.9	0.91	0.019
855.7	293,924	1001.8	435.2	0.909	0.019
870.2	256,004	1002.1	442.4	0.908	0.019

Table B.9: Injector flowback BHP Solution for Cap Rock TVD 410 m; Solution at [$\Delta \mathbf{BHP}$ = -2 psi].

$BHP^{FB}_{available}$	S (Eq. 3.3)	N_{Re} (Eq. 3.4)	f (Eq. 3.5)	$BHP^{FB}_{required}$	$\Delta BHP_{available-required}$
psia	---	---	---	psia	psi
824.5	3.638E-02	2.52E+07	1.461E-02	831.7	-7
825.2	3.638E-02	2.50E+07	1.461E-02	826.8	-2
826.0	3.638E-02	2.49E+07	1.461E-02	821.9	4
826.7	3.638E-02	2.48E+07	1.461E-02	817.5	9
841.2	3.644E-02	2.19E+07	1.462E-02	721.7	119
855.7	3.640E-02	2.23E+07	1.462E-02	735.0	121
870.2	3.642E-02	1.94E+07	1.462E-02	640.1	230

Appendix C: Rotameter manufacturer's calibration table

$Q_g = Q_g^* \times (\rho_{(P\ top)}/\rho_{(P\ atmospheric)})$ (Eq. C.1)

$\rho_{gas} = (P \times M_{wt})/(z \times R \times T)$ (Eq. C.2)

$Q_g = Q_g^* \times (P_{top}/P_{atmospheric})$ (Eq. C.3)

Table C.1: Rotameter Calibration Table.

Rotameter	Qg*	Qg*	P top	Qg	P top	Qg	P top	Qg
reading	L/min	rcf/D	psi	scf/D	psi	scf/D	psi	scf/D
130	51.787	2634	30.6	5478	73.8	13221	103.2	18485
120	47.220	2401	30.6	4995	73.8	12055	103.2	16855
110	43.006	2187	30.6	4550	73.8	10980	103.2	15351
100	38.650	1965	30.6	4089	73.8	9867	103.2	13796
90	34.548	1757	30.6	3655	73.8	8820	103.2	12332
80	30.479	1550	30.6	3224	73.8	7781	103.2	10879
70	26.271	1336	30.6	2779	73.8	6707	103.2	9377
60	22.204	1129	30.6	2349	73.8	5669	103.2	7926
50	18.068	919	30.6	1911	73.8	4613	103.2	6449
40	14.459	735	30.6	1530	73.8	3691	103.2	5161
30	10.506	534	30.6	1111	73.8	2682	103.2	3750
20	6.523	332	30.6	690	73.8	1665	103.2	2328
10	2.924	149	30.6	309	73.8	747	103.2	1044

Appendix D: Klinkenberg permeability calculation

$$Q_g^{sc} = K_g \times \frac{\alpha_c\, A\, \left(\Phi^2_{upstream} - \Phi^2_{downstream}\right)}{\bar{T}\ \bar{z}\ \overline{\mu_g}\ L} \qquad \text{(Eq. D.1)}$$

$$Q_g^{sc} = K_g \times (x - axis) \qquad \text{(Eq. D.2)}$$

Table F.1: Eq. D.1 Parameters.

Term	Magnitude	USC Unit
L	1.017	ft
A	0.196	ft^2
T	520	R
β	0.0197	(L/min)/(scf/D)
μg	0.01791	cP
α_c	0.1119	
z	1.0	

Table D.2: Klinkenberg Permeability Calculation Used in **Figure 5.13**.

Parameter	Qg*	Qg	x-axis	Top Pressure	Outlet Pressure	Average Pressure	Average Pressure Reciprocal	K
units	rcf/D	scf/D	scf/D-md	psia	psia	psia	1/psia	md
K1	1965	4089	1.63	30.58	15.26	22.9	0.044	2508
K2	1965	11194	6.41	83.72	65.16	74.4	0.013	1745
K3	1965	15575	10.61	116.49	94.86	105.7	0.009	1468
K1'	1965	3887	1.44	29.07	14.92	22.0	0.045	2690
K2'	1965	11350	6.73	84.89	65.64	75.3	0.013	1687
K3'	1965	15777	11.11	118.03	95.60	106.8	0.009	1421

K1, K2 and K3 are the initial permeabilities when back pressure regulator was set at 0, 50, and 80 psig, respectively; however, K1’, K2’ and K3’ are the final permeabilities when back pressure regulator was set at 0, 50 and 80 psig.

Table D.2: Klinkenberg Permeability Calculation Used in **Figure 5.14**.

Parameter	Qg*	Qg	x-axis	Top Pressure	Outlet Pressure	Average Pressure	Average Pressure Reciprocal	K
units	rcf/D	scf/D	scf/D-md	psia	psia	psia	1/psia	md
K1	1965	4089	1.63	30.58	15.26	22.9	0.044	2508
K2	735	3691	2.79	73.80	65.16	69.5	0.014	1325
K3	534	3750	3.82	103.18	94.86	99.0	0.010	981
K1'	1965	3887	1.44	29.07	14.92	22.0	0.045	2690
K2'	735	3721	2.85	74.40	65.64	70.0	0.014	1307
K3'	534	3728	3.21	102.57	95.60	99.1	0.010	1163

K1, K2 and K3 are the initial permeabilities when back pressure regulator was set at 0, 50, and 80 psig, respectively; however, K1', K2' and K3' are the final permeabilities when back pressure regulator was set at 0, 50 and 80 psig.

Appendix E: Permeability measurements under variable stress

Appendices C and D were used in the calculation for this appendix.

Table E.1: Permeability Calculation at (50 psig Axial Stress) Used in **Figure 5.20**.

rotameter	Q_g^*	Q_g	x-axis	Top pressure	Outlet pressure	Mean pressure
units	rcf/D	scf/D	scf/D-md	psia	psia	psia
20	331.7	361.0	0.110	16.00	14.44	15.22
40	735.3	884.8	0.241	17.69	14.45	16.07
60	1129.1	1508.7	0.409	19.64	14.48	17.06
80	1550.0	2270.5	0.587	21.53	14.52	18.03
100	1965.5	3167.2	0.809	23.69	14.58	19.14

Table E.2: Permeability Calculation at (100 psig Axial Stress) Used in **Figure 5.20**.

rotameter	Q_g^*	Q_g	x-axis	Top pressure	Outlet pressure	Mean pressure
units	rcf/D	scf/D	scf/D-md	psia	psia	psia
20	331.7	359.4	0.105	15.93	14.44	15.18
40	735.3	886.0	0.243	17.71	14.45	16.08
60	1129.1	1505.2	0.405	19.60	14.47	17.04
80	1550.0	2289.3	0.604	21.71	14.53	18.12
100	1965.5	3192.9	0.829	23.88	14.59	19.24

Table E.3: Permeability Calculation at (150 psig Axial Stress) Used in **Figure 5.20**.

rotameter	Q_g^*	Q_g	x-axis	Top pressure	Outlet pressure	Mean pressure
units	rcf/D	scf/D	scf/D-md	psia	psia	psia
20	331.7	362.4	0.115	16.06	14.44	15.25
40	735.3	898.1	0.263	17.95	14.45	16.20
60	1129.1	1538.3	0.444	20.03	14.48	17.25
80	1550.0	2346.3	0.660	22.25	14.52	18.39
100	1965.5	3272.5	0.897	24.48	14.59	19.53

Table E.4: Permeability Calculation at (200 psig Axial Stress) Used in **Figure 5.20**.

rotameter	Q_g^*	Q_g	x-axis	Top pressure	Outlet pressure	Mean pressure
units	rcf/D	scf/D	scf/D-md	psia	psia	psia
20	331.7	364.4	0.123	16.15	14.42	15.29
40	735.3	905.3	0.276	18.10	14.45	16.27
60	1129.1	1559.9	0.471	20.31	14.47	17.39
80	1550.0	2388.3	0.702	22.65	14.52	18.59
100	1965.5	3329.0	0.945	24.90	14.59	19.74

Table E.5: Permeability Calculation at (250 psig Axial Stress) Used in **Figure 5.20**.

rotameter	Q_g^*	Q_g	x-axis	Top pressure	Outlet pressure	Mean pressure
units	rcf/D	scf/D	scf/D-md	psia	psia	psia
20	331.7	366.1	0.128	16.22	14.42	15.32
40	735.3	916.5	0.296	18.32	14.43	16.38
60	1129.1	1580.5	0.497	20.58	14.47	17.52
80	1550.0	2418.3	0.731	22.94	14.52	18.73
100	1965.5	3383.5	0.992	25.31	14.59	19.95

Table E.6: Permeability Calculation at (300 psig Axial Stress) Used in **Figure 5.20**.

rotameter	Q_g^*	Q_g	x-axis	Top pressure	Outlet pressure	Mean pressure
units	rcf/D	scf/D	scf/D-md	psia	psia	psia
20	331.7	366.6	0.129	16.25	14.43	15.34
40	735.3	921.2	0.303	18.42	14.45	16.43
60	1129.1	1588.3	0.506	20.68	14.48	17.58
80	1550.0	2445.5	0.760	23.19	14.51	18.85
100	1965.5	3424.1	1.029	25.61	14.58	20.10

Table E.7: Permeability Calculation at (100 psig Axial Stress) Used in **Figure 5.21**.

rotameter	Q_g^*	Q_g	x-axis	Top pressure	Outlet pressure	Mean pressure
units	rcf/D	scf/D	scf/D-md	psia	psia	psia
20	331.7	366.9	0.135	16.26	14.36	15.31
40	735.3	921.6	0.308	18.42	14.38	16.40
60	1129.1	1600.0	0.525	20.83	14.41	17.62
80	1550.0	2450.8	0.769	23.24	14.45	18.85
100	1965.5	3431.1	1.039	25.66	14.52	20.09

Table E.8: Permeability Calculation at (150 psig Axial Stress) Used in **Figure 5.21**.

rotameter	Q_g^*	Q_g	x-axis	Top pressure	Outlet pressure	Mean pressure
units	rcf/D	scf/D	scf/D-md	psia	psia	psia
20	331.7	367.7	0.137	16.30	14.38	15.34
40	735.3	921.9	0.308	18.43	14.39	16.41
60	1129.1	1594.6	0.519	20.76	14.40	17.58
80	1550.0	2447.6	0.765	23.21	14.46	18.84
100	1965.5	3442.1	1.048	25.74	14.53	20.14

Table E.9: Permeability Calculation at (200 psig Axial Stress) Used in **Figure 5.21**.

rotameter	Q_g^*	Q_g	x-axis	Top pressure	Outlet pressure	Mean pressure
units	rcf/D	scf/D	scf/D-md	psia	psia	psia
20	331.7	366.7	0.133	16.25	14.38	15.31
40	735.3	924.1	0.312	18.47	14.39	16.43
60	1129.1	1594.3	0.518	20.76	14.41	17.58
80	1550.0	2448.1	0.766	23.22	14.46	18.84
100	1965.5	3444.2	1.050	25.76	14.53	20.15

Table E.10: Permeability Calculation at (250 psig Axial Stress) Used in **Figure 5.21**.

rotameter	Q_g^*	Q_g	x-axis	Top pressure	Outlet pressure	Mean pressure
units	rcf/D	scf/D	scf/D-md	psia	psia	psia
20	331.7	367.1	0.134	16.27	14.38	15.32
40	735.3	924.0	0.311	18.47	14.39	16.43
60	1129.1	1593.2	0.516	20.74	14.42	17.58
80	1550.0	2443.0	0.760	23.17	14.47	18.82
100	1965.5	3451.6	1.056	25.82	14.54	20.18

Table E.11: Permeability Calculation at (300 psig Axial Stress) Used in **Figure 5.21**.

rotameter	Q_g^*	Q_g	x-axis	Top pressure	Outlet pressure	Mean pressure
units	rcf/D	scf/D	scf/D-md	psia	psia	psia
20	331.7	367.1	0.134	16.27	14.39	15.33
40	735.3	925.3	0.314	18.50	14.39	16.44
60	1129.1	1593.3	0.516	20.74	14.42	17.58
80	1550.0	2465.2	0.783	23.38	14.47	18.92
100	1965.5	3458.3	1.062	25.86	14.54	20.20